MITIGATING THE ADVERSE EFFECTS OF INTERNAL LATERAL IMPACTS IN STRUCTURES EQUIPPED WITH FRICTIONAL ISOLATORS

Original
MITIGATING THE ADVERSE EFFECTS OF INTERNAL LATERAL IMPACTS IN STRUCTURES EQUIPPED WITH FRICTIONAL ISOLATORS / AUAD ALVAREZ, GASPAR ANDRES. - (2022 Sep 07), pp. 1-254.

Publisher:
Politecnico di Torino

Published
DOI:

PONTIFICIA UNIVERSIDAD CATOLICA DE CHILE
SCHOOL OF ENGINEERING

MITIGATING THE ADVERSE EFFECTS OF INTERNAL LATERAL IMPACTS IN STRUCTURES EQUIPPED WITH FRICTIONAL ISOLATORS

GASPAR A. AUAD ALVAREZ

Thesis submitted to Pontificia Universidad Católica de Chile and Politecnico di Torino in partial fulfillment of the requirements for the Degree of Doctor in Engineering Sciences and Dottore in Ingegneria Civile e Ambientale.

Advisors:
JOSE LUIS ALMAZAN CAMPILLAY
PAOLO CASTALDO

Santiago de Chile, (September, 2022)

PONTIFICIA UNIVERSIDAD CATOLICA DE CHILE
SCHOOL OF ENGINEERING

MITIGATING THE ADVERSE EFFECTS OF INTERNAL LATERAL IMPACTS IN STRUCTURES EQUIPPED WITH FRICTIONAL ISOLATORS

GASPAR ANDRÉS AUAD ÁLVAREZ

Members of the Committee:

JOSE LUIS ALMAZÁN Jose Luis Almazan

PAOLO CASTALDO Paolo Castaldo

DIEGO LÓPEZ-GARCÍA Diego Lopez-Garcia

ROSITA JÜNEMANN Rosita Junemann

RAFAEL RUIZ Rafael Ruiz

GASTÓN FERMANDOIS Gaston Fermandois

LUCA GIORDANO

GUSTAVO LAGOS Gustavo Lagos

Thesis submitted to Pontificia Universidad Católica de Chile and Politecnico di Torino in partial fulfillment of the requirements for the Degree of Doctor in Engineering Sciences and Dottore in Ingegneria Civile e Ambientale.

Santiago of Chile, September, 2022

To my wife Javiera and my son Román, who accompanied me on this journey

ACKNOWLEDGMENTS

I would like to thank my advisor at Pontificia Universidad Católica de Chile, Professor Jose Luis Almazán, for accepting me as his doctoral student and allowing me to develop a topic that he had already put on hold some years ago. From his great scientific experience, Professor Almazán guided me in this beautiful project.

I would like to thank Professor Paolo Castaldo from Politecnico di Torino for accepting me as his (first) foreign doctoral student. I have felt his confidence in me from the first contact we had. Professor Paolo Castaldo was probably the most important person for my family and me upon arriving in a new country days before the start of the COVID-19 pandemic. I will always be grateful.

A would like to thank Dirección de Postgrado and Vicerrectoria de Investigación at Pontificia Universidad Católica de Chile, and Scuole di Dottorato (ScuDo) at Politecnico di Torino for supporting my doctoral research and giving me the opportunity to carry out a dual-degree Ph.D. program.

Finally, I thank the Agencia Nacional de Investigación y Desarrollo (ANID) for supporting this research through the ANID-PCHA/Doctorado Nacional/2018-21180434 grant.

CONTENTS

Pág.

LIST OF TABLES

LIST OF FIGURES

ABSTRACT

This dissertation investigates two alternatives to mitigate the problems generated by internal lateral impacts in structures equipped with frictional isolators. Seismic isolation represents one of the best alternatives in protecting structures. Extreme ground motions that induce internal lateral impacts between sliders of frictional devices and restraining rims of sliding surfaces jeopardize the benefits of using this technology. The first part of this investigation assesses using variable curvature isolators with smooth-hardening behavior as a strategy to mitigate the adverse effects of internal impacts. Although the use of smooth-hardening isolators decreases the probability of observing internal impacts or decreases their intensity, in some cases, employing these devices can decrease the seismic performance of base-isolated structures. Driven by this limitation, the second part of this study presents a new frictional device. The Lateral Impact Resilient Double Concave Friction Pendulum (LIR-DCFP) bearing has an enhanced inner slider. The presence of a plane high-friction interface inside the inner slider provides a mechanism of limiting the maximum force during an internal impact. Furthermore, due to the presence of an internal gap, an additional source of energy dissipation is generated. The last part of this research presents a comprehensive parametric analysis aiming to determine the structural properties that highlight the benefits of using LIR-DCFP devices. LIR-DCFP bearings are recommended for structures designed to behave essentially elastic if the lateral capacity of the isolation system is not overcome. If the non-linear response of the superstructure is exhibited even in the absence of internal impacts, using the new isolator is suggested for rigid structures or for building with relatively high post-yield stiffness. Reductions in the probabilities of exceeding ductility demand thresholds up to 20% are achieved by using LIR-DCFP bearings.

Keywords: Seismic isolation; three-dimensional formulation; Friction Pendulum System; LIR-DCFP isolator; internal lateral impact; high-friction interface; seismic reliability; ductility demand.

RESUMEN

Esta tesis investiga dos alternativas para mitigar los problemas generados por impactos laterales internos en estructuras equipadas con aisladores friccionales. El aislamiento sísmico representa una de las mejores alternativas en la protección de estructuras. Los terremotos extremos que inducen impactos laterales internos entre los deslizadores de los dispositivos de fricción y los bordes de contención de las superficies de deslizamiento ponen en peligro los beneficios del usar esta tecnología. La primera parte de esta investigación evalúa el uso de aisladores de curvatura variable con comportamiento de endurecimiento suave como estrategia para mitigar los efectos adversos de los impactos internos. Aunque el uso de aisladores de endurecimiento suave disminuye la probabilidad de observar impactos internos o disminuye su intensidad, en algunos casos, el empleo de estos dispositivos puede disminuir el desempeño sísmico de las estructuras con asilamiento sísmico. Impulsado por esta limitación, la segunda parte de este estudio presenta un nuevo aislador. El Péndulo de Fricción Cóncavo Doble Resistente al Impacto Lateral (LIR-DCFP) tiene un deslizador interno mejorado. La presencia de una interfaz plana de alta fricción dentro del deslizador interno proporciona un mecanismo para limitar la fuerza máxima durante un impacto interno. Más aún, debido a la presencia de un *gap* interno, se genera una fuente adicional de disipación de energía. La última parte de esta investigación presenta un análisis paramétrico integral con el objetivo de determinar las propiedades estructurales que resaltan los beneficios del uso de dispositivos LIR-DCFP. Los aisladores LIR-DCFP se recomiendan para estructuras diseñadas para comportarse esencialmente elásticas si no se supera la capacidad lateral del sistema de aislamiento. Si la respuesta no lineal de la superestructura se presenta incluso en ausencia de impactos internos, se sugiere usar el nuevo aislador para estructuras rígidas o para edificios con una rigidez post-fluencia relativamente alta. Reducciones de hasta un 20% en las probabilidades de exceder los umbrales de demanda de ductilidad se logran mediante el uso de rodamientos LIR-DCFP.

Palabras clave: Aislamiento sísmico; formulación tridimensional; Sistema Péndulo de Fricción; aislador LIR-DCFP; impacto lateral interno; interfaz de alto roce; confiabilidad sísmica; demanda de ductilidad.

1. INTRODUCTION

During the last four decades, Earthquake Engineering has developed two great ideas that have contributed to creating a new paradigm for the discipline: (i) the Performance-Based Design philosophy (PBD) and (ii) Seismic Protection Technologies (SPTs). Among SPTs, one of the most significant influences has been made by Seismic Isolation Systems (SISs). On the one hand, the objective of the conventional earthquake-resistant design is to avoid structural collapse and protect the lives of people during the design earthquake (DE). On the other hand, structures equipped with SISs aim to ensure continuity of operation after the DE. In the last 30 years, during the occurrence of high magnitude earthquakes (i.e., Loma Prieta, USA, 1989; Northridge, USA, 1994; Kobe, Japan, 1995; Maule, Chile, 2010), structures equipped with SISs have shown a better seismic performance than fixed-base structures (Chimamphant & Kasai, 2016; Nagarajaiah & Xiaohong, 2000; Shenton & Lin, 1993).

Conventional SIS involves placing a laterally-flexible and vertically-rigid horizontal interface between the ground and the structure. If the superstructure behaves as a rigid body, this system generates three low-frequency lateral-torsional modes and three high-frequency vertical-rocking modes. The elongation of the natural periods of the dynamic system is one of the most effective strategies for protecting non-slender buildings from strong ground motions.

Two of the most used devices in the materialization of SISs are the elastomeric isolator (Kelly, 1993) and the Friction Pendulum System (FPS) (Zayas et al., 1990). An illustration of the FPS bearing is shown in Figure 1-1. This doctoral research is focused mainly on the numerical development and evaluation of seismic isolators that work based on transferring frictional forces.

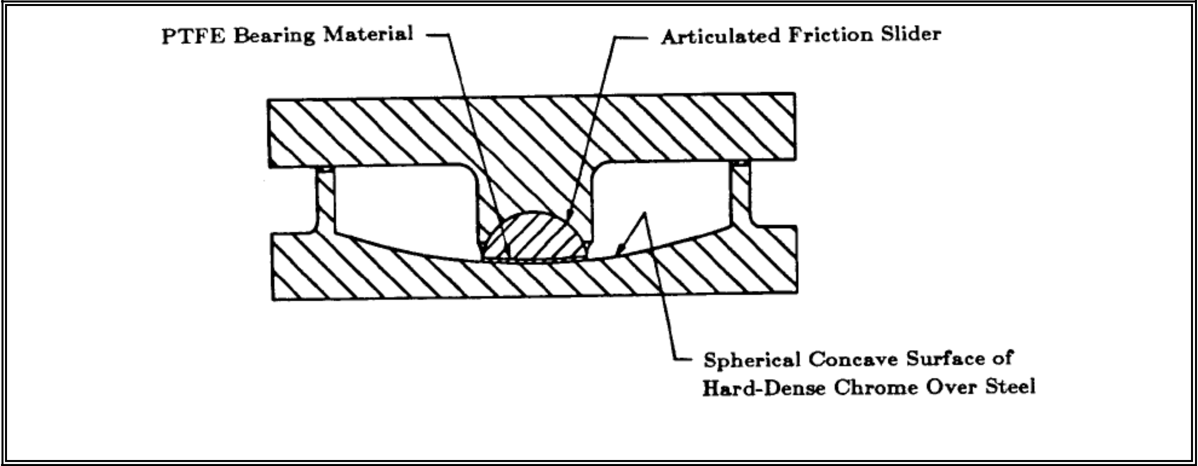

Figure 1-1: Illustration of the Friction Pendulum System (Zayas et al., 1990)

1.1 Achieving seismic isolation using frictional devices

In general, friction pendulum bearings (FPBs) consist of single or multiple sliding concave plates and single or multiple inner sliders. The numbers of plates and sliders depend on the specific configuration of the device. While the concave plates provide the re-centering capacity, the energy dissipation is provided by the friction force developed between the different bodies of the isolator. These frictional devices have demonstrated an outstanding performance against high magnitude earthquakes (M. Constantinou et al., 1990; Fenz & Constantinou, 2006, 2008b, 2008a; Mokha et al., 1990; Morgan & Mahin, 2010). The fundamental idea materialized in the FPS consists of only one spherical concave surface of hard-dense chrome over steel and one articulated friction slider. The lateral force transmitted by the FPS bearing given a lateral displacement v and a velocity of displacement $\dot{v}$ of the articulated friction slider and assuming small displacements can be expressed using the following equation:

$$f = f_p + f_\mu = \frac{N}{R}v + \mu N\, sign(\dot{v}) \tag{1.1}$$

in which f is the total lateral force, $f_p = \frac{N}{R}v$ is the pendular force, $f_\mu = \mu N\, sign(\dot{v})$ is the friction force, N is the developed normal force, R is the radius of curvature of the sliding surface and, $sign()$ is the signum function. All the mentioned forces are plotted in Figure 1-2 for incremental cyclic displacement imposed on the top plate of the isolator.

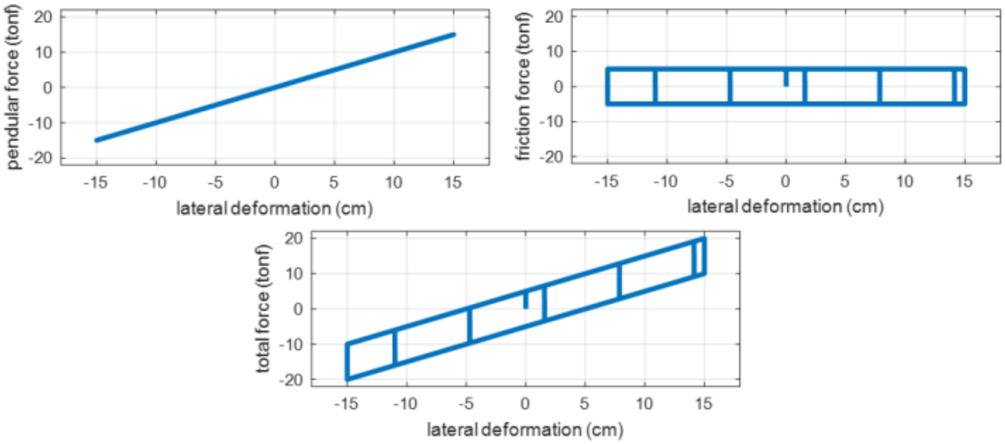

Figure 1-2: Lateral forces transmitted by the Friction Pendulum System (FPS) bearing

Among seismic isolators with multiple sliding surfaces (SIMSSs), the double concave Frictional Pendulum (DCFP) bearing (Fenz & Constantinou, 2006) and the triple concave Frictional Pendulum (TCFP) bearing (Fenz & Constantinou, 2008b, 2008a) are commonly used in real projects. A representation of both SIMSSs is presented in Figure 1-3. The DCFP bearing consists of two facing concave surfaces and an articulated slider. This articulated body is required to accommodate differential movements along the two sliding surfaces. A non-articulated slider can be used if the two surfaces present identical geometry and the same friction coefficient. As the DCFP bearing, the TCFP bearing consists of two facing concave surfaces. The main difference is that an internal nested slider assembly separates the two sliding surfaces. This slider consists of two concave plates separated by a non-articulated slider. Unlike the FPS bearing, both DCFP and TCFP bearings exhibit passive adaptive behavior. Both described isolators can accommodate larger displacements in a smaller isolator size. Even more, if different radii and friction coefficients are chosen to construct the sliding surfaces, the isolator will change its stiffness and damping at specific displacements.

Other SIMSSs devices based on concave surfaces and with adaptive behavior are the Spherical Isolation Pendulum-Adaptive (SIP-Adaptive) bearing (Weber et al., 2018), the Trench Friction Pendulum System (TFPS) (Tsai, Chen, & Lu, 2006), and the Multiple Trench Friction Pendulum System (Tsai & Lin, 2009). These last two seismic isolators have trench-curved sliding surfaces instead of spherical.

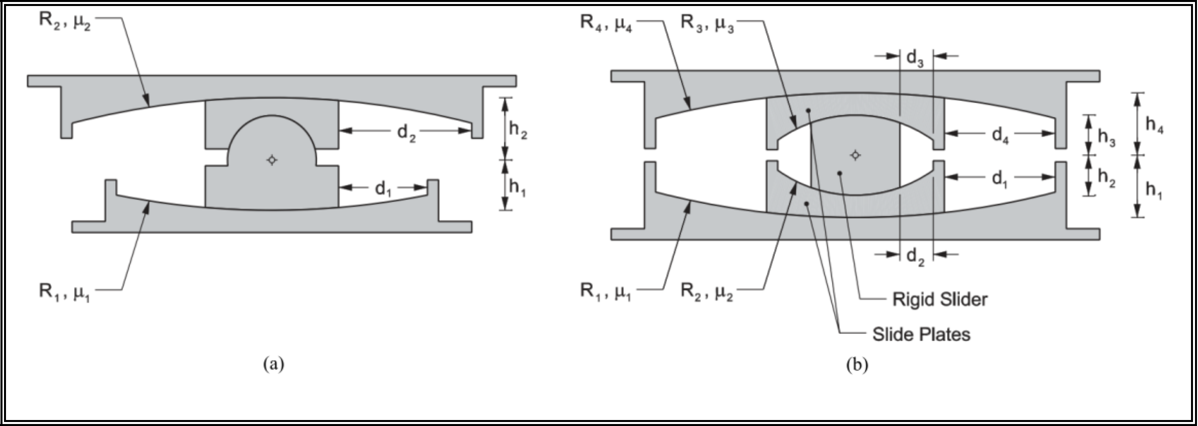

Figure 1-3: Frictional isolators with multiple sliding surfaces. (a) The double concave Frictional Pendulum (DCFP) bearing. (b) The triple concave Frictional Pendulum (TCFP) bearing. (Fenz & Constantinou, 2008b)

The FPS bearing is an attractive starting point for developing adaptive passive devices. The design parameters of the FPS bearing, the radius of the sliding surface, and the friction coefficient of the sliding surface may change as the lateral displacement of the device varies. Instead of having a constant stiffness due to its spherical sliding surface, a frictional isolator with variable curvature has an adaptive stiffness that constantly varies as the lateral displacement of the isolator changes. Different geometries of the sliding surface have been proposed and studied. The Variable Frequency Pendulum Isolator (VFPI) is one example of a variable curvature frictional isolator (Murnal & Sinha, 2002; Pranesh & Sinha, 2000). This device has an upper bound for the restoring force, leading to a force-softening mechanism. A finite element formulation to study the dynamic behavior of the Variable Curvature Friction Pendulum System (VCFPS) is presented in (Tsai et al., 2003). In the mentioned theoretical study, the analyzed device has a radius of curvature that is lengthened with an increase of the lateral isolator displacement. This strategy is proper to shift the base-isolated period from the predominant period of near-fault ground motion. Polynomial Sliding Isolators with Variable Curvature (PSIVCs) with a fifth-order and a third-order function have been studied (L.-Y. Lu et al., 2011). Interesting studies have been carried out to evaluate the performance of PSIVCs devices to control the displacement of floor isolation systems (FISs) (Gidaris et al., 2016; L. Y. Lu et al., 2013). The effectiveness of different types of sliding variable curvature isolators, such as the Conical Friction Pendulum Isolator, the PSIVC, the VFPI, and the VCFPS, has been assessed as alternatives to mitigate the resonance phenomenon that the conventional FPS bearing exhibits (Shahbazi & Taghikhany, 2017; Shaikhzadeh & Karamoddin, 2016). One challenge of developing a variable curvature frictional isolator is to construct an internal slider capable of adapting its shape to the changes in the curvature of the sliding surface. Several experimental tests have been conducted, showing that this challenge can be overcome (Han et al., 2020; S.-C. Lin et al., 2020; L.-Y. Lu et al., 2011; L. Y. Lu et al., 2013, 2021; Wang & Lu, 2018). In those studies, comparisons with numerical models have been made, obtaining good agreements between numerical simulations and experimental responses. Figure 1-4 shows the hysteretic loops of a tested isolator with variable curvature and compares this experimental response with the theoretical.

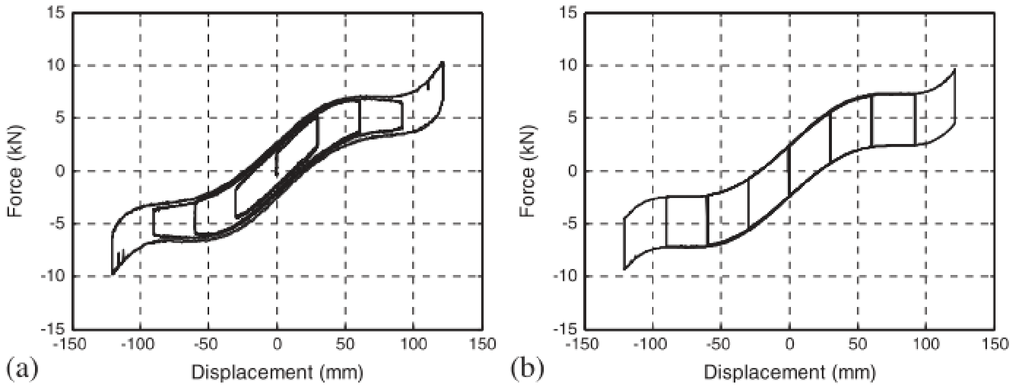

Figure 1-4: Hysteretic loops of an isolator with variable curvature. (a) Experimental response. (b) Theorical response. (L.-Y. Lu et al., 2011)

1.2 Motivation

The dynamic response of a base-isolated structure subjected to an intense ground motion with high low-frequency content, such as the perpendicular components of near-fault earthquakes, could cause excessive displacement of the isolation system (Hall et al., 1995a; Jangid, 2005; Jangid & Kelly, 2001b; Jónsson et al., 2010; Mazza, 2018; Mazza et al., 2017; Mazza & Vulcano, 2012). One alternative to control the excessive base displacement demand is to include passive dampers acting parallel with the isolation devices. The first building constructed with this technology in the United States was the San Bernardino County Medical Center (Asher et al., 1996). The dampers can effectively reduce the displacement in the isolation interface. However, the rise in the damping of the dynamic system could affect the performance of the isolation system by increasing inter-story drifts and absolute accelerations in the superstructure (Kelly, 1999).

In frictional isolators, large displacements could cause internal impacts between the inner sliders and the restraining rims of the concave sliding surfaces. This phenomenon could generate damage to the isolation devices and their potential uplift. Under extreme ground motions, lateral internal impacts have been considered one of the most significant contributors to the failure of DCFP and TCFP devices (Bao et al., 2017; Becker et al., 2017). Additionally, the internal lateral impact or the impact between the base of a seismically isolated building against moat walls produces a dramatic increment in the ductility demand of the superstructure (Bao et al., 2018; Bao & Becker, 2018a, 2018c; Komodromos, 2008; Mavronicola et al., 2017; Polycarpou & Komodromos, 2010).

1.2 Objectives, research questions and hypothesis

Driven by the aforementioned negative consequences of internal lateral impacts, this research aims to evaluate the use of passive adaptive technology to improve the performance of base-isolated structures subjected to internal lateral impacts under extreme seismic conditions. If the adverse effects of internal lateral impacts can be diminished, the outcomes of this investigation will lead to helpful design suggestions in constructing safer isolation systems.

The answers to the following questions must be elucidated to fulfill the general objectives of this research: It is possible to reduce the maximum base displacement demand using variable curvature devices? Reducing the maximum base displacement demand ensures a better seismic performance? Using variable curvature frictional isolators, what is the achievable percentage of reduction of the maximum base displacement demand and the maximum ductility demand? Is it possible to propose a new frictional isolator based on multiple sliding surfaces that ensure a better or an equal seismic performance if the lateral internal impact occurs? What structural properties optimize the benefits of using enhanced isolation systems?

The following specific objectives are defined to accomplish the general objectives and answer the research questions:

1) Identify and evaluate a specific Variable Curvature Frictional Isolator (VCFI) as an alternative to mitigate the adverse effects of internal lateral impacts.
2) Develop a new passive adaptive frictional isolator that exhibits an enhanced lateral impact behavior compared to classical frictional bearings.
3) Determine the dynamic and structural properties of the base-isolated structure that highlight the benefits of using the new frictional isolator.

Within the defined framework, the following hypotheses have been defined:

1) The use of frictional isolators with elliptical variable curvature allows obtaining a lateral behavior that exhibits a soft-hardening behavior that reduces the base displacement demand and, consequently, decreases the probabilities of observing structural damage due to lateral impacts.
2) It is possible to construct a new frictional isolator that limits the impact force and dissipates an additional amount of energy, enhancing the impact lateral behavior.
3) Important reduction in the probabilities of observing structural damage can be achieved by ensuring a better impact behavior. Since rigid structures are sensitive

to impact forces, the benefits of using isolators with an improved lateral impact behavior will be highlighted in stiff structures.

1.4 Organization of the thesis

This thesis document has been written considering three independent articles as its format. The following three chapters (Chapters 2, 3, and 4) are self-contained papers that have been published or are in the peer-revision stage.

The articles follow the logical development of the research The first paper presents an evaluation of the effectiveness of using variable curvature frictional isolators as a solution to the problem of later internal impacts. The relevant results show that using this kind of device helps decrease the probability of exceeding limit state thresholds related to maximum base displacement and, consequently, reduces the probability of observing internal lateral impacts under extreme ground motions. However, this feature is accompanied by an increase in the base shear that the superstructure must resist. This rise in the lateral force transmitted by the isolation system could lead to worse seismic performance of the superstructure. In the second paper, a new frictional isolator is presented to overcome the disadvantages of using variable curvature isolators to mitigate the adverse effects of later internal impacts. Finally, in the third article, the benefits of using the proposed isolator are assessed.

In the following subsection, a brief description of the methodology and main conclusions of each paper is presented.

1.4.1 Using friction isolators as a solution to internal lateral impacts

In Chapter 2, an evaluation of the use of variable curvature frictional isolators to mitigate the negative effects of the internal lateral impact is presented. One specific geometry of the sliding surface was studied. The shape of the sliding surface is obtained by revolving an ellipse around a vertical axis. Due to the shape of the sliding surface, the pendular force transmitted by the bearing exhibits a smooth hardening behavior. The first step to assessing the effectiveness of using this passive adaptive alternative was to develop a physical model for dynamic analysis of base-isolated structures equipped with variable curvature frictional bearings. This numerical model can account for essential modeling features such as large displacement, P-Δ effects, sticking, uplift, and lateral and vertical impact behavior. The physical model was compared with a Finite Element Model (FEM), showing its accuracy. In Figure 1-5, the comparison between both models is shown. Note that, in Figure 1-5(b), the smooth-hardening feature of the studied device is expressed.

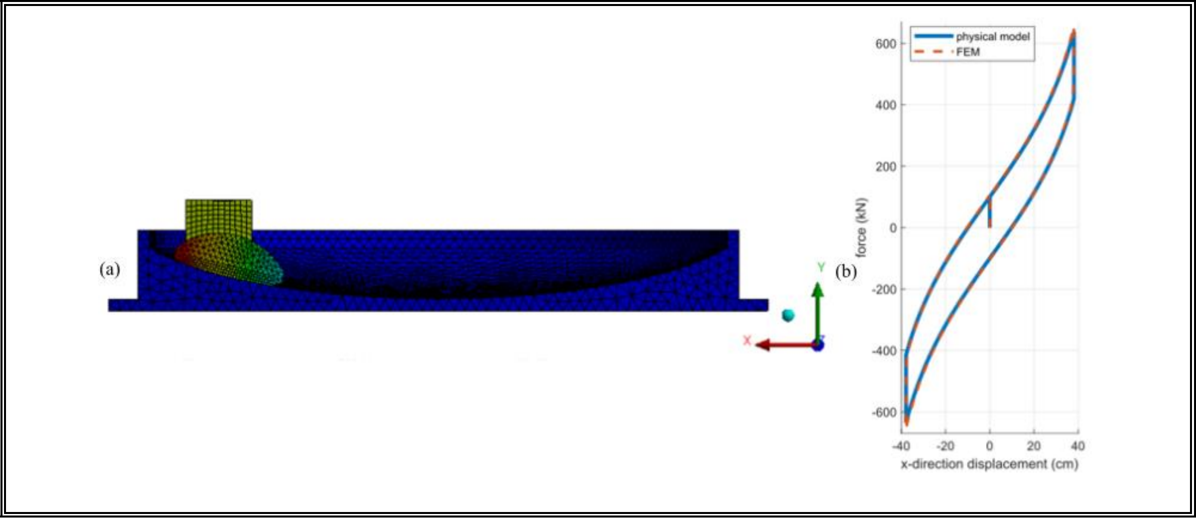

Figure 1-5: Comparison between the developed physical model of a variable curvature isolator and its Finite Element representation. (a) Finite Element model of the beating. (b) Comparison of the obtained responses.

The next step of evaluating the strategy of using variable curvature isolators was to identify the behavior of isolation systems formed by passive adaptive devices under three different base displacement demands. For low-intensity ground motions, the response of an isolation system formed by elliptical shape sliding surfaces devices is almost the same as the response obtained using classical FPS bearings. The smooth-hardening behavior is not exhibited since low base displacement demands are observed. If the structure equipped with variable curvature isolators is subjected to high magnitude earthquakes, but without exceeding the lateral capacity of the isolation system (i.e., the internal impact is not observed), the use of isolation devices with hardening behavior raises the seismic force transmitted to the superstructure. Hence, this passive adaptive strategy could worsen seismic performance in some cases. Under extreme conditions (i.e., the lateral impact is observed if FPS bearings are used to isolate the superstructure), the use of smooth-hardening frictional devices can be helpful by avoiding the occurrence of the internal impact or decreasing the magnitude of the forces developed during the internal impact.

Within a parametric analysis, the seismic performance of the studied isolator was evaluated. Several equivalent non-linear models were employed considering different properties of the isolation system and characteristics of the superstructure. For each simplified non-linear model, an incremental dynamic analysis (IDA) was conducted. Different sets of natural seismic records able to match conditional spectra for a site in Riverside (California) were selected to consider the aleatory uncertainties of the seismic input. Additionally, the large velocity friction coefficient was considered as a random variable. Using the information of the IDAs and by defining limit states thresholds related to the maximum base displacement demand and the maximum ductility demand, fragility curves were constructed. The seismic reliability of structures equipped with frictional isolators with smooth-hardening behavior was evaluated and compared with classical isolation systems formed by FPS bearings employing seismic hazard curves and the derived fragility curves. Frictional isolators with smooth-hardening behavior are helpful to reduce probabilities of exceeding limit state thresholds related to maximum base displacement demands. Variable curvature frictional isolators are recommended to mitigate the adverse effects of lateral internal impact if the superstructure is stiff, has a high mass distribution ratio, a relatively high post-yield stiffness, and is designed to behave essentially elastic if the lateral capacity is not reached. One significant limitation was identified, if the superstructure is design to exhibit non-linear behavior (material plasticity) before the occurrence of the inter impact, using the smooth-hardening alternative leads to worse seismic performance.

1.4.2 A new frictional isolator

Motivated by the limitation found in the functioning of variable curvature isolation devices as an alternative to mitigate the adverse effects of the internal lateral impact, a new frictional isolator based on multiple sliding surfaces was proposed. The Lateral Impact Resilient Double Concave Friction Pendulum (LIR-DCFP) bearing has an improved inner slider with an internal gap capable of limiting the magnitude of the internal impact between the inner sliders and the restraining rims of the concave sliding surfaces. This feature is achieved by constructing a plane high friction interface between the top rigid body and the bottom rigid body that compose the inner slider. By ensuring a correct design of the bearing, the relative displacement between the two plane high friction surfaces is developed only if the internal lateral impact occurs. In addition to limiting the force of the internal impact, the high friction interface can dissipate a significant amount of additional energy. In Figure 1-6, a graphical representation of the lateral behavior of the LIR-DCFP bearings is presented.

A detailed three-dimensional formulation based on rigid body dynamic is presented for modeling the dynamic response of structures equipped with this type of devices. Each rigid part of the isolator is represented as a rigid body with six degrees-of-freedom. This numerical formulation can capture important modeling aspects of the dynamic behavior of the device under extreme seismic condition, such as: uplift, lateral impact behavior, large displacement, $P - \Delta$ effects, kinematic constraints, and the explicit failure of the isolator.

A comparative example of a three-dimensional structure isolated through LIR-DCFP and classical Double Concave Frictional Pendulum (DFCP) devices subjected to three seismic records is presented to demonstrate the benefits of using the proposed isolator. Important reductions in the base shear, inter-story drifts, and absolute accelerations are achieved using LIR-DCFP bearings. Consequently, the proposed isolator is valuable as an alternative to mitigate the negative effects of internal lateral impacts.

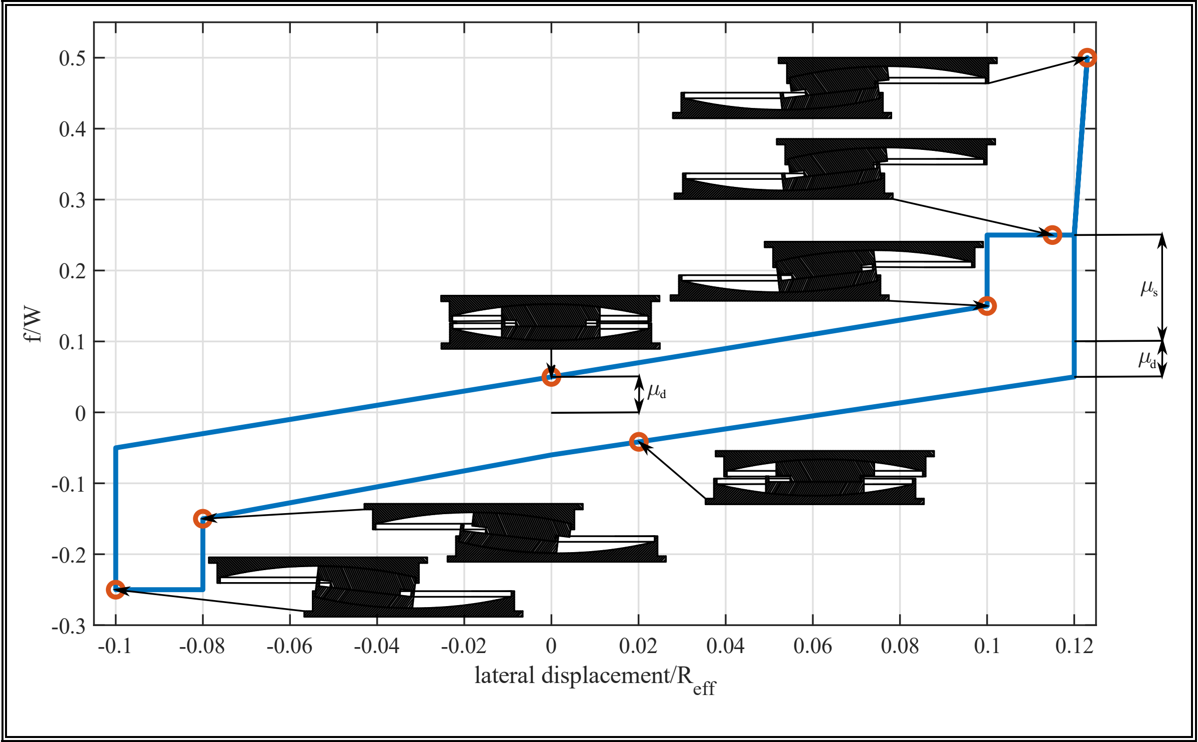

Figure 1-6: Representation of the lateral behavior of the Lateral Impact Resilient Double Concave Friction Pendulum (LIR-DCFP) bearing.

1.4.3 Seismic reliability of structures equipped with LIR-DCFP bearings

The third article deals with the seismic reliability of non-linear base-isolated structures equipped with LIR-DCFP devices. The main objective of this phase of the research is to identify the structural properties that highlight the benefits of using the proposed isolator. A simplified model represents the dynamic system. While the dynamic behavior of the superstructure is represented by a simplified one-degree-of-freedom model describing its lateral flexibility and considering the non-linear range, the isolation system is characterized by a model based on rigid body dynamics, also including the lateral impact behavior. A comprehensive parametric analysis is developed for several system properties, accounting for 1,152 equivalent models. Within the parametric analysis, the isolated period, the superstructure period, the mass ratio, the numerical coefficient related to the type of seismic force-resisting system above the isolation system, the post-yield hardening or softening ratio, and the internal gap size of the LIR-DCPF device were selected as the fundamental variables.

Each equivalent model was assessed using the same approach described in section 1.4.2. Incremental dynamic analyses were performed considering the friction coefficients and the main characteristics of the seismic inputs as random variables. The relevant limit states thresholds were defined based on the maximum ductility demand of the superstructure. The main annual rate exceeding the limit states was determined through the convolution integral between fragility curves and the hazard curves. With this information and using a Poisson distribution, seismic reliability curves in a time frame of 50 years were derived. These curves were a valuable tool to compare the performance of classic isolation systems formed by DCFP bearing enhanced isolation interfaces composed of LIR-DCFP devices.

For increasing values of the internal gap, structures equipped with LIR-DCFP devices exhibit better seismic performance concerning classical DCFP bearings, especially if the superstructure is designed to behave essentially elastic when the lateral capacity of the isolation level is not reached, or the hardening post-yield stiffness of the superstructure is relatively high. Reductions up to 20% in the exceeding probabilities within 50 years related to the ductility demand are achievable using the suggested LIR-DCFP isolator.

1.5 Future work

This work evaluated numerically two strategies to mitigate the adverse effects of internal lateral impacts produced under extreme seismic conditions. Static (or pseudo-dynamic) experimental tests must be conducted to validate the lateral behavior of the studied isolations devices. The research team already has some preliminary results that show both alternatives, variable curvature devices and isolators with high-friction interfaces, are feasible. Regarding variable curvature frictional devices, one crucial challenge is to test different materials searching for proper configurations to achieve an inner slider capable of adapting curvature changes. Another critical task is to experimentally characterize the frictional properties of materials that can be employed to construct the high-friction interface of the LIR-DCFP bearings.

Several non-linear dynamics analyses were performed during the development of this thesis. In the future, it is necessary to carry out experimental dynamic analysis of reduced scale base-isolated structures equipped with the proposed isolator considering the impact between inner sliders and restraining rims of sliding surfaces.

The most important conclusions obtained in the research are based on the response of equivalent simplified models. Future works should be orientated in the numerical evaluation of more complex structural systems considering geometric nonlinearities and modeled using elements with distributed plasticity, degrading features, and accounting for the interaction between the forces developed during a strong ground motion.

In Chapter 3, the Impact Resilient Double Concave Friction Pendulum (IR-DCFP) bearing is presented. This device has not only a lateral resisting inner slider, but it is also able to resist a vertical impact induced by the uplift of the top plate of the bearing. An elastomeric seal is placed in the gap that the bottom and top slider leave. Additionally, two elastomeric supports are arranged between the inner sliders and the low friction pieces (i.e., the polymeric plates). In Figure 1-7, an illustration of the IR-DCFP bearing is presented. Due to the presence of these flexible parts, it is expected that vertical impacts generate forces with lower magnitudes than in cases where classical frictional devices are employed. Attractive future work could be the characterization of the dynamic vertical behavior of the IR-DFCP bearing and the evaluation of the seismic performance of this device under extreme seismic conditions.

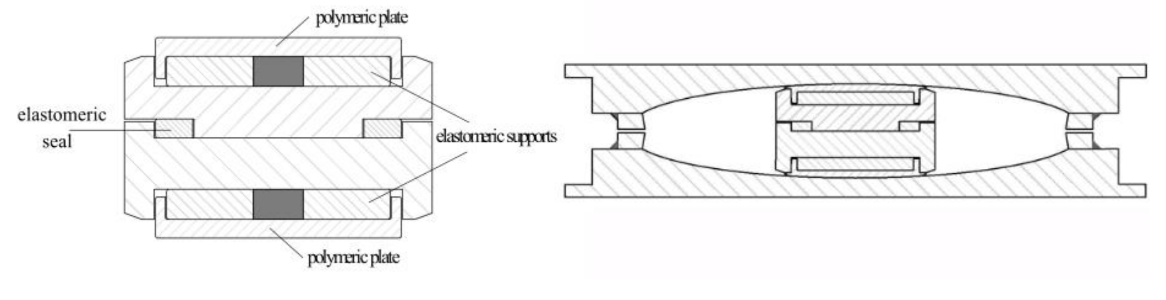

Figure 1-7: The Impact Resilient Double Concave Friction Pendulum (IR-DCFP) bearing

2. EVALUATING THE USE OF VARIABLE CURVATURE FRICTIONAL ISOLATOR TO MITIGATE THE ADVERSE EFFECTS OF INTERNAL LATERAL IMPACTS

2.1 Introduction

In the last decades, structures equipped with seismic isolation systems have shown better seismic performance than fixed-base buildings (Chimamphant & Kasai, 2016; Nagarajaiah & Xiaohong, 2000; Shenton & Lin, 1993). A conventional isolation system is generated by placing a laterally flexible and vertically rigid interface between the ground and the structure. If the superstructure behaves as a rigid body, the isolation interface generates three low-frequency lateral-torsional vibration modes. The elongation of the natural periods of the dynamic system is one of the most effective alternatives to protect non-slender structures from high magnitude ground motions. Two of the most used devices to achieve seismic isolation are the elastomeric bearing (Kelly, 1993) and the Friction Pendulum System (FPS) bearing (Zayas et al., 1990).

The dynamic response of a base-isolated structure subjected to an intense ground motion with high low-frequency content, such as the perpendicular components of near-fault earthquakes, could cause excessive displacement of the isolation system (Hall et al., 1995a; Jangid, 2005; Jangid & Kelly, 2001b; Jónsson et al., 2010; Mazza, 2018; Mazza et al., 2017; Mazza & Vulcano, 2012). One alternative to control the excessive base displacement demand is to include passive dampers acting in parallel with the isolation devices. The first building constructed with this technology in the United States was the San Bernardino

County Medical Center (Asher et al., 1996). The dampers can effectively reduce the displacement in the isolation interface. However, the rise in the damping of the dynamic system could affect the performance of the isolation system by increasing inter-story drifts and absolute accelerations in the superstructure (Kelly, 1999). One suggested alternative to avoid this problem is to develop adaptive systems that exhibit changes in dynamic properties under different displacement demands (Kelly, 1999).

The FPS bearing is an attractive starting point for the development of adaptive passive devices. The design parameters of the FPS bearing: the radius of the sliding surface and the friction coefficient, may change as the lateral displacement of the device varies. Instead of having a constant stiffness due to its spherical sliding surface, a frictional isolator with variable curvature has an adaptive stiffness that constantly varies as the lateral displacement of the isolator changes. Different geometries of the sliding surface have been proposed and studied. The Variable Frequency Pendulum Isolator (VFPI) is one example of a variable curvature frictional isolator (Murnal & Sinha, 2002; Pranesh & Sinha, 2000). This device has an upper bound for the restoring force that leads to a force-softening mechanism. A finite element formulation to study the dynamic behavior of the Variable Curvature Friction Pendulum System (VCFPS) is presented in (Tsai et al., 2003). In the mentioned theoretical study, the analyzed device has a radius of curvature that is lengthened with an increase of the lateral isolator displacement. This strategy is proper to shift away the base-isolated period from the predominant period of near-fault ground motion. Polynomial Sliding Isolators with Variable Curvature (PSIVCs) with a fifth-order and a third-order function have been studied (L.-Y. Lu et al., 2011). Interesting studies have been carried out to evaluate the performance of PSIVCs devices to control the displacement of floor isolation systems (FISs) (Gidaris et al., 2016; L. Y. Lu et al., 2013). The effectiveness of different types of sliding variable curvature isolators, such as the Conical Friction Pendulum Isolator, the PSIVC, the VFPI, and the VCFPS, has been assessed as alternatives to mitigate the resonance phenomenon that the conventional FPS bearing exhibits (Shahbazi & Taghikhany, 2017; Shaikhzadeh & Karamoddin, 2016). One challenge of developing a variable curvature frictional isolator is to construct an internal slider capable of adapt its shape to the change in the curvature of the sliding surface. Several experimental tests have been conducted, showing that this challenge can be overcome (Han et al., 2020; S.-C. Lin et al., 2020; L.-Y. Lu et al., 2011; L. Y. Lu et al., 2013, 2021; Wang & Lu, 2018). In those studies, comparisons with numerical models have been made, obtaining good agreements between numerical simulations and experimental responses.

As mentioned above, another alternative to achieve adaptive passive devices is to develop variable friction isolators (Calvi et al., n.d.; Panchal & Jangid, 2008, 2009; Shang et al., 2021). Isolators with multiple sliding surfaces, such as the Double Concave Friction Pendulum (DCFP) bearing (Fenz & Constantinou, 2006) and the Triple Friction Pendulum (TFP) bearing (Fenz & Constantinou, 2008b, 2008a), are commonly used as passive adaptive options. The analysis of both types of isolators, devices with variable friction and devices with multiple sliding surfaces, is out of the scope of this work.

As far as the authors know, frictional devices with variable curvature have not been evaluated as an alternative to mitigate the adverse effects of internal impacts between the inner slider and the restraining rim of the sliding surface. This internal impact has been indicated as one of the most important causes to the failure of frictional devices (Bao et al., 2017; Becker et al., 2017). In the cited papers related to variable curvature isolators, the presence of the restraining rim has not been considered in the numerical simulations, so the internal lateral impact behavior has not been studied. The Multiple-Variable Frequency Pendulum Isolator (MVFPI) (Han et al., 2020) is constructed using high-performance materials to improve durability and control displacement. The mechanism to control the displacement is based on shape memory alloy (SMA) wires that produce a hardening stage at large displacement. Despite this feature, this mechanism was not evaluated as a solution to avoid the adverse effects of lateral impacts.

The main objective of this investigation is to evaluate the use of frictional isolators with variable curvature to mitigate the negative effects of internal lateral impacts. One specific shape of the sliding surface is analyzed. The geometry of the sliding surface is obtained by revolving a plane ellipse around a vertical axis. In this way is possible to obtain a smooth-hardening behavior since the radius of curvature of the device gets smaller as the frictional bearing is laterally deformed. The negative effects of lateral impacts are mitigated if the smooth-hardening behavior avoids the occurrence of the impact or, if the impact is observed, by decreasing its magnitude.

In this paper, a physical model for dynamic analysis of structure equipped with variable curvature devices is presented. This model was compared and validated with a Finite Element Model of the frictional bearing. The dynamic behavior of a three-dimensional base-isolated structure with smooth-hardening devices was shown and examined by subjecting the dynamic system to three different base displacement demands. Finally, within a parametric analysis of an equivalent nonlinear model, the seismic performance of the suggested isolator was assessed. The use of elliptical-based geometry of the sliding surface decreases the probabilities of exceedance limit states thresholds related to maximum base displacement demands. Under some superstructure properties, using a frictional isolator with variable curvature can reduce the probabilities of exceedance limit states related to ductility demand thresholds.

2.2 Physical model of the friction isolator with variable curvature

In this section, a methodology is proposed to determine the forces transmitted by a frictional isolator with variable curvature given a motion in the local nodes of the element. One of the aims of this work is to extend the physical model of the Friction Pendulum System (PM-FPS) (José L. Almazán & De la Llera, 2003), which has a spherical sliding surface, to any algebraic surface described by an implicit equation (Equation (2-1)) and incorporate the lateral impact behavior.

$$F = F(x, y, z) = 0 \tag{2-1}$$

A physical model of a frictional isolator can account for essential effects such as sticking or sliding phases, large displacement, $P - \Delta$ effects, horizontal interaction between the components of pendular and frictional forces generated inside the bearing, among other important phenomena. The axial flexibility of the device can be easily included using a nonlinear gap element. Since gap elements do not transmit tension, the uplift and vertical impact of the isolator are considered in the three-dimensional numerical formulation. Furthermore, by adopting a large value in the axial stiffness of the gap element, the physical model forces the superstructure to describe a trajectory in the horizontal and vertical directions satisfying the kinematic constraints imposed by the shape of the sliding surface.

In the present paper, a frictional isolator with a single sliding surface is studied. The shape of the sliding surface has a specific typology. The sliding surface is obtained by revolving an ellipse around its vertical axis. This ellipse has a width of $2a$, a height of $2b$ and is offset by b in the z-direction. The ellipse and the generated surface (described by the Eq. (2)) are presented in Figure 2-1.

$$F_e(x, y, z) = \frac{x^2 + y^2}{a^2} + \frac{(z - b)^2}{b^2} - 1 = 0 \tag{2-2}$$

2.2.1 Local system of coordinates

The definition of the local system of coordinates is fundamental. An illustration of the position of the local system of coordinates is presented in Figure 2-2. The local system, $\mathfrak{I}_2 = \{O\colon x\ y\ z\}$, is defined in the sliding surface having its origin in the point O. This local system is solidary with the sliding surface. The instantaneous position of the slider relative to the local coordinates system S describes the displacement of the device: $\boldsymbol{\delta} = \overline{OS} = \left[\delta_x,\ \delta_y,\ \delta_z\right]^T$. The studied surface imposes two vertical kinematic constraints that must be satisfied at every time step:

$$\delta_z = b - \sqrt{b^2 - \frac{b^2}{a^2}\left(\delta_x^2 + \delta_y^2\right)} \tag{2-3}$$

$$\dot{\delta}_z = \frac{b^2}{a^2}\left(\frac{\delta_x\dot{\delta}_x + \delta_y\dot{\delta}_y}{b - \delta_z}\right) \tag{2-4}$$

Physically, these kinematic constraints imposed by the sliding surface represent the component in the local z-direction of the trajectory and the velocity of the slider.

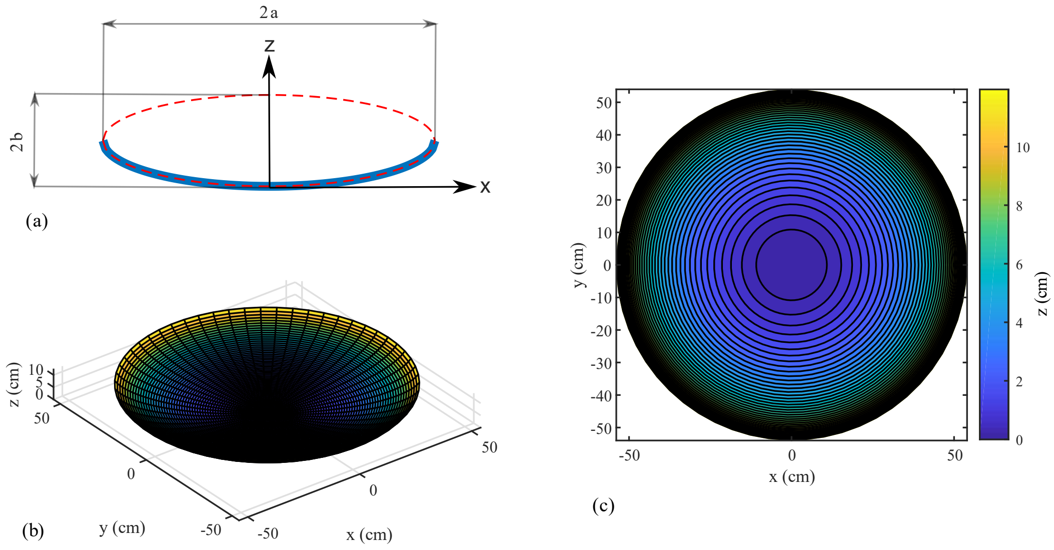

Figure 2-1: (a) Plane ellipse with its mean geometric parameters. (b) Generated surface - isometric view. (c) Generated surface - contour lines.

Additionally, in Figure 2-2(a), the geometric parameters of the device are illustrated, being: l_i and l_j, the vertical distances between the nodes J and I and the origin O in the undeformed configuration, respectively; b_s, the width of the inner slider; $r^{(p)}$, the planar radius of the sliding surface; and L_c, the lateral capacity of the isolator. Note that, although the contacts between different bodies of the isolator are concentrated in contact points, it is possible to consider the geometry of the articulated slider to determine the lateral capacity of the device as follows:

$$L_c = r^{(p)} - b_s/2 \tag{2-5}$$

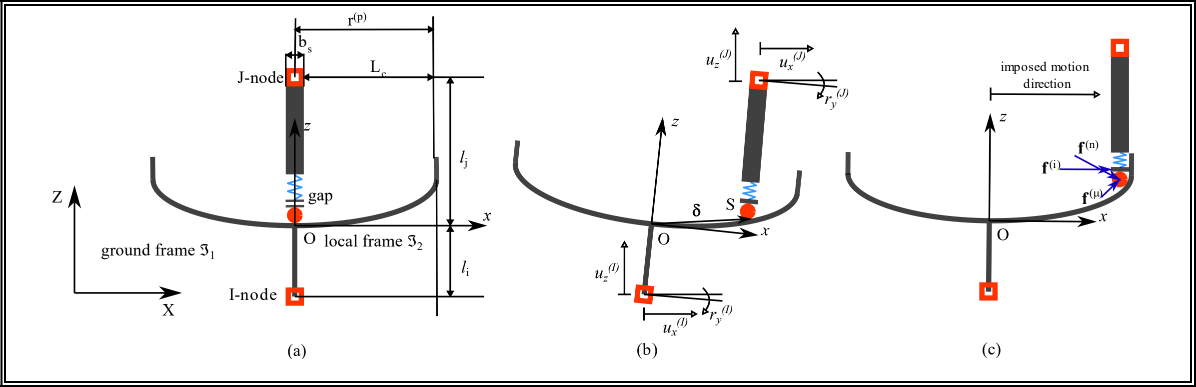

Figure 2-2: Schematic view of the physical model: (a) Undeformed configuration. (b) Deformed configuration. (c) Configuration under internal lateral impact. (Modified from Almazán and De la Llera (José L. Almazán & De la Llera, 2003)).

2.2.2 Non-linear kinematics

In this subsection, the equations that represent the kinematic relationship between the degrees of freedom (DOFs) of the structure $\boldsymbol{q}$ and the displacement of the device $\boldsymbol{\delta}$ are presented. The kinematic relationship is nonlinear since large displacements are considered. Considering a set of nodal displacements and rotations $\boldsymbol{u} = [\boldsymbol{u}^{(J)}; \boldsymbol{u}^{(J)}]$, in which $\boldsymbol{u}^{(J)} = \left[u_x^{(J)}\ u_y^{(J)}\ u_z^{(J)}\ r_x^{(J)}\ r_y^{(J)}\ r_z^{(J)}\right]^T$ and $\boldsymbol{u}^{(I)} = \left[u_x^{(I)}\ u_y^{(I)}\ u_z^{(I)}\ r_x^{(I)}\ r_y^{(I)}\ r_z^{(I)}\right]^T$ are the motions of nodes J and I, respectively, the nodal displacement of the isolator and the nodal motion of the structure are linearly related as follow:

$$\boldsymbol{u} = \boldsymbol{P}\boldsymbol{q} \tag{2-6}$$

in which **P** is the linear nodal kinematic transformation matrix of the device. The nodal velocities are also linearly related by the following equation:

$$\dot{\boldsymbol{u}} = \boldsymbol{P}\dot{\boldsymbol{q}} \tag{2-7}$$

Assuming small nodal rotations and neglecting infinitesimal terms of order higher than one (José Luis Almazán, 2001), the displacement of the isolator $\boldsymbol{\delta}$ and the velocity of displacement $\dot{\boldsymbol{\delta}}$ are related by the following expressions:

$$\boldsymbol{\delta} = \overline{\boldsymbol{S}}(\boldsymbol{u})\boldsymbol{u} \tag{2-8}$$

$$\dot{\boldsymbol{\delta}} = \frac{\partial \boldsymbol{\delta}}{\partial \boldsymbol{u}}\frac{d\boldsymbol{u}}{dt} = \widehat{\boldsymbol{S}}(\boldsymbol{u})\dot{\boldsymbol{u}} \tag{2-9}$$

in which

$$\overline{\boldsymbol{S}}(\boldsymbol{u}) \tag{2-10}$$

$$= \begin{bmatrix} 1 & 0 & 0 & 0 & -l_j & 0 & -1 & 0 & 0 & 0 & -(\Delta u_z + l_i) & \Delta u_y \\ 0 & 1 & 0 & l_j & 0 & 0 & 0 & -1 & 0 & \Delta u_z + l_i & 0 & -\Delta u_x \\ 0 & 0 & 1 & 0 & 0 & 0 & 0 & 0 & -1 & -\Delta u_y & \Delta u_x & 0 \end{bmatrix}$$

and

$$\widehat{\boldsymbol{S}}(\boldsymbol{u}) \tag{2-11}$$

$$= \begin{bmatrix} 1 & r_z^{(I)} & r_y^{(I)} & 0 & -l_j & 0 & -1 & -r_z^{(I)} & r_y^{(I)} & 0 & -(\Delta u_z + l_i) & \Delta u_y \\ -r_z^{(I)} & 1 & r_x^{(I)} & l_j & 0 & 0 & r_z^{(I)} & -1 & -r_x^{(I)} & \Delta u_z + l_i & 0 & -\Delta u_x \\ r_y^{(I)} & r_x^{(I)} & 1 & 0 & 0 & 0 & -r_y^{(I)} & r_x^{(I)} & -1 & -\Delta u_y & \Delta u_x & 0 \end{bmatrix}$$

being $\Delta u_x = \left(u_x^{(J)} - u_x^{(I)}\right), \Delta u_y = \left(u_y^{(J)} - u_y^{(I)}\right),$ and $\Delta u_z = \left(u_z^{(J)} - u_z^{(I)}\right)$ the relative displacements between nodes J and I.

2.2.3 Action-deformation

The force developed in the friction isolator with variable curvature can be expressed as the sum of the pendular force $\boldsymbol{f}^{(n)}$, the frictional force $\boldsymbol{f}^{(\mu)}$ and the impact force $\boldsymbol{f}^{(i)}$:

$$\boldsymbol{f} = \boldsymbol{f}^{(n)} + \boldsymbol{f}^{(\mu)} + \boldsymbol{f}^{(i)} \tag{2-12}$$

These three vectorial forces are illustrated in Figure 2-2(c). The pendular force can be determined using the following equation:

$$\boldsymbol{f}^{(n)} = N\hat{\boldsymbol{n}} = N\hat{\boldsymbol{n}}(\boldsymbol{\delta}) \tag{2-13}$$

in which N is the magnitude of the normal force and $\hat{\boldsymbol{n}}$ is the unitary vector in the normal direction of the trajectory of the slider. One crucial step of the procedure is to determine the unitary normal vector $\hat{\boldsymbol{n}}$ at any surface point. This vector can be calculated using the following equation:

$$\hat{\boldsymbol{n}}(\boldsymbol{\delta}) = \frac{\nabla F_e(x,y,z)}{\|\nabla F_e(x,y,z)\|} = \frac{1}{\sqrt{\frac{\delta_x^2}{a^4} + \frac{\delta_y^2}{a^4} + \frac{(\delta_z - b)^2}{b^4}}} \left[\frac{\delta_x}{a^2}, \frac{\delta_y}{a^2}, \frac{(\delta_z - b)}{b^2}\right]^T \tag{2-14}$$

The frictional force developed in the isolator can be computed as:

$$\boldsymbol{f}^{(\mu)} = \bar{\eta}\mu_d N\hat{\boldsymbol{s}} = \bar{\eta}\mu_d N\hat{\boldsymbol{s}}(\boldsymbol{\eta}, \alpha) \tag{2-15}$$

in which $\hat{\boldsymbol{s}}$ is the unitary vector in the tangential direction of the trajectory of the slider, μ_d is the friction coefficient, $\boldsymbol{\eta} = \left[\eta_x \; \eta_y\right]^T$ is the state vector of the Park-Wen model (Park et al., 1986), $\bar{\eta} = \|\boldsymbol{\eta}\|$, and α is the angle between the frictional force and the local xy-plane. For the studied surface, the unitary vector $\hat{\boldsymbol{s}}$ can be computed using the following equation:

$$\hat{\boldsymbol{s}} = \left[\frac{\eta_x}{\|\boldsymbol{\eta}\|} cos(\alpha), \frac{\eta_y}{\|\boldsymbol{\eta}\|} cos(\alpha), \; sin(\alpha)\right]^{\boldsymbol{T}} \tag{2-16}$$

Since the frictional force and the unitary vector $\hat{\boldsymbol{n}}$ are orthogonal (i.e., $\hat{\boldsymbol{n}}^T \boldsymbol{f}^{(\mu)} = 0$), it is possible to calculate α at every time step using the following expression:

$$\alpha = atan\left(\frac{\left(\frac{\eta_x \delta_x}{\|\boldsymbol{\eta}\| a^2} + \frac{\eta_y \delta_y}{\|\boldsymbol{\eta}\| a^2}\right)}{\frac{b - \delta_z}{b^2}}\right) \tag{2-17}$$

The nonlinear dependence of the friction coefficient μ_d with the velocity of sliding $\dot{v}$ is considered using the expression provided by Constantinou *et al.* (M. Constantinou et al., 1990):

$$\mu_d = f_{max} - (f_{max} - f_{min})\exp(-r\dot{v}) \tag{2-18}$$

in which f_{max} is the friction coefficient at high velocity of sliding, f_{min} is the friction coefficient at slow velocity, and r es the rate parameter.

The impact between the slider and the restraining rim of the isolator is observed if the lateral displacement capacity of the frictional bearing L_c is exceeded (i.e., $\|\boldsymbol{\delta}(1:2)\| > L_c = r^{(p)} - b_s/2$). Under this scenario, the magnitude of the impact force can be estimated using the Kelvin-Voigt model (Anagnostopoulos, 2004) (spring-dashpot element). In inelastic impact problems of two bodies, the following expression can be used to determine the impact magnitude I_{kv}:

$$I_{kv} = k_{kv}\,\Delta + c_{kv}\,\dot{\Delta} \tag{2-19}$$

in which k_{kv} and c_{kv} are the stiffness and damping coefficient of the Kelvin-Voigt model, Δ and $\dot{\Delta}$ are the displacement and velocity of displacement of the element. The damping coefficient can be determined using the following expressions:

$$c_{kv} = 2\xi\sqrt{\frac{k_{kv}m_1m_2}{(m_1+m_2)}}\;,\quad \xi = -\frac{ln(e)}{\sqrt{\pi^2 + (ln(e))^2}} \tag{2-20}$$

In the expressions in Equation (2-20), m_1 and m_2 are the two masses colliding, and e is the coefficient of restitution for inelastic impact. For steel to steel impacts, the coefficient of restitution varies from 0.4 to 0.7 (Bao et al., 2017). Considering the physical model with lateral impact behavior presented in this study, the impact magnitude can be estimated employing the following equation:

$$I_i = \begin{Bmatrix} k_i(\|\boldsymbol{\delta}(1:2)\| - L_c) + c_i \left\|\dot{\boldsymbol{\delta}}(1:2)\right\|, & \text{if} \quad (\|\boldsymbol{\delta}(1:2)\| - L_c) \geq 0 \\ 0, & \text{otherwise} \end{Bmatrix} \tag{2-21}$$

in which k_i and c_i are the stiffness and damping coefficient of the impact behavior of the physical model. The symbols $\boldsymbol{\delta}(1:2)$ and $\dot{\boldsymbol{\delta}}(1:2)$ represent the two first components of the displacement and velocity of displacement vectors of the device, respectively. The stiffness k_i and the coefficient of restitution e used in modeling the internal lateral impact in the physical model were obtained by fitting the dynamic response of a Finite Element Model. Note that, according to Equation (2-21), the impact will last as long as the condition $(\|\boldsymbol{\delta}(1:2)\| - L_c) \geq 0$ is met. Assuming that the components of the impact force $\boldsymbol{f}^{(i)}$ are normal to the contact plane, the impact force can be computed using the following expression:

$$\boldsymbol{f}^{(i)} = I_i \frac{[\boldsymbol{\delta}(1:2); 0]}{\|\boldsymbol{\delta}(1:2)\|} \tag{2-22}$$

2.2.4 Equilibrium

The projection of the restoring force $\boldsymbol{f}$ into the global coordinate system $\Im_1$, solidary with the ground, is calculated as:

$$\boldsymbol{Q} = \left[\frac{\partial \boldsymbol{\delta}}{\partial \boldsymbol{q}}\right]^T \boldsymbol{f} = \left(\boldsymbol{P^T}\, \widehat{\boldsymbol{S}}^{\boldsymbol{T}}\right) \boldsymbol{f} = \boldsymbol{P^T F} \tag{2-23}$$

in which $\boldsymbol{F} = \left[\boldsymbol{F}_{\boldsymbol{x}}^{(J)}; \boldsymbol{F}_{\boldsymbol{y}}^{(I)}\right]$ is the vector force at nodes J and I projected into the global coordinate system.

2.2.5 Design parameters

The radius of curvature at initial configuration R_0 and the half-width of the ellipse are chosen as design parameters. The initial configuration is defined as when no lateral displacement is presented in the device (i.e., $\boldsymbol{\delta}(1{:}2) = [0, 0]^T$). The initial radius R_0 is related to the parameters of the ellipse by the following equation:

$$R_0 = \frac{a^2}{b} \tag{2-24}$$

The half-width parameter a is related to the hardening stage of the lateral behavior of the frictional isolator. The lower the parameter value is, the lower the lateral displacement of the device will be needed to reach the hardening stage. The case in which $a = R_0$, does not present hardening at any lateral displacement. In fact, in this case, $b = R_0$ and the shape of the sliding surface is a portion of a sphere with radius R_0 (the numerical model represents the physical model of the FPS bearing). In Figure 2-3(a) and Figure 2-3(c), different plane ellipses are shown. Additionally, Figure 2-3(b) and Figure 2-3(d) show the hysteretic loops of isolators with surfaces generated with those ellipses. In all cases, a constant friction coefficient $\mu_d = 0.05$ was employed (arbitrary selection). In the plotted curves, if $a < R_o$, the lateral force transmitted by the bearings has soft stiffness changes, without exhibiting abrupt variations. That is why the studied device has been called “smooth hardening FPS” (SH-FPS).

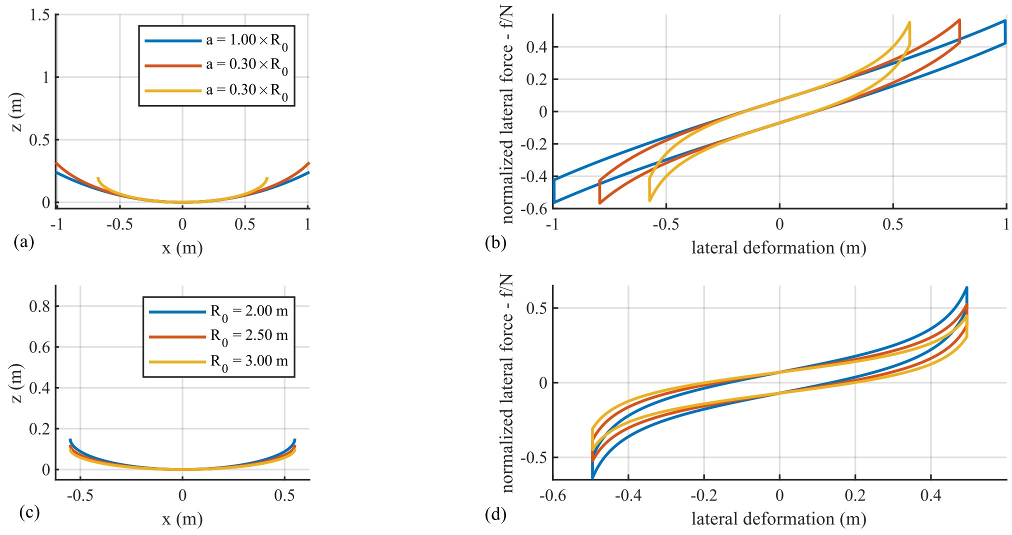

Figure 2-3: (a) Plane ellipses with $R_0 = 2$ m. (b) Hysteretic loops of SH-FPS bearings with $R_0 = 2$ m. (c) Plane ellipses with $a = 0.55$ m. (d) Hysteretic loops of SH-FPS bearings with $a = 0.55$ m.

2.3 Smooth hardening FPS bearing: the finite element model

A Finite Element Model (FEM) of the studied seismic isolator was developed using the Finite Element Analysis (FEA) ANSYS software (Lee, 2018) to validate the equations presented in Section 2. This software has helped model different seismic isolators, including devices that transmit frictional forces (G. A. Auad & Almazán, 2017; Colombo & Almazán, 2017). An SH-FPS bearing with a variable curvature sliding surface defined by the following geometric parameters was analyzed: $R_0 = 2.25$ m, and $a = 0.25 \times R_0$. The geometry of the frictional device is shown in Figure 2-4(a). The planar radius of the sliding surface $r^{(p)} = 0.52$ m, and the width of the articulate slider $b_s = 0.24$ m set the lateral capacity to $L_c = 0.40$ m.

As shown in Figure 2-4(a), two materials, Structural Steel and Ertalyte (De Baets et al., 2002), were used to model the frictional bearing. This last material is employed to construct a body that adapts to curvature changes. This material is commonly used in constructing sliding pieces subjected to dynamic high magnitude loads due to its high mechanical resistance, stiffness, and low friction coefficient. A small sliding disc made of Ertalyte with an annular shape on its bottom surface is placed below the articulated slider generating a low friction interaction with the elliptical sliding surface. The properties of the materials used in the FEM are reported in Table 2-1. On the one hand, all the pieces made of Structural Steel are modeled considering the nonlinear behavior of the material. On the other hand, accounting for the evidence of experimental tests (see Appendix A), the sliding plate made of Ertalyte is assumed to behave elastically.

The isolator with variable curvature has been modeled using two types of 3D-solid elements: SOLID186 (hexahedral, defined by 20 nodes) and SOLID187 (tetrahedral, defined by ten nodes). The FEM is presented in Figure 2-4((b), and (c)) in undeformed and deformed configurations. The Large Deformation option was activated to consider the effects of geometric nonlinearities. A fixed support was imposed on the bottom face of the isolator, restraining all the degrees of freedom contained in that surface. On the top face of the articulated slider, a Remote Displacement Support was assigned. This boundary condition restricts the rotations and imposes lateral displacements on this face without constraining the vertical displacement.

Almost all contacts between different bodies were defined as Frictional using a constant friction coefficient (for simplicity) and employing the Augmented Lagrange formulation. The only exception was the defined impact contact between the slider and the restraining rims. This contact was modeled as Frictionless. While the friction coefficient of Structural Steel to Structural Steel contacts was defined as $\mu_d = 0.10$, the friction coefficient of Structural Steel to Ertalyte contacts was set as $\mu_d = 0.07$. In all the FEM conducted analyses, a constant vertical load of 853 kN (or an equivalent mass of 86,952 kg) is applied (assigned) on the top face of the articulated slider. The annular area of the sliding plate in contact with the elliptical sliding surface was designed to transmit the vertical load with a contact pressure of 60 MPa. According to the experimental tests, under that pressure, a friction coefficient at large velocity of $\mu_d = 0.07$ is measured (see Appendix A).

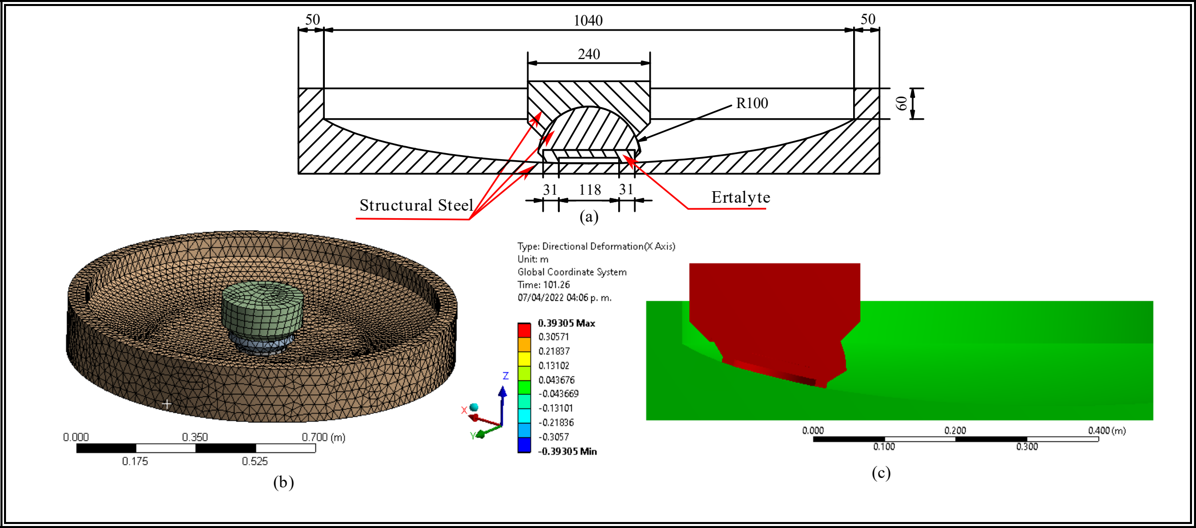

Figure 2-4: (a) Geometric and material properties of the SH-FPS bearing, dimensions are in mm. (b) Finite Element Model of the SH-FPS bearing. (c) Deformed configuration of the device.

Table 2-1: Material properties used in the finite element model

Material	Young's Modulus (MPa)	Poisson's Ratio (-)	Yield strength (MPa)
Structural Steel	200,000	0.30	360
Ertalyte (De Baets et al., 2002)	3,200	0.30	-

2.3.1 Static analyses

Two static analyses were performed to validate the proposed physical model of SH-FPS bearings that includes smooth-hardening behavior and coupling between the pendular force $\boldsymbol{f}^{(n)}$ and the frictional force $\boldsymbol{f}^{(\mu)}$. The first static analysis consisted of a horizontal controlled displacement of 0.39 m in the global x-direction. The second analysis involved a bidirectional motion defined by a displacement in the x-direction described by $u_x = u_0 \sin(\omega t)$ and a displacement in the y-direction described by $u_y = u_0 \sin(2\omega t)$. An amplitude of $u_0 = 0.31$ m was selected. Since the analyses are static, the effects of the angular frequency ω are negligible. In both cases, before applying the controlled displacement, a vertical load of 853 kN was applied on the top face of the articulated slider. A comparison of the first analyzed case is presented in Figure 2-5(a). The physical and FEM models provide almost identical results, even for large displacements once the hardening behavior is reached. A preliminary experimental test has been conducted in order to verify the smooth-hardening behavior of bearings based on elliptical-shaped sliding surfaces under unidirectional horizontal displacement. The results of this preliminary test are reported in Appendix A.

The results of the second studied case are shown in Figure 2-5((c), and (d)). The horizontal path of the slider is shown in Figure 2-5(b). Again, similar results are obtained. The interaction of the components of the frictional force $\boldsymbol{f}^{(\mu)}$ is apparent in Figure 2-5(c). Note that, in points (2) and (4), the trajectory of the slider has a zero component in the y-direction, developing the entire frictional force in the plane formed by the global x and z-axes. The interaction between the two components of the pendular force $\boldsymbol{f}^{(n)}$ is clear in Figure 2-5(c). Even though at point (3) the slider reaches the maximum displacement in the x-direction, a softening behavior is observed between points (2) and (3) due to the decrease of the displacement in the y-direction. The results presented in Figure 2-5((c), and (d)) are consistent with previous experimental and numerical studies (M. Constantinou et al., 1990; Mokha et al., 1990; Nagarajaiah et al., 1991). In the cited papers, a similar shape of the hysterical loops of the friction force in the x-direction was reported due to the influence of the displacement in the y-direction. For example, the trajectory angle, defined as $\theta = \tan^{-1}(\dot{u}_x/\dot{u}_y)$, at point (1) is larger than 45° leading to a frictional component in the y-direction larger than the frictional component in the x-direction. The same peaks of the friction force in points (2) and (4) were signaled. These peaks are produced because the trajectory angle is equal to zero (i.e., all the friction is developed in the x-direction).

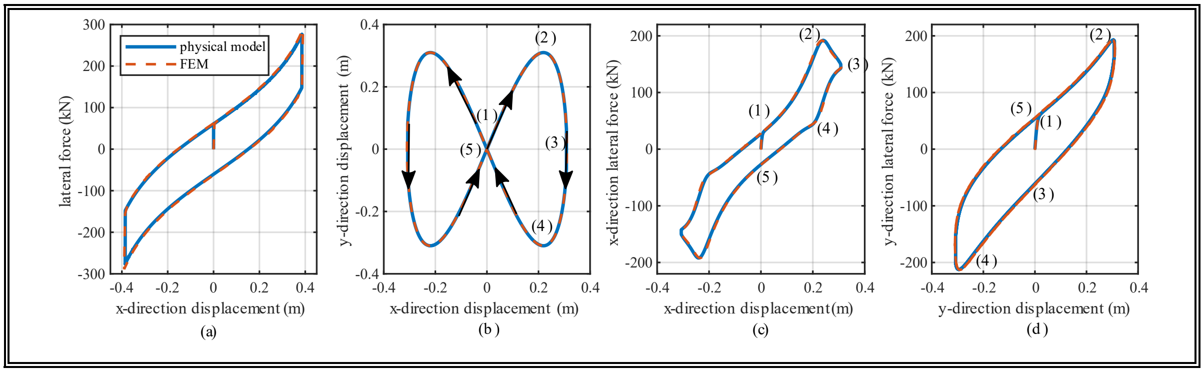

Figure 2-5: (a) Hysteretic loop under unidirectional displacement. (b) Bidirectional trajectory. (c) Hysteretic normalized loop in the x-direction under bidirectional displacement. (d) Hysteretic normalized loop in the y-direction under bidirectional displacement.

2.3.2 Dynamic analyses

Three comparative dynamic analyses were performed to validate the physical model under dynamic excitations. Additionally, these dynamics analyses allow determining the appropriate values of the parameters that define the lateral impact behavior of the isolator. Firstly, two dynamic analyses were conducted applying symmetric Ricker pulses (Ricker, 1944) in one horizontal direction. A symmetric Ricker pulse is defined by its amplitude A_p and period T_p. With these two parameters, it is possible to describe a ground acceleration $\ddot{u}_g$ as follow:

$$\ddot{u}_g = A_p \left(1 - \frac{2\pi^2 t^2}{T_p^2}\right) \exp\left(-\frac{\pi^2 t^2}{T_p^2}\right) \tag{2-25}$$

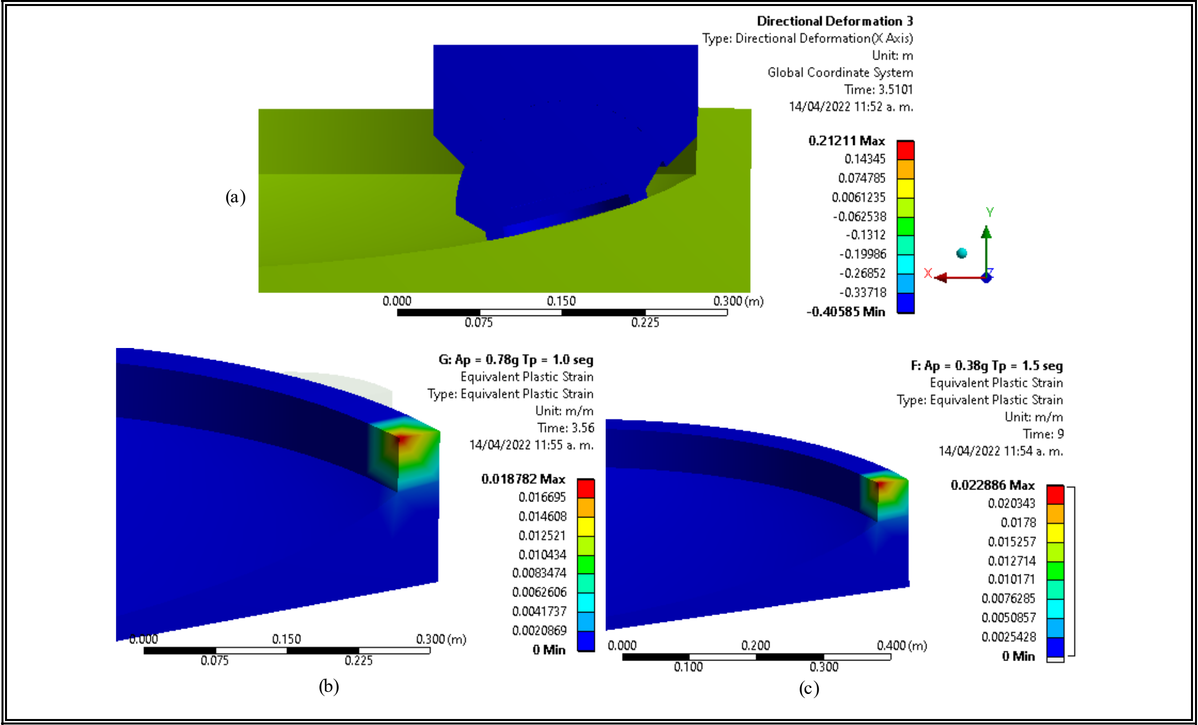

Figure 2-6: (a) FEM under internal lateral impact condition. (b) Equivalent Plastic Strain developed during a Ricker Pulse defined by $A_p = 0.78$g and $T_p = 1.0$ sec. (c) Equivalent Plastic Strain developed during a Ricker Pulse defined by $A_p = 0.38$g and $T_p = 1.5$ sec.

Two Ricker pulses characterized with the following parameters: $A_p = 0.78$g - $T_p = 1.0$ sec, and $A_p = 0.38$g - $T_p = 1.5$ sec, were applied to the FEM as transient accelerations. The Transient Structural Analysis System of the Finite Element Analysis (FEA) ANSYS software was employed to execute the analyses. The amplitude of the pulses was scaled until observing the internal lateral impact between the slider and the restraining rim of the sliding surface. During the internal impact, the nonlinear behavior of the restraining rim is reached, demonstrating the importance of considering the nonlinear material effects in the numerical modeling. In Figure 2-6((b), and (c)), the impact configuration of the FEM and the Equivalent Plastic Strain in the restraining rim are shown for both defined Ricker pulses.

The comparison of the time-history response between the FEM and the physical model of the SH-FPS with parameters $R_0 = 2.25\ \mathrm{m}$ and $a = 0.25 \times R_0$ subjected to the two mentioned Ricker pulses is shown in Figures 2-7 and 2-8. The impact parameters of the physical model were determined by fitting its dynamic impact response with the results obtained from the FEM. An impact stiffness of $k_i = 4.5 \times 10^5$ kN/m and a coefficient of restitution of $e = 0.65$ give a good agreement between both developed models. The impact parameters influence the maximum value of the impact force and the displacement of the slider. The lateral displacement (Figures 2-7(a), and 2-8(a)) and vertical displacement (Figures 2-7(d), and 2-8(d)) of the slider are adequately represented by using the physical model. Note that large displacement are accounted for in both numerical models (FEM and physical model). As described in Section 2.2, the numerical formulation of the physical model uses nonlinear kinematics to describe the relationship between the nodal motions and the displacement of the element. Furthermore, the numerical formulation also considers the angle at which the frictional force is transmitted. It is important to highlight that the physical model allows accounting for the coupling between the horizontal movement of the slider and its vertical displacement. This phenomenon is represented by satisfying at every time step the vertical constrain that the sliding surface imposes on the frictional isolator. This vertical movement can affect the vertical dynamic of superstructures equipped with frictional isolators. The comparison of the lateral force transmitted to the superstructure of both models is presented in Figures 2-7((c), and (d)) and 2-8((c), and (d)) by reporting the time-history response and the hysteretic loops developed in the device. With the defined impact parameters, it is possible to make a good estimation of the maximum forces transmitted during internal lateral impacts. An error of 10% and 2% in the maximum magnitude of the impact force is committed using the proposed numerical model for the pulses characterized by $A_p = 0.78\text{g}$ - $T_p = 1.0$ sec, and $A_p = 0.38\text{g}$ - $T_p = 1.5$ sec, respectively.

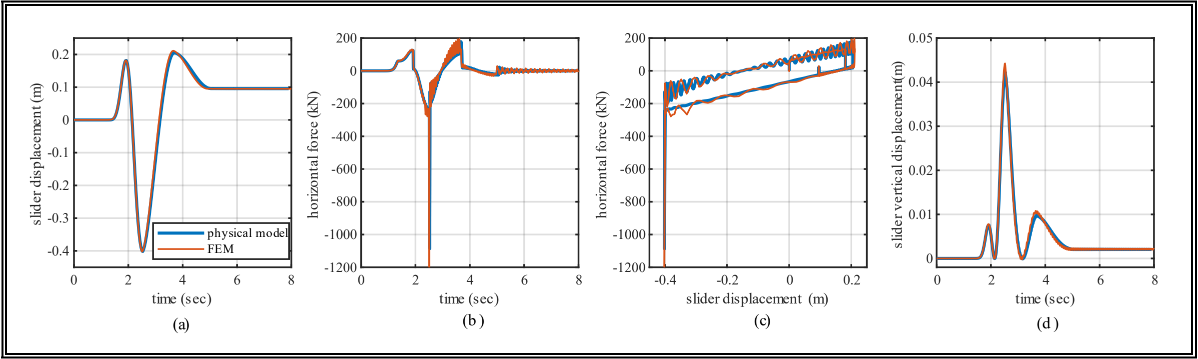

Figure 2-7: Comparative response between the physical model and the FEM subjected to a Ricker Pulse defined by $A_p = 0.78\text{g}$ and $T_p = 1.0$ sec: (a) Lateral slider displacement. (b) Lateral force transmitted by the SH-FPS bearing. (c) Hysteretic loops of the SH-FPS bearings. (d) Vertical displacement of the slider.

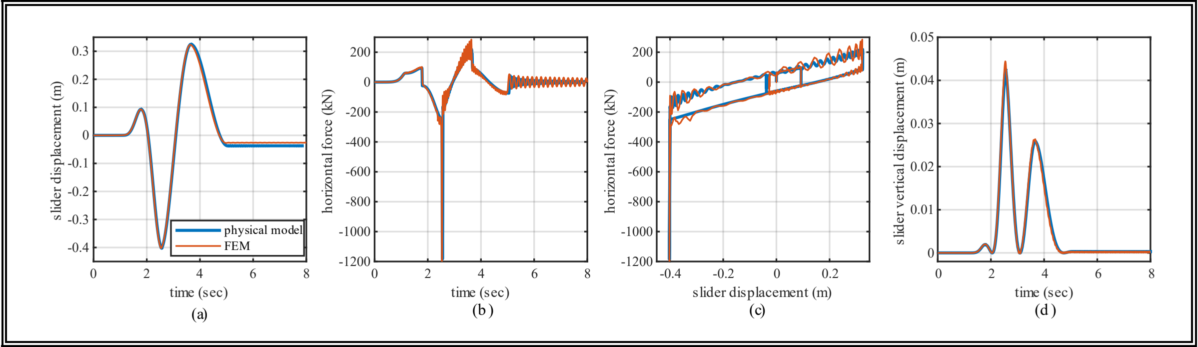

Figure 2-8: Comparative response between the physical model and the FEM subjected to a Ricker Pulse defined by $A_p = 0.38\text{g}$ and $T_p = 1.5$ sec: (a) Lateral slider displacement. (b) Lateral force transmitted by the SH-FPS bearing. (c) Hysteretic loops of the SH-FPS bearings. (d) Vertical displacement of the slider.

The last comparative dynamic analysis between the FEM and the physical model corresponds to a bidirectional natural ground motion applied as transient acceleration in both horizontal directions. The Sylmar - Olive View Med FF record (GM19, Northridge-01 earthquake) (PEER, 2013) was applied in the global x and y-axes. The main characteristics of the ground motion are presented in Table 2-2. The record was scaled by a factor of 0.86 to observe the lateral impact. The impact configuration and the Equivalent Plastic Strain of the restraining rim of the FEM are reported in Figure 2-9.

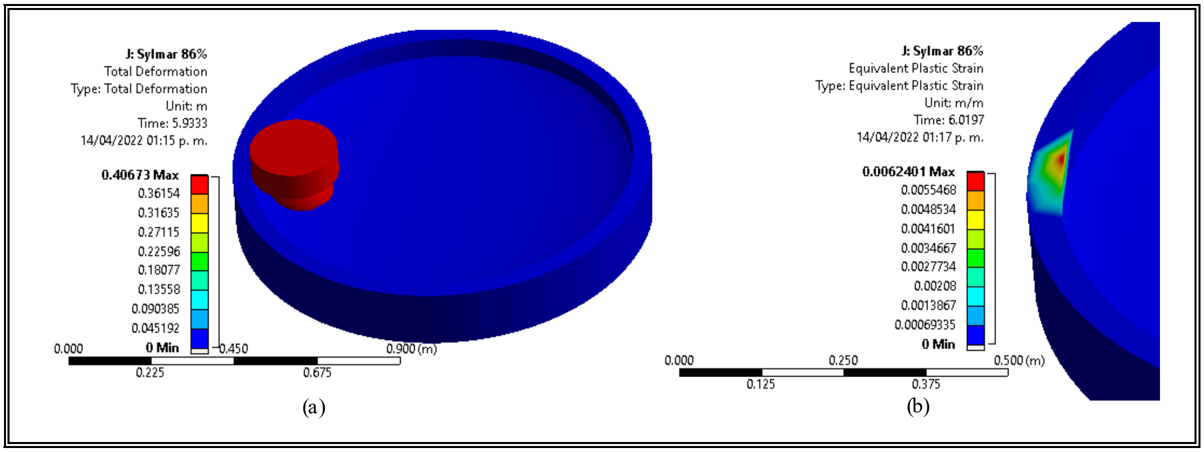

(a)

(b)

Figure 2-9: (a) FEM under internal lateral impact condition during a bidirectional ground motion. (b) Equivalent Plastic Strain developed during the Sylmar - Olive View Med FF record.

A comparison of the displacement time-history response of the slider along the two horizontal directions is presented in Figure 2-10. The two studied models provide very similar results, validating the accuracy of the proposed numerical model in representing the displacement evolution, also in the presence of large displacements and internal lateral impacts.

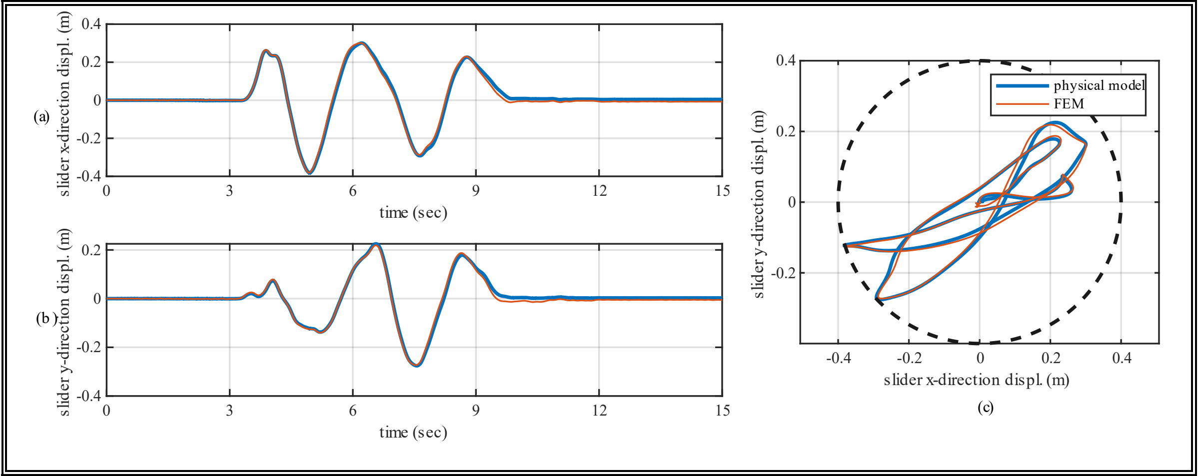

Figure 2-10: Comparative displacement response between the physical model and the FEM subjected to the Sylmar - Olive View Med FF record: (a) Displacement of the slider in the x-direction. (b) Displacement of the slider in the y-direction. (c) Trajectory of the slider.

The comparative response of the forces developed in the SH-FPS bearing is presented in Figure 2-11. The physical model is capable of describing the evolution of the force transmitted by the isolator properly (Figure 2-11((a), and (b))). Also, the direction of the impact force is well represented by the suggested model of variable curvature frictional isolators. Note that, the maximum magnitude of the two components of the impact forces obtained using the physical model has similar values compared to the FEM. The internal lateral impact is observed mainly in the x-direction, explaining why the component in the y-direction has a lower magnitude than the component in the x-direction.

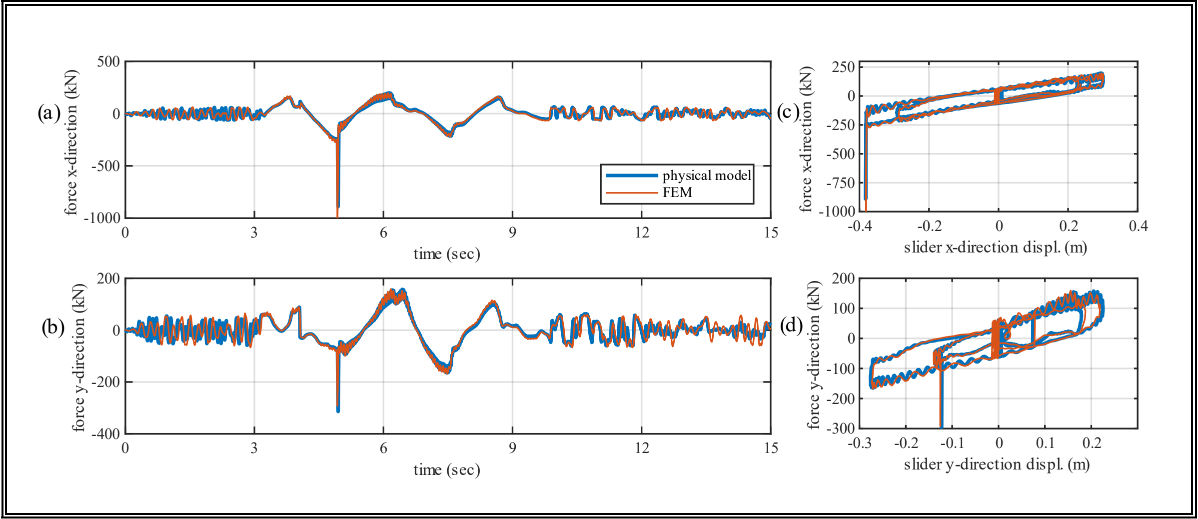

Figure 2-11: Comparative force response between the physical model and the FEM subjected to the Sylmar record: (a) Time-history response of the lateral force in the x-direction. (b) Time-history response of the lateral force in the y-direction. (c) Hysteretic loops in the x-direction. (d) Hysteretic loops in the y-direction.

The described results of this Section indicate that the physical model can be adopted as an accurate element in the representation of variable curvature frictional isolator subjected to internal impacts and large displacements. The comparison of the dynamic response between the physical model and the FEM was a valuable tool to identify the appropriate values of the impact parameters that describe the impact behavior of the SH-FPS bearing. The parameters that define this phenomenon depend on some aspects, such as the geometry of the restraining rims, the masses involved in the impacts, the mechanical properties of the structural steel, and the shape of the slider, among other factors. Hence, it is essential to mention that the selected properties of the impact behavior are related to the device described in Figure 2-4(a). It is suggested to conduct new studies for other frictional isolators subjected to internal impacts.

2.4 Comparative three-dimensional dynamic analysis

In this Section, three-dimensional time-history analyses results are presented, aiming to characterize the lateral behavior of the isolation systems formed by SH-FPS bearings. A three-dimensional structure model equipped with frictional isolators (with and without smooth-hardening behavior) is developed to present a comparison between the response of classical FPS isolators and variable curvature devices, indicating the main differences in the dynamic response.

A three-story, two-bay-by-one-bay, reinforced concrete moment-frame structure was chosen to analyze the earthquake response of a dynamic system seismically isolated with SH-FPS bearings. A similar superstructure has been used to analyze the dynamic behavior of buildings equipped with frictional seismic isolators (José L. Almazán & De la Llera, 2003; G. Auad & Almazán, 2021; P. Castaldo et al., 2015, 2016). The numerical model of the base-isolated building has been fully developed in the MATLAB environment (Hunt et al., 2006). The bay width in both horizontal directions was taken as 8.0 m. The story height was taken as 3.5 m. The superstructure was modeled as a three-dimensional linear elastic multi-degree-of-freedom system. While the columns were modeled with linear frame elements with square sections of 50×50 cm^2, the beams were shaped with rectangular sections of 50×65 cm^2. The slabs were modeled with linear shell elements with a thickness of 15 cm. Based on the physical model described in this paper, six frictional bearings were included to model the isolation system. The nonlinearity of the dynamic system is concentrated in the isolation interface. The elastic modulus of the concrete was set equal to $E_c = 23.4$ GPa. The Poisson's ratio of the material was assumed as $\upsilon = 0.2$. A seismic weight of $w = 10$ kN/m^2 was assigned in all stories, leading to a total weight of $W_s = 5{,}120$ kN. The average vertical load applied on each isolator is 853 kN (i.e., the same load used in the analyses performed in Section 3). The damping matrix was determined using a constant damping ratio of $\xi = 0.02$ to construct the modal base defined by the fixed-base structure (José Luis Almazán, 2001; G. Auad & Almazán, 2021). An illustration of the analyzed three-dimensional isolated building is presented in Figure 2-12.

Two geometries of the sliding surface of the isolators were employed to compare the dynamic behavior of the studied variable curvature frictional isolator. The first geometry represents a spherical-shaped sliding surface with a constant radius of curvature of $R_0 = 2.25$ m ($a = 1.00 \times R_0$). The second geometry of the sliding surface is obtained by revolving an ellipse with geometric parameters of $R_0 = 2.25$ and $a = 0.25 \times R_0$ around the local z-axis. While the first case corresponds to a classical FPS bearing, the second case represents an SH-FPS bearing with the geometry described in Section 3. A friction coefficient at high velocity of $f_{max} = 0.07$ and a frictional coefficient at slow velocity of sliding of $f_{min} = 0.04$ were used in both cases. A lateral capacity of $L_c = 0.40$ m was assumed in both studied isolation systems. The isolated building was subjected to three ground motions to reach three different base displacement demands. The main characteristics of ground motions used in this study are presented in Table 2-2.

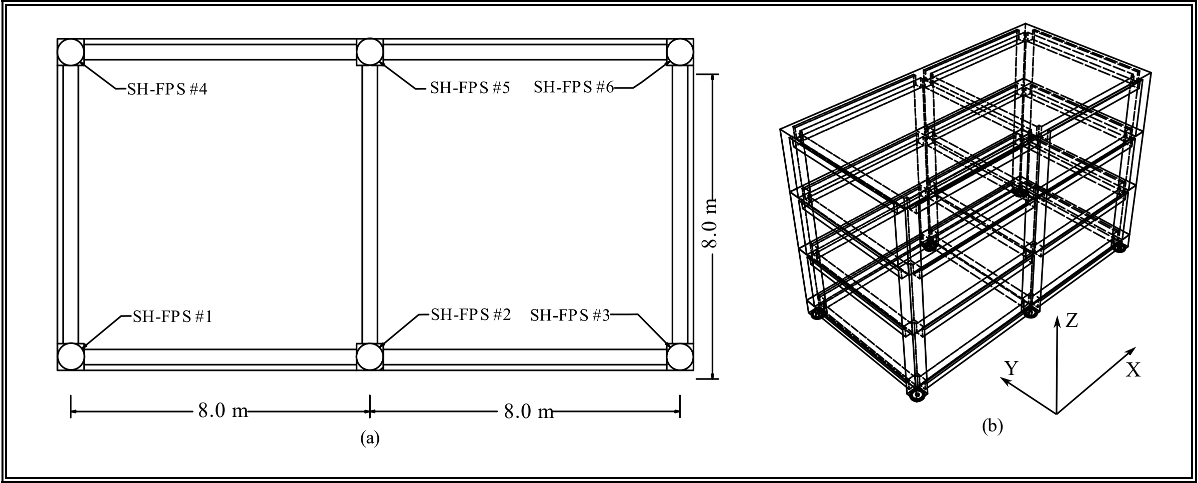

Figure 2-12: (a) Position of the isolators. (b) Model of the three-dimensional structure equipped with frictional isolators. (Modified from Auad and Almazán (G. Auad & Almazán, 2021)).

2.4.1 Low base displacement demand

The base displacement time-history responses of the two considered base-isolated structures subjected to the EC Country Center FF record (GM3, Imperial Valley earthquake, 1979) (PEER, 2013) are presented in Figure 2-13. The base displacements measured at the centroid of the base in the x-direction $U_x(t)$ and in the y-direction U_y(t) are shown in Figure 2-13((a), and (b)), respectively. The trajectory of the centroid of the base is plotted in Figure 2-13((c), and (d)) for the isolation system formed by FPS bearings and the isolation system formed by SH-FPS bearings, respectively. The trajectory of the two analyzed isolation systems is almost identical since the maximum vectorial displacement of the isolation level, defined as $u_{b,max} = \max\left(\sqrt{U_x(t)^2 + U_y(t)^2}\right)$, is less than 0.17 m for both considered isolation systems. At a low level of base displacement, the changes in the curvature of the SH-FPS devices are not significant, and the smooth-hardening feature is not exhibited. The reduction in the maximum vectorial displacement of the isolation interface is less than 1% by using SH-FPS bearings.

At a low base displacement demand, the forces transmitted to the structure are similar no matter what type of isolators is considered, with or without changes in curvature. In Figure 2-14, the forces generated in both isolation systems are presented. The base shear in the x-direction $V_x(t)$, normalized by the total vertical reaction $R_z(t)$ at every time step, is shown in Figure 2-14(a). The normalized base shear in the y-direction $V_y(t)/R_z(t)$ is plotted in Figure 2-14(b). The normalized hysteretic loops of the isolation interfaces (i.e., considering the contribution of all the six isolators) in the x and y-directions are presented in Figure 2-14((c), and (d)), respectively. Note that the hardening stage is not reached for base displacement demand lower than 0.17 m. Consequently, the force response of the isolation system is similar despite using or not using variable curvature frictional isolators. Under low magnitude ground motion, an elliptical-shaped based frictional isolator does not generate changes in the dynamic response of the displacement of the centroid of the base or in forces transmitted to the superstructure.

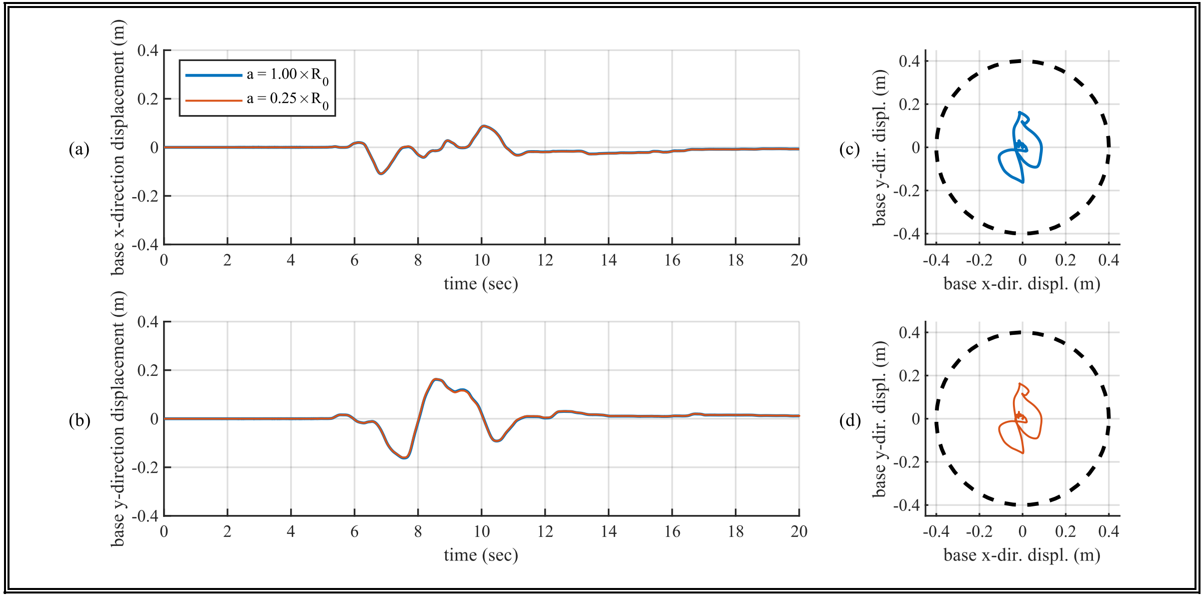

Figure 2-13: Comparison between the two studied isolation systems subjected to the EC Country Center FF record: (a) Displacement of the centroid of the base in the x-direction. (b) Displacement of the centroid of the base in the y-direction. (c) Trajectory of the centroid of the base using FPS bearings. (d) Trajectory of the centroid of the base using SH-FPS bearings.

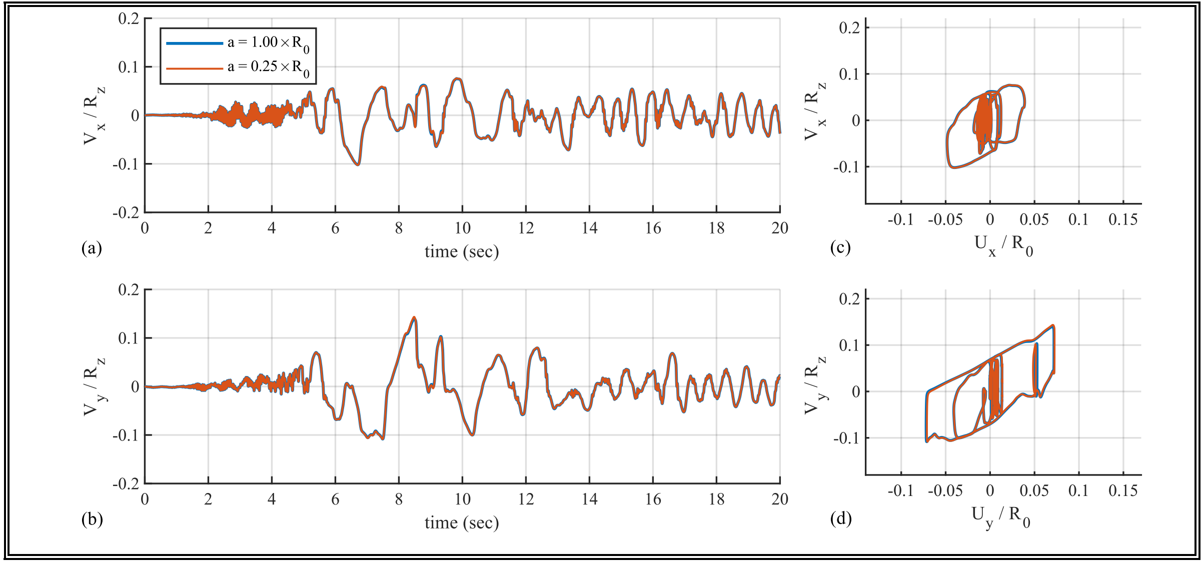

Figure 2-14: Comparison between the two studied isolation systems subjected to the EC Country Center FF record: (a) Normalized base shear in the x-direction. (b) Normalized base shear in the y-direction. (c) Normalized hysteretic loops in the x-direction. (d) Normalized hysteretic loops in the y-direction.

2.4.2 High base displacement demand without internal lateral impact

The comparison of the base displacement time-history responses of the two considered dynamic systems subjected to the Petrolia record (GM14, Cape Mendocino earthquake, 1992) (PEER, 2013) is presented in Figure 2-15. Under the action of this seismic input, a high base displacement demand is observed. In Figure 2-15((c), and (d)), the trajectory of the base is plotted for the isolation system formed by FPS and SH-FPS bearings, respectively. Despite the rise in the displacement of the isolation interface, the impact between the inner slider and the restraining rims of the frictional bearings is not produced. The reduction of the maximum vectorial displacement of the base is noticeable. This 3% reduction in the displacement response is produced by the hardening behavior that SH-FPS isolators exhibit.

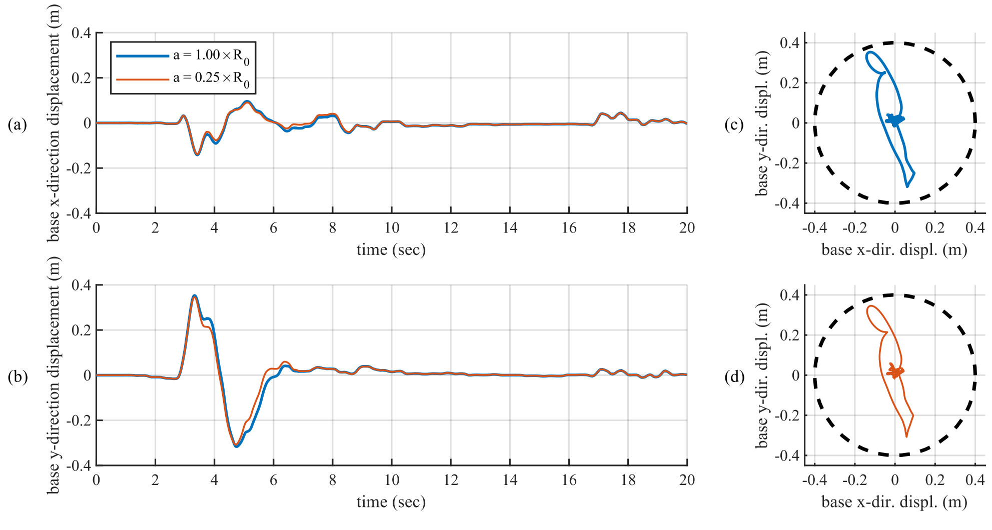

Figure 2-15: Comparison between the two studied isolation systems subjected to the Petrolia record: (a) Displacement of the centroid of the base in the x-direction. (b) Displacement of the centroid of the base in the y-direction. (c) Trajectory of the centroid of the base using FPS bearings. (d) Trajectory of the centroid of the base using SH-FPS bearings.

A comparison between the forces that each considered isolation system transmits to the superstructure if the dynamic system is subjected to the Petrolia record (GM14, Cape Mendocino earthquake, 1992) (PEER, 2013) is presented in Figure 2-16. In both analyzed cases, the maximum value of the base shear is developed mainly in the global y-direction. The hardening phase of the isolation system formed by SH-FPS bearings can be observed in Figure 2-16(d). If large displacements are generated in the isolation system, close to exceeding the lateral capacity $L_c = 0.4$ m, a non-desired rise in the base shear is caused by frictional isolators that exhibit smooth hardening behavior. Under the action of the Petrolia record, an increment of 12.5% in the maximum vectorial base shear, defined as $V_{max} = \max\left(\sqrt{V_x(t)^2 + V_y(t)^2}\right)$, is obtained if the isolation system consists of SH-FPS bearings.

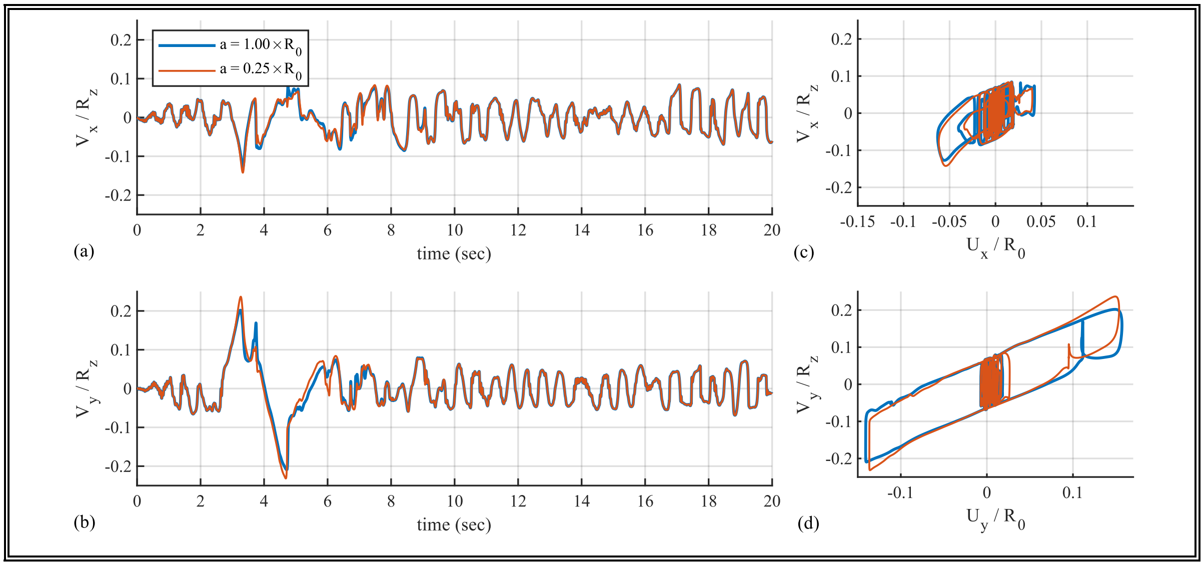

Figure 2-16: Comparison between the two studied isolation systems subjected to the Petrolia record: (a) Normalized base shear in the x-direction. (b) Normalized base shear in the y-direction. (c) Normalized hysteretic loops in the x-direction. (d) Normalized hysteretic loops in the y-direction.

The increment in the shear base produced by the SH-FPS bearings under high base displacement demands can affect the seismic performance of the superstructure in terms of inter-story drifts. In Figure 2-17, the inter-story response of the superstructure is shown. As presented in Figure 2-16(d), the increment in the force is developed mainly in the y-direction; in consequence, a non-negligible rise in the maximum inter-story drifts in that direction is detected. In this case, the maximum drift of the first story in the y-direction is increased by 2.7% using elliptical variable curvature frictional isolators. Note that, in the x-direction, the use of SH-FPS bearings does not generate a rise in the maximum inter-story drift response.

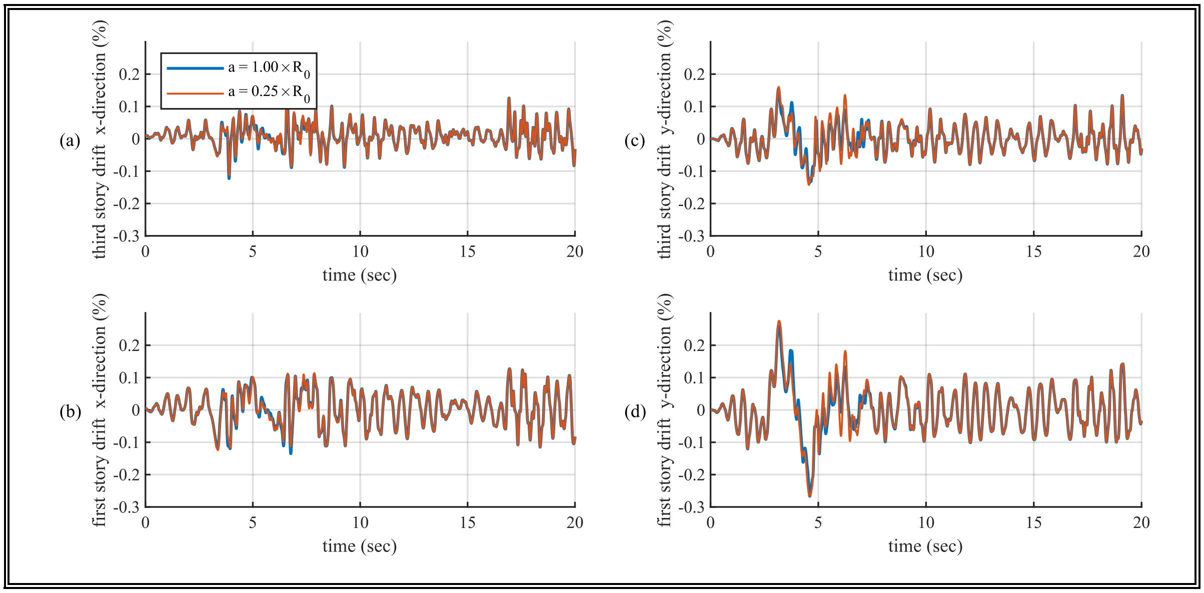

Figure 2-17: Comparison between the two studied isolation systems subjected to the Petrolia record: (a) Third story drift in the x-direction. (b) First story drift in the x-direction. (c) Third story drift in the y-direction. (d) First story drift in the x-direction.

2.4.3 High base displacement demand with internal lateral impact

The comparison of the base displacement time-history response of the seismically isolated building subjected to the El Centro Array#4 record (GM4, Imperial Valley-06 earthquake, 1979) (PEER, 2013) is presented in Figure 2-18. Under the action of this seismic input, and considering an isolation system formed by FPS bearings, one impact is observed (Figure 2-18(c)). The impact is avoided if SH-FPS are employed (Figure 2-18(d)).

The comparison of the base shear time-history response of the dynamic systems subjected to El Centro Array #4 is presented in Figure 2-19. The internal lateral impact occurs at $t = 6$ sec, and it is the most critical contributor to the dramatic rise in the maximum base shear response. Figure 2-19(d) shows the normalized hysteretic loops of the isolation systems in the global y-direction. It is possible to notice that the hardening phase of the isolation interface formed by SH-FPS bearings is reached. The smooth-hardening behavior reduces the maximum base displacement demand and avoids the occurrence of a high magnitude internal impact, decreasing the maximum base shear in the y-direction by 240%. A substantial reduction in the maximum base shear in the x-direction is also measured. The use of elliptical variable curvature isolators reduces the maximum value of this last parameter by 200%.

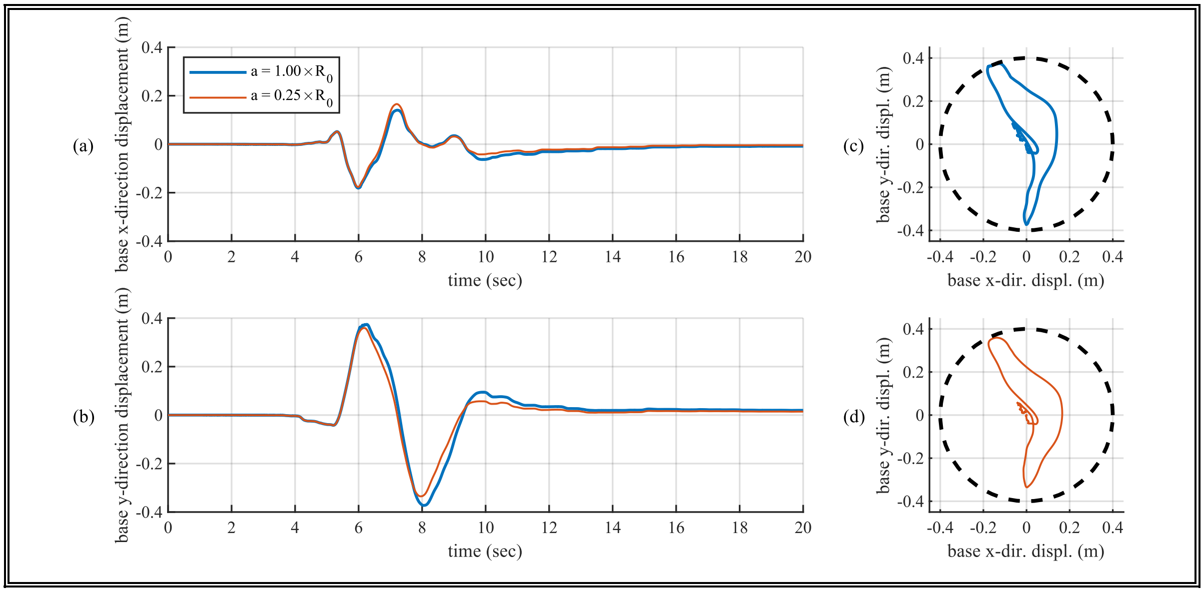

Figure 2-18: Comparison between the two studied isolation systems subjected to the El Centro Array #4 record: (a) Displacement of the centroid of the base in the x-direction. (b) Displacement of the centroid of the base in the y-direction. (c) Trajectory of the centroid of the base of using FPS bearings. (d) Trajectory of the centroid of the base using SH-FPS bearings.

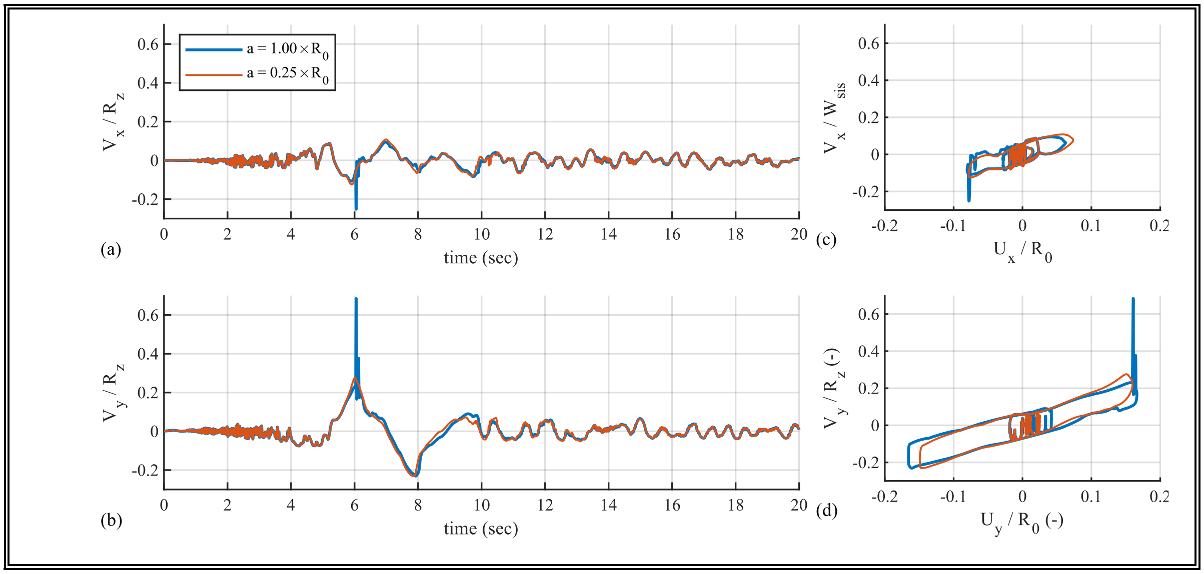

Figure 2-19: Comparison between the two studied isolation systems subjected to the El Centro Array #4: (a) Normalized base shear in the x-direction. (b) Normalized base shear in the y-direction. (c) Normalized hysteretic loops in the x-direction. (d) Normalized hysteretic loops in the y-direction.

The comparison of the inter-story drift response of both analyzed cases subjected to the El Centro Array #4 is presented in Figure 2-20. The occurrence of the high magnitude lateral internal impact in the isolation system causes a dramatic rise in the maximum value of the inter-story drift responses in the y-direction. By avoiding the occurrence of lateral impacts or by decreasing the intensity of the impacts, it is possible to control the increment in this Engineering Demand Parameter. One alternative to achieve better seismic performance is to use the smooth-hardening feature. If SH-FPS bearings form the isolation system, the maximum first story drift in the x-direction is reduced by 37%. A reduction of 57% is reached in the third story drift by using isolators with variable curvature.

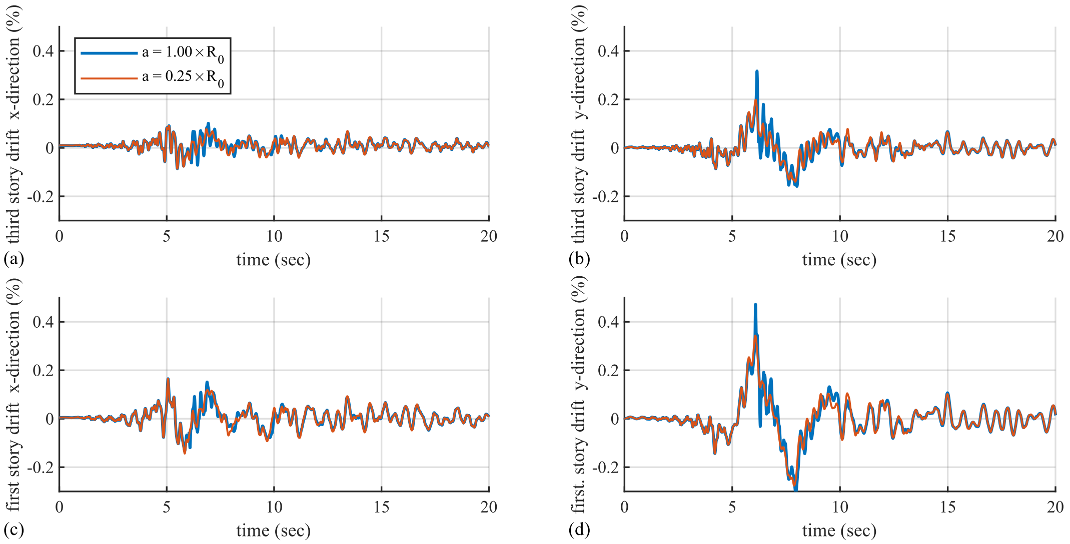

Figure 2-20: Comparison between the two studied isolation systems subjected to the El Centro Array #4: (a) Third story drift in the x-direction. (b) First story drift in the x-direction. (c) Third story drift in the y-direction. (d) First story drift in the x-direction.

2.5 Comparative seismic performance of two-dimensional nonlinear reinforced concrete moment frame equipped with FPS and SH-FPS bearings

In this Section, a comparative analysis of the maximum response related to the isolation system (in terms of maximum base displacement and maximum shear base transmitted to the superstructure) and the superstructure (in terms of maximum inter-story drifts) is performed in order to evaluate the benefits of using frictional isolator with smooth-hardening behavior under strong ground motions. In structures equipped with frictional devices, extreme seismic inputs could cause the internal lateral impact and trigger a dramatic increase in the ductility demand of the superstructure (Bao et al., 2018; Bao & Becker, 2018a, 2018c). For this reason, it is essential to model both columns and beams properly to accurately estimate the maximum dynamic responses of the studied dynamic systems. The superstructure is represented using two-dimensional Euler-Bernoulli beam-column elements in the state-space form (Bao & Becker, 2018a). This formulation allows to include plasticity (i.e., material nonlinearity), stiffness and force degradations, and second-order geometric effects (i.e., geometric nonlinearity). The geometric effects are considered by using the co-rotational approach (Le et al., 2011). The plasticity and degradation are included using a degrading Bouc-Wen model for the flexural and axial behavior. The reinforced concrete moment frame studied in this Section corresponds to the three-story, two-bay frame of the building presented in Section 3. The total seismic weight acting on the frame is $W_s = 2{,}560$ kN. The moment frame and its reinforcement in plastic hinges zones are presented in Figure 2-21. The elements used to represent the nonlinear degrading behavior of columns and beams must be calibrated to model the response of the superstructure accurately. For this purpose, the degrading parameters were calibrated using fiber elements implemented in OpenSees (Mazzoni et al., 2006). In Figure 2-22, the calibrated models for the columns and beams are compared with the results obtained using fiber elements.

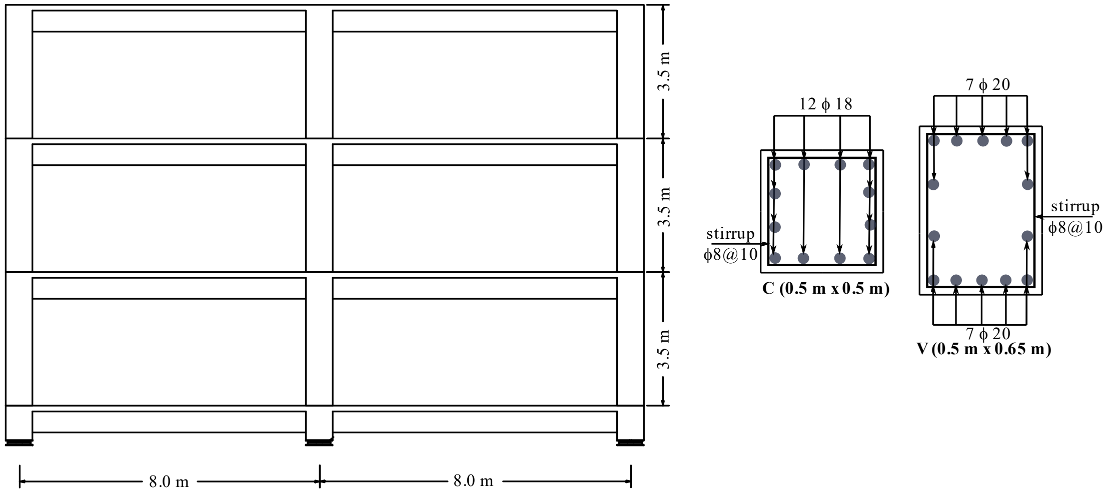

Figure 2-21: Two-dimensional reinforced concrete moment frame equipped with frictional isolators

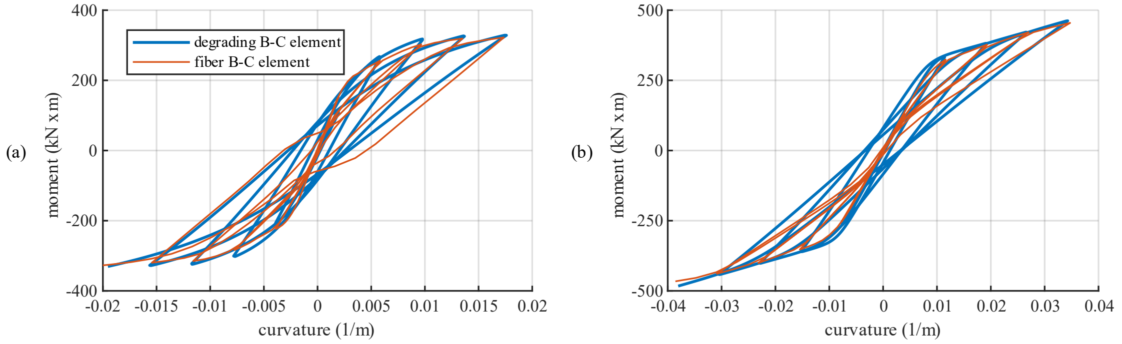

Figure 2-22: Calibrated two-dimensional Euler-Bernoulli beam-column elements in state-space form: (a) Columns. (b) Beams

2.5.1 Design of the base-isolated reinforced concrete moment frame

The design of the base-isolated structure was carried out following the criteria of the American standard AISC-SEI 7-16 (ASCE, 2016). The seismically isolated structure is located in Riverside, California, and founded in a site class C (i.e., $V_{s30} = 530$ m/s). The values of the Maximum Considered Earthquake (MCE) design spectrum are: $S_s = 1.67$g and $S_1 = 0.62$g. The equivalent lateral force procedure was employed to design the isolation system and the superstructure elements.

The design of the isolation system is performed assuming classical FPS bearings. Considering frictional isolators with a radius of $R_0 = 2.25$ m (isolated period of $T_b = 3$ sec) and a friction coefficient of $\mu_d = 0.07$, the maximum displacement of the base was estimated as $D_M = 0.35$ m. Following the minimum criteria of the ASCE/SEI 7-16, the total lateral capacity was defined as $L_c = D_{TM} = 1.15 D_M = 0.40$ m. This rise in the lateral capacity is added to account for accidental torsion effects. The isolators are designed to have restraining rims limiting the maximum displacement at 0.4 m. With the defined lateral capacity and friction coefficient, the isolation system is characterized by an effective period of 2.49 sec, an equivalent damping ratio of 0.20, and a base shear of the isolation system of $V_b = 0.23 W_s$.

Since the building is regular and the effective period of the isolation system is greater than three times the natural period of the fixed-base frame (0.5 sec), the lateral force procedure was used to design the superstructure. For the design of the structural elements, a reduction factor of $R_I = 9/8$ was employed. The design shear was estimated as $V_{st} = 0.17W_s$. With this seismic load, the reinforcement presented in Figure 21 was adopted.

2.5.2 Ground motion selection

The ground motion selection was made aiming to represent the record-to-record variability. For this purpose, 20 accelerometer registrations were included in the analysis. The seismic records have less than 50 km epicentral distances and moment magnitudes between 6 < Mw < 7.5. The information of the 20 selected seismic records is reported in Table 2-2.

Table 2-2: Selected ground motions (PEER, 2013).

Ground motion ID	Records sequence number	Earthquake	Year	Station Name	Magnitude	Epicentral distance (km)	PGA (g)	Vs30 (m/s)
GM1	6	Imperial Valley-02	1940	El Centro Array #9	6.95	13	0.18	213
GM2	68	San Fernando	1971	LA - Hollywood Stor FF	6.61	39	0.16	316
GM3	170	Imperial Valley-06	1979	EC County Center FF	6.53	29	0.24	192
GM4	179	Imperial Valley-06	1979	El Centro Array #4	6.53	27	0.29	209
GM5	182	Imperial Valley-06	1979	El Centro Array #7	6.53	28	0.58	211
GM6	183	Imperial Valley-06	1979	El Centro Array #8	6.53	28	0.47	206
GM7	185	Imperial Valley-06	1979	Holtville Post Office	6.53	20	0.26	203
GM8	187	Imperial Valley-06	1979	Parachute Test Site	6.53	49	0.16	349
GM9	451	Morgan Hill	1984	Coyote Lake Dam	6.19	25	0.39	561
GM10	459	Morgan Hill	1984	Gilroy Array #6	6.19	36	0.41	663
GM11	776	Loma Prieta	1989	Hollister - South & Pine	6.93	48	0.20	282
GM12	801	Loma Prieta	1989	San Jose - Santa Teresa H.	6.93	20	0.23	672
GM13	827	Cape Mendocino	1992	Fortuna - Fortuna Blvd	7.01	30	0.05	457
GM14	828	Cape Mendocino	1992	Petrolia	7.01	5	0.17	422
GM15	829	Cape Mendocino	1992	Rio Dell Overpass - FF	7.01	23	0.20	312
GM16	879	Landers	1992	Lucerne	7.28	44	0.82	1369
GM17	982	Northridge-01	1994	Jensen Filter Plant A.B.	6.69	13	0.35	373
GM18	1063	Northridge-01	1994	Rinaldi Receiving Sta	6.69	11	0.96	282
GM19	1086	Northridge-01	1994	Sylmar - Olive View Med	6.69	17	0.54	441
GM20	1087	Northridge-01	1994	Tarzana - Cedar Hill A	6.69	5	1.05	257

The selected ground motions were modified in order to match the MCE spectrum related to the site in Riverside (California). In Figure 23(a), the spectra of all the chosen seismic records are plotted. In Figure 23(b), the average spectrum of the 20 records is compared with the MCE spectrum.

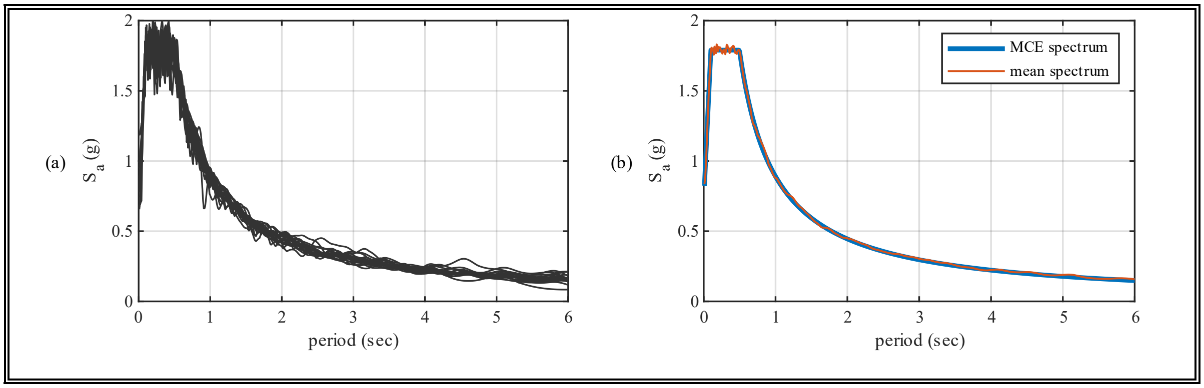

Figure 2-23: (a) Spectra of the 20 selected seismic records modified to match the MCE spectrum. (a) Comparison of the average spectrum of the selected seismic records and the MCE spectrum

2.5.3 Comparative time-history response of the nonlinear reinforced concrete moment frame

In this Subsection, a comparative analysis of the structural Engineering Demand Parameters (EDPs) of interest is presented, aiming to evaluate the benefits of using SH-FPS bearings. Five EDPs were defined: (i) maximum base displacement, (ii) maximum base shear, (iii) maximum first story drift, (iii) maximum second story drift, and (v) maximum third story drift. Five isolators were considered to form the isolation system, each with an initial radius of $R_0 = 2.25$ m. Five values of the a parameter of the SH-FPS bearings were selected: $a = 1.00 \times R_0$, $a = 0.40 \times R_0$, $a = 0.35 \times R_0$ and $a = 0.30 \times R_0$ and $a = 0.25 \times R_0$. Consider that isolators with parameters $R_0 = 2.25$ m and $a = 1.00 \times R_0$ represent FPS bearings (i.e., an isolator with a spherical sliding surface). A frictional bearing with parameters $R_0 = 2.25$ m and $a = 0.25 \times R_0$ represents a device identical to the one presented in Section 2-3. The hysteretic loops of the considered isolators generated with a vertical load of 853 kN are shown in Figure 2-24.

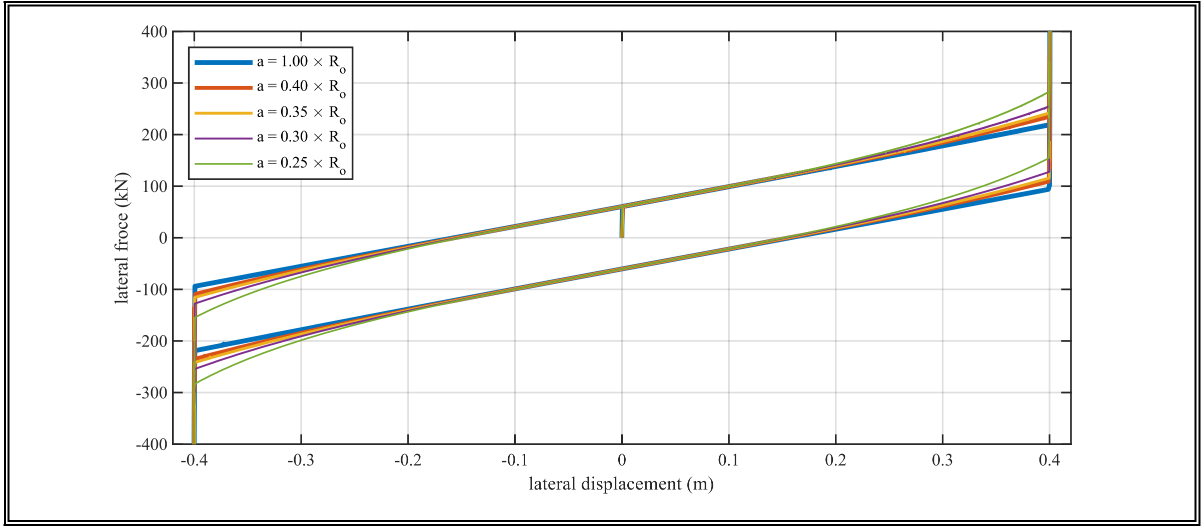

Figure 2-24: Hysteretic loops of SH-FPS bearings with $R_0 = 2.25$ m for different values of the parameter a

The time-story response of four isolation systems is presented in Figures 2-25 and 2-26 to illustrate the changes in the dynamic response produced by using variable curvature seismic isolators with smooth-hardening behavior. In this illustrative comparison four isolation systems ($R_0 = 2.5$ m and $a = 1.00 \times R_0$, $R_0 = 2.5$ m and $a = 0.40 \times R_0$, $R_0 = 2.5$ m and $a = 0.35 \times R_0$, $R_0 = 2.5$ m and $a = 0.35 \times R_0$) were subjected to the modified Petrolia record (GM14, Cape Mendocino earthquake, 1992) (PEER, 2013). The roof and base displacements relative to the ground are shown in Figure 2-25((a), and (b)). The smooth hardening feature allows reducing the maximum base displacement demand. In Figure 2-25(c), the hysteretic loops of the isolation system acquired summing the contribution of all the isolators of the isolation interface, normalized by the seismic weight of the structure W_s, are plotted. The mitigation of one of the adverse effects of internal lateral impacts: a dramatic rise in the magnitude of the seismic forces transmitted to the superstructure, can be achieved by decreasing the magnitude of impacts (isolation system formed by $R_0 = 2.5$ m and $a = 0.40 \times R_0$ devices) or by avoiding the occurrence of impacts (isolation system formed by $R_0 = 2.5$ m and $a = 0.35 \times R_0$ or structure equipped with $R_0 = 2.5$ m and $a = 0.25 \times R_0$ devices). The rise in the base shear transmitted to the superstructure affects the performance of the reinforced concrete frame. In Figure 2-26, the inter-story drift response is shown. Note that the lateral displacement of the superstructure is concentrated in the first story. The higher the story, the lower the maximum drift response. The benefits of using SH-FPS bearings to reduce the maximum inter-story drift response are maximized for the isolation system formed by devices with geometric parameters of $R_0 = 2.5$ m and $a = 0.35 \times R_0$. It is important to mention that a reduction in the a parameter (i.e., the smooth hardening behavior is observed for lower lateral displacements of the base) does not ensure a better seismic performance. The isolation system formed by SH-FPS bearings with $a = 0.25 \times R_0$ generates higher inter-story drifts than the isolation system formed by SH-FPS bearings with $a = 0.35 \times R_0$.

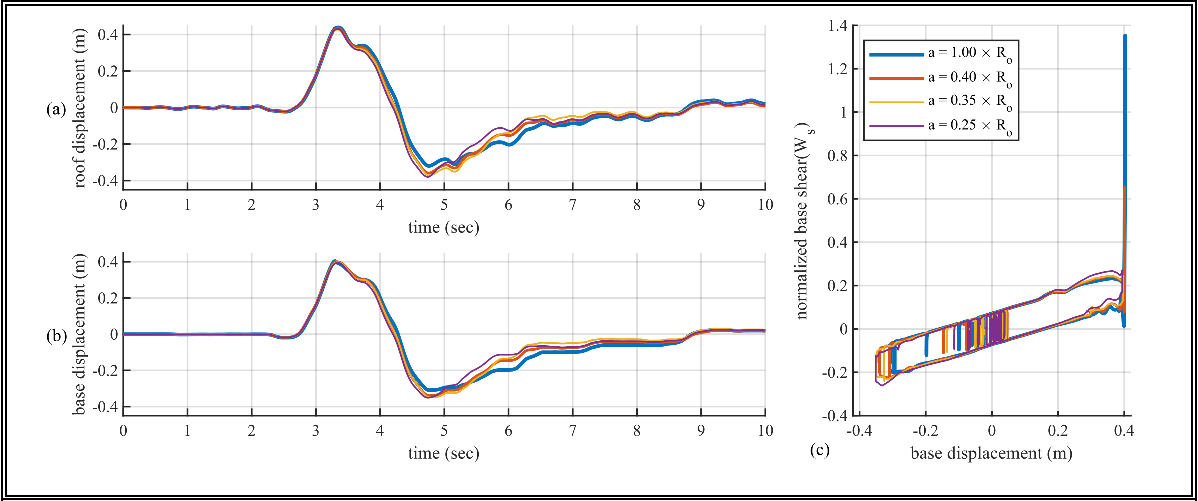

Figure 2-25: Time-history comparison of the nonlinear reinforced frame: (a) Roof displacement. (b) Base Displacement. (c) Hysteretic loops of the isolation system.

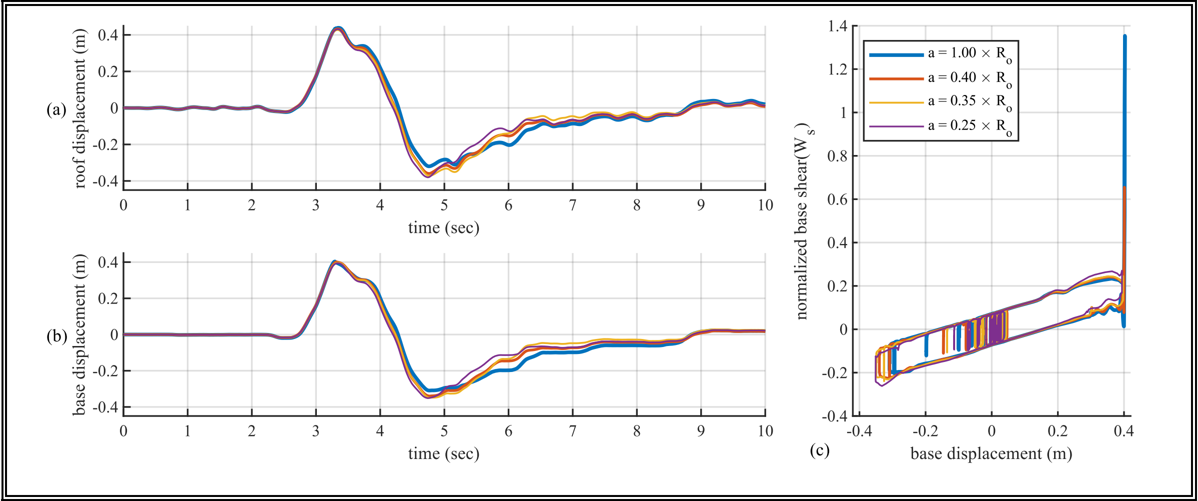

Figure 2-26: Time-history comparison of the inter-story drifts developed in the reinforced concrete frame: (a) First story drift. (b) Second story drift. (c) Third story drift.

Figures 2-27 to 2-31 show the maximum values of the defined EDPs for the five studied isolation systems subjected to the 20 seismic records modified to match the MCE spectrum. The last bars of Figures 2-27 to 2-31 correspond to the average value of the corresponding EDP. Blue bars represent FPS bearings (i.e., isolators with spherical sliding surfaces). Other colors represent variable curvature devices. In Figure 2-27, the maximum base displacement demand is shown. In general, SH-FPS bearings reduce the maximum displacement of the isolation interface. The maximum reduction in this EDP is obtained for the isolation system formed by SH-FPS with geometric parameters of $R_0 = 2.5$ m and $a = 0.30 \times R_0$. In this case, the determined reduction of the maximum base displacement is 5%.

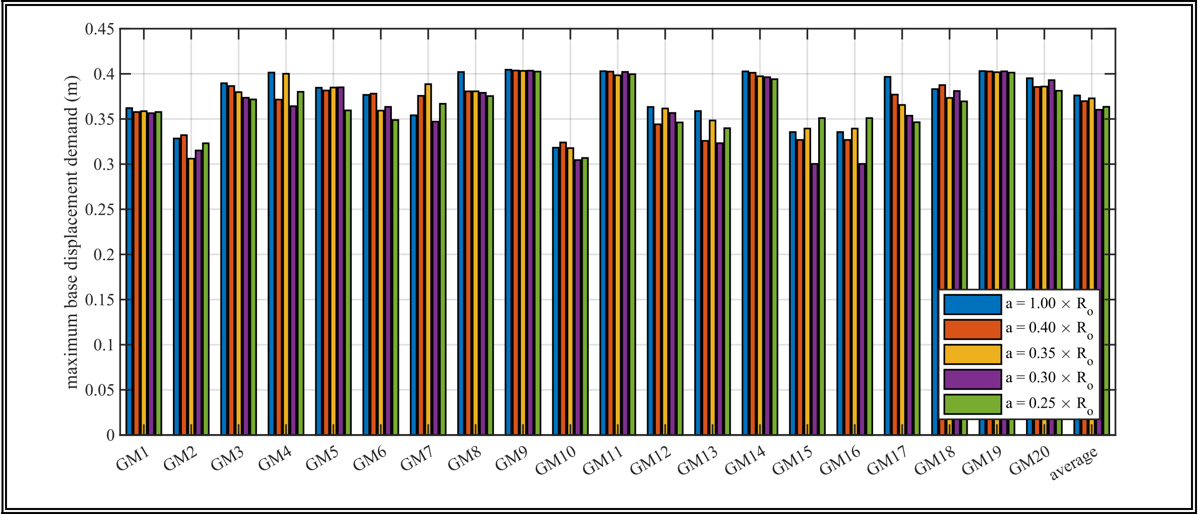

Figure 2-27: Maximum base displacement demand for different isolation systems subjected to the 20 selected ground motions.

In Figure 2-28, the maximum normalized base shear transmitted to the superstructure is reported for all the selected seismic records and analyzed isolation systems. If the structure is subjected to GM4 or GM8, SH-FPS bearings avoid the internal impact, achieving an important reduction of the maximum shear base. Using variable curvature isolators can help reduce the magnitude of the internal impact. This way of mitigating the adverse effects of internal lateral impacts can be observed under the action of the following seismic records: GM9, GM11, GM14, and GM19. In general, if the internal impact is not observed (GM1, GM2, GM3, GM5, GM6, GM7, GM10, GM12, GM13, GM15, GM16, GM17, GM18, and GM20), a rise in the geometric parameter a of SH-FPS bearings leads to a rise in the maximum base shear. Considering the average responses, reductions up to 44% are achievable using isolators with elliptical sliding surfaces.

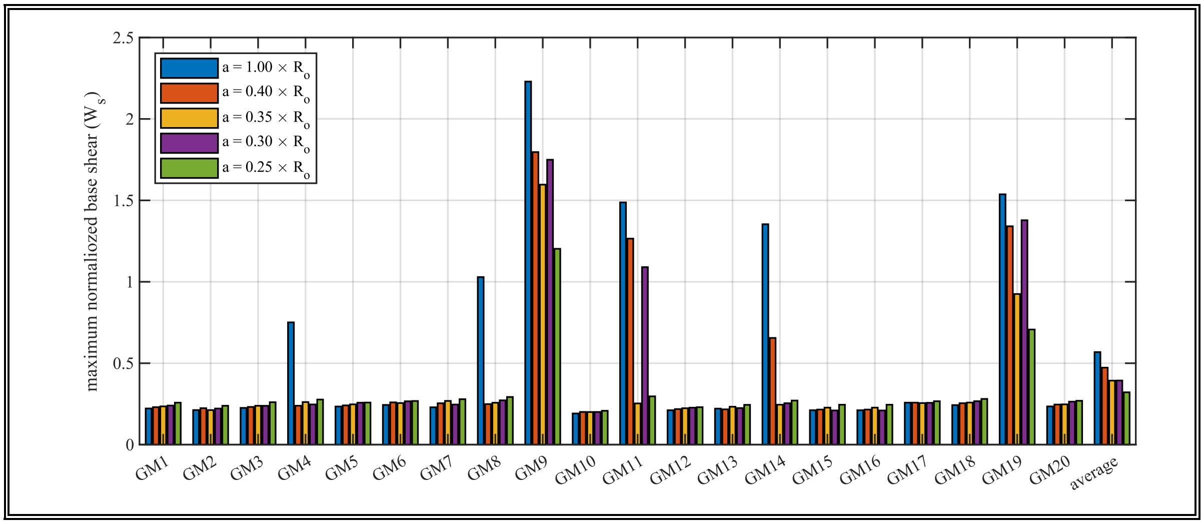

Figure 2-28: Maximum normalized base shear for different isolation systems subjected to the 20 selected ground motions.

The maximum inter-story drifts of the first, second, and third stories are shown in Figures 2-29 to 2-31, respectively. For ground motions that generate the internal impact, reductions of the inter-story drift response are possible using SH-FPS bearings. An optimum isolation system can be found, considering the average reduction of the maximum first and second story drifts (the critical stories). The use of SH-FPS bearings with geometric parameters of $R_0 = 2.25\,\mathrm{m}$ and $a = 0.35 \times R_0$ maximizes the reduction of these EDPs. Average reductions of 11% and 8% are obtained in the maximum first and second story drifts, respectively, using the optimal isolation system. A not negligible reduction of 6% in the maximum third story drift was obtained using the optimal isolation system. The smooth-hardening behavior can worsen seismic performance if the lateral impact is not observed. This phenomenon is apparent in the isolation system formed by SH-FPS bearings with geometric parameters of $R_0 = 2.25$ m and $a = 0.25 \times R_0$. This isolation system is typified as the one with the most considerable curvature change. Low values of the a parameter can jeopardize the benefits of using SH-FPS isolators in terms of reducing the maximum nonlinear displacement of the superstructure.

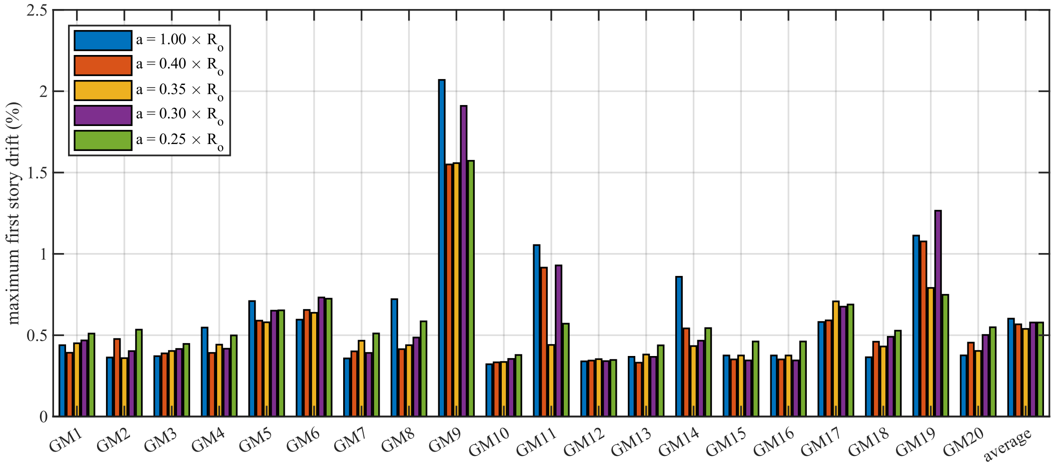

Figure 2-29: Maximum first story drift for different isolation systems subjected to the 20 selected ground motions.

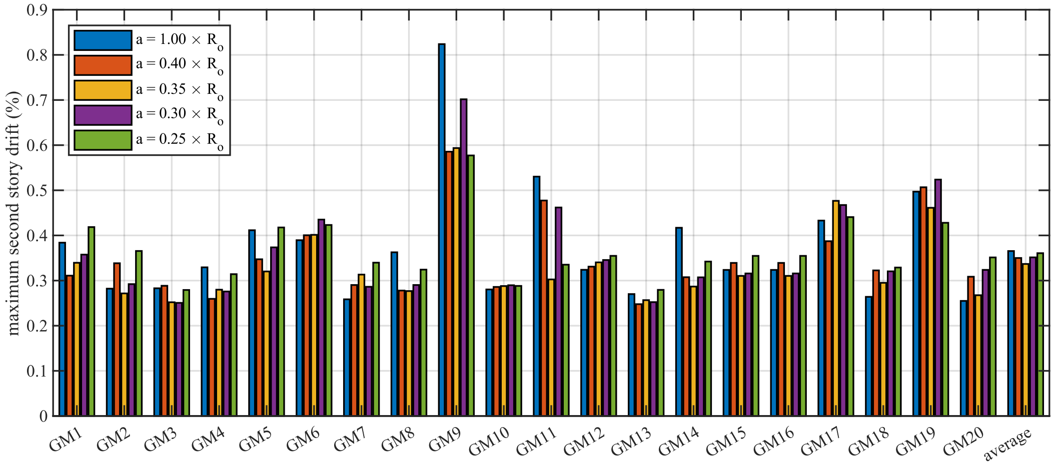

Figure 2-30: Maximum second story drift for different isolation systems subjected to the 20 selected ground motions.

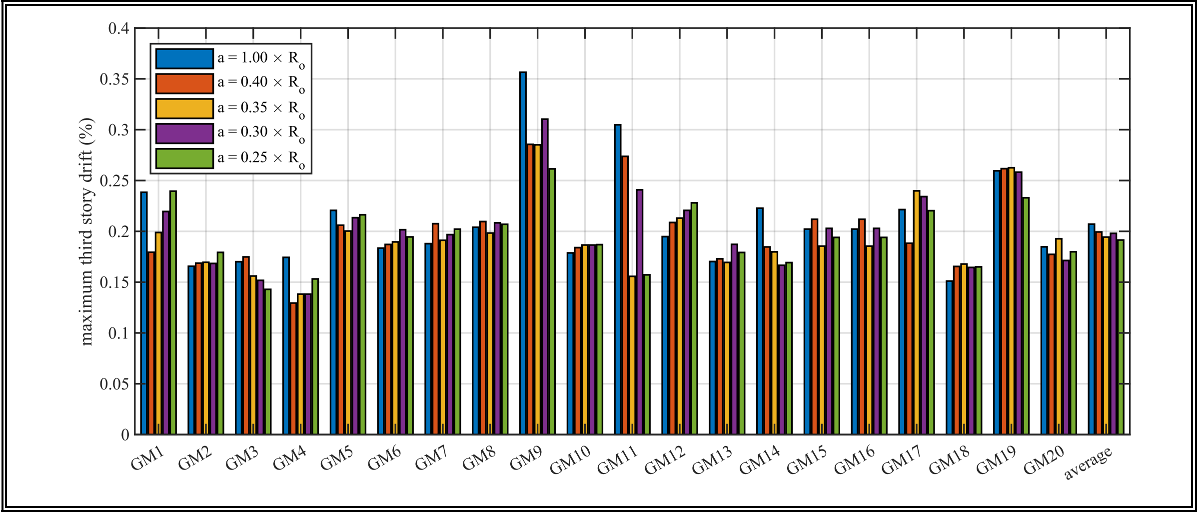

Figure 2-31: Maximum third drift for different isolation systems subjected to the 20 selected ground motions.

2.5.3 Sensitivity analysis of the impact parameters

In this Subsection, the effects of variation in the impact parameters are investigated. Sensitivity analyses are performed by variating the value of the impact stiffness k_i and the coefficient of restitution e. The restraining rims may have different heights and thicknesses affecting the impact parameters or can be constructed using steel with different yield strengths. Five values of the impact stiffness have been examined, varying from 0.5 to 1.5 times the value of $k_i = 4.5 \times 10^5$ kN employed in Sections 2.3, 2.4, and 2.5. Five values of coefficient of restitution, $e = 0.4$; 0.5; 0.6 ; 0.65; and 0.7, were analyzed, covering the range commonly used in steel-to-steel impacts (Bao et al., 2017).

The EDPs affected by impacts (i.e., maximum shear base and maximum inter-story drifts) were calculated to measure the effects of variations in the impact parameters. The nonlinear frame presented in Section 5 equipped with FPS bearings was subjected to the Hollister -

South & Pine records (GM11, Loma Prieta earthquake, 1989) (PEER, 2013) to perform the sensitivity analysis. The results of the sensitivity analysis are reported in Figure 2-32.

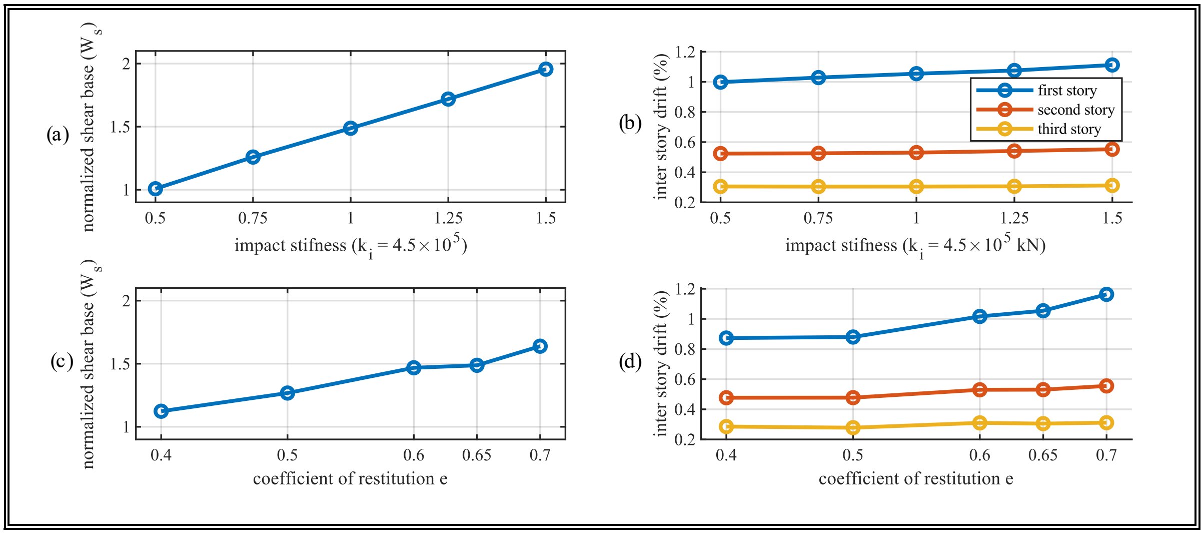

Figure 2-32: Sensitivity analysis of the impact parameters. (a) Maximum base shear for different values of impact stiffness k_i and $e = 0.65$. (b) Maximum inter-story drifts for different values of impact stiffness k_i and $e = 0.65$. (c) Maximum base shear for different values of the coefficient of restitution e and $k_i = 4.5 \times 10^5$ kN. (d) Maximum inter-story drifts different values of the coefficient of restitution e and $k_i = 4.5 \times 10^5$ kN.

The impact stiffness greatly influences the maximum base shear transmitted to the superstructure (see 2-Figure 32(a)). An increase of 50% in the k_i parameter raises the base shear by 32%. The opposite happens if the impact stiffness is decreased. The lower the impact stiffness, the lower the maximum base shear. The maximum inter-story drift response is less influenced by changes in the impact stiffness (see Figure 2-32(b)). A rise of 50% in this parameter only increases the maximum first story drift by 6%. The variation in the maximum drift of the second and third stories is even lower.

The effects of changing the value of the coefficient of restitution e on the maximum base shear and maximum inter-story drifts are reported in Figure 2-32((c), and (d)), respectively.

Low values of this parameter imply larger energy dissipation during impact. On the contrary, a unitary value of the restitution coefficient represents an elastic impact. The normalized shear base is affected by changes in this parameter. A rise of 7.7% (from 0.65 to 0.7) increases the maximum base shear by 10%. The maximum inter-story drift is also affected by the value of the coefficient of restitution, especially for high values. An important rise of 10% in the maximum first story drift is detected if the studied parameter is increased by 7.7%. The lower the e parameter, the lower the maximum inter-story drifts are generated since a larger amount of energy is dissipating during impact and it is not transferred to the superstructure.

Both impact parameters affect the maximum structural responses. For this reason, the values of the impact properties used in this study are suggested only for the geometry of the isolator presented in Section 2.3 and the superstructures described in Sections 2.4 and 2.5. Proper calibration of the impact parameters must be conducted to study a different dynamic system.

2.6 Seismic reliability of inelastic base-isolated structures equipped with SH-FPS

Internal impacts between the inner sliders and the restraining rims of frictional isolators can produce a dramatic increment in the lateral displacement demand of the superstructure. This increment in the displacement usually leads to nonlinear behavior of the isolated building (Bao et al., 2017, 2018; Bao & Becker, 2018b, 2018c; Kitayama & Constantinou, 2019a, 2019b). For this reason, the nonlinear behavior of the superstructure must be considered to assess alternatives to reduce the adverse effects of lateral impacts. In this research as a starting point simplified models of dynamics systems equipped with SH-FSP bearings are evaluated. An equivalent model can be an excellent alternative to evaluate a wide range of dynamic systems, highlighting under what structural properties the use of isolators with smooth hardening behavior is recommended. One possible alternative to compare in a robust way the seismic performance of the studied technology is by obtaining reliability curves in a time frame of 50 years. With these curves, it is possible to determine the probability of exceeding limit states and compare them with the curves obtained by using classical frictional isolators such as FPS bearings.

2.6.1 Inelastic model of a base-isolated structure equipped with SH-FPS bearings

A simplified model of four-degrees-of-freedom, adapted from the model proposed by Kelly (Naeim & Kelly, 1999) to consider the inelastic hardening response of the superstructure and the features of the physical model described in this paper, is used to evaluate the seismic performance of structures equipped with frictional isolators. This equivalent model has been extensively used to evaluate the seismic performance of structures equipped with frictional devices (P. Castaldo & Alfano, 2020; Paolo Castaldo et al., 2018; Paolo Castaldo, Palazzo, et al., 2017). The adapted model is illustrated in Figure 2-33.

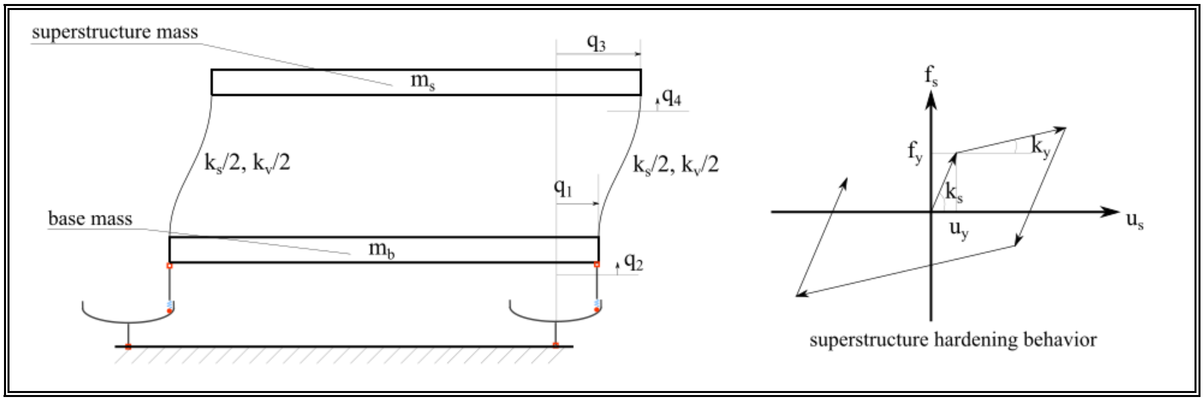

Figure 2-33: Four-degrees-of-freedom model of an inelastic hardening building isolated with frictional devices.

The mass distribution of the superstructure is characterized by two parameters, the mass of the base m_b and the mass of the superstructure m_s. With these two parameters, the mass ratio is defined as $\gamma = m_s/(m_s + m_b)$. The elastic stiffness of the superstructure is denoted by k_s. The yielding lateral displacement u_y limits the elastic behavior. If this limit is exceeded, a change in the stiffness is observed, being k_y the post-yield hardening stiffness. The ratio between the hardening and the elastic stiffness is defined as $r_H = k_y/k_s$. The behavior of the superstructure in the vertical direction is assumed linear, and the vertical stiffness k_v defines it. The lateral elastic circular frequency of the structure is determined as $\omega_s = \sqrt{k_s/m_s}$. With this parameter, the structural period of vibration is defined as $T_s = 2\pi/\omega_s$. If frictional devices with constant curvature form the isolation system, the isolation circular frequency is determined by $\omega_b = \sqrt{k_b/(m_s + m_b)} = \sqrt{g/R_0}$ and the isolation period as $T_b = 2\pi/\omega_b$. The forces developed in the isolation system are calculated using the physical model described in section 2. In this study, only one isolated period is studied, $T_b = 3$ sec ($R_0 = 2.25$ m).

The nonlinear lateral force of the superstructure f_s is modeled using a Bouc-Wen element (Park et al., 1986). This nonlinear lateral force can be computed as:

$$f_s = r_H k_s d + (1 - r_H) k_s u_y z_s \tag{2-26}$$

in which d is the displacement of the element and z_s the hysteretic parameter of the nonlinear element. The differential equation associated with z_s can be expressed as:

$$\dot{z}_s = u_y \dot{d}\left(A - \left(\beta \operatorname{sign}\left(z_s \dot{d}\right) + \gamma\right)|z_s|^e\right) \tag{2-27}$$

in which $\dot{d}$ is the velocity of displacement of the element and A, β, γ and e are parameters of the hysteretic model.

2.6.2 Uncertainties within the seismic reliability of structures equipped with SH-FSP bearings

The friction coefficient at large velocity f_{max} and the earthquake event characteristics had been selected as the relevant random variables. Other uncertainties such as the properties of the superstructure and the geometric properties of the isolation device are considered deterministic since they do not produce important effects on the statistical values of the response parameters, especially for high values of isolation degree $I_d = T_b/T_s$ (Adam et al., 2004; Palazzo, 1991).

As shown in experimental tests (M. Constantinou et al., 2007; Mokha et al., 1990), the friction phenomenon developed in this kind of seismic isolators cannot be modeled using the Coulomb friction law (constant friction coefficient during sliding) but as a velocity-dependent phenomenon. The uncertainty on the sliding friction coefficient at large velocity

f_{max} is considered by using an appropriate Gaussian PDF, truncated on both sides to 3% and 7%, with a mean value equal to 5%. The considered standard deviation is taken equal to the dispersion of the corresponding uniform PDF. Fifteen values of f_{max} were sampled using the Latin Hypercube Sampling (LHS) method. The friction coefficient at slow velocity f_{min} of sliding is assumed to be correlated with f_{max}. The ratio between these two frictional parameters is set as $f_{max}/f_{min} = 2$.

An intensity measure (IM) is introduced into the probabilistic analysis to separate the uncertainties of the seismic input intensity and the characteristics of the records. In this work, the selected IM is the spectral acceleration at the isolated period $S_a(T_b)$. This parameter is associated with a particular location and soil condition and linked with a specific return period T_r according to the seismic hazard of the specific site. Ten return periods were selected (43; 144; 289; 475; 949; 1,485; 2,475; 3,899; 7,462; and 10,000 years) to determine ten different values of the IM.

2.6.3 Ground motion selection

The ground motion selection was performed matching Conditional Spectra (CSs) (T. Lin et al., 2013a, 2013c) and considering their distribution for each defined IM level. Firstly, it is necessary to define a specific location (Riverside, California; latitude/longitude = 33.979/-117.335) and soil condition (soil class C, $V_s = 537$ m/s). After the location and the soil condition are defined, it is possible to determine the main characteristics of the mean causal earthquake related to each considered T_r. The magnitude, the distance, and the conditional standard deviation of each mean causal earthquake are obtained from de-aggregation of the ground motion hazard using the Unified Hazard Tool (*Unified Hazard Tool*, n.d.). The model of Boore *et al.* (Boore et al., 2014) and the model of Baker and Jayaram (Baker & Jayaram, 2008) were employed to construct Conditional Mean Spectra (CMSs), using the information of the mean causal earthquakes. The conditioning period T^* was set equal to the isolated period $T^* = T_b = 3$ sec. The CMS related to each T_r are plotted in Figure 2-34(a). For each T_r, a set of 30 seismic records were selected. The spectra of two sets of 30 seismic records corresponding to a T_r of 475 and 2,475 years are shown in Figures 2-34(b) and 2-34(c), respectively.

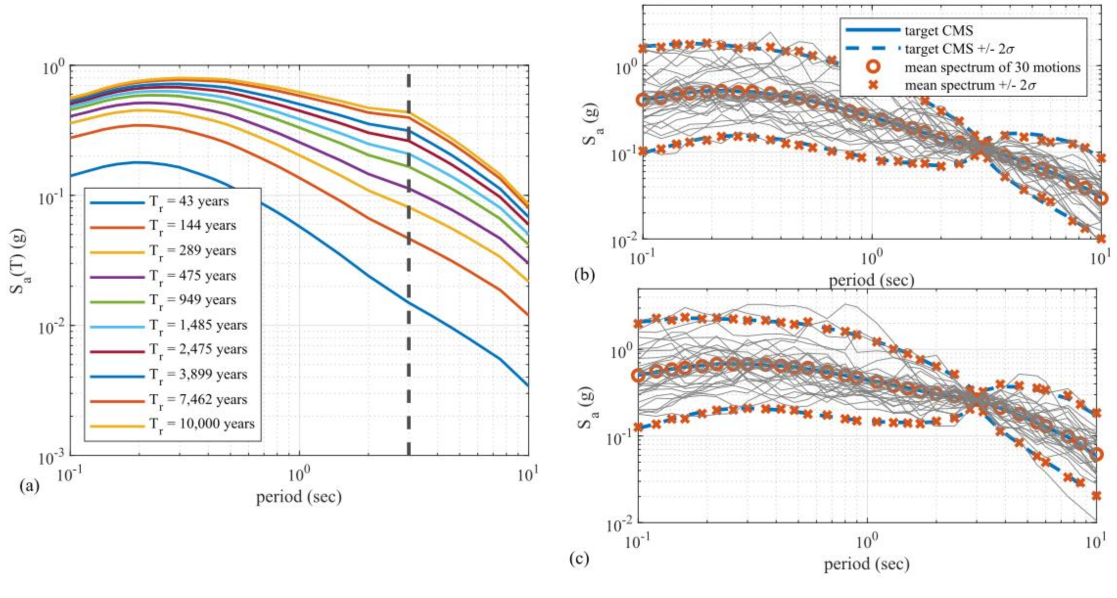

Figure 2-34: (a) Conditional Mean Spectra for different return period T_r. (b) Spectra of the 30 scaled selected ground motions for a return period of $T_r = 475$ years matched with the corresponding Conditional Spectrum. (c) Spectra of the 30 scaled selected ground motions for a return period of $T_r = 2{,}475$ years matched with the corresponding Conditional Spectrum.

2.6.4 Design of the isolation system and the superstructure

The design of the isolation system was made using the criteria of the ASCE/SEI 7-16 standard (ASCE, 2016). The definition of the lateral capacity is done considering an isolation system formed by FPS bearings with an isolated period of $T_b = 3$ sec. The Response History Analysis Procedure was employed to estimate the maximum displacement of the base D_M. The D_M was defined using 30 seismic records scaled to the Maximum Considered Earthquake (MCE$_R$). The minimum sampled value of the friction coefficient at large velocity of sliding $f_{max} = 0.03$ was used in this design stage. The D_M was defined as the average response of the maximum base displacement obtained on each time-history analysis. Following the minimum criteria of the ASCE/SEI 7-16, the total lateral capacity was defined as $L_c = D_{TM} = 1.15D_M = 0.41$ m. This rise in the lateral capacity is added to account for the effects of accidental torsion.

The yielding lateral displacement of the superstructure is determined using the unreduced lateral seismic design force on elements above the base level V_{st}, employing the Equivalent Lateral Force Procedure and the highest value of the friction coefficient at large velocity of sliding $f_{max} = 0.07$. The isolated building is designed to behave essentially elastic under the MCE$_R$ using this strategy. Studies about the effects of allowing the inelastic response of simplified models have been carried out (Kikuchi et al., 2008; Vassiliou et al., 2013). If the inelastic behavior of the superstructure is reached, an important rise in the ductility demand is observed. This increment in the ductility demand is more significant than in conventional fixed-base structures. In the following parametric analysis, the inelastic behavior of the superstructure before exceeding the lateral capacity of the isolation system will be allowed by applying the numerical coefficient related to the type of force-resisting system above the isolation system R_I. In cases with $R_I > 1.00$, the design force of the superstructure is computed as V_{st}/R_I. The yielding displacement of each considered superstructure is calculated using the following expression:

$$u_y = \frac{V_{st}}{k_s R_I} = \frac{u_y^{(R_I=1)}}{R_I} \tag{2-28}$$

in which, $u_y^{(R_I=1)} = V_{st}/k_s$ is the yielding displacement computed without reducing the lateral seismic design force. This last parameter is presented for different values of the period of the superstructure ($T_s = 0.3; T_s = 0.6$) in Table 2-3.

Table 2-3: Design parameters of isolated dynamic systems

Isolation period, T_b (sec)	Superstructure period, T_s (sec)	Lateral capacity, L_c (cm)	$u_y^{(R_I=1)}$ related to cases with γ = 0.7 (cm)	$u_y^{(R_I=1)}$ related to cases with γ = 0.9 (cm)
3	0.3	41	0.46	0.53
3	0.6	41	1.86	2.13

2.6.5 Parametric study

In the present work, several values related to the elastic and inelastic properties of the superstructure are used to estimate the probabilistic distribution of the Engineering Demand Parameters (EDPs) of interest. These properties were combined with the fifteen sampled inputs values of the friction coefficient at large velocity f_{max}. In total, 64 equivalent dynamic systems were considered. Within the parametric analysis, the isolated period is taken as $T_b =$

3 sec ($R_0 = 2.25$ m) and the superstructure period as $T_s = 0.3$ sec and $T_s = 0.6$ sec; the mass ratio is assumed as $\gamma = 0.7$ and $\gamma = 0.9$; the post-yield hardening ratio equal to $r_H = 0.10$ and $r_H = 0.20$; the numerical coefficient related to the type of seismic force-resisting system above the isolation system is set as $R_I = 1.00$ and $R_I = 1.20$; four values of the a parameter of the SH-FPS bearings were selected $a = 1.00 \times R_0$, $a = 0.35 \times R_0$, $a = 0.30 \times R_0$, and $a = 0.25 \times R_0$. Note that the cases in which $a = 1.00 \times R_0$ correspond to an isolation system formed by FPS bearings. These cases are analyzed to compare the seismic performances of SH-FPS bearings with classical frictional isolators.

2.6.6 Incremental dynamic analyses (IDAs)

One incremental dynamic analysis (IDA) was performed per each dynamic system defined in the parametric study. One IDA consists of 4,500 numerical simulations. The 10 sets of 30 natural seismic records scaled to 10 different IM ($S_a(T_b)$) values are combined with the 15 samples of f_{max}. The differential equation of motion has been repeatedly solved using the ode23t solver available in the MATLAB environment (Hunt et al., 2006). The IDAs allow estimating the engineering demand parameters (EDPs). Two EDPs are studied: the maximum base displacement u_b and the ductility demand $\mu = u_{s,max}/u_y$, in which $u_{s,max}$ is the maximum lateral displacement of the superstructure during the ground motion excitation. The response parameters are assumed to follow lognormal distributions. This distribution allows estimating the responses in terms of different percentile levels. The lognormal distribution is fitted by estimating the sample lognormal mean $\mu_{ln}(EDP)$ and the sample lognormal standard deviation $\sigma_{ln}(EDP)$ using the maximum likelihood estimation method.

2.6.7 Seismic fragility of base-isolated structures

The next step is the evaluation of the seismic fragility. The seismic fragility is defined as the probabilities P_f of exceeding different limit states (LSs) at each IM level. The limit state thresholds must be defined to determine the seismic fragility curves. The performance levels related to the superstructure are defined based on the ductility demand of the superstructure μ. Thirty-seven threshold values have been defined, ranging from $\mu = 1$ to $\mu = 10$ with a step of 0.25. A total of eight limit state thresholds were defined, ranging from $u_b = 0.05$ m to $u_b = 0.40$ m, to evaluate the probability of exceedance lateral displacement demands of the base. The probabilities P_f of exceeding different LSs at each IM level were determined by fitting complementary CDF lognormal distributions.

2.6.8 Seismic reliability of base-isolated structures

Through the convolution integral between the obtained fragility curves and the seismic hazard curve, expressed in terms of the same IM (i.e., $S_a(T_b)$), it is possible to calculate the mean annual rate of exceeding LSs. The following equation can be used:

$$\lambda_{LS}(EDP > y) = \int_0^\infty P(EDP > y \mid S_D(T_b) = x) |\lambda(\mathrm{d}S_a(T_b) > x)| \tag{2-29}$$

in which, $\lambda(\mathrm{d}S_a(T_b) > x)$ is the derivative of the hazard curve for $S_a(T_b)$ multiplied by an increment of $dS_a(T_b)$, and $P(EDP > y \mid S_a(T_b) = x)$ is the probability of EDP exceeding y (for example, a specific LS) given a ground motion with $S_a(T_b) = x$. This last term is represented by the fragility curves described above. The seismic hazard curve for the specific location and soil condition in terms of $S_a(T_b)$ is presented in Figure 2-35.

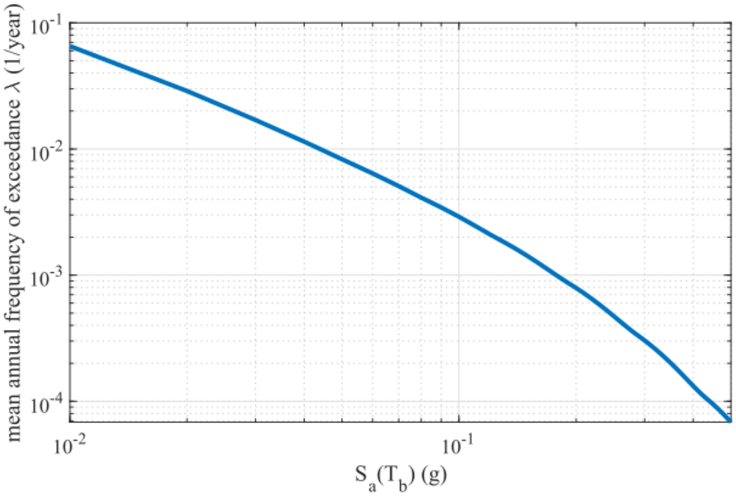

Figure 2-35: Seismic hazard curve related to $T_b = 3$ sec for Riverside site (California).

The evaluation of the seismic reliability of base-isolated systems can be achieved by using a Poisson distribution considering a time frame (e.g., 50 years) and the results of the convolution integral:

$$P_f(50\,years) = 1 - \exp\left(-\lambda_{LS} \cdot (50\,years)\right) \tag{2-30}$$

The reliability curves of the isolation system in terms of the maximum base displacement u_b are shown in Figure 2-36 for cases related to $r_H = 0.10$ and in Figure 2-37 for cases related to $r_H = 0.20$. It is possible to observe that these reliability curves are slightly affected by T_s and γ if the superstructure is designed to behave essentially elastic if the internal impact is not observed (i.e., $R_I = 1.00$). An increment in T_s or γ slightly decreases the reliability curves. A more important role has the parameter R_I. The reliability curves are reduced by a rise in this parameter. The post-yield stiffness ratio r_H affects the probability of exceedance limit state thresholds only in cases in which the nonlinear behavior of the superstructure is exhibit even if the lateral capacity is not exceeded ($R_I = 1.20$). An increment in r_H leads to an increment of the reliability curves.

The effects of using SH-FSP bearings in reducing the probability of exceeding LSs related to the maximum base displacement are noticeable in Figures 2-36 and 2-37. The lower the values of the half-width of the ellipse (lower values of the a parameter), the lower probabilities of exceeding LSs. In cases with $a = 0.25 \times R_0$, an average reduction of 11% in the probability of u_b exceeding 0.4 m is reached by using isolators with smooth-hardening behavior. Under extreme seismic inputs, this reduction in the reliability curves can lead to avoiding the occurrence of internal impacts and their negative consequences. The reduction in the probability of exceedance LSs thresholds is highlighted for cases with high values of T_s, low values of γ, and high values of R_I. The effects of rising the value of r_H are evident only for cases with $R_I = 1.2$, decreasing the reliability curves by increasing r_H.

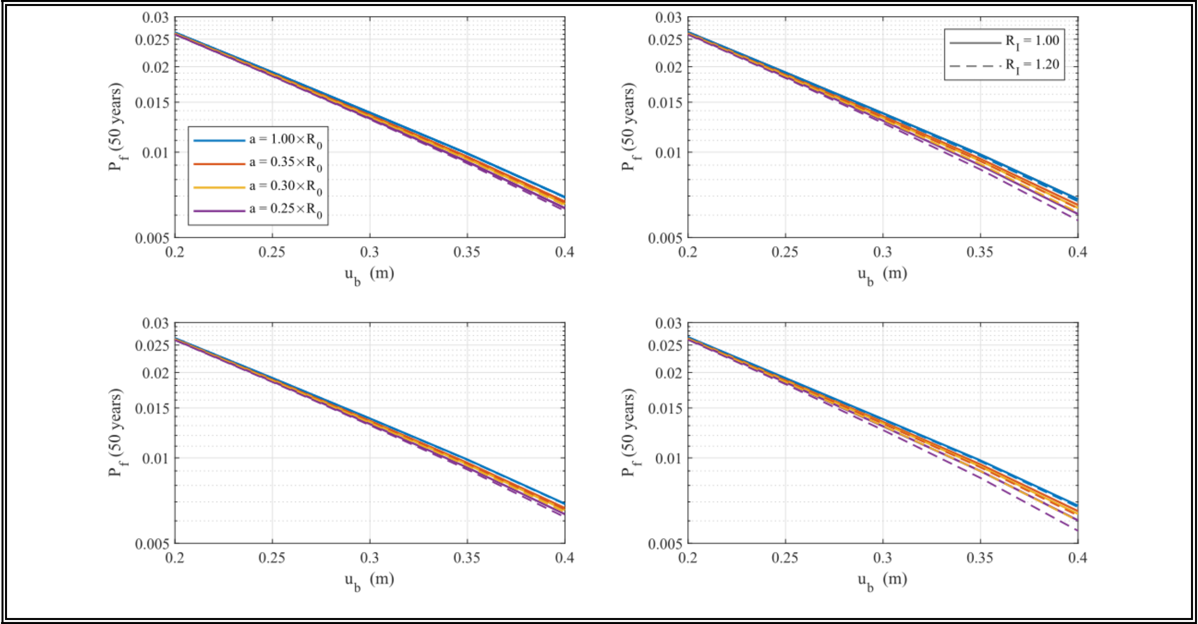

Figure 2-36: Seismic reliability of the isolation level related to $r_H = 0.10$. (a) $\gamma = 0.7$ and $T_s = 0.3$ sec. (b) $\gamma = 0.7$ and $T_s = 0.6$ sec. (c) $\gamma = 0.9$ and $T_s = 0.9$ sec. (d) $\gamma = 0.9$ and $T_s = 0.6$ sec.

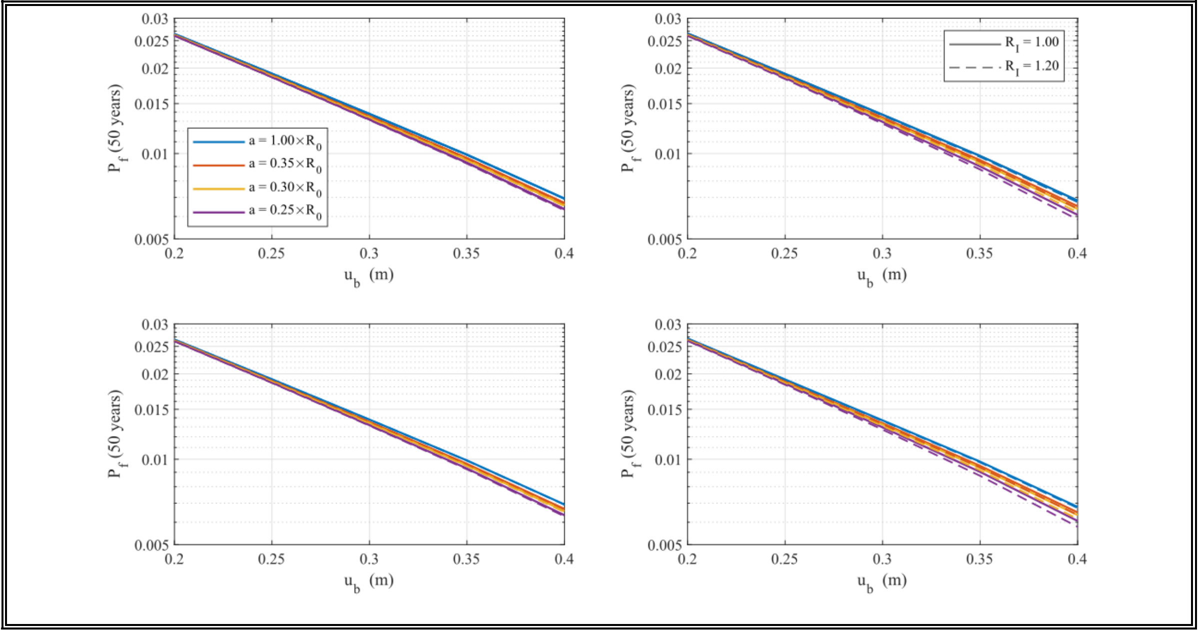

Figure 2-37: Seismic reliability of the isolation level related to $r_H = 0.10$. (a) $\gamma = 0.7$ and $T_s = 0.3$ sec. (b) $\gamma = 0.7$ and $T_s = 0.6$ sec. (c) $\gamma = 0.9$ and $T_s = 0.9$ sec. (d) $\gamma = 0.9$ and $T_s = 0.6$ sec.

The reliability curves of the superstructure in terms of the maximum ductility demand μ are shown in Figure 2-38 for all the cases related to $r_H = 0.10$ and in Figure 2-39 for all the cases related to $r_H = 0.20$. It is possible to observe that the reliability curves are affected by all the studied parameters described in the parametric analysis. An increment in T_s, γ, or in r_h, decreases the reliability curves. As expected, the role of the parameter R_I is crucial. Since using a value of R_I larger than one implies that the superstructure will reach the post-yielding behavior before the occurrence of the internal lateral impact, larger values of ductility demand are anticipated.

The effects of using seismic isolators with smooth-hardening behavior are noticeable in Figures 2-38 and 2-39. In general, the probability of exceedance LSs related to maximum ductility demand is reduced if the isolation system consists of SH-FPS bearings in cases related to $R_I = 1.0$ (superstructures designed to behave essentially elastic if the internal lateral impact is not observed). Under this scenario, a decrease in the half-width of the ellipse (the hardening behavior is reached for lower values of the base displacement) leads to a reduction of the probability of exceedance LSs higher than $\mu = 2$. Reduction up to 9.5% in the probability of exceedance the LS threshold of $\mu = 10$ are achieved if the building is equipped with SH-FPS isolators. The benefits of using frictional isolators with smooth hardening behavior, in terms of reduction of the probability of exceedance LSs related to maximum ductility demand, are highlighted for low values of T_s and high values of γ and r_H.

As discussed in section 2.4, using SH-FPS bearings can lead to an undesired rise in the base shear that the superstructure must resist if large displacements, but not the impacts, are generated in the isolation system. This phenomenon explains why the probability of exceedance of the threshold $\mu = 1$ is higher for some cases with $R_I = 1.0$ and in which the superstructure is equipped with variable curvature devices. The effects of this undesired rise in the base shear are more significant for cases related to $R_I = 1.2$ than for cases related to $R_I = 1.0$. Worse seismic performance is observed, between LSs thresholds equal to $\mu = 1$ and $\mu = 8$ if the superstructure is designed using the reduced base shear ($R_I > 1.0$), especially if the hardening ratio is relatively low ($r_H = 0.10$).

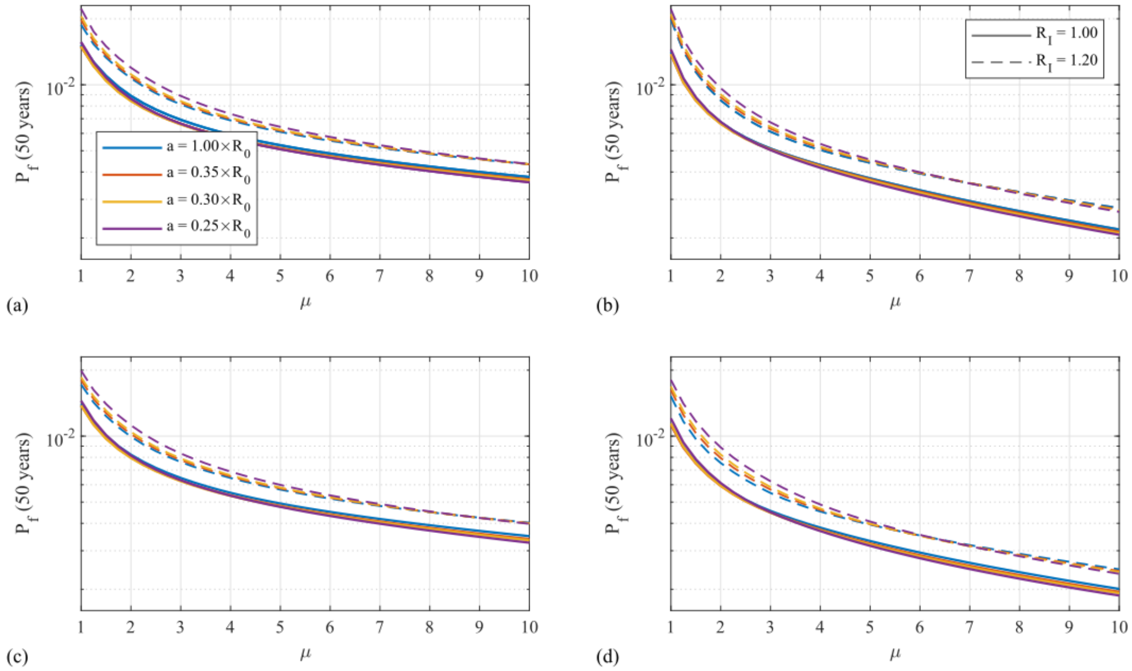

Figure 2-38: Seismic reliability of the superstructure related to $r_H = 0.10$. (a) $\gamma = 0.7$ and $T_s = 0.3$ sec. (b) $\gamma = 0.7$ and $T_s = 0.6$ sec. (c) $\gamma = 0.9$ and $T_s = 0.3$ sec. (d) $\gamma = 0.9$ and $T_s = 0.6$ sec.

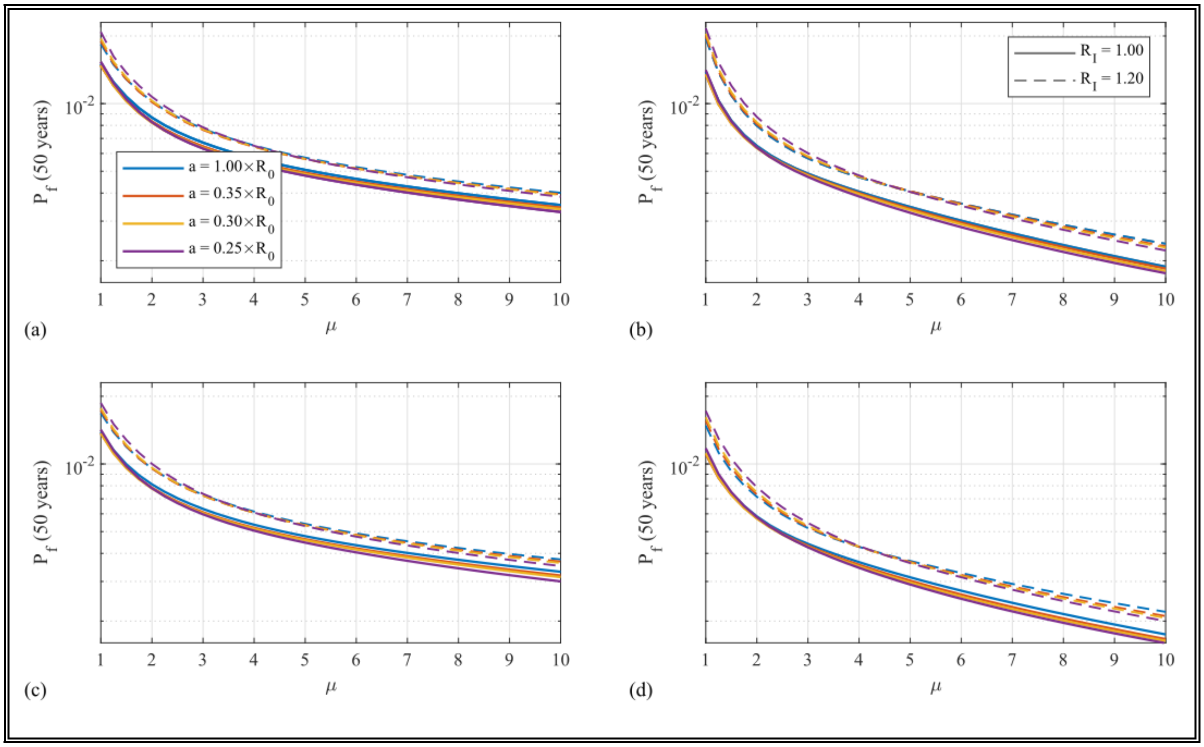

Figure 2-39: Seismic reliability of the superstructure related to $r_H = 0.20$. (a) $\gamma = 0.7$ and $T_s = 0.3$ sec. (b) $\gamma = 0.7$ and $T_s = 0.6$ sec. (c) $\gamma = 0.9$ and $T_s = 0.3$ sec. (d) $\gamma = 0.9$ and $T_s = 0.6$ sec.

2.7 Conclusions

This research aims to evaluate the use of frictional isolators with variable curvature to mitigate the adverse effects of the internal lateral impact between the inner slider and the restraining rim of the device. A physical model for analyzing base-isolated structures equipped with variable curvature frictional isolators was developed. This physical model contains important modeling aspects such as uplift, lateral and vertical impact behavior, large displacements, and $P-\Delta$ effects, among other physical features. A simple methodology was proposed to obtain the constitutive equations of devices for any sliding surface described by an implicit equation. A particular shape of the sliding surface, generated by revolving a plane curve of an ellipse around a vertical axis, was studied. The proposed isolator has a smooth-hardening behavior, unlike the classic Friction Pendulum System (FPS) bearing. The stiffness of the isolator changes continuously as the frictional isolator is deformed without presenting abrupt variations. The examined isolator has been denominated Smooth Hardening Friction Pendulum System (SH-FPS) isolator.

A Finite Element Model was developed to validate the proposed constitutive equations. Static and dynamic analyses were performed, considering unidirectional and bidirectional loads. Additionally, the FEM was used to determine the parameters (stiffness and coefficient of restitution) that describe the lateral impact behavior of the studied isolator. The obtained results of the FEM were nearly the same as the results obtained using the proposed physical model. Thus, the suggested physical model is an accurate instrument to represent the behavior of devices with variable curvature in three-dimensional dynamic analyses.

A three-dimensional model of a base-isolated structure equipped with SH-FPS bearing was developed to examine the dynamics behavior under three base displacement demands. The time-history response of the isolation system formed by the studied variable curvature isolator is almost the same as the response of an isolation system formed by FPS bearing at low base displacements demands. For low values of displacement vof the isolation interface, the hardening stage is not reached. Consequently, the response is influenced mainly by the initial radius of the SH-FPS bearings. A second scenario was analyzed, a high demand of the base displacement but without the occurrence of the internal impact. In this case, using an elliptical-based geometry in constructing the sliding surface can lead to an undesired rise in the base shear. The final studied base displacement demand was related to the exceedance of the lateral capacity of the isolation system. The use of SH-FPS bearings can mitigate the adverse effects of internal lateral impacts by avoiding the occurrence of the impact or decreasing its magnitude.

A nonlinear model considering the material and geometric nonlinearities of a reinforced concrete moment frame was developed to evaluate the benefits of using SH-FPS bearings. Twenty seismic records were selected to represent the record-to-records variability in the analysis. These records were modified to match the spectrum of the Maximum Considered Earthquake (MCE). Five isolation systems were examined, one formed by FPS bearings and four by SH-FPS devices. The use of variable curvature isolators can mitigate the adverse effects of internal lateral impacts by reducing the maximum shear base, maximum first inter-story drift, maximum second inter-story drift, and maximum third inter-story drift in 44%, 11%, 8%, and 6%, respectively.

A parametric analysis employing an equivalent nonlinear model was performed to assess the effectiveness of using SH-FPS bearings to mitigate the adverse effects of internal lateral impacts. Within the parametric analysis, 64 equivalent dynamic systems were analyzed. Reliability curves related to the isolation system (in term of maximum base displacement demand) and the superstructure (in term of ductility demand of the superstructure) were obtained, considering a broad set of seismic inputs and the friction coefficient as random variable. The use of smooth-hardening frictional devices can effectively reduce the probability of exceeding base displacement thresholds, decreasing the probability of observing lateral impacts. The parametric analysis was a valuable tool to identify the structural properties needed to reach a better seismic performance if the use of SH-FPS bearings is planned. The benefits of using SH-FPS bearings are highlighted for superstructures designed to behave essentially elastic if the impact is not produced. Additionally, better seismic performance is obtained for low values of the period of the superstructure, high values of mass distribution ratio and a relatively high values of post-yield stiffness.

2.7 Acknowledgements

This research has been funded by the Agencia Nacional de Investigación y Desarrollo (ANID) through the ANID-PCHA/Doctorado Nacional/2018-21180434 and the FONDECYT project Nº1201841, the authors are grateful for the support. The authors are thankful to Ph.D.(c) Diego Quizanga for sharing his experimental data.

3. LATERAL IMPACT RESILIENT DOUBLE CONCAVE FRICTION PENDULUM (LIR-DCFP) BEARING: FORMULATION, PARAMETRIC STUDY OF THE SLIDER AND THREE-DIMENSIONAL EXAMPLE

3.1 Introduction

Seismic isolation has been one of the most effective alternatives in protecting rigid non-slender structures. Buildings with seismic isolation interfaces have shown a better performance than those with a fixed-base (Chimamphant & Kasai, 2016; Nagarajaiah & Xiaohong, 2000; Shenton & Lin, 1993). This better seismic performance is achieved by reducing inter-story drifts and absolute accelerations in the superstructure. Two of the most used and well-known devices are the elastomeric isolator (Kelly, 1993) and the Friction Pendulum System (FPS) (Zayas et al., 1990).

In general, friction pendulum bearings (FPBs) consist of single or multiple sliding concave plates and single or multiple inner sliders. The numbers of plates and sliders depend on the specific configuration of the device. While the re-centering capacity is provided by the concave plates, the energy dissipation is provided by the friction force developed between the different bodies of the isolator. These frictional devices have demonstrated an outstanding performance against high magnitude earthquakes (M. Constantinou et al., 1990; Fenz & Constantinou, 2006, 2008b, 2008a; Mokha et al., 1990; Morgan & Mahin, 2010). The fundamental idea, the FPS (Zayas et al., 1990), was introduced by Zayas et al. and consists of only one spherical concave surface of hard-dense chrome over steel and one articulated friction slider. Among seismic isolators with multiple sliding surfaces (SIMSSs), the double concave Frictional Pendulum (DCFP) bearing (Fenz & Constantinou, 2006), and the triple concave Frictional Pendulum (TCFP) bearing (Fenz & Constantinou, 2008b, 2008a) are commonly used. The DCFP bearing consists of two facing concave surfaces and an articulated slider. This articulated body is required to accommodate differential movements along the two sliding surfaces. A non-articulated slider can be used if the two surfaces present identical geometry and the same friction coefficient. As the DCFP bearing, the TCFP bearing consists of two facing concave surfaces. The main difference is that an internal nested slider assembly separates the two sliding surfaces. This slider consists of two concave plates separated by a non-articulated slider. Unlike the FPS bearing, both DCFP and TCFP bearings exhibit passive adaptive behavior. Other SIMSSs devices based on concave surfaces and with adaptive behavior are the Spherical Isolation Pendulum-Adaptive (SIP-Adaptive) bearing (Weber et al., 2018), the Trench Friction Pendulum System (TFPS) (Tsai, Chen, & Lu, 2006) and, the Multiple Trench Friction Pendulum System (Tsai & Lin, 2009). These last two seismic isolators have trench-curved sliding surfaces instead of spherical.

The dynamics response of base-isolated structures during a high magnitude earthquake with high low-frequency content, such as near-fault events, could produce excessive displacement in the isolation devices (Hall et al., 1995a; Jangid & Kelly, 2001a; Jónsson et al., 2010; Mazza, 2018; Mazza et al., 2017; Mazza & Vulcano, 2012). Considering frictional isolators, large displacements could cause internal impact between the inner slider and the restraining rims of the concave sliding surfaces. This phenomenon could generate damage and the potential uplift in the bearings. Under extreme ground motions, lateral internal impact behavior is one of the most significant contributors to the failure of DCFP and TCFP devices

(Bao et al., 2017; Becker et al., 2017). The bearing uplift can be produced even if the internal impact does not occur. Under extreme seismic inputs, the vertical acceleration, and the overturning moment (especially in relative slender structures) imposed by the ground motion could generate this problem.

This paper presents a new type of frictional devices called Impact Resilient Frictional Pendulum (IR-FP) bearings. The main feature that differentiates an IR-FP bearing from other SIMSSs devices is its improved response to the vertical and lateral impact produced by extreme seismic inputs. Furthermore, due to the components that make up the inner slider, it can be conceived as an isolator with variable curvature. This study analyzes the dynamic behavior of the simplest version of the IR-FP bearing, which only has an enhanced behavior if an internal lateral impact is produced. This device has been called Lateral Impact Resilient double concave Frictional Pendulum (LIR-DCFP).

3.2 Description of the proposed frictional isolator

Impact Resilient Frictional Pendulum (IR-FP) bearings have an improved inner slider, which is highly resilient to internal impacts produced by extreme seismic inputs. The inner slider is characterized by incorporating energy dissipation elements. The inner slider consists of two contact bodies arranged one on top of the other, called top slider and bottom slider. Each component has an external side in contact with one of the sliding surfaces of the device. The inner sides of the top slider and the bottom slider are in contact with each other generating a plane interface. A thin-thickness non-stick sheet is placed in between these surfaces to prevent the attachment. As a result of the high friction coefficient between the materials of the non-stick sheet and top and bottom sliders, high friction forces are generated at the interface. This interface has been called “high friction interface”. An elastomeric seal, able to be laterally compressed, is placed in the surrounding space that leaves the coupling between the upper slider and the bottom slider. This elastomeric seal has a triple function: (i) avoids steel to steel impact, (ii) generates a re-centering force that tends to decrease residual displacement at the high friction interface and, (iii) dissipates energy. The inner slider of the frictional isolator has one or two low friction sliding plates. These sliding plates are preferably made of polymeric materials such as Polytetrafluoroethylene (PTFE) or Ultra High Molecular Weight Polyethylene (UHMWPE) (Braun, 2009; M. C. Constantinou et al., 2007; M.C.Constantinou et al., 1993; Quaglini et al., 2012; Tsai, Chen, Chiang, et al., 2006). These polymeric plates are in contact with the sliding surfaces of the concave (or plane) top and bottom steel plates of the isolator. Between the polymeric plates and the niches of the bottom and top sliders, there are confined high damping elastomeric compression supports. As an example, a detailed scheme of the inner slider of the Impact Resilient double concave Friction Pendulum (IR-DCFP) bearing is presented in Figure 3-1.

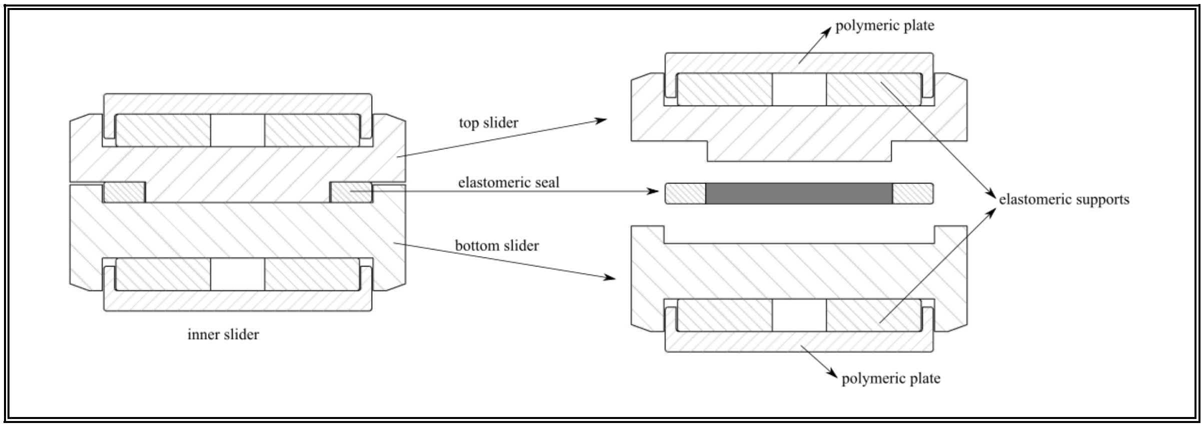

Figure 3-1: Detailed scheme of the inner slider of the IR-DCFP bearing.

The IR-DCFP bearing assembly is shown in Figure 3-2. The IR-DCFP device without vertical load is shown in Figure 3-2(a). The configuration of the isolator under the self-weight of the superstructure is presented in Figure 3-2(b). Note that, under vertical loads, the empty spaces inside of the internal slider are filled as the flexible parts deform. Since the polymeric plates and elastomeric supports are made with highly incompressible materials, and steel walls confine them, the isolator exhibits rigid axial behavior if the device is withstanding vertical loads. The configuration of the isolator, if uplift occurs, is presented in Figure 3-2(c). If there is no presence of vertical load on the bearing, the internal parts of the slider will tend to recover their initial shape. The axial stiffness of the device will be less at the beginning of the vertical impact, increasing as the flexible elements occupy the empty spaces inside the slider. Due to this phenomenon, added to the high damping of the elastomeric supports, the generated vertical load under vertical impact will have a lower magnitude than the vertical load generated in a traditional vertically stiff frictional isolator. The configuration under internal lateral impact is shown in Figure 3-2(d). The lateral impact causes a relative displacement between the top slider and the bottom slider. This relative displacement develops friction forces that dissipate a large amount of energy. As sliding occurs at the high friction interface, the elastomeric seal is compressed against the surrounding space walls.

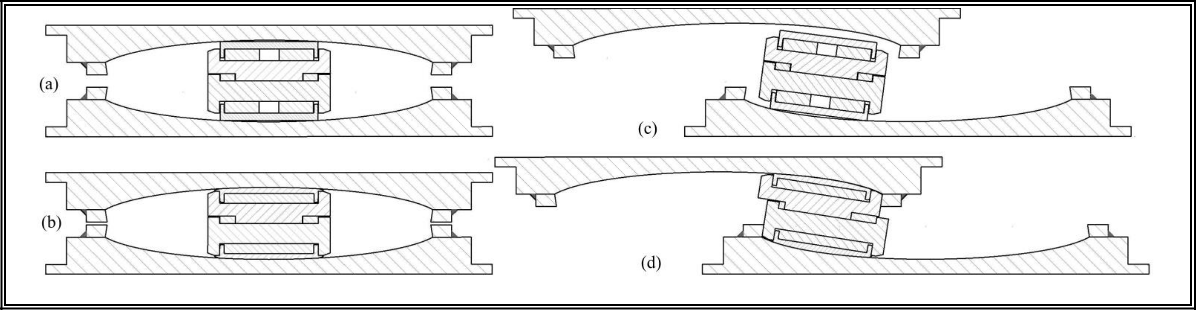

Figure 3-2: Impact Resilient double concave Friction Pendulum (IR-DCFP) bearing. (a) Undeformed. (b) Deformed by the self-weight of the superstructure. (c) Uplift. (d) Internal lateral impact.

Another alternative, the Impact Resilient Friction Pendulum System (IR-FPS) bearing, is shown in Figure 3-3. This device is not the only possible alternative. An IR-FP bearing could be constructed using plane sliding surfaces. Furthermore, due to the flexibility of the internal parts (polymeric plates and elastomeric supports), the slider of an IR-FP bearing can adapt to sliding surfaces with variable curvature (L.-Y. Lu et al., 2011; L. Y. Lu et al., 2013; Murnal & Sinha, 2002; Pranesh & Sinha, 2000; Shahbazi & Taghikhany, 2017).

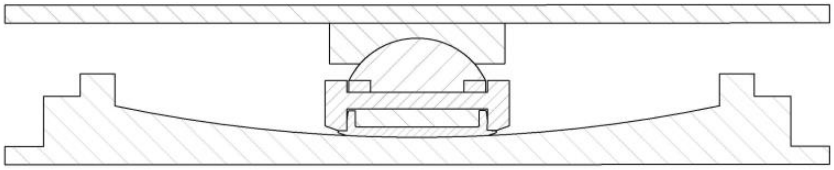

Figure 3-3: Impact Resilient Friction Pendulum System (IR-FPS) bearing.

3.3 Formulation of the Lateral Impact Resilient double concave Friction Pendulum (LIR-DCFP) bearing

In this section, the three-dimensional numerical formulation of the LIR-DCFP bearing for dynamic analysis is described in detail. A proper model must be developed to accurately incorporate the internal lateral impact behavior between the inner slider and the restraining rims of the isolator. Several studies have focused on the planar behavior of frictional isolators (P. Castaldo & Alfano, 2020; Paolo Castaldo, Amendola, et al., 2017; Fenz & Constantinou, 2006, 2008b; Morgan & Mahin, 2010; Sarlis & Constantinou, 2016; Zayas et al., 1990). Other studies have analyzed the dynamics response of frictional bearing considering the bi-directional behavior (Becker & Mahin, 2012; Fenz & Constantinou, 2008c; Nagarajaiah et al., 1991; Park et al., 1986; Tsai et al., 2010). The studies mentioned above ignore the coupling between horizontal and vertical motions that frictional isolators with re-centering capacity presents. One exception is the physical model of the FPS bearing developed by Almazán and De la Llera (José L. Almazán & De la Llera, 2003). Another limitation of these numerical models is that the lateral impact behavior is not considered if the maximum displacement capacity is exceeded.

A suitable numerical model of the double concave Friction Pendulum (DCFP) bearing (with a non-articulated inner slider) has been proposed in a recent study carried out by Bao and Becker (Bao & Becker, 2019). Furthermore, in the research, a procedure for developing other numerical models for frictional devices is proposed. The present study uses the method suggested by Bao and Becker to develop the numerical model of the LIR-DCFP bearing. Some advantages of using this methodology are: (i) the potential coupling due to the existence of the azimuth angle is taken in account, (ii) impact-induced uplift under extreme earthquake inputs is considered, (iii) the model considers the torsional resistance of the frictional isolator, (iv) the numerical model considers the real geometry of the frictional bearing and, (v) the use of contact points between the different bodies of the isolator allows studying the force distribution inside the isolator.

3.3.1 Description of the LIR-DCFP bearing

The LIR-DCFP bearing is composed of two facing plates. Each plate has a spherical concave sliding surface. The sliding surface of the top and bottom plates have identical radius of curvature R and frictional coefficient μ. A non-articulated slider faced with polymeric material on its external sides separates both spherical sides of the plates. The inner slider consists of two parts: the top slider and the bottom slider. The inner sides of the top slider and the bottom slider are in contact with each other generating a plane interface. In between the two contacted sides, a non-stick sheet is placed generating a high friction contact with a friction coefficient of μ_s. This interface has been called “high friction interface”. The LIR-DCFP bearing, having no flexible elements acting in the axial direction, only has an improved internal lateral impact behavior. All the pieces that make up the isolator and the main geometrical design parameters are indicated in Figure 3-4. The plates have a radius of curvature of R. The vertical distance between the centroid of the plates to the concave sliding surface has been denoted as d. The inner width of the top plate and bottom plates have been defined as b_{tp} and b_{bp}, respectively. The heights of the restraining rims of the top plate and the bottom plate have been called l_{tp} and l_{bp}, respectively. The vertical distance between the centroid of the bottom slider and its concave surface has been denoted d_{bs}. The effective height of the bottom slider is h_{bs}. The inner width of the bottom slider is defined as b_{bs}. The restraining rim of the bottom slider is characterized by its height l_{bs} and its thickness e_{bs}. The vertical distance between the centroid of the top slider and its curved surface is denoted by d_{ts}. The height of this piece is defined by h_{ts}. The inner diameter of the top slider is b_{ts}, and the outer diameter is D_s. The difference between the outer radius $D_s/2$ and the inner radius $b_{ts}/2$ of the top slider has been defined as e_{ts}.

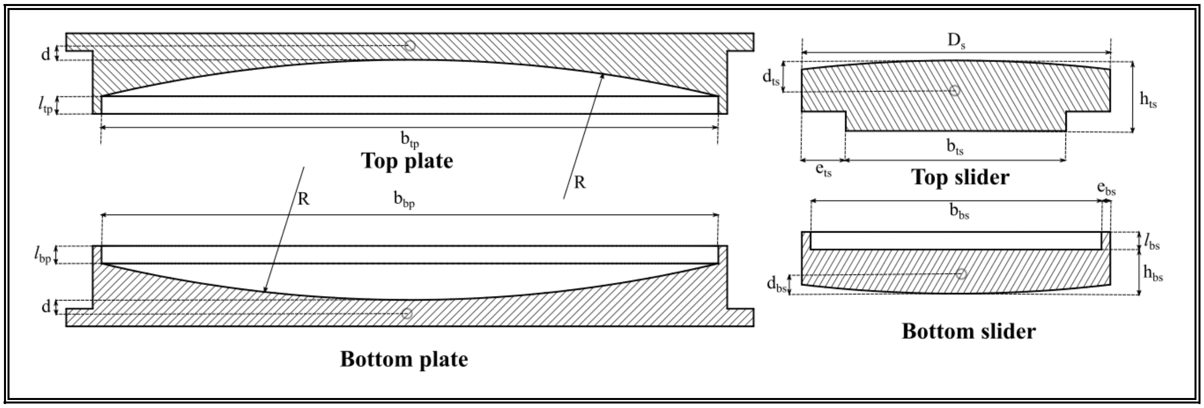

Figure 3-4: Geometrical design parameters of the LIR-DCFP bearing.

The general normalized force-displacement relationship for LIR-DCFP bearing is shown in Figure 3-5. The force transmitted by the bearing has been normalized by the vertical load W applied on its top plate. The lateral displacement has been normalized by the effective radius of the frictional isolator $R_{eff} = 2R - h_{ts} - h_{bs}$ (Fenz & Constantinou, 2006). The total lateral force f transmitted by the frictional device to the superstructure can be divided into two forces, the pendular force f_p and the frictional force f_μ. Additionally, four stages of the lateral behavior had been illustrated in Figure 3-5: (1) the beginning of the low friction sliding between the inner slider and the concave surfaces, (2) the impact between the inner slider and the restraining rims of the plates, (3) the internal sliding at the high friction interface (note that, the internal impact between the top slider and the bottom slider does not occur) and, (4) the returning of the bottom slider to its original position. At the end of the stage (4), the isolator remains with a residual displacement of $0.01 \times R_{eff}$. Between the stages (1) and (2), the normalized pendular force continuously increases with a unitary slope. The changes in the pendular force are produced by the variation of the normal vector that describes the direction of the contact between the inner slider and the plates of the isolator. Between stages (2) and (3), the normal force remains constant because the normal vector does not change (the internal sliding occurs in a plane surface). The path between stages (3) and (4) is produced with a unitary normalized stiffness since the sliding occurs in the low friction interfaces. The magnitude of the friction force f_{μ} depends on the place where the sliding occurs. On the one hand, from the stage (1) to stage (2) and from the stage (3) to stage (4), low friction forces are developed because the sliding occurs between the inner slider and the concave surfaces. The friction coefficient between the sliders and the plates is μ. On the other hand, from the stage (2) to stage (3) high friction forces are produced due to sliding between the top slider and the bottom slider. The friction coefficient between the top slider and the bottom slider has been denoted as μ_s. Note that, for the illustrated force-displacement relationship $\mu_s > \mu$.

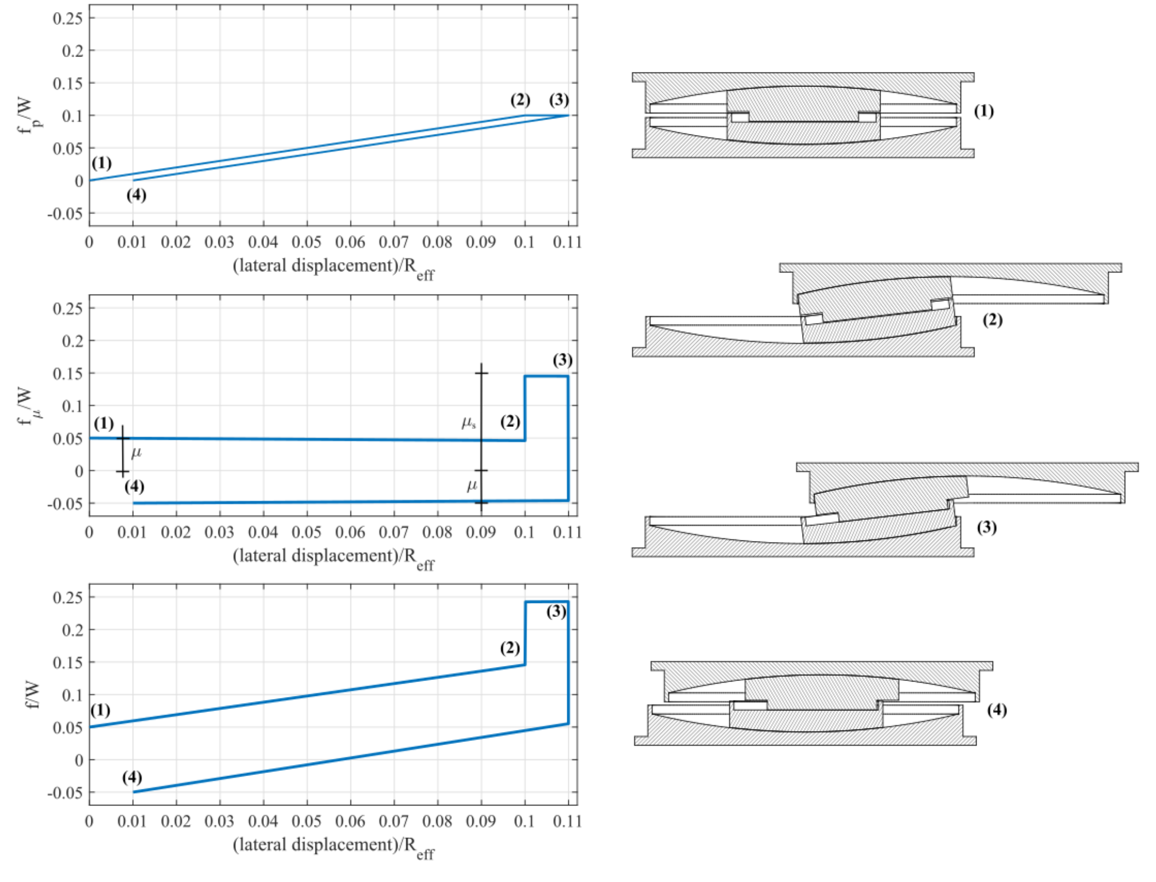

Figure 3-5: General normalized force-displacement relationship for LIR-DCFP bearings.

As far as the authors know, a similar idea of an improved slider with a plane high frictional sliding surface has not been proposed. This idea is different from the concept of the TCFP bearing (Fenz & Constantinou, 2008b, 2008a). The sliding regime V of the TCFP device is characterized by a stiff pendular force and a low friction force, opposed characteristics to those presented by the LIR-DCFP bearing after the internal impact between the inner slider and the restraining rims of the top and bottom plates.

3.3.2 Three-dimensional formulation

Assuming that the bottom plate of the isolator is rigidly connected to the ground, the device has eighteen degrees-of-freedom (i.e., three translational and three rotational degrees-of-freedom for the bottom slider, the top slider and the top plate). The six degrees-of-freedom of the bottom slider are:

$$\boldsymbol{q_{bs}} = [x_{bs}\ y_{bs}\ z_{bs}\ \alpha_{bs}\ \beta_{bs}\ \gamma_{bs}\ ]^T \tag{3-1}$$

Similarly, the top slider and the top plate have three translational and three rotational degrees-of-freedom:

$$\boldsymbol{q_{ts}} = [x_{ts}\ y_{ts}\ z_{ts}\ \alpha_{ts}\ \beta_{ts}\ \gamma_{ts}\ ]^T \tag{3-2}$$

$$\boldsymbol{q_{tp}} = \left[x_{tp}\ y_{tp}\ z_{tp}\ \alpha_{tp}\ \beta_{tp}\ \gamma_{tp}\ \right]^T \tag{3-3}$$

The eighteen degrees-of-freedom of the element measured at the centroid of each rigid body are arranged in the following vector:

$$\boldsymbol{q} = \begin{bmatrix} \boldsymbol{q_{bs}} \\ \boldsymbol{q_{ts}} \\ \boldsymbol{q_{tp}} \end{bmatrix} \tag{3-4}$$

The velocities of the eighteen degrees-of-freedom are arranged in the following vector:

$$\dot{\boldsymbol{q}} = \begin{bmatrix} \dot{\boldsymbol{q}}_{\boldsymbol{bs}} \\ \dot{\boldsymbol{q}}_{\boldsymbol{ts}} \\ \dot{\boldsymbol{q}}_{\boldsymbol{tp}} \end{bmatrix} = \begin{bmatrix} \dot{x}_{bs}\ \dot{y}_{bs}\ \dot{z}_{bs}\ \dot{\alpha}_{bs}\ \dot{\beta}_{bs}\ \dot{\gamma}_{bs}\ \dot{x}_{ts}\ \dot{y}_{ts}\ \dot{z}_{ts}\ \ldots \\ \dot{\alpha}_{ts}\ \dot{\beta}_{ts}\ \dot{\gamma}_{ts}\ \dot{x}_{tp}\ \dot{y}_{tp}\ \dot{z}_{tp}\ \dot{\alpha}_{tp}\ \dot{\beta}_{tp}\ \dot{\gamma}_{tp} \end{bmatrix}^T \tag{3-5}$$

Following the order of the local degrees-of-freedom, the mass and rotational inertia matrix is defined as:

$$\boldsymbol{M} = \begin{bmatrix} \boldsymbol{M_{bs}} & \boldsymbol{0} & \boldsymbol{0} & \boldsymbol{0} & \boldsymbol{0} & \boldsymbol{0} \\ \boldsymbol{0} & \boldsymbol{J_{bs}} & \boldsymbol{0} & \boldsymbol{0} & \boldsymbol{0} & \boldsymbol{0} \\ \boldsymbol{0} & \boldsymbol{0} & \boldsymbol{M_{ts}} & \boldsymbol{0} & \boldsymbol{0} & \boldsymbol{0} \\ \boldsymbol{0} & \boldsymbol{0} & \boldsymbol{0} & \boldsymbol{J_{ts}} & \boldsymbol{0} & \boldsymbol{0} \\ \boldsymbol{0} & \boldsymbol{0} & \boldsymbol{0} & \boldsymbol{0} & \boldsymbol{M_{tp}} & \boldsymbol{0} \\ \boldsymbol{0} & \boldsymbol{0} & \boldsymbol{0} & \boldsymbol{0} & \boldsymbol{0} & \boldsymbol{J_{tp}} \end{bmatrix} \tag{3-6}$$

in which

$$\boldsymbol{M_{bs}} = \begin{bmatrix} m_{bs} & 0 & 0 \\ 0 & m_{bs} & 0 \\ 0 & 0 & m_{bs} \end{bmatrix}, \boldsymbol{M_{ts}} = \begin{bmatrix} m_{ts} & 0 & 0 \\ 0 & m_{ts} & 0 \\ 0 & 0 & m_{ts} \end{bmatrix}, \boldsymbol{M_{tp}} = \begin{bmatrix} m_{tp} & 0 & 0 \\ 0 & m_{tp} & 0 \\ 0 & 0 & m_{tp} \end{bmatrix} \tag{3-7}$$

$$\boldsymbol{J_{bs}} = \begin{bmatrix} J_{x,bs} & 0 & 0 \\ 0 & J_{y,bs} & 0 \\ 0 & 0 & J_{z,bs} \end{bmatrix}, \boldsymbol{J_{ts}} = \begin{bmatrix} J_{x,ts} & 0 & 0 \\ 0 & J_{y,ts} & 0 \\ 0 & 0 & J_{z,ts} \end{bmatrix}, \boldsymbol{J_{tp}} = \begin{bmatrix} J_{x,tp} & 0 & 0 \\ 0 & J_{y,tp} & 0 \\ 0 & 0 & J_{z,tp} \end{bmatrix} \tag{3-8}$$

being m_{bs}, m_{ts} and, m_{tp} the masses of the bottom slider, top slider, and top plate, respectively. As an example, the rotational inertia of the bottom slider around the x-axis of the co-rotational local system is denoted as $J_{x,bs}$.

To compute the projected forces transmitted by the isolator into the global reference system is necessary to define transformation matrices. The transformation matrices for the bottom slider, the top slider, and the top plate are:

$$\boldsymbol{Q_{bs}} = \boldsymbol{Q_{\gamma_{bs}}} \boldsymbol{Q_{\beta_{bs}}} \boldsymbol{Q_{\alpha_{bs}}} \tag{3-9}$$

$$\boldsymbol{Q_{ts}} = \boldsymbol{Q_{\gamma_{ts}}} \boldsymbol{Q_{\beta_{ts}}} \boldsymbol{Q_{\alpha_{ts}}} \tag{3-10}$$

$$\boldsymbol{Q_{tp}} = \boldsymbol{Q_{\gamma_{tp}}} \boldsymbol{Q_{\beta_{tp}}} \boldsymbol{Q_{\alpha_{tp}}} \tag{3-11}$$

in which

$$\boldsymbol{Q}_{\boldsymbol{\alpha_{bs}}} = \begin{bmatrix} \cos\alpha_{bs} & \sin\alpha_{bs} & 0 \\ -\sin\alpha_{bs} & \cos\alpha_{bs} & 0 \\ 0 & 0 & 1 \end{bmatrix}, \boldsymbol{Q}_{\boldsymbol{\beta_{bs}}} = \begin{bmatrix} \cos\beta_{bs} & 0 & -\sin\beta_{bs} \\ 0 & 1 & 0 \\ \sin\beta_{bs} & 0 & \cos\beta_{bs} \end{bmatrix}, \tag{3-12}$$

$$\boldsymbol{Q}_{\boldsymbol{\gamma_{bs}}} = \begin{bmatrix} 1 & 0 & 0 \\ 0 & \cos\gamma_{bs} & \sin\gamma_{bs} \\ 0 & -\sin\gamma_{bs} & \cos\gamma_{bs} \end{bmatrix}$$

$$\boldsymbol{Q}_{\boldsymbol{\alpha_{ts}}} = \begin{bmatrix} \cos\alpha_{ts} & \sin\alpha_{ts} & 0 \\ -\sin\alpha_{ts} & \cos\alpha_{ts} & 0 \\ 0 & 0 & 1 \end{bmatrix}, \boldsymbol{Q}_{\boldsymbol{\beta_{ts}}} = \begin{bmatrix} \cos\beta_{ts} & 0 & -\sin\beta_{ts} \\ 0 & 1 & 0 \\ \sin\beta_{ts} & 0 & \cos\beta_{ts} \end{bmatrix}, \tag{3-13}$$

$$\boldsymbol{Q}_{\boldsymbol{\gamma_{ts}}} = \begin{bmatrix} 1 & 0 & 0 \\ 0 & \cos\gamma_{ts} & \sin\gamma_{ts} \\ 0 & -\sin\gamma_{ts} & \cos\gamma_{ts} \end{bmatrix}$$

$$\boldsymbol{Q}_{\boldsymbol{\alpha_{tp}}} = \begin{bmatrix} \cos\alpha_{tp} & \sin\alpha_{tp} & 0 \\ -\sin\alpha_{tp} & \cos\alpha_{tp} & 0 \\ 0 & 0 & 1 \end{bmatrix}, \boldsymbol{Q}_{\boldsymbol{\beta_{tp}}} = \begin{bmatrix} \cos\beta_{tp} & 0 & -\sin\beta_{tp} \\ 0 & 1 & 0 \\ \sin\beta_{ts} & 0 & \cos\beta_{tp} \end{bmatrix}, \tag{3-14}$$

$$\boldsymbol{Q}_{\boldsymbol{\gamma_{tp}}} = \begin{bmatrix} 1 & 0 & 0 \\ 0 & \cos\gamma_{tp} & \sin\gamma_{tp} \\ 0 & -\sin\gamma_{tp} & \cos\gamma_{tp} \end{bmatrix}$$

3.3.2.1 Contact forces

To compute the contact forces is necessary to pre-define contact points. For the LIR-DCFP bearing, three sets of points are required. The set points are denoted as $A_i = \{A_1, A_2, \dots, A_p\}$, $B_j = \{B_1, B_2, \dots, B_p\}$ and $C_k = \{C_1, C_2, \dots, C_p\}$, each one containing a number of "p" contact points. The first set is located at the upper surface of the top slider, the second set is located at the lower surface of the bottom slider, and the third set is located at the lower surface of the top slider. An illustration of a device modeled with $p = 4$ contact points is presented in Figure 3-6.

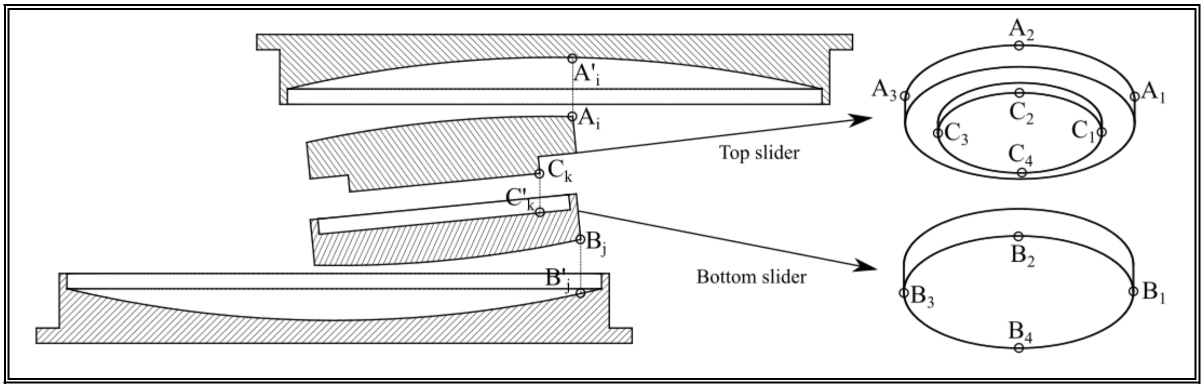

Figure 3-6: Contact points.

The position of any point "a" contained in a body "b" in the global reference system can be described as:

$$\boldsymbol{r_a} = \boldsymbol{r_c^b} + \boldsymbol{r_a^{(l)}} \boldsymbol{Q_b} \tag{3-15}$$

in which $\boldsymbol{r_c^b}$ is the position of the centroid of the body "b" expressed using the global reference system, $\boldsymbol{r_a^{(l)}}$ is the vector originating from the centroid of the body "b" to the point "a" expressed using the local reference system, and $\boldsymbol{Q_b}$ is the transformation matrix of the body "b". The vectors $\boldsymbol{r_a}$, $\boldsymbol{r_c^b}$ and $\boldsymbol{r_a^{(l)}}$ are illustrated in Figure 3-7.

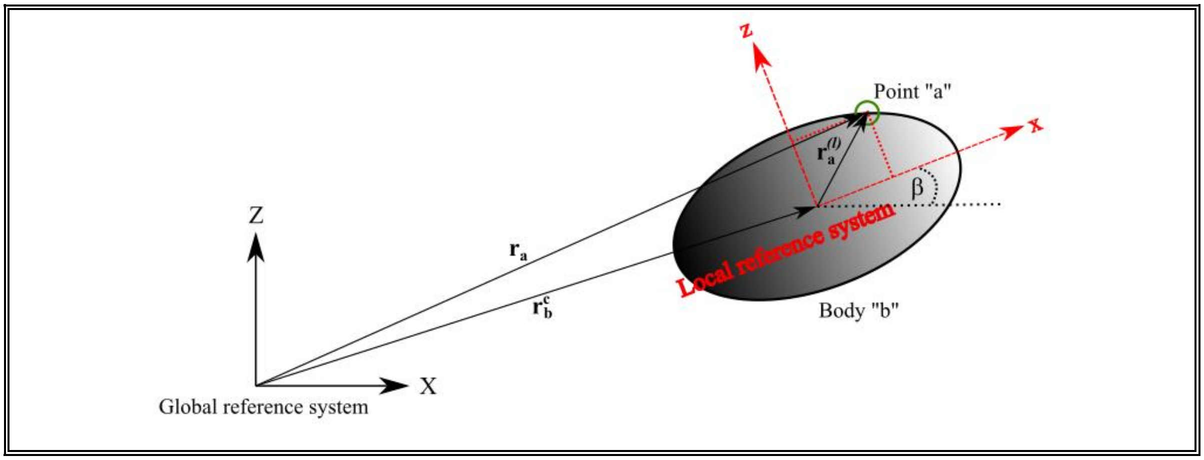

Figure 3-7: Definition of point "a".

The position of the contact points can be expressed in the global reference system as:

$$\boldsymbol{r_{A_i}} = \boldsymbol{r_c^{ts}} + \boldsymbol{r_{A_i}^{(l)} Q_{ts}} \tag{3-16}$$

$$\boldsymbol{r_{B_j}} = \boldsymbol{r_c^{bs}} + \boldsymbol{r_{B_j}^{(l)} Q_{bs}} \tag{3-17}$$

$$\boldsymbol{r_{C_k}} = \boldsymbol{r_c^{ts}} + \boldsymbol{r_{C_k}^{(l)} Q_{ts}} \tag{3-18}$$

in which:

$$\boldsymbol{r_c^{bs}} = \boldsymbol{q}(1{:}\,3)^{\boldsymbol{T}} = [x_{bs}, y_{bs}, z_{bs}] \tag{3-19}$$

$$\boldsymbol{r_c^{ts}} = \ \boldsymbol{q}(7{:}\,9)^{\boldsymbol{T}} = [x_{ts}, y_{ts}, z_{ts}] \tag{3-20}$$

The local vectors can be computed as:

$$\boldsymbol{r_{A_i}^{(l)}} = \left[x_i, \qquad y_i, \qquad d_{ts} - \left(R - \sqrt{R^2 - (x_i^2 + y_i^2)}\,\right)\right] \tag{3-21}$$

$$\boldsymbol{r_{B_j}^{(l)}} = \left[x_j, \qquad y_j, \qquad -\,d_{bs} + \left(R - \sqrt{R^2 - \left(x_j^2 + y_j^2\right)}\,\right)\right] \tag{3-22}$$

$$\boldsymbol{r_{C_k}^{(l)}} = [x_k, \qquad y_k\,, \quad -\,(h_{ts} - d_{ts})] \tag{3-23}$$

in which x_i and y_i are the x and y local coordinates of the contact points of the set A_i. Similarly, x_j, y_j, x_k and y_k are defined as the local coordinates of the contact points of the sets B_j and C_k, respectively.

To calculate the normal forces, the projections of the contact points are needed. The projections of the contact points A_i are in the sliding surface of the top plate and are denoted as A_i'. Similarly, the projections of the contact points B_j are located in the sliding surface of the bottom plate and, the projections of the contact points C_k are located in the top face of the bottom slider. The projections of the contact points are shown in Figure 3-6.

As shown in the work of Bao and Becker (Bao & Becker, 2019), to calculate the projection points in a spherical surface is necessary to define the center of the pendulum arm of the bottom plate $\boldsymbol{r}_{\boldsymbol{pr}}^{\boldsymbol{bp}}$ and the center of the pendulum arm of the top plate $\boldsymbol{r}_{\boldsymbol{pr}}^{\boldsymbol{tp}}$:

$$\boldsymbol{r}_{\boldsymbol{pr}}^{\boldsymbol{bp}} = [0, \quad 0, \quad d + R] \tag{3-24}$$

$$\boldsymbol{r}_{\boldsymbol{pr}}^{\boldsymbol{tp}} = \begin{bmatrix} x_{tp}, & y_{tp}, & z_{tp} \end{bmatrix} + [0, \quad 0, \quad -d - R]\boldsymbol{Q}_{\boldsymbol{tp}} \tag{3-25}$$

The coordinates of the projection points of the two sets A'_i and B'_j into the global reference system can be computed as:

$$\boldsymbol{r}'_{\boldsymbol{A}_i} = \left[\boldsymbol{r}_{\boldsymbol{A}_i}(1), \boldsymbol{r}_{\boldsymbol{A}_i}(2), \boldsymbol{r}_{\boldsymbol{pr}}^{\boldsymbol{tp}}(3) + \sqrt{R^2 - \left(\boldsymbol{r}_{\boldsymbol{A}_i}(1) - \boldsymbol{r}_{\boldsymbol{pr}}^{\boldsymbol{tp}}(1)\right)^2 - \left(\boldsymbol{r}_{\boldsymbol{A}_i}(2) - \boldsymbol{r}_{\boldsymbol{pr}}^{\boldsymbol{tp}}(2)\right)^2}\right] \tag{3-26}$$

$$\boldsymbol{r}'_{\boldsymbol{B}_j} = \left[\boldsymbol{r}_{\boldsymbol{B}_j}(1), \boldsymbol{r}_{\boldsymbol{B}_j}(2), \boldsymbol{r}_{\boldsymbol{pr}}^{\boldsymbol{bp}}(3) - \sqrt{R^2 - \left(\boldsymbol{r}_{\boldsymbol{B}_j}(1) - \boldsymbol{r}_{\boldsymbol{pr}}^{\boldsymbol{bp}}(1)\right)^2 - \left(\boldsymbol{r}_{\boldsymbol{B}_j}(2) - \boldsymbol{r}_{\boldsymbol{pr}}^{\boldsymbol{bp}}(2)\right)^2}\right] \tag{3-27}$$

Since sets A'_i and B'_j contain projection points, the first two components of vectors $\boldsymbol{r}'_{\boldsymbol{A}_i}$ and $\boldsymbol{r}'_{\boldsymbol{B}_j}$ are the same that the first two coordinates of the vectors $\boldsymbol{r}_{\boldsymbol{A}_i}$ and $\boldsymbol{r}_{\boldsymbol{B}_j}$. The vertical components are determined from geometry.

In the same way, the first two components of the projection vector $\boldsymbol{r}'_{\boldsymbol{C}_k}$ are the same as those of the contact point vector $\boldsymbol{r}_{\boldsymbol{C}_k}$. To determine the third component is convenient to define a local vector from the centroid of the bottom slider to the projection point C'_k. This vector is defined as $\boldsymbol{r}_{\boldsymbol{bs}|\boldsymbol{C}'_{\boldsymbol{k}}}^{(\boldsymbol{l})}$. It is important to note that the third component of this last vector is constant and its value is $\boldsymbol{r}_{\boldsymbol{bs}|\boldsymbol{C}'_{\boldsymbol{k}}}^{(\boldsymbol{l})}(3) = (h_{bs} - d_{bs})$. Since $\boldsymbol{r}'_{\boldsymbol{C}_k}$ is in a rigid body, the following equation is valid:

$$\boldsymbol{r}'_{\boldsymbol{C_k}} = \boldsymbol{r}_{\boldsymbol{c}}^{\boldsymbol{bs}} + \boldsymbol{r}^{(\boldsymbol{l})}_{\boldsymbol{bs}|\boldsymbol{C}'_{\boldsymbol{k}}}\boldsymbol{Q}_{\boldsymbol{bs}} \tag{3-28}$$

This equation leads to a system of three equation and three unknowns:

$$\begin{bmatrix} \boldsymbol{r}_{\boldsymbol{C_k}}(1) - x_{bs} \\ \boldsymbol{r}_{\boldsymbol{C_k}}(2) - y_{bs} \\ \boldsymbol{r}'_{\boldsymbol{C_k}}(3) - z_{bs} \end{bmatrix} = \boldsymbol{Q}^{\boldsymbol{T}}_{\boldsymbol{bs}} \begin{bmatrix} \boldsymbol{r}^{(\boldsymbol{l})}_{\boldsymbol{bs}|\boldsymbol{C}'_{\boldsymbol{k}}}(1) \\ \boldsymbol{r}^{(\boldsymbol{l})}_{\boldsymbol{bs}|\boldsymbol{C}'_{\boldsymbol{k}}}(2) \\ h_{bs} - d_{bs} \end{bmatrix} \tag{3-29}$$

The unknowns are $\boldsymbol{r}'_{\boldsymbol{C_k}}(3)$, $\boldsymbol{r}^{(\boldsymbol{l})}_{\boldsymbol{bs}|\boldsymbol{C}'_{\boldsymbol{k}}}(1)$ and $\boldsymbol{r}^{(\boldsymbol{l})}_{\boldsymbol{bs}|\boldsymbol{C}'_{\boldsymbol{k}}}(2)$. The first two equations can be solved as follow:

$$\begin{bmatrix} \boldsymbol{r}^{(\boldsymbol{l})}_{\boldsymbol{bs}|\boldsymbol{C}'_{\boldsymbol{k}}}(1) \\ \boldsymbol{r}^{(\boldsymbol{l})}_{\boldsymbol{bs}|\boldsymbol{C}'_{\boldsymbol{k}}}(2) \end{bmatrix} = \left(\boldsymbol{Q}^{\boldsymbol{T}}_{\boldsymbol{bs}}(1{:}\,2{,}1{:}\,2)\right)^{-1} \begin{bmatrix} \boldsymbol{r}_{\boldsymbol{c}}(1) - x_{bs} - \boldsymbol{Q}^{\boldsymbol{T}}_{\boldsymbol{bs}}(1{,}3)(h_{bs} - d_{bs}) \\ \boldsymbol{r}_{\boldsymbol{c}}(2) - y_{bs} - \boldsymbol{Q}^{\boldsymbol{T}}_{\boldsymbol{bs}}(2{,}3)(h_{bs} - d_{bs}) \end{bmatrix} \tag{3-30}$$

Knowing $\boldsymbol{r}^{(\boldsymbol{l})}_{\boldsymbol{bs}|\boldsymbol{C}'_{\boldsymbol{k}}}(1)$ and $\boldsymbol{r}^{(\boldsymbol{l})}_{\boldsymbol{bs}|\boldsymbol{C}'_{\boldsymbol{k}}}(2)$, it is possible to determine the third component of the projection vector of the contact point C_k:

$$\boldsymbol{r}'_{\boldsymbol{C_k}}(3) = \boldsymbol{Q}^{\boldsymbol{T}}_{\boldsymbol{bs}}(3{,}1{:}\,3) \begin{bmatrix} \boldsymbol{r}^{(\boldsymbol{l})}_{\boldsymbol{bs}|\boldsymbol{C}'_{\boldsymbol{k}}}(1) \\ \boldsymbol{r}^{(\boldsymbol{l})}_{\boldsymbol{bs}|\boldsymbol{C}'_{\boldsymbol{k}}}(2) \\ h_{bs} - d_{bs} \end{bmatrix} + z_{bs} \tag{3-31}$$

As in the work of Bao and Becker (Bao & Becker, 2019), the normal force is modeled using a Kelvin-Voigt element (Anagnostopoulos, 2004). That is why, the velocity of the contact point and the projections points are required. The velocity of any point “a” in a body “b” into the global reference system can be expressed as:

$$\dot{\boldsymbol{r}}_{\boldsymbol{a}} = \dot{\boldsymbol{r}}_{\boldsymbol{b}} + \overline{\boldsymbol{\omega}}_{\boldsymbol{b}} \times \left(\boldsymbol{r}^{(\boldsymbol{l})}_{\boldsymbol{a}}\boldsymbol{Q}_{\boldsymbol{b}}\right) \tag{3-32}$$

in which $\overline{\boldsymbol{\omega}}_{\boldsymbol{b}}$ is the angular velocity of the body “b” expressed in the global reference system. The velocity of the contact points can be expressed as:

$$\dot{\boldsymbol{r}}_{\boldsymbol{A_i}} = \dot{\boldsymbol{r}}_{\boldsymbol{ts}} + \overline{\boldsymbol{\omega}}_{\boldsymbol{ts}} \times \left(\boldsymbol{r}^{(\boldsymbol{l})}_{\boldsymbol{A_i}}\boldsymbol{Q}_{\boldsymbol{ts}}\right) \tag{3-33}$$

$$\dot{\boldsymbol{r}}_{\boldsymbol{B_j}} = \dot{\boldsymbol{r}}_{\boldsymbol{bs}} + \overline{\boldsymbol{\omega}}_{\boldsymbol{bs}} \times \left(\boldsymbol{r}^{(l)}_{\boldsymbol{B_j}} \boldsymbol{Q}_{\boldsymbol{bs}}\right) \tag{3-34}$$

$$\dot{\boldsymbol{r}}_{\boldsymbol{C_k}} = \dot{\boldsymbol{r}}_{\boldsymbol{ts}} + \overline{\boldsymbol{\omega}}_{\boldsymbol{ts}} \times \left(\boldsymbol{r}^{(l)}_{\boldsymbol{C_k}} \boldsymbol{Q}_{\boldsymbol{ts}}\right) \tag{3-35}$$

The velocities of the projection points are described as:

$$\dot{\boldsymbol{r}}'_{\boldsymbol{A_i}} = \dot{\boldsymbol{r}}_{\boldsymbol{tp}} + \overline{\boldsymbol{\omega}}_{\boldsymbol{tp}} \times \left(\boldsymbol{r}'_{\boldsymbol{A_i}}\right) \tag{3-36}$$

$$\dot{\boldsymbol{r}}'_{\boldsymbol{B_j}} = [0, 0, 0] \tag{3-37}$$

$$\dot{\boldsymbol{r}}'_{\boldsymbol{C_k}} = \dot{\boldsymbol{r}}_{\boldsymbol{bs}} + \overline{\boldsymbol{\omega}}_{\boldsymbol{bs}} \times \left(\boldsymbol{r}'_{\boldsymbol{C_k}}\right) \tag{3-38}$$

in which:

$$\dot{\boldsymbol{r}}_{\boldsymbol{bs}} = \dot{\boldsymbol{q}}(1:3)^{\boldsymbol{T}}, \quad \dot{\boldsymbol{r}}_{\boldsymbol{ts}} = \dot{\boldsymbol{q}}(7:9)^{\boldsymbol{T}}, \qquad \dot{\boldsymbol{r}}_{\boldsymbol{tp}} = \dot{\boldsymbol{q}}(13:15)^{\boldsymbol{T}} \tag{3-39}$$

The angular velocity of each rigid body can be computed as:

$$\begin{aligned}\overline{\boldsymbol{\omega}}_{\boldsymbol{bs}} = \big[&\cos\alpha_{bs}\cos\beta_{bs}\,\dot{\gamma}_{bs} - \sin\alpha_{bs}\ \dot{\beta}_{bs},\\ &\sin\alpha_{bs}\cos\beta_{bs}\ \dot{\gamma}_{bs} + \cos\alpha_{bs}\ \dot{\beta}_{bs}, \qquad \dot{\alpha}_{bs} - \sin\beta_{bs}\ \dot{\gamma}_{bs}\big]\end{aligned} \tag{3-40}$$

$$\begin{aligned}\overline{\boldsymbol{\omega}}_{\boldsymbol{ts}} = \big[&\cos\alpha_{ts}\cos\beta_{ts}\,\dot{\gamma}_{ts} - \sin\alpha_{ts}\ \dot{\beta}_{ts},\\ &\sin\alpha_{ts}\cos\beta_{ts}\ \dot{\gamma}_{ts} + \cos\alpha_{ts}\ \dot{\beta}_{ts}, \qquad \dot{\alpha}_{ts} - \sin\beta_{ts}\ \dot{\gamma}_{ts}\big]\end{aligned} \tag{3-41}$$

$$\begin{aligned}\overline{\boldsymbol{\omega}}_{\boldsymbol{tp}} = \big[&\cos\alpha_{tp}\cos\beta_{tp}\,\dot{\gamma}_{tp} - \sin\alpha_{tp}\ \dot{\beta}_{tp},\\ &\sin\alpha_{tp}\cos\beta_{tp}\ \dot{\gamma}_{tp} + \cos\alpha_{tp}\ \dot{\beta}_{tp}, \qquad \dot{\alpha}_{tp} - \sin\beta_{tp}\ \dot{\gamma}_{tp}\big]\end{aligned} \tag{3-42}$$

The normal forces acting on the contact points are determined using the following equations:

$$N_{A_i} = \left\{\begin{matrix} k\left(\boldsymbol{r}_{\boldsymbol{A_i}}(3) - \boldsymbol{r}'_{\boldsymbol{A_i}}(3)\right) + c\left(\dot{\boldsymbol{r}}_{\boldsymbol{A_i}}(3) - \dot{\boldsymbol{r}}'_{\boldsymbol{A_i}}(3)\right), if \left(\boldsymbol{r}_{\boldsymbol{A_i}}(3) - \boldsymbol{r}'_{\boldsymbol{A_i}}(3)\right) \geq 0 \\ 0, \qquad otherwise \end{matrix}\right\} \tag{3-43}$$

$$N_{B_j} = \left\{\begin{matrix} k\left(\boldsymbol{r}'_{\boldsymbol{B_j}}(3) - \boldsymbol{r}_{\boldsymbol{B_j}}(3)\right) + c\left(\dot{\boldsymbol{r}}'_{\boldsymbol{B_j}}(3) - \dot{\boldsymbol{r}}_{\boldsymbol{B_j}}(3)\right), if \ \left(\boldsymbol{r}'_{\boldsymbol{B_j}}(3) - \boldsymbol{r}_{\boldsymbol{B_j}}(3)\right) \geq 0 \\ 0, \qquad otherwise \end{matrix}\right\} \tag{3-44}$$

$$N_{C_k} = \left\{\begin{matrix} k\left(\boldsymbol{r}'_{\boldsymbol{C_k}}(3) - \boldsymbol{r}_{\boldsymbol{C_k}}(3)\right) + c\left(\dot{\boldsymbol{r}}'_{\boldsymbol{C_k}}(3) - \dot{\boldsymbol{r}}_{\boldsymbol{C_k}}(3)\right), if \ \left(\boldsymbol{r}'_{\boldsymbol{C_k}}(3) - \boldsymbol{r}_{\boldsymbol{C_k}}(3)\right) \geq 0 \\ 0, \qquad otherwise \end{matrix}\right\} \tag{3-45}$$

in which k is the contact stiffnes and c is the damping coefficient. The contact stiffness k must be sufficiently large to avoid unrealistic penetration and depends on the number of contact points considered. For example, if the isolator is modeled with four contacts point, a stiffness of $k = 2.0 \times 10^6$ kN/m can be used. The damping coefficient c can be determined using the following equation:

$$= 2\xi \sqrt{\frac{k(m_{bs} + m_{ts})m_{tp}}{(m_{bs} + m_{ts} + m_{tp})}}\ , \xi = -\frac{\ln(e)}{\sqrt{\pi^2 + (\ln(e))^2}} \tag{3-46}$$

In this study, a coefficient of restitution of $e = 0.65$ has been selected. Once the normal forces have been calculated, it is possible to determine the friction force acting on each contact point:

$$\boldsymbol{f}_{\boldsymbol{\mu},\boldsymbol{A}_{\boldsymbol{i}}} = -\mu N_{A_i} \boldsymbol{z}_{\boldsymbol{A}_{\boldsymbol{i}}} \tag{3-47}$$

$$\boldsymbol{f}_{\boldsymbol{\mu},\boldsymbol{B}_{\boldsymbol{j}}} = -\mu N_{B_j} \boldsymbol{z}_{\boldsymbol{B}_{\boldsymbol{j}}} \tag{3-48}$$

$$\boldsymbol{f}_{\boldsymbol{\mu},\boldsymbol{C}_{\boldsymbol{k}}} = -\mu_S N_{C_k} \boldsymbol{z}_{\boldsymbol{C}_{\boldsymbol{k}}} \tag{3-49}$$

in which $\boldsymbol{z}_{\boldsymbol{A}_{\boldsymbol{i}}}$, $\boldsymbol{z}_{\boldsymbol{B}_{\boldsymbol{j}}}$, and $\boldsymbol{z}_{\boldsymbol{C}_{\boldsymbol{k}}}$ are the dimensionless hysteretic parameters of the biaxial Bouc-Wen's model (Park et al., 1986) associated to the contact points A_i, B_j, and C_k, respectively.

The final step is to project the contact forces into the global reference system. An additional local reference system is needed for each contact point. The z-axes of these local systems, $\boldsymbol{e}_{\boldsymbol{z},\boldsymbol{A}_{\boldsymbol{i}}}$ and $\boldsymbol{e}_{\boldsymbol{z},\boldsymbol{B}_{\boldsymbol{j}}}$, are calculated as:

$$\boldsymbol{e}_{\boldsymbol{z},\boldsymbol{A}_{\boldsymbol{i}}} = \frac{\boldsymbol{r}_{\boldsymbol{pr}}^{\boldsymbol{tp}} - \boldsymbol{r}'_{\boldsymbol{A}_{\boldsymbol{i}}}}{\left\|\boldsymbol{r}_{\boldsymbol{pr}}^{\boldsymbol{tp}} - \boldsymbol{r}'_{\boldsymbol{A}_{\boldsymbol{i}}}\right\|} \tag{3-50}$$

$$\boldsymbol{e}_{\boldsymbol{z},\boldsymbol{B}_{\boldsymbol{j}}} = \frac{\boldsymbol{r}_{\boldsymbol{pr}}^{\boldsymbol{bp}} - \boldsymbol{r}'_{\boldsymbol{B}_{\boldsymbol{j}}}}{\left\|\boldsymbol{r}_{\boldsymbol{pr}}^{\boldsymbol{bp}} - \boldsymbol{r}'_{\boldsymbol{B}_{\boldsymbol{j}}}\right\|} \tag{3-51}$$

The other two axes of each additional co-rotational system are obtained using the following equations:

$$\boldsymbol{a}_{\boldsymbol{x},\boldsymbol{A}_{\boldsymbol{i}}} = [1\ 0\ 0] - \frac{\boldsymbol{e}_{\boldsymbol{z},\boldsymbol{A}_{\boldsymbol{i}}}(1)}{\boldsymbol{e}_{\boldsymbol{z},\boldsymbol{A}_{\boldsymbol{i}}} \cdot \boldsymbol{e}_{\boldsymbol{z},\boldsymbol{A}_{\boldsymbol{i}}}} \boldsymbol{e}_{\boldsymbol{z},\boldsymbol{A}_{\boldsymbol{i}}}, ; \boldsymbol{e}_{\boldsymbol{x},\boldsymbol{A}_{\boldsymbol{i}}} = \frac{\boldsymbol{a}_{\boldsymbol{x},\boldsymbol{A}_{\boldsymbol{i}}}}{\left\|\boldsymbol{a}_{\boldsymbol{x},\boldsymbol{A}_{\boldsymbol{i}}}\right\|};\ \boldsymbol{e}_{\boldsymbol{y},\boldsymbol{A}_{\boldsymbol{i}}} = \boldsymbol{e}_{\boldsymbol{z},\boldsymbol{A}_{\boldsymbol{i}}} \times \boldsymbol{e}_{\boldsymbol{x},\boldsymbol{A}_{\boldsymbol{i}}} \tag{3-52}$$

$$\boldsymbol{a}_{\boldsymbol{x},\boldsymbol{B}_{\boldsymbol{j}}} = [1\ 0\ 0] - \frac{\boldsymbol{e}_{\boldsymbol{z},\boldsymbol{B}_{\boldsymbol{j}}}(1)}{\boldsymbol{e}_{\boldsymbol{z},\boldsymbol{B}_{\boldsymbol{j}}} \cdot \boldsymbol{e}_{\boldsymbol{z},\boldsymbol{A}_{\boldsymbol{i}}}} \boldsymbol{e}_{\boldsymbol{z},\boldsymbol{B}_{\boldsymbol{j}}};\ \boldsymbol{e}_{\boldsymbol{x},\boldsymbol{B}_{\boldsymbol{j}}} = \frac{\boldsymbol{a}_{\boldsymbol{x},\boldsymbol{B}_{\boldsymbol{j}}}}{\left\|\boldsymbol{a}_{\boldsymbol{x},\boldsymbol{B}_{\boldsymbol{j}}}\right\|};\ \boldsymbol{e}_{\boldsymbol{y},\boldsymbol{B}_{\boldsymbol{j}}} = \boldsymbol{e}_{\boldsymbol{z},\boldsymbol{B}_{\boldsymbol{j}}} \times \boldsymbol{e}_{\boldsymbol{x},\boldsymbol{B}_{\boldsymbol{j}}} \tag{3-53}$$

The transformation matrices used to project from the local co-rotation system of each contact point A_i and B_j to the global system are:

$$\boldsymbol{Q}_{\boldsymbol{A}_{\boldsymbol{i}}} = \begin{bmatrix} \boldsymbol{e}_{\boldsymbol{x},\boldsymbol{A}_{\boldsymbol{i}}} \\ \boldsymbol{e}_{\boldsymbol{y},\boldsymbol{A}_{\boldsymbol{i}}} \\ \boldsymbol{e}_{\boldsymbol{z},\boldsymbol{A}_{\boldsymbol{i}}} \end{bmatrix} \tag{3-54}$$

$$\boldsymbol{Q}_{\boldsymbol{B}_{\boldsymbol{j}}} = \begin{bmatrix} \boldsymbol{e}_{\boldsymbol{x},\boldsymbol{B}_{\boldsymbol{j}}} \\ \boldsymbol{e}_{\boldsymbol{y},\boldsymbol{B}_{\boldsymbol{j}}} \\ \boldsymbol{e}_{\boldsymbol{z},\boldsymbol{B}_{\boldsymbol{j}}} \end{bmatrix} \tag{3-55}$$

Since the contact forces acting in points C_k are generated between two plane surfaces, the additional local co-rotational systems coincide with the co-rotational system of the bottom slider. Hence $\boldsymbol{Q}_{\boldsymbol{C}_{\boldsymbol{k}}} = \boldsymbol{Q}_{\boldsymbol{bs}}$.

Finally, to obtain the contact forces in the global reference system, the following equations can be used:

$$\boldsymbol{f}_{\boldsymbol{cont},\boldsymbol{A}_{\boldsymbol{i}}} = \left[\boldsymbol{f}_{\boldsymbol{\mu},\boldsymbol{A}_{\boldsymbol{i}}}, N_{A_i}\right] \boldsymbol{Q}_{\boldsymbol{A}_{\boldsymbol{i}}} \tag{3-56}$$

$$\boldsymbol{f}_{\boldsymbol{cont},\boldsymbol{B}_{\boldsymbol{j}}} = \left[\boldsymbol{f}_{\boldsymbol{\mu},\boldsymbol{B}_{\boldsymbol{j}}}, N_{\boldsymbol{B}_{\boldsymbol{j}}}\right] \boldsymbol{Q}_{\boldsymbol{B}_{\boldsymbol{j}}} \tag{3-57}$$

$$\boldsymbol{f}_{\boldsymbol{cont},\boldsymbol{C_k}} = \left[\boldsymbol{f}_{\boldsymbol{\mu},\boldsymbol{C_k}}, N_{\boldsymbol{C_k}}\right]\boldsymbol{Q}_{\boldsymbol{C_k}} \tag{3-58}$$

The relative sliding velocities are needed to update the hysteretic parameters. The following expressions can be used to compute these vectors:

$$\dot{\boldsymbol{r}}_{A_i'|A_i} = \left(\dot{\boldsymbol{r}}_{\boldsymbol{A_i}} - \dot{\boldsymbol{r}}'_{A_i}\right)\boldsymbol{Q}^{\boldsymbol{T}}_{\boldsymbol{A_i}} \tag{3-59}$$

$$\dot{\boldsymbol{r}}_{B_j'|B_j} = \left(\dot{\boldsymbol{r}}_{\boldsymbol{B_j}} - \dot{\boldsymbol{r}}'_{B_j}\right)\boldsymbol{Q}^{\boldsymbol{T}}_{\boldsymbol{B_j}} \tag{3-60}$$

$$\dot{\boldsymbol{r}}_{C_k'|C_k} = \left(\dot{\boldsymbol{r}}_{\boldsymbol{C_k}} - \dot{\boldsymbol{r}}'_{C_k}\right)\boldsymbol{Q}^{\boldsymbol{T}}_{\boldsymbol{C_k}} \tag{3-61}$$

For example, the ordinary differential equations that describe the evolution of the dimensionless hysteretic parameters $\boldsymbol{z}_{\boldsymbol{A_i}}$ can be expressed as:

$$\dot{\boldsymbol{z}}_{\boldsymbol{A_i}} = \frac{1}{\Delta s}\begin{bmatrix} A - a_x \boldsymbol{z}_{\boldsymbol{A_i}}(1)^2 & -a_y \boldsymbol{z}_{\boldsymbol{A_i}}(1)\boldsymbol{z}_{\boldsymbol{A_i}}(2) \\ -a_x \boldsymbol{z}_{\boldsymbol{A_i}}(1)\boldsymbol{z}_{\boldsymbol{A_i}}(2) & A - a_y \boldsymbol{z}_{\boldsymbol{A_i}}(2)^2 \end{bmatrix} \dot{\boldsymbol{r}}_{A_i'|A_i}(1{:}\,2)^T \tag{3-62}$$

in which $\Delta s = \max\left(\frac{\mu N_{A_i}}{k_s},\ \Delta s_{min}\right)$ is the displacement at which sliding occurs with k_s the stiffness during the sticking phase and Δs_{min} the minimum value of Δs used to avoid numerical problems in the integration of the first-order state equation; $a_x = \beta + \gamma \mathrm{sgn}\left(\dot{\boldsymbol{r}}_{A_i'|A_i}(1)\ \boldsymbol{z}_{\boldsymbol{A_i}}(1)\right)$ and $a_y = \beta + \gamma \mathrm{sgn}\left(\dot{\boldsymbol{r}}_{A_i'|A_i}(2)\ \boldsymbol{z}_{\boldsymbol{A_i}}(2)\right)$ are the variables that represent the phase of the element (sliding phase or sticking phase); A, β and γ are dimensionless constants. In this study, the following values are taken: $A = 1$, $\beta = 0.5$, and $\gamma = 0.5$.

3.3.2.2 Impact forces

Three cases produce an internal impact force: (i) if the top slider contacts the restraining rim of the top plate, (ii) if the bottom slider contacts the restraining rim of the bottom plate, or

(iii) if the top slider contacts the restraining rim of the bottom slider. To monitoring the two first cases, two vectors from the centroid of the plates to the corresponding contact points using local co-rotational system coordinates are needed:

$$\boldsymbol{r}^{(\boldsymbol{l})}_{\boldsymbol{c_{tp}}|\boldsymbol{A_i}} = \left(\boldsymbol{r}_{\boldsymbol{A_i}} - \boldsymbol{r}^{\boldsymbol{tp}}_{\boldsymbol{c}}\right)\boldsymbol{Q}^{\boldsymbol{T}}_{\boldsymbol{tp}} \tag{3-63}$$

$$\boldsymbol{r}^{(\boldsymbol{l})}_{\boldsymbol{c_{bp}}|\boldsymbol{B_j}} = \left(\boldsymbol{r}_{\boldsymbol{B_j}} - \boldsymbol{r}^{\boldsymbol{bt}}_{\boldsymbol{c}}\right) \tag{3-64}$$

A vector from the centroid of the bottom slider to the contact point C_k is required to check the third case:

$$\boldsymbol{r}^{(\boldsymbol{l})}_{\boldsymbol{c_{bs}}|\boldsymbol{C_k}} = \left(\boldsymbol{r}_{\boldsymbol{C_k}} - \boldsymbol{r}^{\boldsymbol{bs}}_{\boldsymbol{c}}\right)\boldsymbol{Q}^{\boldsymbol{T}}_{\boldsymbol{bs}} \tag{3-65}$$

This third case is considered to include the internal impact behavior beyond the maximum displacement capacity of the LIR-DCFP bearing model. The displacement capacity of the proposed isolator is defined by the inner width of the plates b_{tp} and b_{bp} and the internal gap between the sliders $(e_{ts} - e_{bs})$. If this capacity is overcome, a stiff impact between the two sliders will be produced. A numerical example of the situation beyond the maximum displacement capacity is presented in section 3-5.

For each case, the impact occurs if:

$$\left\|\boldsymbol{r}^{(l)}_{\boldsymbol{c_{tp}}|\boldsymbol{A_i}}(1:2)\right\| \geq \frac{b_{tp}}{2} \;\; \& \;\; \boldsymbol{r}^{(\boldsymbol{l})}_{\boldsymbol{c_{tp}}|\boldsymbol{A_i}}(3) \geq -\left(l_{tp} + d + R - \sqrt{R^2 - \left(R - \frac{b_{tp}}{2}\right)^2}\right) \tag{3-66}$$

$$\left\|\boldsymbol{r}^{(\boldsymbol{l})}_{\boldsymbol{c_{bp}}|\boldsymbol{B_j}}(1:2)\right\| \geq \frac{b_{bp}}{2} \;\; \& \;\; \boldsymbol{r}^{(\boldsymbol{l})}_{\boldsymbol{c_{bp}}|\boldsymbol{B_j}}(3) \leq \left(l_{bp} + d + R - \sqrt{R^2 - \left(R - \frac{b_{bp}}{2}\right)^2}\right) \tag{3-67}$$

$$\left\|\boldsymbol{r}^{(\boldsymbol{l})}_{\boldsymbol{c_{bs}}|\boldsymbol{C_k}}(1:2)\right\| \geq \frac{b_{bs}}{2} \;\; \& \;\; \boldsymbol{r}^{(\boldsymbol{l})}_{\boldsymbol{c_{bs}}|\boldsymbol{C_k}}(3) \leq (h_{bs} - d_{bs} + l_{bs}) \tag{3-68}$$

The impact velocities, for each considered case, can be estimated using the following equations:

$$\dot{\boldsymbol{r}}_{\boldsymbol{A_i|A_i'}} = \left(\dot{\boldsymbol{r}}_{\boldsymbol{A_i}} - \dot{\boldsymbol{r}}'_{\boldsymbol{A_i}}\right)\boldsymbol{Q}_{\boldsymbol{tp}}^{\boldsymbol{T}} \tag{3-69}$$

$$\dot{\boldsymbol{r}}_{\boldsymbol{B_j|B_j'}} = \left(\dot{\boldsymbol{r}}_{\boldsymbol{B_j}} - \dot{\boldsymbol{r}}'_{\boldsymbol{B_j}}\right) \tag{3-70}$$

$$\dot{\boldsymbol{r}}_{\boldsymbol{C_k|C_k'}} = \left(\dot{\boldsymbol{r}}_{\boldsymbol{C_k}} - \dot{\boldsymbol{r}}'_{\boldsymbol{C_k}}\right)\boldsymbol{Q}_{\boldsymbol{bs}}^{\boldsymbol{T}} \tag{3-71}$$

If an impact occurs, the magnitude of the impact force is calculated using the Kelvin-Voigt model:

$$I_{A_i} = k_{imp}\left(\left\|\boldsymbol{r}^{(\boldsymbol{l})}_{\boldsymbol{c_{tp}|A_i}}(1{:}\,2)\right\| - \frac{b_{tp}}{2}\right) + c_{imp}\left\|\dot{\boldsymbol{r}}_{\boldsymbol{A_i|A_i'}}(1{:}\,2)\right\| \tag{3-72}$$

$$I_{B_j} = k_{imp}\left(\left\|\boldsymbol{r}^{(\boldsymbol{l})}_{\boldsymbol{c_{bp}|B_j}}(1{:}\,2)\right\| - \frac{b_{bp}}{2}\right) + c_{imp}\left\|\dot{\boldsymbol{r}}_{\boldsymbol{B_j|B_j'}}(1{:}\,2)\right\| \tag{3-73}$$

$$I_{C_k} = k_{imp}\left(\left\|\boldsymbol{r}^{(\boldsymbol{l})}_{\boldsymbol{c_{bs}|C_k}}(1{:}\,2)\right\| - \frac{b_{bs}}{2}\right) + c_{imp}\left\|\dot{\boldsymbol{r}}_{\boldsymbol{C_k|C_k'}}(1{:}\,2)\right\| \tag{3-74}$$

In this study, an impact stiffness of $k_{imp} = 4.0 \times 10^4$ kN/m is used. The impact damping coefficient c_{imp} is determined using Equation (3-46) employing k_{imp} and $e = 0.65$ as input parameters. It is assumed that the impact force is generated in the x-y plane of the local reference system. The following vectors are defined to decompose the impact force in the local x-y plane:

$$\boldsymbol{a}^{(\boldsymbol{imp})}_{\boldsymbol{A_i}} = \left(\boldsymbol{r}'_{\boldsymbol{A_i}} - \boldsymbol{r}^{\boldsymbol{tp}}_{\boldsymbol{c}}\right)\boldsymbol{Q}_{\boldsymbol{tp}}^{\boldsymbol{T}} \tag{3-75}$$

$$\boldsymbol{a}^{(\boldsymbol{imp})}_{\boldsymbol{B_j}} = \left(\boldsymbol{r}'_{\boldsymbol{B_j}} - \boldsymbol{r}^{\boldsymbol{bp}}_{\boldsymbol{c}}\right) \tag{3-76}$$

$$\boldsymbol{a}^{(\boldsymbol{imp})}_{\boldsymbol{C_k}} = \left(\boldsymbol{r}'_{\boldsymbol{C_k}} - \boldsymbol{r}^{\boldsymbol{bs}}_{\boldsymbol{c}}\right)\boldsymbol{Q}_{\boldsymbol{bs}}^{\boldsymbol{T}} \tag{3-77}$$

Finally, the impact forces projected into the global reference system, can be calculated using the following equations:

$$\boldsymbol{f}_{\boldsymbol{imp},\boldsymbol{A_i}} = -\left(\frac{I_{A_i}}{\left\|\boldsymbol{a}_{\boldsymbol{A_i}}^{(\boldsymbol{imp})}(1:2)\right\|}\left[\boldsymbol{a}_{\boldsymbol{A_i}}^{(\boldsymbol{imp})}(1:2), 0\right]\right)\boldsymbol{Q}_{\boldsymbol{tp}} \tag{3-78}$$

$$\boldsymbol{f}_{\boldsymbol{imp},\boldsymbol{B_j}} = -\left(\frac{I_{B_j}}{\left\|\boldsymbol{a}_{\boldsymbol{B_j}}^{(\boldsymbol{imp})}(1:2)\right\|}\left[\boldsymbol{a}_{\boldsymbol{B_j}}^{(\boldsymbol{imp})}(1:2), 0\right]\right) \tag{3-79}$$

$$\boldsymbol{f}_{\boldsymbol{imp},\boldsymbol{C_k}} = -\left(\frac{I_{C_k}}{\left\|\boldsymbol{a}_{\boldsymbol{C_k}}^{(\boldsymbol{imp})}(1:2)\right\|}\left[\boldsymbol{a}_{\boldsymbol{C_k}}^{(\boldsymbol{imp})}(1:2), 0\right]\right)\boldsymbol{Q}_{\boldsymbol{bs}} \tag{3-80}$$

3.3.2.3 Generalized forces

The generalized forces can be expressed in the following formulation:

$$\boldsymbol{F}_{\boldsymbol{q}\{18\times1\}} = \sum_{n}\frac{\partial \boldsymbol{r_c}}{\partial \boldsymbol{q}}\cdot \boldsymbol{f_n} + \sum_{n}\big((\boldsymbol{r_n} - \boldsymbol{r_c})\times \boldsymbol{f_n}\big)\cdot\frac{\partial \overline{\boldsymbol{\omega}}}{\partial \boldsymbol{q}} \tag{3-81}$$

in which $\boldsymbol{f_n}$ is the nth external force acting on the bearing, $\boldsymbol{r_c}$ is the vector from the origin of the global system to the centroid of the body where the force is generated and, $\overline{\boldsymbol{\omega}}$ is the angular velocity of the rigid body in global reference. For the studied dynamic system, it is convenient to define the following matrices to determine the generalized forces:

$$\boldsymbol{D}_{\boldsymbol{\partial(\Phi_{bs})}} = \left[\frac{\partial\overline{\boldsymbol{\omega}}_{\boldsymbol{bs}}}{\partial\dot{\alpha}_{bs}};\frac{\partial\overline{\boldsymbol{\omega}}_{\boldsymbol{bs}}}{\partial\dot{\beta}_{bs}};\frac{\partial\overline{\boldsymbol{\omega}}_{\boldsymbol{bs}}}{\partial\dot{\gamma}_{bs}}\right] = \begin{bmatrix} 0 & 0 & 1 \\ -\sin\alpha_{bs} & \cos\alpha_{bs} & 0 \\ \cos\alpha_{bs}\sin\beta_{bs} & \sin\alpha_{bs}\cos\beta_{bs} & -\sin\beta_{bs} \end{bmatrix} \tag{3-82}$$

$$\boldsymbol{D}_{\boldsymbol{\partial(\Phi_{ts})}} = \left[\frac{\partial\overline{\boldsymbol{\omega}}_{\boldsymbol{ts}}}{\partial\dot{\alpha}_{ts}};\frac{\partial\overline{\boldsymbol{\omega}}_{\boldsymbol{ts}}}{\partial\dot{\beta}_{ts}};\frac{\partial\overline{\boldsymbol{\omega}}_{\boldsymbol{ts}}}{\partial\dot{\gamma}_{tt}}\right] = \begin{bmatrix} 0 & 0 & 1 \\ -\sin\alpha_{ts} & \cos\alpha_{ts} & 0 \\ \cos\alpha_{ts}\sin\beta_{ts} & \sin\alpha_{ts}\cos\beta_{ts} & -\sin\beta_{ts} \end{bmatrix} \tag{3-83}$$

$$\boldsymbol{D}_{\boldsymbol{\partial(\Phi_{tp})}} = \left[\frac{\partial\overline{\boldsymbol{\omega}}_{\boldsymbol{tp}}}{\partial\dot{\alpha}_{tp}};\frac{\partial\overline{\boldsymbol{\omega}}_{\boldsymbol{tp}}}{\partial\dot{\beta}_{tp}};\frac{\partial\overline{\boldsymbol{\omega}}_{\boldsymbol{tp}}}{\partial\dot{\gamma}_{tp}}\right] = \begin{bmatrix} 0 & 0 & 1 \\ -\sin\alpha_{tp} & \cos\alpha_{tp} & 0 \\ \cos\alpha_{tp}\sin\beta_{tp} & \sin\alpha_{tp}\cos\beta_{tp} & -\sin\beta_{tp} \end{bmatrix} \tag{3-84}$$

The generalized forces can be obtained using the following equations:

$$\boldsymbol{F_q}(1:3) = \sum \left(\boldsymbol{f}^{\boldsymbol{T}}_{\boldsymbol{cont},\boldsymbol{B_j}} + \boldsymbol{f}^{T}_{\boldsymbol{imp},\boldsymbol{B_j}}\right) - \sum \left(\boldsymbol{f}^{\boldsymbol{T}}_{\boldsymbol{cont},\boldsymbol{C_k}} + \boldsymbol{f}^{\boldsymbol{T}}_{\boldsymbol{imp},\boldsymbol{C_k}}\right) \tag{3-85}$$

$$\begin{aligned}\boldsymbol{F_q}(4:6) = \Big(&\sum \left(\boldsymbol{r_{B_j}} - \boldsymbol{r_c^{bs}}\right) \times \left(\boldsymbol{f}^{\boldsymbol{T}}_{\boldsymbol{cont},\boldsymbol{B_j}} + \boldsymbol{f}^{T}_{\boldsymbol{imp},\boldsymbol{B_j}}\right) \boldsymbol{D}^{\boldsymbol{T}}_{\boldsymbol{\partial(\Phi_{bs})}} \\ &- \sum \left(\boldsymbol{r'_{C_k}} - \boldsymbol{r_c^{bs}}\right) \times \left(\boldsymbol{f}^{\boldsymbol{T}}_{\boldsymbol{cont},\boldsymbol{C_k}} + \boldsymbol{f}^{T}_{\boldsymbol{imp},\boldsymbol{C_k}}\right) \boldsymbol{D}^{\boldsymbol{T}}_{\boldsymbol{\partial(\Phi_{bs})}}\Big)^{\boldsymbol{T}}\end{aligned} \tag{3-86}$$

$$\boldsymbol{F_q}(7:9) = \sum \left(\boldsymbol{f}^{\boldsymbol{T}}_{\boldsymbol{cont},\boldsymbol{A_i}} + \boldsymbol{f}^{T}_{\boldsymbol{imp},\boldsymbol{A_i}}\right) + \sum \left(\boldsymbol{f}^{\boldsymbol{T}}_{\boldsymbol{cont},\boldsymbol{C_k}} + \boldsymbol{f}^{\boldsymbol{T}}_{\boldsymbol{imp},\boldsymbol{C_k}}\right) \tag{3-87}$$

$$\begin{aligned}\boldsymbol{F_q}(10:12) = \Big(&\sum \left(\boldsymbol{r_{A_i}} - \boldsymbol{r_c^{ts}}\right) \times \left(\boldsymbol{f}^{\boldsymbol{T}}_{\boldsymbol{cont},\boldsymbol{A_i}} + \boldsymbol{f}^{T}_{\boldsymbol{imp},\boldsymbol{A_i}}\right) \boldsymbol{D}^{\boldsymbol{T}}_{\boldsymbol{\partial(\Phi_{ts})}} \\ &+ \sum \left(\boldsymbol{r_{C_k}} - \boldsymbol{r_c^{ts}}\right) \times \left(\boldsymbol{f}^{\boldsymbol{T}}_{\boldsymbol{cont},\boldsymbol{C_k}} + \boldsymbol{f}^{T}_{\boldsymbol{imp},\boldsymbol{C_k}}\right) \boldsymbol{D}^{\boldsymbol{T}}_{\boldsymbol{\partial(\Phi_{ts})}}\Big)^{\boldsymbol{T}}\end{aligned} \tag{3-88}$$

$$\boldsymbol{F_q}(13:15) = -\sum \left(\boldsymbol{f}^{\boldsymbol{T}}_{\boldsymbol{cont},\boldsymbol{A_i}} + \boldsymbol{f}^{T}_{\boldsymbol{imp},\boldsymbol{A_i}}\right) \tag{3-89}$$

$$\boldsymbol{F_q}(16:18) = \left(\sum \left(\boldsymbol{r'_{A_i}} - \boldsymbol{r_c^{tp}}\right) \times \left(-\boldsymbol{f}^{\boldsymbol{T}}_{\boldsymbol{cont},\boldsymbol{A_i}} - \boldsymbol{f}^{T}_{\boldsymbol{imp},\boldsymbol{A_i}}\right) \boldsymbol{D}^{\boldsymbol{T}}_{\boldsymbol{\partial(\Phi_{tp})}}\right)^{\boldsymbol{T}} \tag{3-90}$$

3.4 Study of the geometric parameters of the inner slider

In this section, a parametric study is made to evaluate the relevance of three important geometric parameters: (i) the slenderness of the slider; (ii) the size of the internal gap between the top slider and the bottom slider and, (iii) the relative highness of the high friction interface. The slenderness of the slider is critical because, during lateral impact, this parameter could influence the possibility of the overturning of the device. The larger the internal gap, the more energy can be dissipated during sliding in the high friction interface. That is why the evaluation of the effects of different gap sizes in the internal dynamic is vital. Finally, understanding the influence of the relative highness makes it possible to propose an adequate position to achieve better seismic performance. The importance of these geometric parameters is evaluated based on the global response of the isolator and the local effects measured at the contact points.

Three geometric ratios are defined. The first one is the slenderness ratio ϵ:

$$\epsilon = \frac{H_s}{D_s} \tag{3-91}$$

in which $H_s = (h_{ts} + h_{bs})$ is the total highness of the slider and $D_s = (b_{ts} + 2e_{ts}) = (b_{bs} + 2e_{bs})$ is the outer diameter of the slider. For this study, the outer diameter of the bottom slider and the outer diameter of the top slider is the same. The following geometric ratio is related to the gap existing between the sliders and it is defined as:

$$r_{gap}^{*} = \frac{2e_{ts}}{b_{ts}} \tag{3-92}$$

If the outer diameter of the slider D_s remains constant and e_{ts} takes different values, a higher r_{gap}^{*} implies a larger internal gap. The third and final ratio is related to the relative highness in which the internal interface of the slider is located and is defined as:

$$r_h^{*} = \frac{h_{ts}}{h_{bs}} \tag{3-93}$$

An effective radius of $R_{eff} = 3.00$ m was selected to obtain a comparable dynamic response for each case. The displacement capacity of each sliding surface was taken as 0.15 m, leading to a total capacity of $C_t = 2 \times (0.15)\text{ m} = 0.30$ m. Since the proposed model considers the real geometry of the isolator, two geometric corrections for each case must be done (Fenz & Constantinou, 2006):

$$R_{eff} = 2R - (h_{ts} + h_{bs}) \rightarrow R = \frac{R_{eff} + (h_{ts} + h_{bs})}{2} = \frac{R_{eff} + H_s}{2} \tag{3-94}$$

$$C_t = b_{tp} - D_s - H_s\beta_{max} \rightarrow b_{tp} = C_t + D_s + H_s \sin(\beta_{max}) \tag{3-95}$$

in which β_{max} is the maximum slider rotation. The maximum rotation is obtained when the slider impacts the restraining rims of the top and bottom plates.

Three values for each geometric ratio were selected to study the importance of the geometric slider shape: $\epsilon = 0.33, \epsilon = 0.66$, and $\epsilon = 1.00$; $r^*_{gap} = 0.30, r^*_{gap} = 0.60$, and $r^*_{gap} = 0.90$; $r^*_h = 0.70, r^*_h = 1.00$, and $r^*_h = 1.40$. The nine different cases are shown in Figure 3-8.

The well-known velocity-dependent friction model (M. Constantinou et al., 1990) was used to determine the friction coefficient μ at every time-step and in each contact point:

$$\mu(\dot{v}) = \mu_{max} - (\mu_{max} - \mu_{min})\exp(-a|\dot{v}|) \tag{3-96}$$

in which μ_{max} represents the maximum value of friction coefficient at large velocities of sliding and μ_{min} the friction coefficient at zero velocity. The sliding velocity is represented by $\dot{v}$, and a is known as the rate parameter. For this study, the following values were used for sets points A_i and B_j: $\mu_{min} = 0.04$; $\mu_{max} = 1.5\mu_{min}$, and $a = 20$ sec/m. For the contact points of the set C_k, a constant friction coefficient of $\mu_s = 0.15$ was employed.

The plates were modeled using a mass of $m_{tp} = 300$ kg to determine the dynamic response. The total mass of the slider was modeled using $(m_{bs} + m_{tp}) = 100$ kg. The mass of the superstructure supported by the bearing is assumed constant during the ground motion being equal to $m_{sp} = 200{,}000$ kg.

The NWH360 component of the Newhall record (Northridge earthquake, 1994 (PEER, 2013)) was applied to obtain the dynamic response. The characteristics of the three components of the record are presented in Table 3-1. The numerical models have been developed in two dimensions, using five contact points for each contact point set A_i, B_j, and C_k (see Figure 3-8). The choice of considering five contact points is based on the hypothesis that a larger number of contact points will lead to a better numerical representation of the transmission mechanism of the forces generated between the bodies of the bearing.

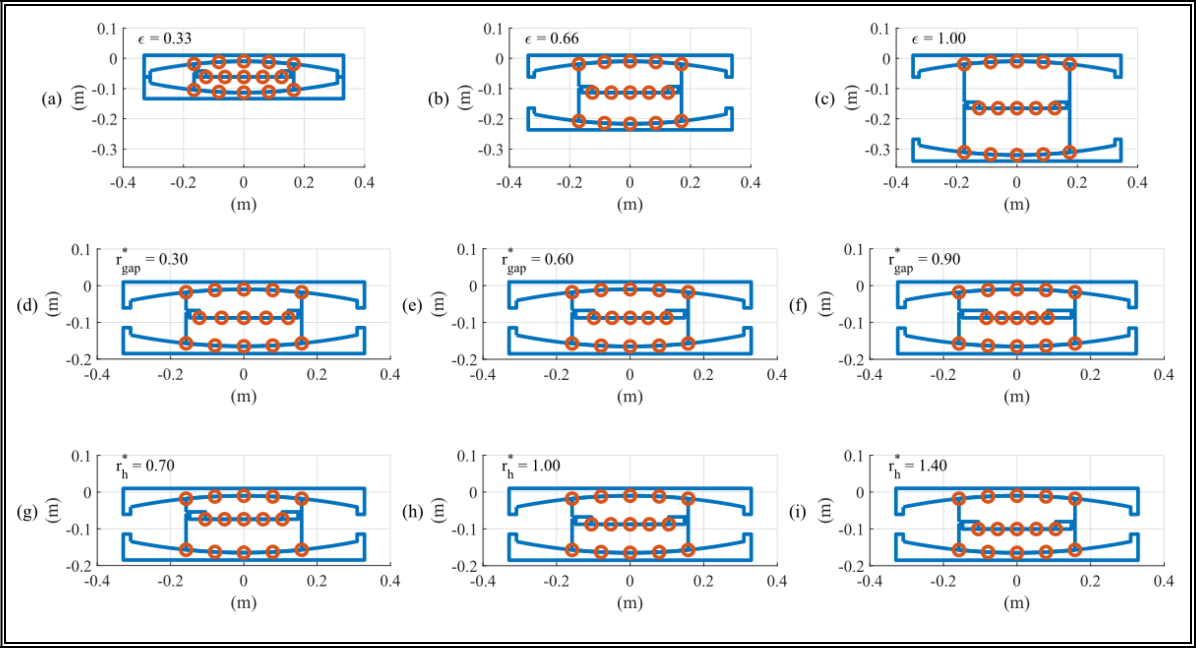

Figure 3-8: Studied cases for the geometric parametric analysis. (a) Slenderness ratio $\epsilon = 0.33$. (b) Slenderness ratio $\epsilon = 0.66$. (c) Slenderness ratio $\epsilon = 1.00$. (d) Gap ratio $r^*_{gap} = 0.30$. (e) Gap ratio $r^*_{gap} = 0.60$. (f) Gap ratio $r^*_{gap} = 0.90$. (g) Relative highness ratio $r^*_h = 0.70$. (h) Relative highness ratio $r^*_h = 1.00$. (i) Relative highness ratio $r^*_h = 1.40$.

Table 3-1: Earthquake record characteristics (PEER ground motion database (PEER, 2013))

Ground motion ID	Record sequence number	Earthquake name	Year	Station name	Earthquake magnitude (Mw)	Epicentral distance (km)	Component	PGA (g)
GM 1	1044	Northridge-01	1994	Newhall - Fire Station	6.69	20.27	NWH090	0.58
							NWH360	0.59
							NWH-UP	0.54
GM 2	828	Cape Mendocino	1992	Petrolia	7.01	4.51	PET000	0.59
							PET090	0.66
							PET-UP	0.16
GM 3	1119	Kobe, Japan	1995	Takarazuka	6.90	38.6	TAZ000	0.69
							TAZ090	0.61
							TAZ-UP	0.42

3.4.1 Slider slenderness

The obtained results for each studied case: $\epsilon = 0.33, \epsilon = 0.66$, and $\epsilon = 1.00$ are plotted in Figure 3-9. The lateral displacement of the top plate is shown in Figure 3-9(a). Despite the height differences of the considered sliders, the dynamic response is similar in all cases. The same happens if the lateral force transmitted by the top plate is analyzed (see Figure 3-9(b)). The maximum obtained values, produced when the impact occurs (time $t = 4.24$ seconds), are equivalent. An increase of the highness of the slider from 10.3 cm ($\epsilon = 0.33$) to 31 cm ($\epsilon = 1.00$) does not produce an important change in the global response of the frictional bearing. The force- displacement loops of the three analyzed cases are displayed in Figures 3-9(c), 3-9 (d), and 3-9(e), respectively. Note that there are differences in the displacement produced by the relative sliding between the top slider and the bottom slider, being maximum for the $\epsilon = 0.66$ case and minimum for the $\epsilon = 1.00$ case. The main results of the global response are summarized in Table 3-2.

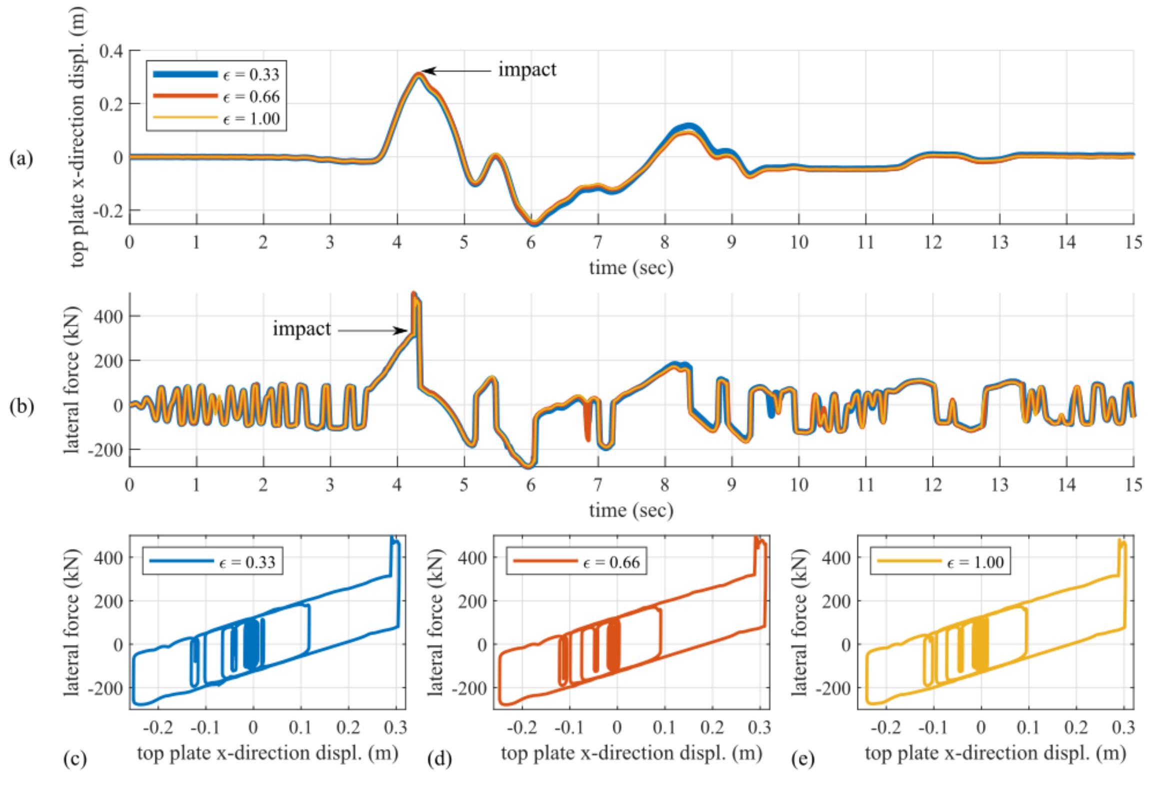

Figure 3-9: Time-story results for different slenderness ratios ϵ: (a) Top plate x-direction displacement. (b) Lateral force transmitted by the top plate. (c) Force displacement loops for the $\epsilon = 0.33$ case. (d) Force displacement loops for the $\epsilon = 0.66$ case. (e) Force displacement loops for the $\epsilon = 1.00$ case.

Table 3-2: Maximum and minimum global responses for different slenderness ratios.

Slenderness ratio ϵ	Maximum lateral force. (kN)	Maximum vertical force (kN)	Minimum vertical force (kN)	Maximum moment (kN x m)	H.F.I.R.D. (cm)	T.P.R.D. (cm)
0.33	495	2205	1835	316	1.8	0.5
0.66	503	2091	1846	344	2.4	0.1
1.00	481	2073	1832	359	1.4	0.0

H.F.I.R.D.: High friction interface residual displacement

T.P.R.D.: Top plate residual displacement

The magnitude of the normal forces produced in the contact points located in the edges (contact points 1 and 5) are shown in Figure 3-10. The contact points defined between the sliders and the concave sliding surfaces are susceptible to slider slenderness. During internal impact (time $t = 4.24$ seconds), the normal force developed in contact points A_5 tends to decrease if the slenderness of the slider rises. The same phenomenon is observed in contact points B_1. Hence, better behavior is observed if the slider has small values of the slenderness ratio ϵ. After the impact, a relative sliding between the sliders is produced. This relative displacement explains a different distribution of normal force at the end of ground motion. Note that, for the $\epsilon = 0.66$ case, at time $t = 15$ seconds, the normal force variation in the contact point C_1 is 73 kN, while at the contact point C_5, the variation is -73 kN. The maximum and minimum values of the normal forces generated in the contact points located in the edges are presented is Table 3-3.

Table 3-3: Maximum and minimum normal forces for different slender ratios (Results are expressed in kN).

Slenderness ratio ϵ	Max. N_{A_1}	Min. N_{A_1}	Max. N_{A_5}	Min. N_{A_5}	Max. N_{B_1}	Min. N_{B_1}	Max. N_{B_5}	Min. N_{B_5}	Max. N_{C_1}	Min. N_{C_1}	Max. N_{C_5}	Min. N_{C_5}
0.33	471	385	423	322	417	281	469	387	480	397	415	316
0.66	502	375	428	278	429	221	533	376	512	398	407	284
1.00	513	360	444	249	445	201	559	362	495	395	406	296

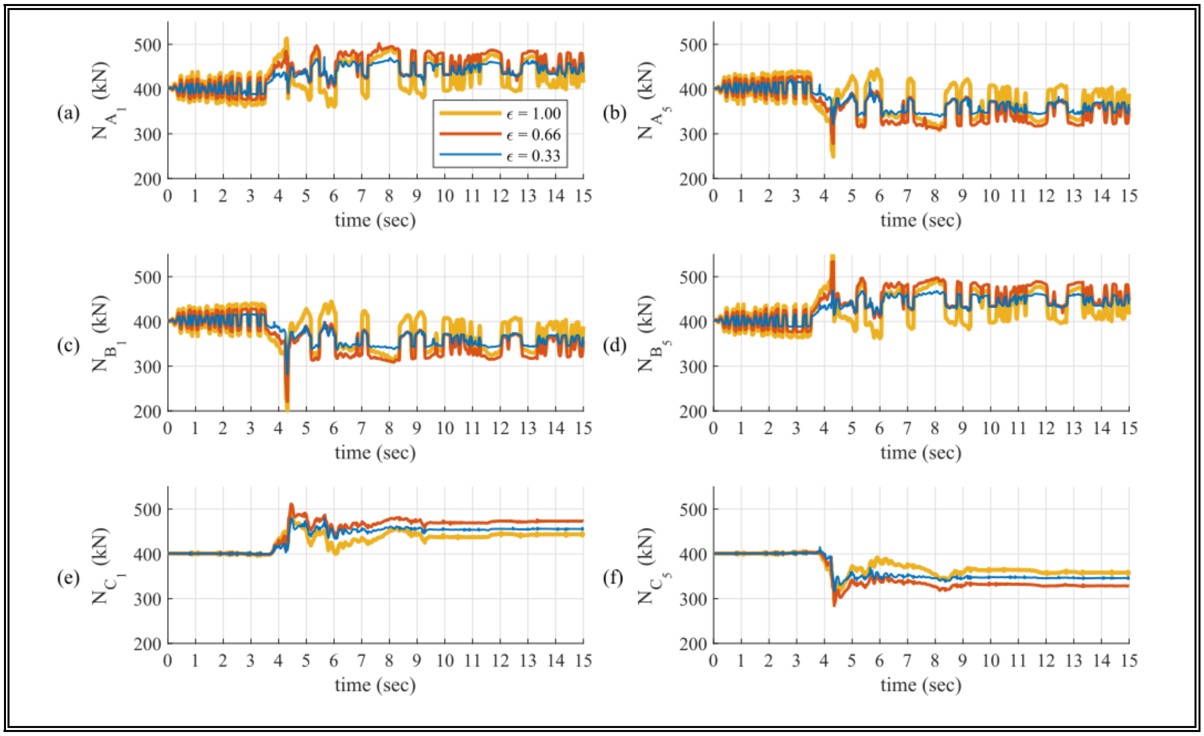

Figure 3-10: Normal forces produced at the contact points located at the edges for different slenderness ratios ϵ: (a) Contact point N_{A_1}. (b) Contact point N_{A_5}. (c) Contact point N_{B_1}. (d) Contact point N_{B_5}. (e) Contact point N_{C_1}. (f) Contact point N_{C_5}.

3.4.2 Size of the internal gap of the slider

The obtained results for each studied case: $r^*_{gap} = 0.30, r^*_{gap} = 0.60$, and $r^*_{gap} = 0.90$ are shown in Figure 3-11. The vertical displacement of the top plate is shown in Figure 3-11(a). This vertical motion is produced by the kinematic constraint that numerical model of the frictional bearing automatically imposes. In all cases, the results are similar. In Figure 3-11(b), the vertical force transmitted by the top plate is plotted. Again, the dynamic response is comparable. It is essential to highlight that although a constant mass m_{sp} was assumed on the isolator and the vertical component of the seismic record was not applied, the vertical load does vary during the ground motion. This variation is produced by the vertical movement of the different parts of the bearing that activated the vertical dynamics of the frictional device. For these three analyzed cases, the coupling between the lateral and vertical displacement produces variation in the vertical force transmitted by the isolator of almost 10%. The main values of the global response for each studied case are summarized in Table 3-4.

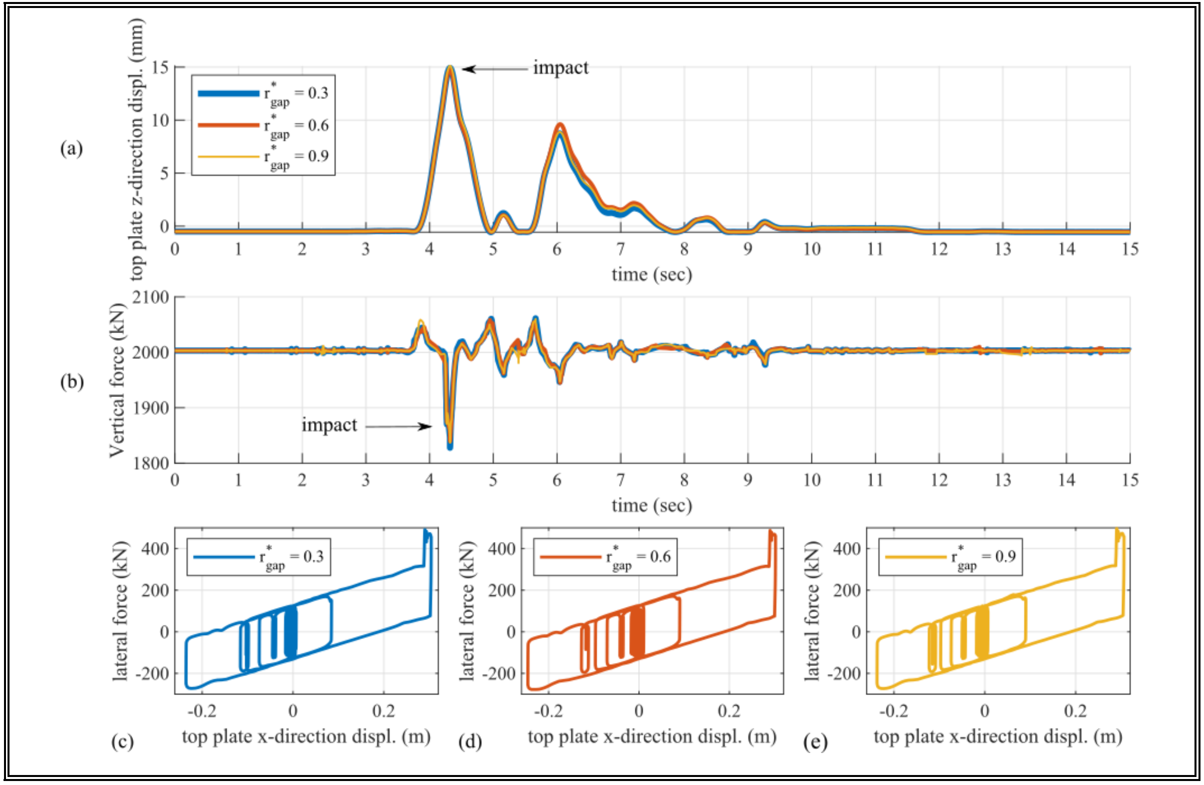

Figure 3-11: Time-story results for different gap ratios r^*_{gap}: (a) Top plate z-direction displacement. (b) Vertical force transmitted by the top plate. (c) Force displacement loops for the $r^*_{gap} = 0.30$ case. (d) Force displacement loops for the $r^*_{gap} = 0.60$ case. (e) Force displacement loops for the $r^*_{gap} = 0.90$ case.

Table 3-4: Maximum and minimum global responses for different gap ratios.

Gap ratio r^*_{gap}	Maximum lateral force. (kN)	Maximum vertical force (kN)	Minimum vertical force (kN)	Maximum moment (kN x m)	H.F.I.R.D (cm)	T.P.R.D. (cm)
0.30	491	2061	1828	327	1.6	0.1
0.60	488	2058	1840	323	1.3	0.1
0.90	497	2060	1837	328	1.8	0.1

H.F.I.R.D.: High friction interface residual displacement

T.P.R.D.: Top plate residual displacement

In Figure 3-12, the changes over time of the normal forces produced in contact points are shown. Note that, for the contact points A_1, A_5, B_1 and B_5, the differences are small. Thus, variations in the size of the internal gap do not significantly affect the distribution of normal forces produced between the inner slider and the top and bottom plates. On the other hand, the normal forces developed in the contact points C_1 and C_5 are affected by changes in the gap ratio r^*_{gap}. During the lateral impact against the restraining rims, a bigger internal gap leads to larger variation in the normal force, being maximum for the $r^*_{gap} = 0.90$ case. In this case, a gap of 6.5 cm was considered. Despite having a large gap, the variation in the maximum normal force in the contact point C_1 is only 26%. Assuming this simplified numerical model of a single isolator, local uplift problems should not occur. The maximum and minimum values of the internal normal forces are presented in Table 3-5.

Table 3-5: Maximum and minimum normal forces for different gap ratios (Results are expressed in kN).

Gap ratio r^*_{gap}	Max. N_{A_1}	Min. N_{A_1}	Max. N_{A_5}	Min. N_{A_5}	Max. N_{B_1}	Min. N_{B_1}	Max. N_{B_5}	Min. N_{B_5}	Max. N_{C_1}	Min. N_{C_1}	Max. N_{C_5}	Min. N_{C_5}
0.30	472	378	425	297	425	256	496	378	482	397	408	314
0.60	468	377	426	308	424	257	496	380	497	397	405	300
0.90	482	380	423	301	424	245	507	380	505	397	409	290

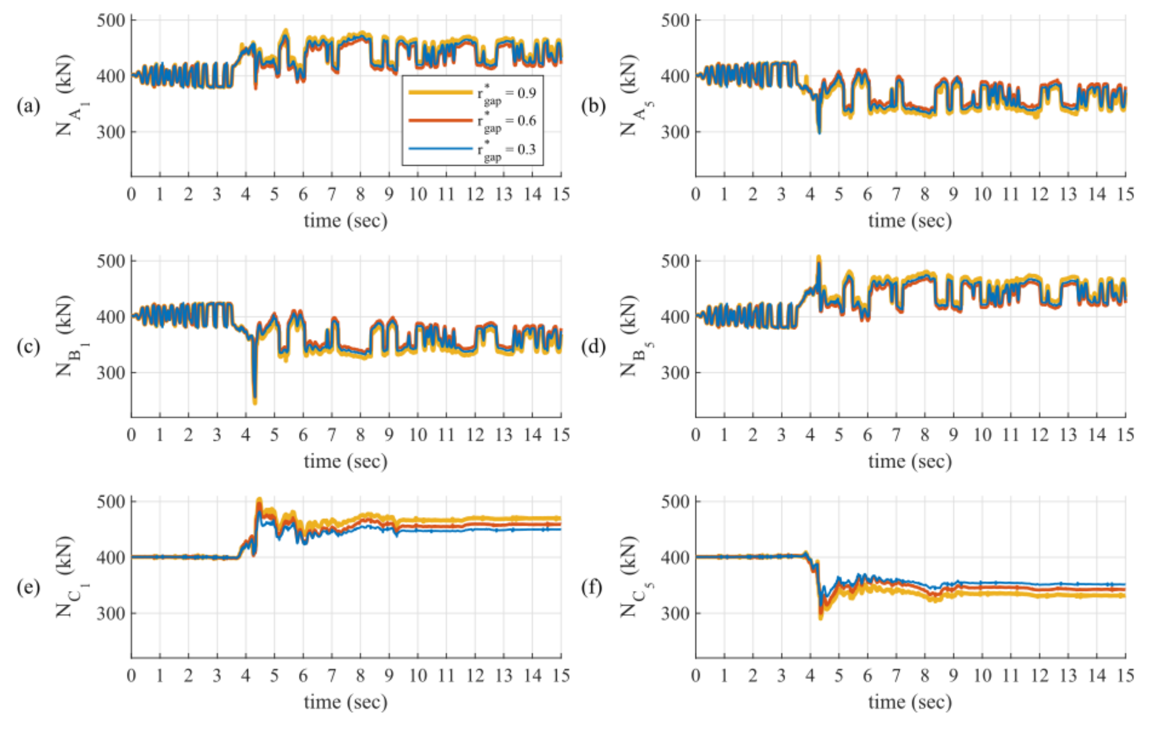

Figure 3-12: Normal forces produced at the contact points located at the edges for different gap ratios r^*_{gap}: (a) Contact point N_{A_1}. (b) Contact point N_{A_5}. (c) Contact point N_{B_1}. (d) Contact point N_{B_5}. (e) Contact point N_{C_1}. (f) Contact point N_{C_5}.

3.4.3 Relative highness of the high friction interface

The obtained results for each studied case: $r^*_h = 0.70, r^*_h = 1.00$, and $r^*_h = 1.40$ are shown in Figure 3-13. While the rotation of the top slider is presented in Figure 3-13(a), the moment that the bearing transmits to the superstructure is shown in Figure 3-13(b). As in the previous subsections, the global response of the isolator is similar for all the studied cases (see Table 3-6).

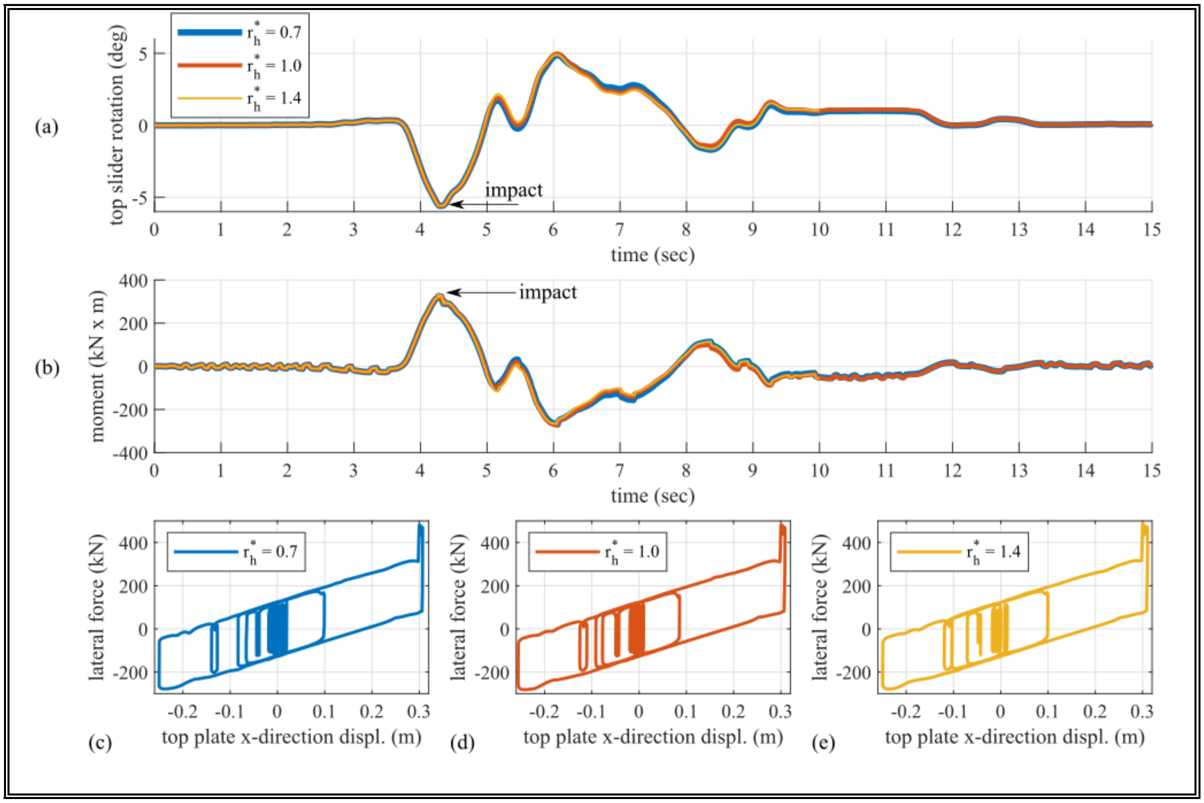

Figure 3-13: Time-story results for different relative highness ratios r_h^*: (a) Top slider rotation. (b) Moment transmitted by the top plate. (c) Force displacement loops for the $r_h^* = 0.70$ case. (d) Force displacement loops for the $r_h^* = 1.00$ case. (e) Force displacement loops for the $r_h^* = 1.40$ case.

Table 3-6: Maximum and minimum global responses for different relative highness ratios.

Relative highness ratio r_h^*	Maximum lateral force. (kN)	Maximum vertical force (kN)	Minimum vertical force (kN)	Maximum moment (kN x m)	H.F.I.R.D (cm)	T.P.R.D. (cm)
0.70	481	2098	1834	326	0.9	0.5
1.00	481	2078	1828	327	1.0	0.5
1.40	489	2079	1823	333	1.2	0.5

H.F.I.R.D.: High friction interface residual displacement

T.P.R.D.: Top plate residual displacement

The variations in the normal forces produced in the contact points are shown in Figure 3-14. Despite the different relative heights where the high friction interface is located, the obtained responses are similar. The summary of the local results is presented in Table 3-7. Due to the shape of the top slider it is convenient to locate the high friction interface as low as possible. The area of the upper surface of the top slider is larger than the area that contacts the bottom slider. This decrease in the contact area generates a ring that transmits the vertical force like a cantilever beam. The higher this ring, the more resistant it will be, avoiding problems during the operation of the device.

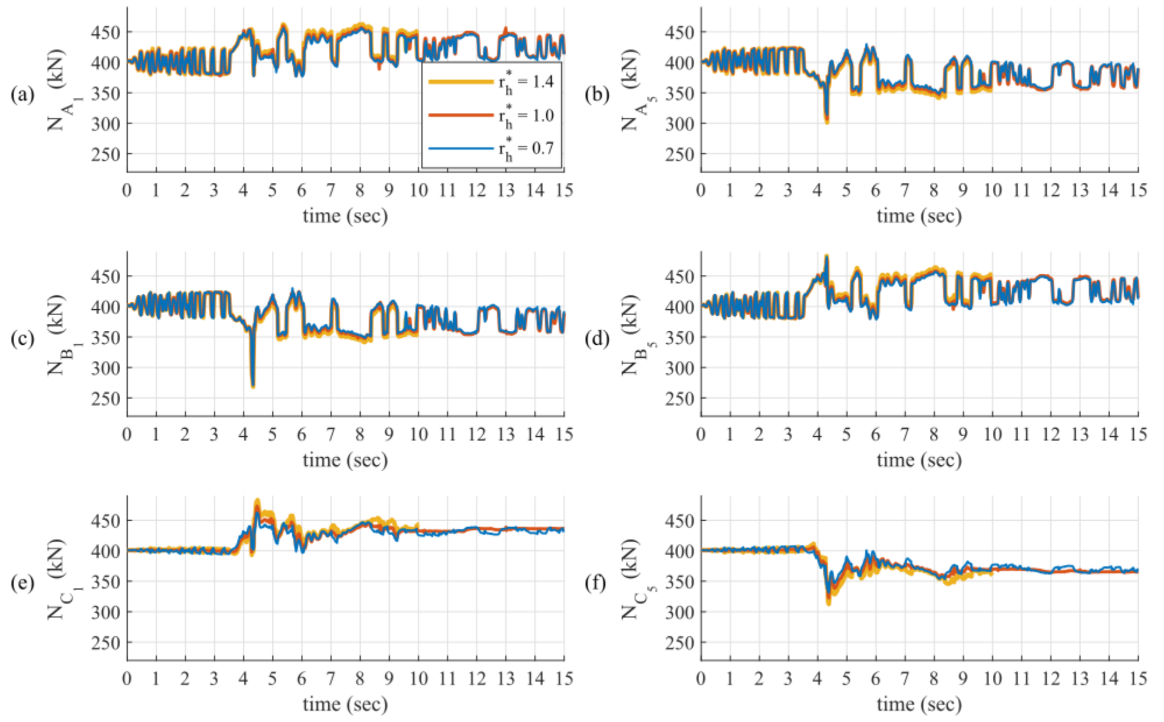

Figure 3-14: Normal forces produced at the contact points located at the edges for different relative highness ratios r_h^*: (a) Contact point N_{A_1}. (b) Contact point N_{A_5}. (c) Contact point N_{B_1}. (d) Contact point N_{B_5}. (e) Contact point N_{C_1}. (f) Contact point N_{C_5}.

Table 3-7: Maximum and minimum normal forces for different relative highness ratios (Results are expressed in kN).

Relative highness ratio r_h^*	Max. N_{A_1}	Min. N_{A_1}	Max. N_{A_5}	Min. N_{A_5}	Max. N_{B_1}	Min. N_{B_1}	Max. N_{B_5}	Min. N_{B_5}	Max. N_{C_1}	Min. N_{C_1}	Max. N_{C_5}	Min. N_{C_5}
0.70	456	376	430	314	430	271	482	379	463	394	407	331
1.00	460	378	425	307	424	272	478	380	473	397	406	323
1.40	462	379	423	301	423	268	483	381	483	393	412	312

3.4.4 Comments on the numerical results

For the nine considered cases, the obtained global response was very similar. If local uplift is not observed, the global responses depend only on the main geometrical parameters (the effective radius R_{eff} and the total lateral capacity C_t) and the employed frictional parameters. The nine cases share these critical properties, explaining why, despite presenting different internal dynamic behavior, the displacements and the total forces transmitted by the bearings are comparable.

Despite obtaining similar results in the global responses, there are differences. On the one hand, the most significant variations are obtained when analyzing differences in the slenderness of the inner slider. Although the effective radius R_{eff} and the lateral capacity C_t is identical in each of the three studied cases, each bearing has a different radius of curvature R in the top plate and the bottom plate (see Equation 3-94). Also, the inner width of the top plate d_{tp} and the bottom plate d_{bp} must be modified to obtain the same total lateral capacity C_t (see Equation 3-95). These significant changes in the isolator geometry make the differences more noticeable. On the other hand, the cases analyzed with different gap ratios and different relative heights where the high friction interface is placed share effective geometric characteristics and the same geometry in the top and bottom plates and in the total height H_s and width D_s of the inner slider. These additional shared geometric parameters explain the more remarkable similarity in the responses.

Any representation of a structural system is affected by uncertainties (Paolo Castaldo et al., 2019, 2020; Celarec & Dolšek, 2013). This highly non-linear dynamics model could be affected by aleatory uncertainties affecting, for example, the geometry of the devices, the properties of the materials, or the friction parameters. This kind of uncertainty has not been considered. All the used parameters have been chosen as deterministic values. The non-linear time story analyses are also affected by epistemic uncertainties. Small changes in the modeling hypotheses or in the numerical parameters can affect the integration of the dynamic response of the isolators. In the cases analyzed, five points of contact were used. Fewer or more points of contact can affect the response obtained. The MATLAB solver ode23t (Hunt et al., 2006) has been used to integrate the motion equation because the problem exhibits stiffness. With another solver that presents numerical damping, the response to be obtained may be different. The same occurs with the tolerances chosen to achieve convergence at each time step. In this way, the small differences obtained, for example, in the residual displacement in the high friction interface when the relative highness of the inner slider is studied, may be explained for the phenomena mentioned above.

3.5 Comparative three-dimensional dynamic analysis

A three-story, two-bay-by-one-bay, reinforced concrete moment-frame structure was modeled to analyze the earthquake response of a dynamic system isolated with friction bearings when impact between the slider and the restraining rims of the plates is produced. The bay width in both directions and the story height were taken as 8.0 m and 3.5 m, respectively. The beams ware shaped with rectangular sections of 40×70 cm^2. The columns were modeled with square sections of 70×70 cm^2. The slabs were modeled with a thickness of 15 cm. Six frictional devices were included to form the isolation system. The structural model, fully developed in the MATLAB environment (Hunt et al., 2006), is shown in Figure 3-15.

The superstructure was modeled as a 3D linear elastic multi-degree-of-freedom system. As mentioned in subsection 3.4.2, even if the vertical component of the records is not applied, the coupling between the lateral and vertical motions of the frictional devices will activate modes of vibrations in the global z-direction. Due to this phenomenon, an appropriate mesh is necessary to accurately represent vertical dynamics, especially in the modeling of beams and slabs. The slabs were modeled using 128 shell elements with an area of 2.0×2.0 m^2. The beams were modeled using 76 frame elements with a length of 2 m. Finally, the columns were incorporated using 36 frame elements with a length of 1.75 m.

The elastic modulus of the concrete was assumed as $E_c = 23.4$ GPa. The Poisson's ratio used was $\nu = 0.2$. A seismic weight of $w = 10$ kN/m^2 was assigned in all stories, leading to a total weight of $W_s = 5{,}120$ kN. A constant damping ratio of $\xi_s = 0.02$ was used for the modal base defined by the fixed-base structure to construct the damping matrix (José Luis Almazán, 2001).

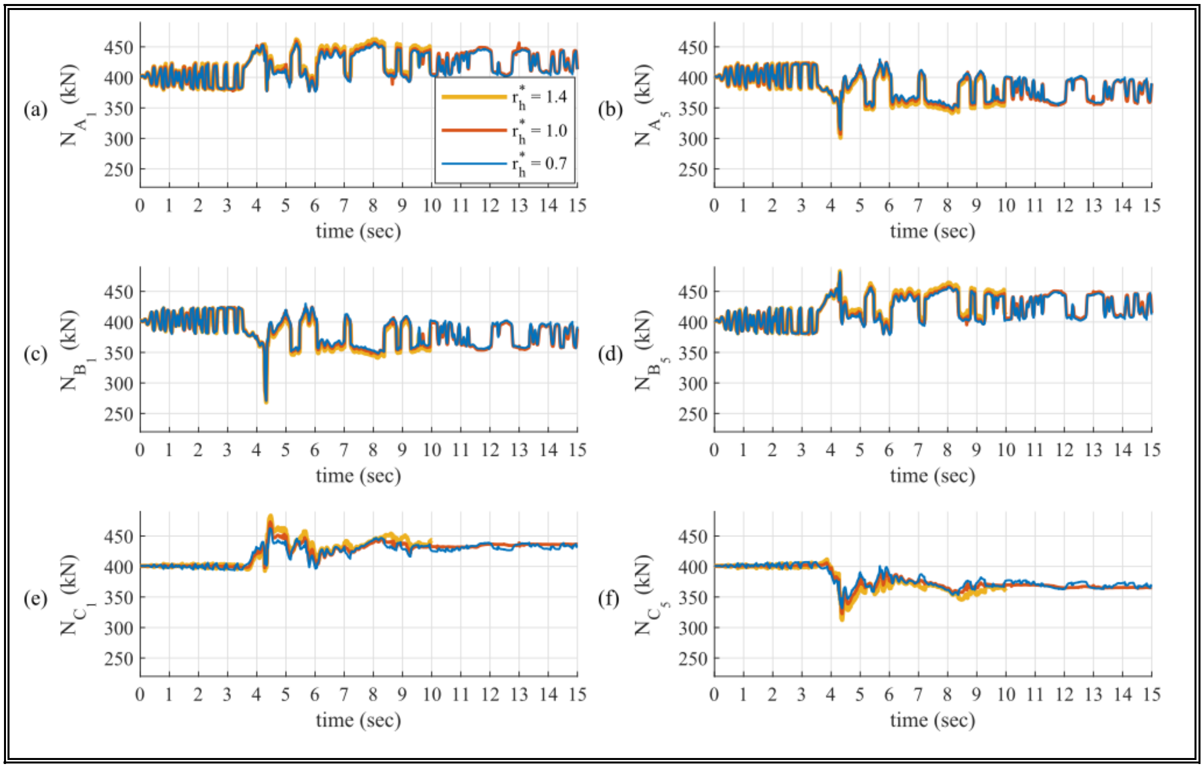

Figure 3-15: Model of the 3D base-isolated structure. (a) Elevation in x-direction. (b) Elevation in y-direction. (c) Position of the isolators. (d) Isometric view.

It is important to highlight that any numerical model representing a structural system is affected by uncertainties in the definition of its global resistance (Paolo Castaldo et al., 2019, 2020; Celarec & Dolšek, 2013). The modeling uncertainties could have an essential role in seismic performance assessment, mainly if the near structural collapse is evaluated. Neglecting these uncertainties could lead to unsafe design. Since one of the aims of this study is to show only one three-dimensional application example, considering the modeling uncertainties is out of the scope of this research.

The two horizontal components of the Newhall record, the Petrolia record, and the Takarazuka record were applied to obtain the dynamic response. The records characteristics are presented in Table 3-1. Two different isolation systems were considered: (i) an isolation system formed by six identical DCFP bearings and, (ii) an isolation system formed by six identical LIR-DCFP bearings. The two types of isolators have identical dynamic behavior if an internal impact does not occur. The geometry of both devices is defined by the following geometric characteristics: $R = 155$ cm, $b_{tp} = b_{bp} = 55$ cm, $l_{tp} = l_{bp} = 2$ cm, $H_s = 10$ cm and, $D_s = 30$ cm. The dimensions of the slider of the LIR-DCFP bearing are: $h_{ts} = 7$ cm, $h_{bs} = 3$ cm, $b_{ts} = 22$ cm, $b_{bs} = 28$ cm, $e_{ts} = 4$ cm, $e_{bs} = 1$ cm, $l_{ts} = 2$ cm and, $l_{bs} = 1.5$ cm. All the geometric parameters are defined and indicated in Figure 3-4. The frictional parameters used in the three-dimensional analysis are the same used in Section 3.4.

Considering the geometric design parameters of the frictional bearings defined above, the internal impact occurs if the lateral displacement of the top plate exceeds 30 cm and the total capacity of the high friction interface is 3 cm. The lateral displacement capacity of $C_t = 30$ cm and the effective radius of $R_{eff} = 300$ cm were selected to produce the internal impact when the structure is subjected to the Newhall and Petrolia seismic records without scaling. To produce the internal impact, the Takarazuka record must be scaled by a factor of 1.10. The friction coefficient at large velocities of sliding of $\mu_{max} = 0.07$ was selected to avoid the relative displacement in the high friction interface before the internal impact. For the described geometry of the isolators, higher values of the friction coefficient μ_{max} could affect the performance of the devices. The friction coefficient in the high friction interface was taken as $\mu_s = 0.15$ because higher friction coefficient μ_s may affect the effectiveness of the isolation system, increasing the inter-story drifts and absolute acceleration during the internal impact.

The base displacement of the two isolation systems is compared in Figure 3-16 when the structure is subjected to the Newhall record. The base displacements measured at the centroid of the base in the x-direction and in the y-direction are shown in Figure 3-16(a) and Figure 3-16(b), respectively. The trajectory of the centroid of the top plate of the isolator #1 is plotted in Figure 3-16(c) and Figure 3-16(d), for the isolation system formed by DCFP bearings and the isolation system formed by LIR-DCFP bearings, respectively. Note that the internal impact occurs mainly in the global x-direction, explaining why the base displacement in the y-direction is similar in both cases. The impact between the sliders and the restraining rims is produced at time $t = 4.24$ seconds.

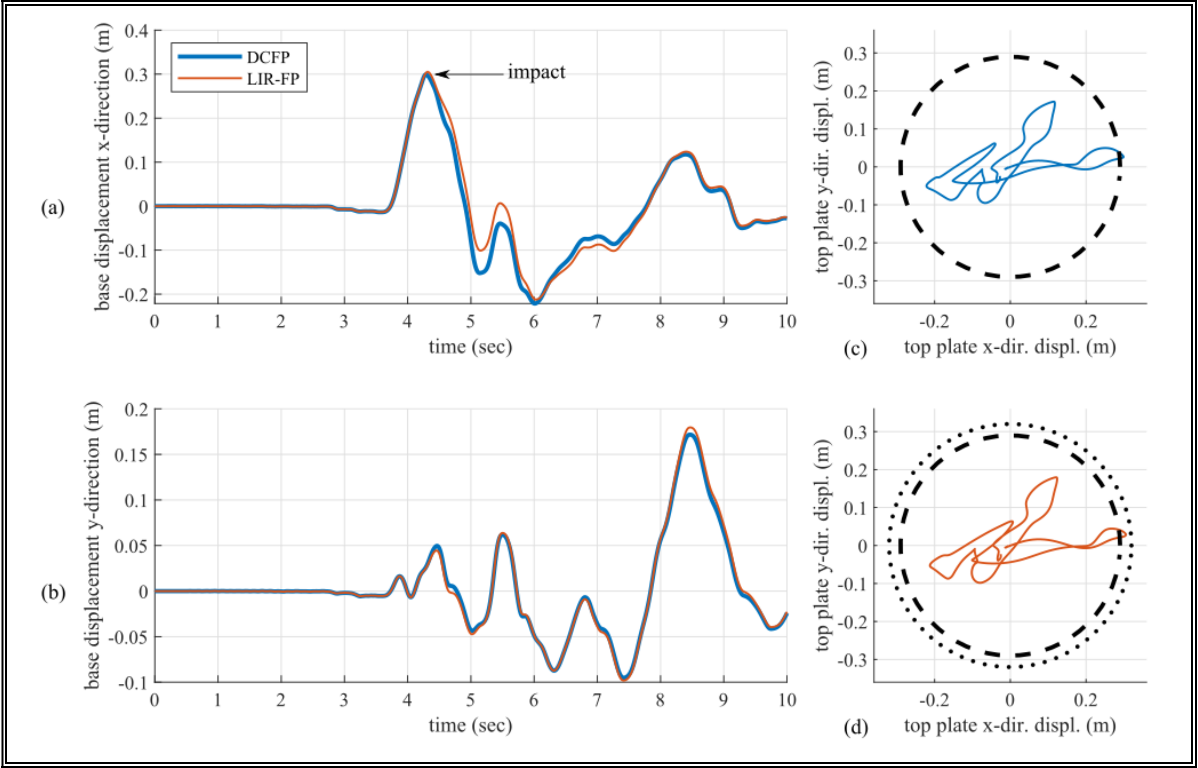

Figure 3-16: Comparison between the two studied isolation systems subjected to the Newhall record: base displacement. (a) Base displacement in x-direction. (b) Base displacement in y-direction. (c) Trajectory of the top plate of the DCFP bearing, isolator #1. (d) Trajectory of the top plate of the LIR-DCFP bearing, isolator #1.

The comparison between the developed forces in the two isolation systems is shown in Figure 3-17. The lateral force in the x-direction transmitted by isolator #1 is shown in Figure 3-17(a). While the maximum load in the DCFP bearing reaches 276 kN, the developed load when the internal impact occurs is 85 kN in the LIR-DCFP bearing. A reduction in the maximum lateral force in the x-direction is produced in the isolator #2 as well, being 432 kN for the DCFP bearing and only 321 kN for the LIR-DCFP bearing. The base shear in the x-direction is presented in Figure 3-17(e). A 42% reduction in base shear is achieved using an isolation system consisting of LIR-DCFP devices. In both cases, the forces transmitted by the isolator #1 and isolator #2 are similar in the y-direction (see Figures 3-17(b) and

317(d)). The maximum forces transmitted by the isolators, for both isolation systems, are summarized in Table 3-8.

Table 3-8: Maximum forces transmitted by the isolators during the impact and residual displacements at time $t = 10$ seconds.

Seismic record	Isolator	LIR-DCFP L.F. x-dir. (kN)	DCFP L.F. x-dir. (kN)	LIR-DCFP L.F. y-dir. (kN)	DCFP L.F. y-dir. (kN)	LIR-DCFP V.F. (kN)	DCFP V.F. (kN)	LIR-DCFP H.F.I.R.D. x-dir. (cm)	LIR-DCFP H.F.I.R.D. y-dir. (cm)	LIR-DCFP T.P.R.D. x-dir. (cm)	LIR-DCFP T.P.R.D. y-dir. (cm)
GM 1	#1	85	276	31	39	351	487	1.64	0.47	2.55	2.27
	#2	321	432	105	98	1290	1466	1.15	0.32	2.55	2.33
	#3	185	356	60	63	728	992	1.44	0.39	2.55	2.38
	#4	122	277	28	32	491	542	1.62	0.48	2.49	2.27
	#5	357	435	107	101	1501	1539	1.11	0.32	2.49	2.33
	#6	210	359	62	67	866	1078	1.39	0.39	2.49	2.38
GM 2	#1	112	180	238	572	806	1624	1.29	2.94	0.24	0.67
	#2	156	211	302	613	1638	2465	1.53	2.89	0.24	0.65
	#3	76	178	198	548	872	1988	1.27	2.85	0.24	0.64
	#4	191	257	347	645	1209	2869	1.52	2.69	0.25	0.67
	#5	259	306	466	692	1899	3014	1.65	2.75	0.25	0.66
	#6	150	228	289	606	777	1472	1.47	2.76	0.25	0.64
GM 3	#1	95	278	90	290	733	1142	1.14	0.33	0.06	1,29
	#2	303	420	196	290	1606	2003	0.58	0.17	0.06	1.27
	#3	178	368	106	272	910	1412	1.05	0.31	0.06	1.25
	#4	78	254	49	300	774	1535	1.32	0.39	0.04	1.29
	#5	262	352	156	276	1527	1900	0.82	0.24	0.04	1.27
	#6	145	295	90	255	763	833	1.27	0.38	0.04	1.25

L.F.: Lateral force
V.F.: Vertical force
H.F.I.R.D.: High friction interface residual displacement
T.P.R.D.: Top plate residual displacement

The inter-story drifts of the superstructure isolated by the two isolation systems are shown in Figure 3-18. As presented in Figures 3-18(a), 3-18(b) and 3-18(c), the maximum drifts of all stories overcome the 2‰ if DCFP bearings form the isolation system. On the other hand, if the isolation system consists of LIR-DCFP bearings, the maximum first story drift is only 1.5‰. The maximum drifts in the x-direction and in the y-direction, for each story and for both isolation systems, are presented in Table 3-9.

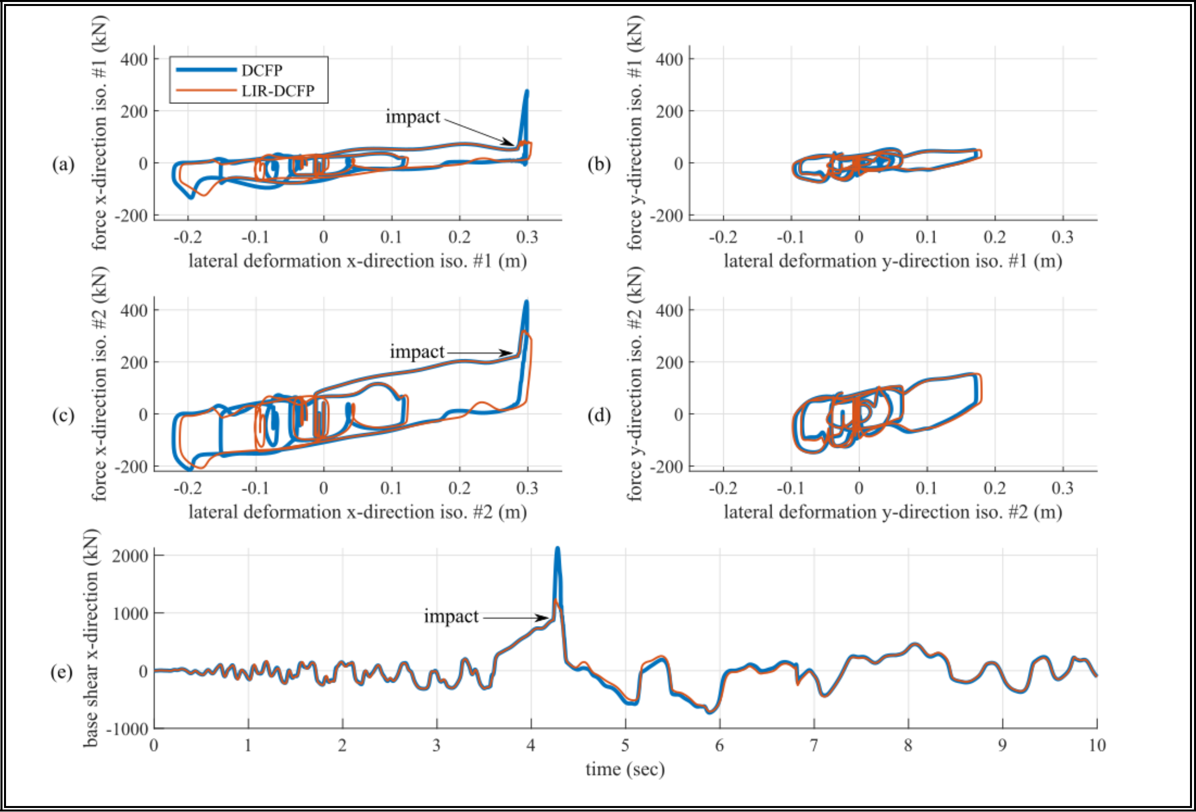

Figure 3-17: Comparison between the two studied isolation systems subjected to the Newhall record: force response. (a) Force displacement loops in x-direction, isolator #1. (b) Force displacement loops in y-direction, isolator #1. (c) Force displacement loops in x-direction, isolator #2. (d) Force displacement loops in y-direction, isolator #2. (e) Base shear in x-direction.

Table 3-9: Maximum inter-story drifts (Results are expressed in ‰)

Seismic record	Isolation system formed by	First story x-dir.	First story y-dir.	Second story x-dir.	Second story y-dir.	Third story x-dir.	Third story y-dir.
GM 1	LIR-DCFP	1.483	1.093	1.291	1.282	0.948	1.090
	DCFP	2.550	1.092	2.432	1.281	2.228	1.088
GM 2	LIR-DCFP	1.250	2.724	1.074	2.413	0.812	1.909
	DCFP	1.694	5.034	1.860	5.363	1.741	5.469
GM 3	LIR-DCFP	1.422	1.214	1.220	1.107	0.818	0.777
	DCFP	2.660	2.084	2.754	2.444	2.161	2.145

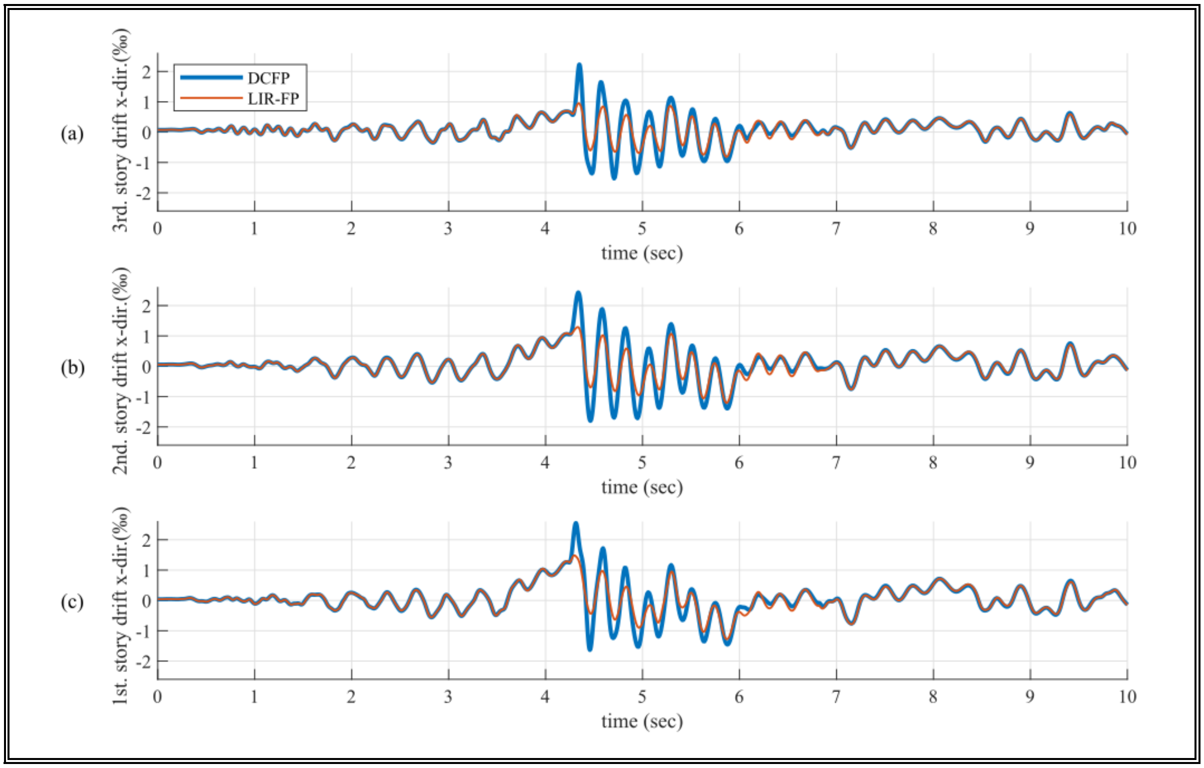

Figure 3-18: Comparison between the two studied isolation systems subjected to the Newhall record: drift response. (a) Third story. (b) Second story. (c) First story.

A comparison of the absolute acceleration response in the x-direction is presented in Figure 3-19. A reduction from 0.86g to a 0.39g in the maximum absolute acceleration of the base is reached if LIR-DCFP isolators are used. A higher reduction is achieved in the maximum absolute acceleration of the roof, from 1.00g to a 0.33g, using the proposed frictional isolator. The maximum absolute acceleration response is presented in Table 3-10.

Table 3-10: Maximum absolute acceleration (Results are expressed in g)

Seismic record	Isolation system formed by	Base x-dir.	Base y-dir.	First story x-dir.	First story y-dir.	Second story x-dir.	Second story y-dir.	Roof x-dir.	Roof y-dir.
GM 1	LIR-DCFP	0.39	0.34	0.31	0.17	0.30	0.21	0.33	0.38
	DCFP	0.86	0.47	0.64	0.20	0.65	0.21	1.00	0.39
GM 2	LIR-DCFP	0.31	0.70	0.25	0.39	0.30	0.53	0.39	0.69
	DCFP	0.60	2.05	0.60	1.23	0.69	1.22	0.63	1.95
GM 3	LIR-DCFP	0.23	0.36	0.22	0.18	0.27	0.15	0.27	0.23
	DCFP	0.63	0.79	0.51	0.53	0.54	0.44	0.76	0.68

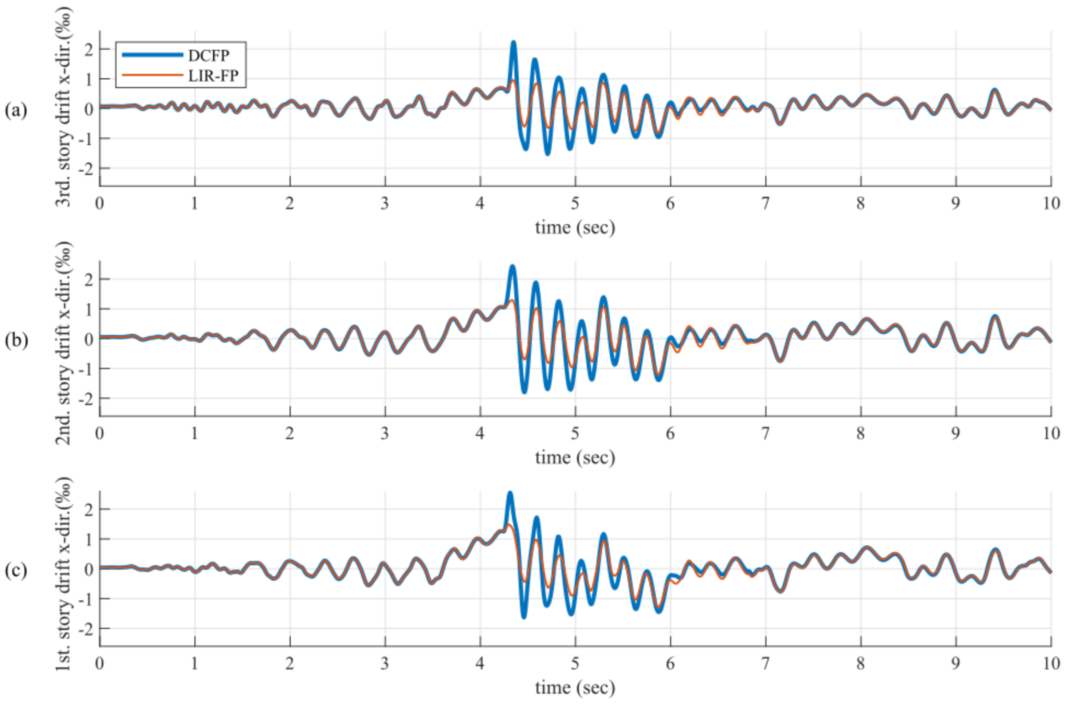

Figure 3-19: Comparison between the two studied isolation systems subjected to the Newhall record: absolute acceleration response. (a) Roof. (b) Base.

The magnitudes of the relative displacement generated at the high friction interface are plotted in Figure 3-20(a) and Figure 3-20(b), for the x-direction and the y-direction, respectively. The vertical loads transmitted by the devices during impact are shown in Figure 3-20(c). The sliding between the top slider and the bottom slider does not occur at the exact same time in all the isolators. This phenomenon is expected because sliding begins if the maximum friction force that the contact can transmit is exceeded. This maximum friction force is proportional to the vertical load that the bearing supports. Since the overturning moment decreases the vertical load on isolator #1 and isolator #4 when the impact occurs, the internal sliding of the inner slider is produced first in these two devices. Then, the relative displacement in the high friction interface is generated in isolators #3 and #6. Finally, the relative displacement between the top slider and the bottom slider is produced in isolators

#2 and #5. These two last bearings are transmitting the largest vertical loads during impact. Hence, the lower the vertical load on the isolator, the sooner the internal sliding in the inner slider will be produced, and larger residual displacement will be reached. Note that the relative displacement in the x-direction is approximately three times longer than in the y-direction. Although residual displacements are generated in the isolators at the end of the ground motion, these are small compared to the effective radius of the isolators (see Table 3-8). It is important to mention that the residual displacements may affect the performance of the isolator in the next ground motion. For example, after the application of the Newhall record a maximum vectorial relative displacement of 1.7 cm is produced in the isolator #1. If another high magnitude ground motion produces an internal impact in the same direction, a lateral capacity of only 1.3 cm is available, less than the half of the original lateral displacement capacity of the high friction interface. For this reason, is important the check the status of the isolation system after the occurrence of a strong earthquake and do regular maintenance of the frictional bearings. Additionally, in Table 3-8, the residual displacement at time $t = 10$ seconds between the top plate and the bottom plate is presented for the six isolators. Note that, although the residual displacement values at the high friction interface differ between different bearings, the total residual displacement displacements of the isolators are almost the same.

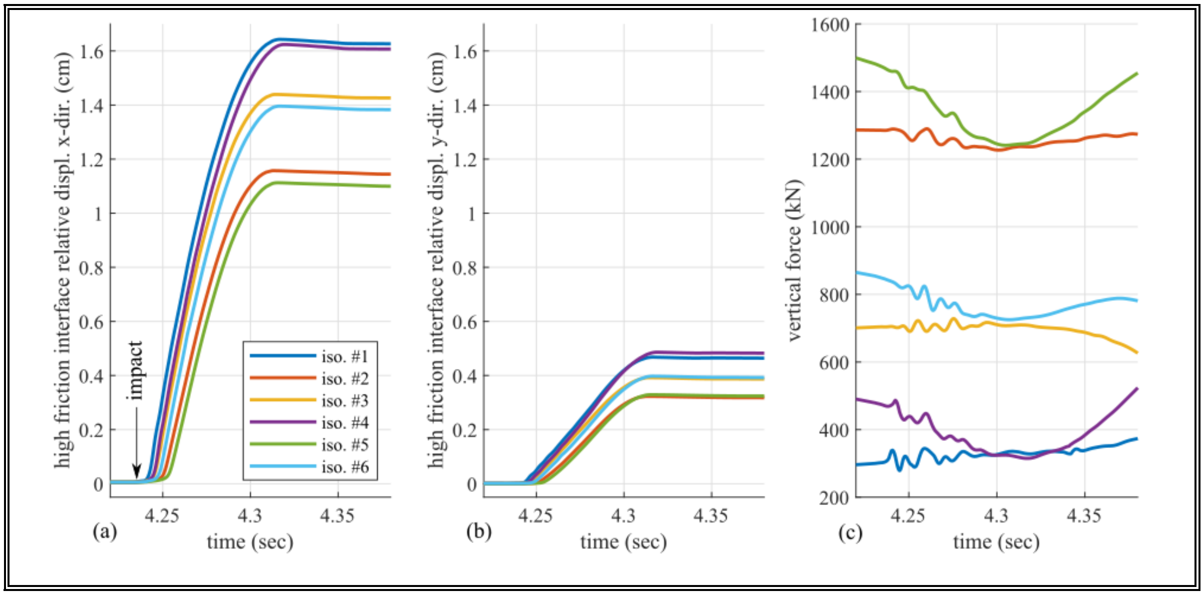

Figure 3-20: (a) Relative displacement at the high friction interface in the x-direction during impact. (b) Relative displacement at the high friction interface in the y-direction during impact. (c) Vertical load transmitted by the LIR-DCFP bearings during impact.

The displacement response of the base subjected to the two horizontal components of the Petrolia ground motion is shown in Figure 3-21. The displacement of the centroid of the base is plotted in Figures 3-21(a) and 3-21(b). The trajectory of the top slider of the DCFP isolator #1 is shown in Figure 3-21(c). In this case the internal impact occurs mainly in the y-direction at time $t = 3.2$ seconds. In Figure 3-21(d), the trajectory of the top slider of the LIR-FP bearing is illustrated. Note that, the Petrolia record produces an important relative displacement between the top slider and the bottom slider. In fact, the capacity of displacement of the high friction interface is overcome (the trajectory of the top plate crosses the dotted line in Figure 3-21(d)).

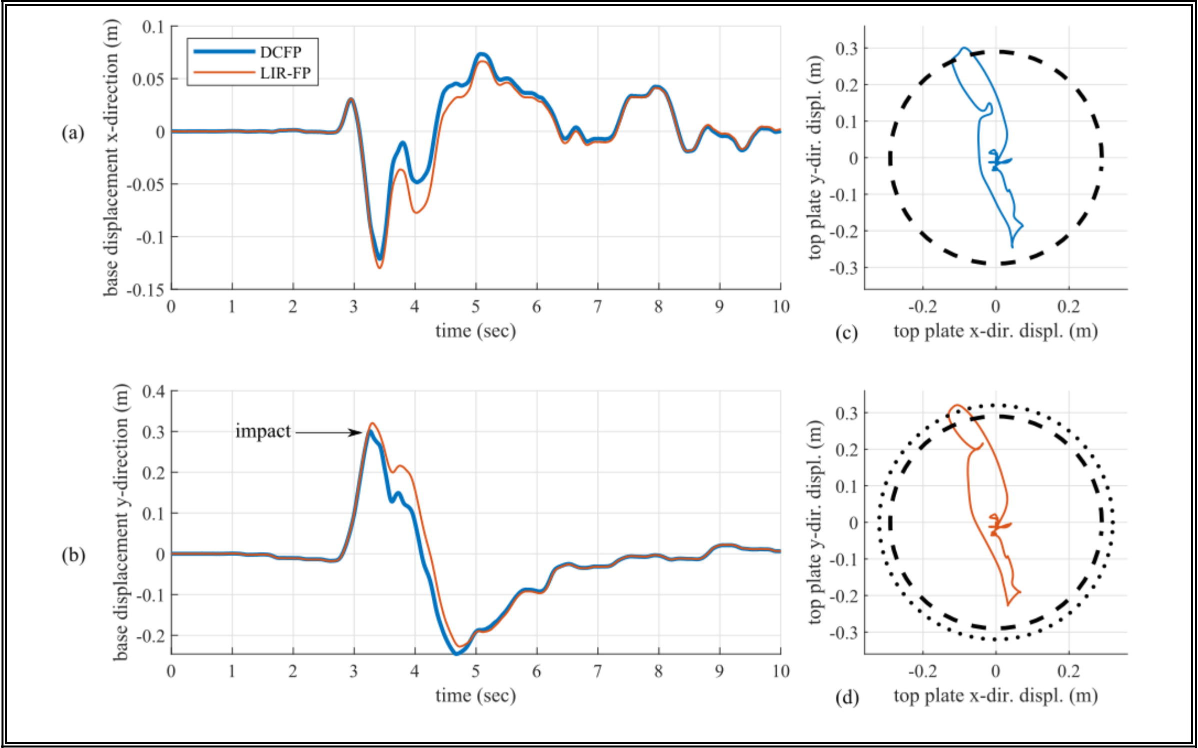

Figure 3-21: Comparison between the two studied isolation systems subjected to the Petrolia record: base displacement. (a) Base displacement in x-direction. (b) Base displacement in y-direction. (c) Trajectory of the top plate of the DCFP bearing, isolator #1. (d) Trajectory of the top plate of the LIR-DCFP bearing, isolator #1.

The force response of the isolation system is shown in Figure 3-22. The force displacement loops in the x and y-directions of the isolators #1 and #2 are presented in Figures 3-22(a), 3-22(b), 3-22(c), and 3-22(d). An important reduction in the forces transmitted by the devices is achieved by using LIR-FP bearings. The maximum force in the y- direction of the isolator #1 is reduced from 572 kN to 238 kN. The reduction for the isolator #2 is from 613 kN to 302 kN. In Figure 3-22(e), the base shear in the y-direction is plotted. Note that, for the case of the isolation system formed by LIR-DCFP bearings two internal impacts are produced. The second impact is produced between the top slider and the bottom slider. Although the capacity of the high friction interface is exceeded, the maximum response in terms of base shear is only the 46% of the response obtained using DCFP bearings.

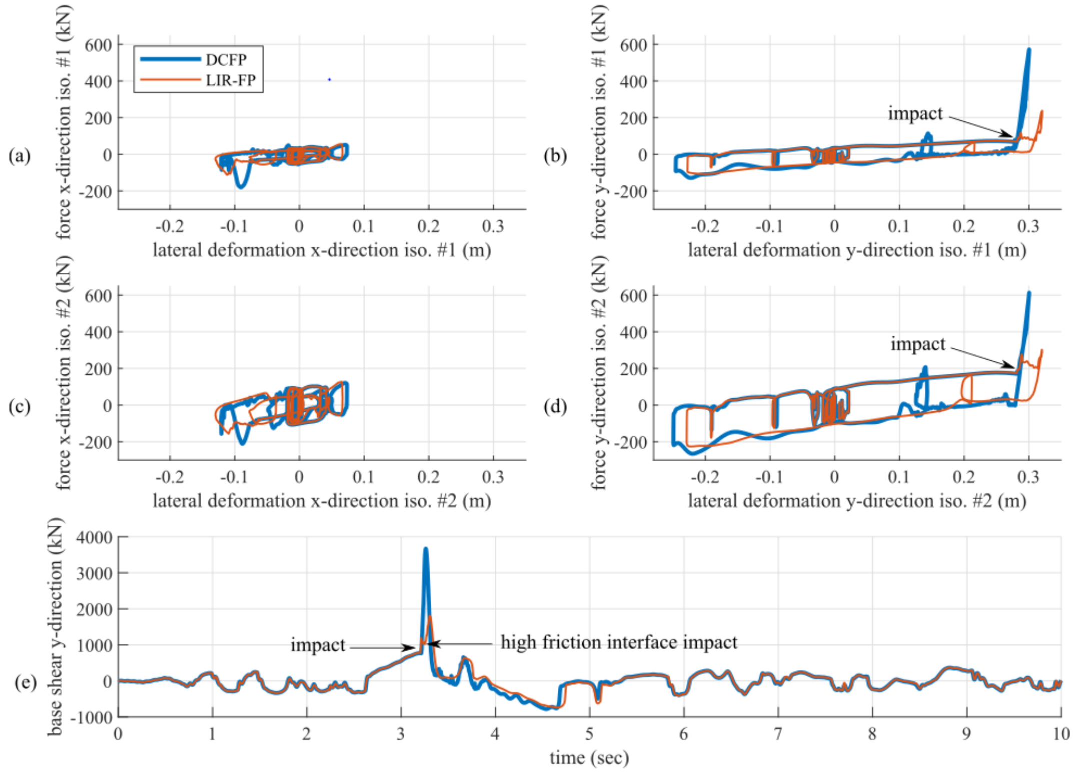

Figure 3-22: Comparison between the two studied isolation systems subjected to the Petrolia record: force response. (a) Force displacement loops in x-direction, isolator #1. (b) Force displacement loops in y-direction, isolator #1. (c) Force displacement loops in x-direction, isolator #2. (d) Force displacement loops in y-direction, isolator #2. (e) Base shear in y-direction.

The maximum absolute acceleration in the y-direction is reduced by using the proposed isolation device. The maximum acceleration in the roof decrease form 1.95g to 0.69g if the isolation system is formed by LIR-FP bearings (see Figure 3-23(a)). The reduction in the base maximum absolute acceleration is from 2.05g to 0.60g (see Figure 3-23(b)).

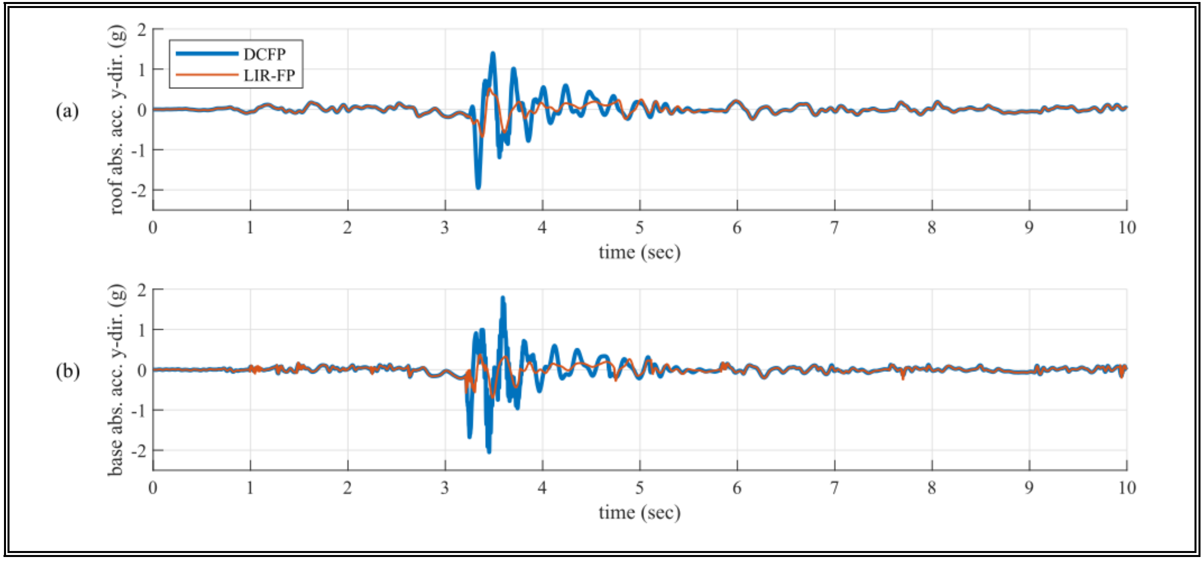

Figure 3-23: Comparison between the two studied isolation systems subjected to the Petrolia record: absolute acceleration response. (a) Roof. (b) Base.

The base displacement response of the structure subjected to the Takarazuka record in the x-direction and y-direction is presented in Figures 3-24(a) and 3-24(b), respectively. The trajectory of the top plate of the DCFP isolator #1 is shown in Figure 3-24(c). In this case, two impacts occur, the first one at time $t = 6.49$ seconds and the second one at time $t = 7.62$ seconds. The trajectory of the centroid of the top plate of the LIR-DCFP isolator #1 is plotted in Figure 3-24(d). Note that, only one impact is produced. The energy dissipated in the first impact avoid the second impact. The amplitude of the displacement response of the isolation system is lower in both horizontal directions after $t = 6.49$ seconds using LIR-DCFP bearings.

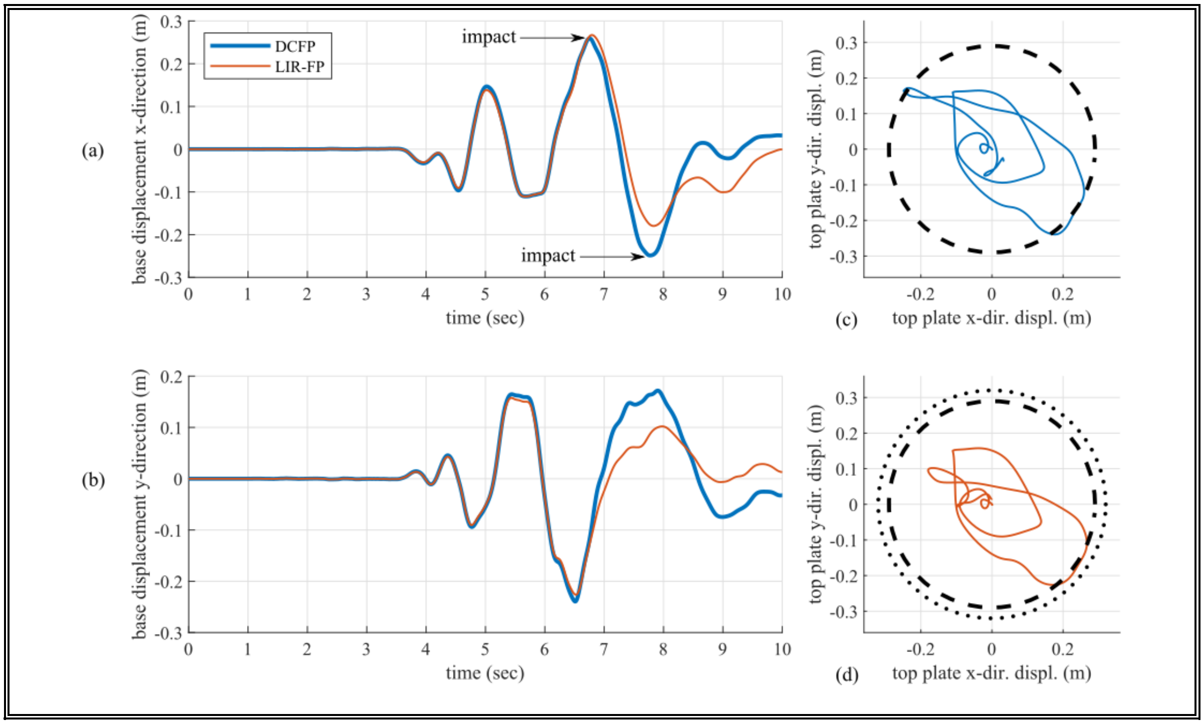

Figure 3-24: Comparison between the two studied isolation systems subjected to the Takarazuka record: base displacement. (a) Base displacement in x-direction. (b) Base displacement in y-direction. (c) Trajectory of the top plate of the DCFP bearing, isolator #1. (d) Trajectory of the top plate of the LIR-DCFP bearing, isolator #1.

The base shear in the x-direction and in the y-direction is shown in Figure 3-25(a) and Figure 3-25(b), respectively. An important reduction in the base shear is achieved in both horizontal directions by using isolators with enhanced sliders. The base shear is reduced from 1,839 kN to 1,015 kN in the x-direction. In the y-direction the base shear is reduced from 1,495 kN to 606 kN. If the structure is subjected to the Takarazuka record, using LIR-DCFP bearing allow to reduce also to inter story drift in both horizontal directions. The third story drift in the x and y-directions is plotted in Figures 3-26(a) and 3-26(b), respectively. In both horizontal directions, the maximum inter story drift overcome the 2‰ if the isolation system is formed by DCFP bearing. Using LIR-DCFP bearing limit these maximum values to less than 1‰.

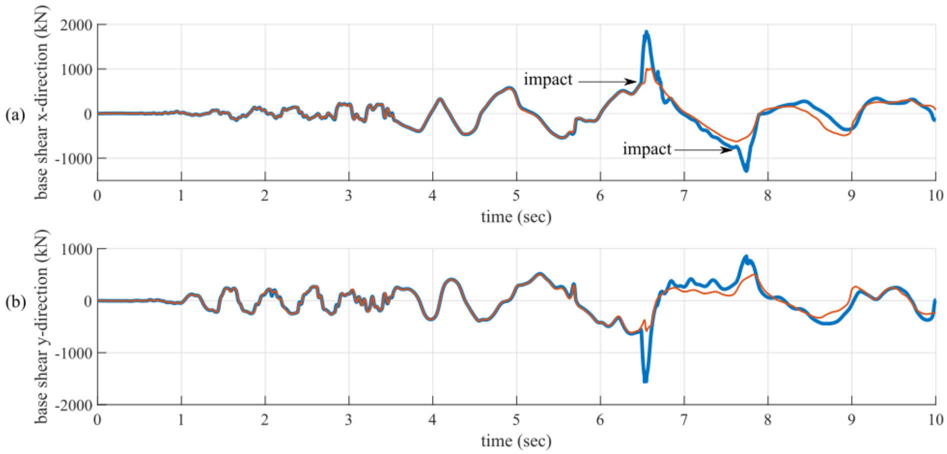

Figure 3-25: Comparison between the two studied isolation systems subjected to the Petrolia record: force response. (a) Base shear in x-direction. (b) Base shear in y-direction.

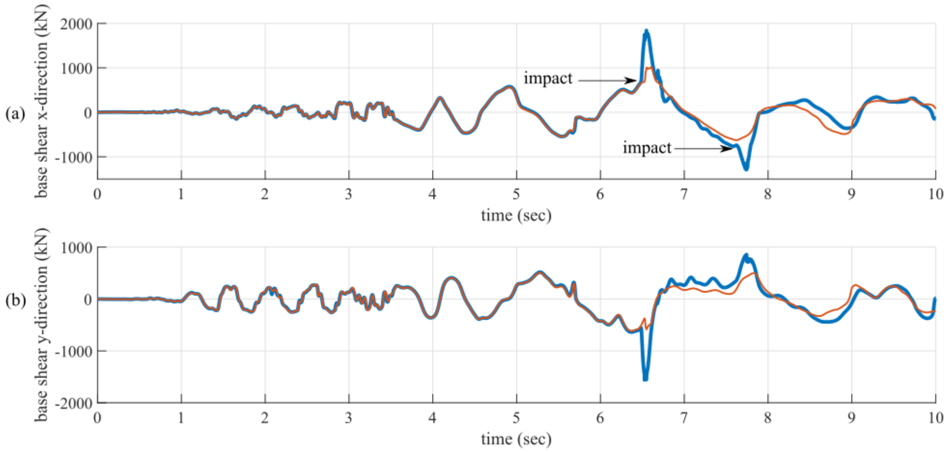

Figure 3-26: Comparison between the two studied isolation systems subjected to the Newhall record: drift response. (a) Third story x-direction. (b) Third story y-direction.

The design advantages of using LIR-FP bearing are patent when the structure is subjected to extreme seismic inputs. In the unlikely scenario of the occurrence of a higher than expected ground motion that exceeds the lateral displacement capacity of the isolation system, the bearing will show a better seismic performance, avoiding its damage. Furthermore, if extreme inputs are considered in the structural design, using of the suggested device will lead to a lower inter-story and absolute acceleration demands.

3.6 Conclusions

Frictional devices are commonly used as an alternative to achieve seismic isolation. Under extreme seismic inputs, the impact between the inner slider and the restraining rims of the plates has been indicated as one of the most important causes of the failure of the bearing. This research study a new frictional isolator called Lateral Impact Resilient double concave Friction Pendulum (LIR-FP) bearing. The proposed device has an improved inner slider that presents better lateral impact behavior. The slider consists of two bodies that generate a plane high friction interface. During a strong internal impact, a relative displacement in the high friction interface is produced, dissipating a large amount of energy.

A three-dimension formulation of the LIR-FP bearing that allows modeling the frictional device in dynamics analyzes is presented. Each part of the isolator is considered as a rigid body with six degrees-of-freedom. This formulation allows essential modeling features such as uplift, lateral impact behavior, large displacement, $P - \Delta$ effects, kinematic constraints, among other vital phenomena.

A parametric analysis was performed to understand the importance of the geometry of the inner slider. The slenderness of the slider, the size of the internal gap, and the relative highness of the high friction interface were studied. The analyzed cases present similar global results. The maximum spatial responses (lateral displacement, vertical displacement, and slider rotation) are essentially the same for all the different geometries. Also, the forces transmitted by the bearing to the superstructure are similar in all cases. Despite obtaining a similar global response, there are differences in the internal behavior of the isolator. The slenderness of the inner slider affects the normal force distributions in the contacts between the slider and the concave plates. The slenderer the slider, the greater the variation in normal forces during impact. The size of the internal gap mainly affects the distribution of normal forces in the high friction interface. The larger the gap, the more variation in the distribution of the normal forces. The relative highness where the internal interface is located does not have an important role in the internal dynamics.

Comparative three-dimensional non-linear time-history analyses were carried out to evaluate the benefits of using LIR-DCFP bearings. A symmetric base-isolated structure model was subjected to three different seismic inputs. For all the considered cases, a better performance is reached using the proposed device, if the dynamic response is compared with an equivalent isolation system formed by double concave Friction Pendulum bearings. If the internal impact increases the base shear in the x-direction, an average reduction of 44% was reached using LIR-DCFP bearing. The average reduction in the shear base, for the cases that presented high maximum values of shear base in the y-direction, was 57%. Considering the three used ground motions, an average reduction of 48% in the maximum inter story drift in the x-direction and in the y-direction was reached. An average reduction in the maximum absolute acceleration in the x-direction of 56% was reached using the proposed frictional isolator. The reduction in y-direction was of 58%.

This purely numerical investigation is the first step to understand the operation of the LIR-DCFP bearing. Experimental tests must be conducted to continue advancing on its application. This path is proposed as future work.

3.7 Acknowledgements

This research has been funded by the National Agency for Research and Development (ANID) through the ANID-PCHA/Doctorado Nacional/2018-21180434 and the FONDECYT project Nº1201841, the authors are grateful for the support. The authors also appreciate the comments received from Paolo Castaldo, Federico Vilca and Diego Quizanga.

4. SEISMIC RELIABILITY OF STRUCTURES EQUIPPED WITH LIR-DCFP BEARINGS IN TERMS OF SUPERSTRUCTURE DUCTILITY AND ISOLATOR DISPLACEMENT

4.1 Introduction

Seismic isolation represents a very effective technique for protecting buildings and infrastructures. The most used devices to achieve seismic isolation are the elastomeric (Kelly, 1993) and Friction Pendulum System (FPS) (Zayas et al., 1990) bearings. Frictional isolators typically consist of one or more sliding concave plates with single or multiple inner sliders, depending on the specific configuration of the device. These frictional devices have shown excellent seismic behavior under high magnitude ground motions (M. Constantinou et al., 2007; Fenz & Constantinou, 2006, 2008a, 2008b; Mokha et al., 1990). Among frictional isolators, two examples of devices, commonly used with passive adaptive behavior, are the Double Concave Friction Pendulum (DCFP) (Fenz & Constantinou, 2006) and Triple Concave Frictional Pendulum (TCFP) bearings (Fenz & Constantinou, 2008b, 2008c). In the following comparisons, DCFP bearings are considered.

Under extreme high magnitude earthquakes, excessive displacements in the isolation devices may occur (Hall et al., 1995b; Jangid & Kelly, 2001a; Mazza, 2018; Mazza & Vulcano, 2012). If the structure is seismically isolated using frictional devices, large base displacements could cause an internal impact between the inner slider and the restraining rims of the sliding surfaces. The internal impact has been indicated as one of the most important causes to the failure of DCFP and TCFP bearings (Bao et al., 2017; Becker et al., 2017). Additionally, the internal lateral impact or the impact between the base of a seismically isolated building against moat walls produces a high increment in the ductility demand of the superstructure (Bao et al., 2018; Bao & Becker, 2018a, 2018c; Komodromos, 2008; Mavronicola et al., 2017; Polycarpou & Komodromos, 2010). Recently, a novel device has been suggested to overcome those problems: the Lateral Impact Resilient Double Concave Friction Pendulum (LIR-DCFP) bearing (G. Auad & Almazán, 2021). The advantage of using a LIR-DCFP bearing over a DCFP device with the same size for both the plates and slider is the improved impact lateral behavior. The new device has an enhanced inner slider with an internal gap and is capable of resisting the internal impact and reducing the inter-story drift demand on the superstructure. The inner slider of the novel isolator consists of two bodies: the top slider and the bottom slider. These two pieces are in contact generating a plane high-friction interface. This interface is activated if the internal impact between the inner slider and the restraining rims occurs. An additional large amount of energy is dissipated if the sliding is produced in the high-friction interface. The concept of the high-friction interface is also different from the sliding regime “V” (Fenz & Constantinou, 2008b, 2008c) of the TCFP bearing. This regime “V” is characterized by a stiff pendular force and a low friction force, opposed to the impact lateral behavior of the LIR-DCFP bearing that dissipates an additional amount of energy and limits the impact magnitude. Auad and Almazán (G. Auad & Almazán, 2021) analyzed the response of one three-dimensional structure isolated with LIR-DCFP devices, subjected to three different ground motions. Further deterministic and probabilistic analyses have to be conducted considering different properties in the isolation system and superstructure.

Seismic reliability-based design (SRBD) analyses of equivalent two-degrees-of-freedom (dof) models of isolated structures equipped with FPS bearings may be found in (P. Castaldo & Ripani, 2016; Paolo Castaldo et al., 2018; Paolo Castaldo, Amendola, et al., 2017; Paolo Castaldo, Palazzo, et al., 2017; Paolo Castaldo & Tubaldi, 2015). Several structural and isolation properties were analyzed in these studies, considering the friction coefficient and the earthquake main characteristics as the relevant random variables. The seismic performance of three-dimensional buildings equipped with FPS bearings has been probabilistically evaluated in Castaldo *et al.* (P. Castaldo et al., 2015) and (P. Castaldo et al., 2016). The effects due to restraining rims in DCFP and TFPC devices in the performance assessment have been investigated by (Bao & Becker, 2018a; Kitayama & Constantinou, 2019a, 2019b). Even if displacement restraint mechanisms are added to isolation devices leading in some cases to a worse performance, base-isolated structures may have lower probabilities to develop damage than non-isolated buildings. According to (Bao & Becker, 2018a; Kitayama & Constantinou, 2019a, 2019b), the last statement is true for superstructures designed using the loads transmitted by the Maximum Considered Earthquake (MCE) or if the design is carried out using the unreduced loads transmitted by the Design Earthquake (DE) (ASCE, 2016).

Considering only DCFP bearings, this research aims to assess the seismic performance of systems equipped with LIR-DCFP bearings having different properties and evaluate their benefits within a comparison with classical DCFP isolators having the same size for both the plates and slider. In this way, it is possible to evaluate the effects of rising the dimension of the internal gap characterizing LIR-DFCP bearings. This paper deals with the seismic reliability of inelastic structures equipped with the above-mentioned frictional bearings. The LIR-DCFP and DCFP isolation systems are represented using a numerical formulation based on rigid body dynamics (G. Auad & Almazán, 2021; Bao & Becker, 2019) capable of considering the internal lateral impact behavior. A random variable was employed to sample the friction coefficient at large sliding velocity as proposed by Mokha *et al*. (Mokha et al., 1990). A 1dof model was defined to represent the lateral flexibility of the superstructure. The uncertainty in the seismic inputs was considered by selecting ten different sets of natural seismic records able to match conditional spectra (Baker & Lee, 2018; T. Lin et al., 2013b, 2013d, 2013a) for increasing return periods at a specific site in California (i.e., Riverside). Incremental dynamic analyses (IDAs) were performed to assess the probabilistic responses related to the superstructure (in terms of ductility (Paolo Castaldo et al., 2018; Paolo Castaldo, Amendola, et al., 2017; Paolo Castaldo, Palazzo, et al., 2017)) and the isolation level (in terms of base displacement (Paolo Castaldo et al., 2018; Paolo Castaldo, Amendola, et al., 2017; Paolo Castaldo, Palazzo, et al., 2017)) through an extensive parametric study for different superstructures properties and isolation system characteristics. Using the IDAs data, the probabilities exceeding appropriate limit state thresholds were computed to construct the seismic fragility curves (Paolo Castaldo et al., 2018; Paolo Castaldo, Amendola, et al., 2017; Paolo Castaldo, Palazzo, et al., 2017). Through the convolution integral between the fragility curves and the seismic hazard curves related to the Riverside site, the exceeding probabilities referred to a lifetime of 50 years were assessed to derive the seismic reliability curves (Paolo Castaldo et al., 2018; Paolo Castaldo, Amendola, et al., 2017; Paolo Castaldo, Palazzo, et al., 2017).

4.2 Description of the LIR-DCFP bearing behavior

In this section, a brief description of the lateral behavior of the LIR-DCFP bearing is presented. A complete description may be found in (G. Auad & Almazán, 2021).

4.2.1 General force-displacement relationship of the LIR-DCFP bearing

The LIR-DCFP seismic isolator consists of two facing plates with spherical sliding surfaces. The sliding surfaces of both plates have the same radius of curvature R and frictional coefficient μ_d. The main feature of the device is its enhanced inner slider that consists of two bodies: the top slider and bottom slider. These two bodies are in contact generating a plane high-friction interface. In fact, this plane interface is constructed with a higher friction coefficient denoted as μ_s. The contact between the two inner sliders generates an internal gap that allows the relative displacement between the top and bottom sliders, adding supplementary energy dissipation capacity to the isolator. By ensuring a correct design of the isolation system, the high-friction sliding starts only if the impact between the inner sliders and the restraining rim of the plates occurs. The normalized force-displacement relationship of the device is presented in Figure 4-1. The force is normalized by the vertical load W applied on its top plate. The total (horizontal) displacement of the top sliding plate relative to the ground is normalized by the effective radius of the device: $R_{eff} = 2R - h_s$, being h_s the total height of the inner slider (Fenz & Constantinou, 2006). This normalization with respect to the geometry of the isolator and the vertical load applied to the device leads to a normalized pendular force with unitary normalized stiffness. In addition, five different stages of the lateral behavior of the isolator are also shown: (1) the beginning of the sliding between the inner sliders and plates, (2) the impact between the sliders and restraining rims of the plates, (3) the sliding between the top and bottom slider, (4) the impact between the top slider and restraining rim of the bottom slider, and (5) the returning of the bottom slider to its original position. The total lateral force in global coordinates F that the bearing transmits to the superstructure is computed as the sum of three forces: the pendular force F_p, the frictional force F_μ and the impact force F_i. This last force is generated if the relative displacement between the sliders exceeds the size of the internal gap. Between stages (1) and (2), the normalized pendular force increases with a constant slope. The pendular force changes due to the variation of the normal vector that defines the direction of the contact between the spherical surfaces of the plates and the spherical surfaces of the top and bottom sliders. This first sliding generates low friction forces. Between stages (2) and (3), high-friction forces are generated since the sliding is produced in the high-friction interface. During these two stages, the pendular force remains constant because the normal vector, that describes the direction of contact, does not change. During the path between stages (3) and (4), the internal impact force, generated inside the enhanced inner slider, is produced, developing a considerable increment in the total force transmitted by the bearing. The other forces tend to remain constant. Finally, between stages (4) and (5), the returning of the bottom slider is produced, generating a unitary normalized pendular stiffness and low friction forces as the sliding is developed between the spherical surfaces. The collapse mechanisms of frictional isolators have been studied by (Bao et al., 2017; Becker et al., 2017). Under extreme seismic inputs, during the impact between the top and bottom (path between stages (3) and (4)), the yielding of the restraining rims may be observed, leading to damage or even the collapse of the isolator. Another collapse mechanism was also identified, produced by large rotations of the inner slider that lead to bearing instability.

In Appendix B, the results of one experimental test of an LIR-DCFP specimen are presented.

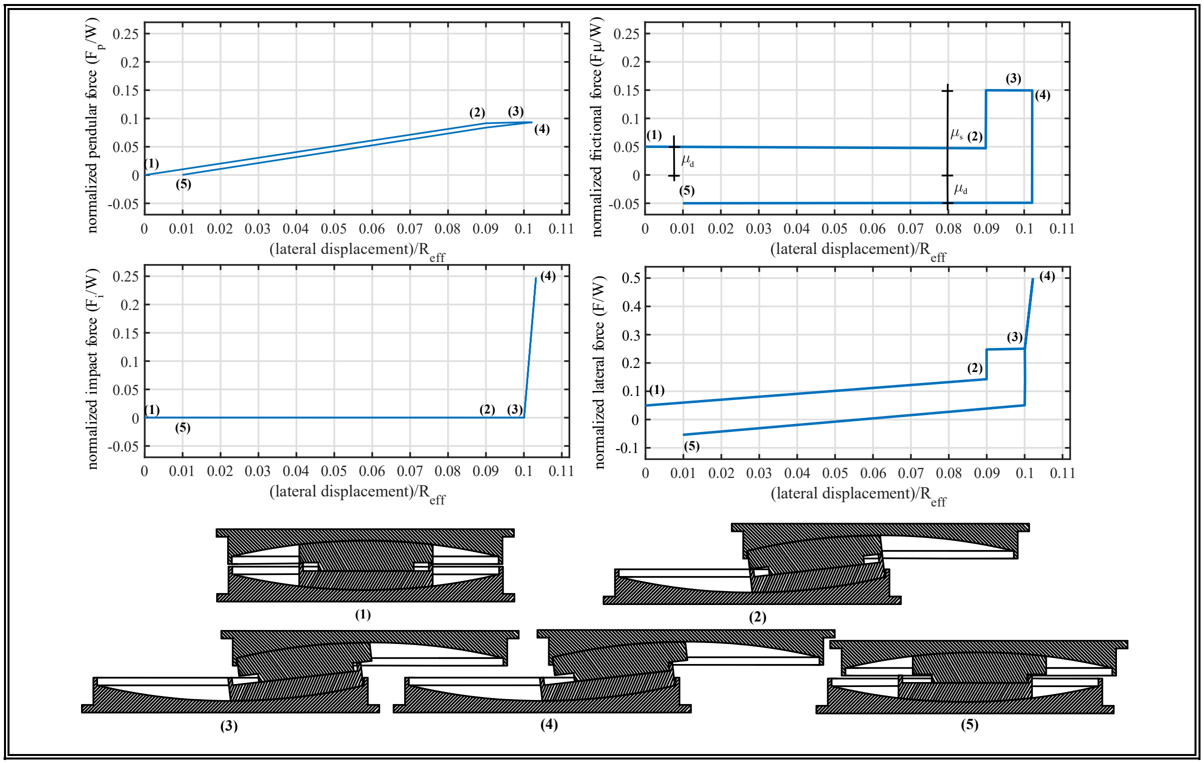

Figure 4-1: General normalized force-displacement relationship for LIR-DCFP bearings (modified from Auad and Almazán (G. Auad & Almazán, 2021)).

4.2.2 Forces developed inside the isolator

The three-dimensional formulation for modeling frictional isolators, proposed by Bao and Becker (Bao & Becker, 2019) and used in the model suggested by Auad and Almazán (G. Auad & Almazán, 2021), is based on rigid body dynamics. The numerical models were implemented in the MATLAB environment (Hunt et al., 2006). It is necessary to define a specific number of sets of contact points to compute the forces that the device transmits to the superstructure. The number of sets of contact points must be equal to the number of contacts between the different bodies that form the device. In detail, four contacts points for each set of contact points have been defined. The same number of contact points has been used in previous studies (G. Auad & Almazán, 2021; Bao & Becker, 2019). On the one hand, three sets of four contact points are needed to model the LIR-DCFP bearing because there are three sliding interactions: (i) top plate - top slider, (ii) top slider - bottom slider, and (iii) bottom slider - bottom plate. On the other hand, only two sets are required to model the DCFP because there are only two sliding interactions: top plate - inner slider, and (ii) inner slider - bottom plate. The spatial representations of the contact points used to model both frictional isolators are shown in Figure 4-2. As shown in Figure 4-2, every contact point has its projection point on another body. For example, the contact point A_1, that is located on the top surface of the inner slider, has its projection point on the spherical sliding surface of the top plate. This projection point is denoted as A_1'.

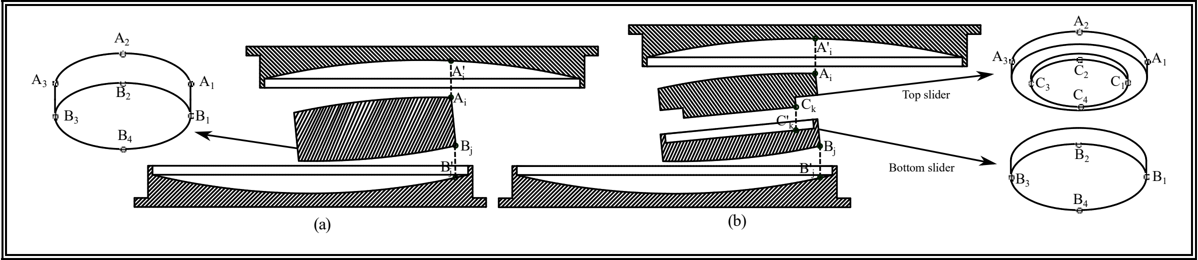

Figure 4-2: Contact points: (a) DCFP bearing; (b) LIR-DCFP bearing (modified from Auad and Almazán (G. Auad & Almazán, 2021)).

By tracking the position $\boldsymbol{r}$ and velocity $\dot{\boldsymbol{r}}$ of each contact point, it is possible to determine the magnitude of the normal force N, the friction force $\boldsymbol{f_{\mu}}$, and the impact force $\boldsymbol{f_{imp}}$ acting on each couple contact - projection points (G. Auad & Almazán, 2021). For example, the magnitude of the normal force N_{A_1} and friction force $\boldsymbol{f}_{\boldsymbol{\mu},\boldsymbol{A}_1}$ generated between points A_1 and A_1' can be computed using the following expressions:

$$N_{A_1} = \left\{\begin{array}{lll} k_{A_1}\left(\boldsymbol{r}_{\boldsymbol{A}_1}(3) - \boldsymbol{r}'_{\boldsymbol{A}_1}(3)\right) + c_{A_1}\left(\dot{\boldsymbol{r}}_{\boldsymbol{A}_1}(3) - \dot{\boldsymbol{r}}'_{\boldsymbol{A}_1}(3)\right) & , & \text{if}\left(\boldsymbol{r}_{\boldsymbol{A}_1}(3) - \boldsymbol{r}'_{\boldsymbol{A}_1}(3)\right) \geq 0 \\ 0 & , & \text{otherwise} \end{array}\right\} \tag{4-1}$$

$$\boldsymbol{f}_{\boldsymbol{\mu},\boldsymbol{A}_1} = -\mu_d N_{A_1} \boldsymbol{z}_{\boldsymbol{A}_1} \tag{4-2}$$

in which k_{A_1} and c_{A_1} are the stiffness and damping coefficient of the interaction between the two points, $\boldsymbol{r}_{\boldsymbol{A}_1}(3)$ and $\boldsymbol{r}'_{\boldsymbol{A}_1}(3)$ are the third component of the vectors that describes the position of points A_1 and A_1', $\dot{\boldsymbol{r}}_{\boldsymbol{A}_1}(3)$ and $\dot{\boldsymbol{r}}'_{\boldsymbol{A}_1}(3)$ are the third component of the vector that describes the velocity of points A_1 and A_1', μ_d is the friction coefficient, and the vector $\boldsymbol{z}_{\boldsymbol{A}_i} = \left[z_{A_{1,x}}, z_{A_{1,y}}\right]^T$ contains the dimensionless hysteretic parameters of the biaxial Bouc-Wen's model (Park et al., 1986). These dimensionless parameters allow to model the friction phenomenon. While the norm of $\boldsymbol{z}_{\boldsymbol{A}_i}$ is equal to one during the sliding phase, values less than one imply sticking phase. The contact force between points A_1 and A_1' can be arranged in a three-dimensional vector in local coordinates as follows:

$$\boldsymbol{f}_{\boldsymbol{cont},\boldsymbol{A}_1} = [\boldsymbol{f}_{\boldsymbol{\mu},\boldsymbol{A}_1}\,;\, N_{A_1}] \tag{4-3}$$

The contact forces must be rotated to the global coordinate system and then projected to the global degrees-of-freedom to obtain, for example, the lateral force in global coordinates transmitted by the isolator to the superstructure described in Section 2.1. In this paper, with the purpose to compute the friction force $\boldsymbol{f}_{\boldsymbol{\mu}}$ developed between contact and projection points located in spherical surfaces, the nonlinear dependence of the friction coefficient μ_d with the sliding velocity $\dot{v}$ is considered using the expression provided by Mokha *et al.* (Mokha et al., 1990) as follows:

$$\mu_d = \mu_{max} - (\mu_{max} - \mu_{min})\exp(-\alpha\dot{v}) \tag{4-4}$$

in which, μ_{max} is the friction coefficient at high sliding velocity, μ_{min} is the friction coefficient at very slow sliding velocity and α is the rate parameter. In this study, the rate parameter has been set equal to 30 sec/m and the ratio between μ_{max} and μ_{min} has been set equal to 2. The friction forces generated in the high-friction interface are computed assuming a constant friction coefficient μ_s. This high-friction coefficient is assumed to be equal to $2\mu_{max}$.

4.3 Equivalent dynamic models for base-isolated structures with DCFP and LIR-DCFP devices

In this study, simplified two-dimensional models are developed to analyze the dynamics response of seismically isolated structures. As the aim of this research is to assess the benefits of using LIR-DCFP bearings, two types of seismic isolators are considered to perform a comparison between DCFP and LIR-DCFP bearings. The isolation system is represented by one two-dimensional isolator using the approaches based on rigid body dynamics (G. Auad & Almazán, 2021; Bao & Becker, 2019), considering three sets of two contact points for LIR-DCFP bearings and two sets of two contact points for DCFP isolators because the two contact points out of plane are not activated for each set. The superstructure is modelled by a 1dof system that exhibits nonlinear behavior in the lateral direction. The two simplified models are shown in Figure 4-3. The model of the LIR-DCFP bearing has 5dof because this device has one additional rigid body with two additional dof (i.e., one translational and one rotational) with respect to the DCFP device. The rotation of the top plate of both isolators is considered constrained. The rotations of the inner sliders can be considered dof to account, for example, the angle at which the frictional force is transmitted. In Figure 4-3, the dynamic parameters of the superstructure have been signaled, being: m_s and m_b the masses of the superstructure and the base, respectively; k_s the linear initial stiffness in the lateral direction; c_s the damping coefficient in the lateral direction (a critical damping ratio of $\xi_s = 0.02$ has been used); and, u_y is the lateral yielding displacement of the superstructure. The mass ratio is defined as $\gamma = m_s/(m_s + m_b)$ (Naeim & Kelly, 1999). The critical damping ratio for the isolation level is assumed zero. If the lateral period of the superstructure T_s is known, it is possible to compute the initial stiffness as $k_s = (2\pi/T_s)^2 m_s$. In this study, a total mass of $(m_s + m_b) = 500$ kN × sec^2/m was used. By setting the mass ratio γ, the superstructure mass can be computed as $m_s = \gamma(m_s + m_b)$.

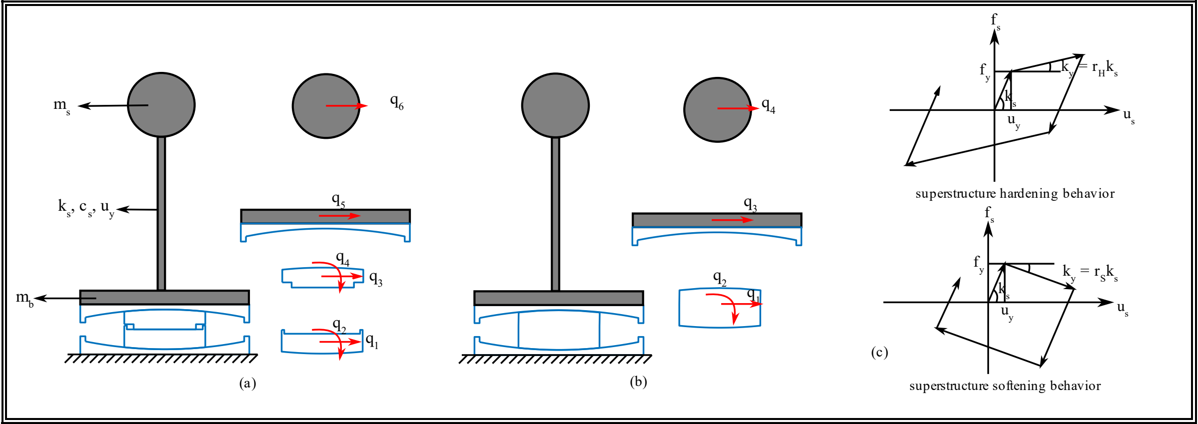

Figure 4-3: Simplified model of an inelastic building isolated with frictional devices: (a) Isolation system composed of LIR-DCFP bearings; (b) Isolation system composed of DCFP bearings; (c) Superstructure behavior. The term q denotes the dof considered.

The nonlinear lateral force of the superstructure is modeled using a Bouc-Wen element (Wen, 1976), as follows:

$$f_s = r_{H|S} k_s u_s + \left(1 - r_{H|S}\right) f_y z_s \tag{4-5}$$

in which, $f_y = k_s u_y$ is the yield force, $r_{H|S}$ is the stiffness ratio (the subscript depends on the post-yield behavior, being r_H for hardening behavior or r_S for softening behavior (Figure 4-3(c))), u_s is the displacement of the superstructure, $\dot{u}_s$ is the rate of lateral displacement and z_s is the hysteretic parameter of the superstructure (Park et al., 1986). Note that, the post-yield stiffness can be computed as $k_y = r_{H|S} k_s$. The hysteretic parameter z_s allows to model the nonlinear behavior of the element. If the absolute value of z_s is less than one, the lateral behavior is represented by the initial stiffness k_s; if the absolute value of z_s is equal to one, the behavior is characterized by the post-yield stiffness.

Solving the differential equations of motion (Chopra, 1995) through the ode23t solver available in the MATLAB environment (Hunt et al., 2006), the time-history responses of a structure isolated by DCPF and LIR-DCFP bearings subjected to the H-E05140 component of the El Centro Array #4 record (Imperial Valley-06 earthquake, 2010) (PEER, 2013) have been evaluated. The results are shown in Figure 4-4 in terms of both u_s and (horizontal) base displacement u_b (including the internal gap displacement for the LIR-DCFP device) to highlight the importance to analyze the impact as well as the advantages deriving from the LIR-DCFP bearings. The following parameters (P. Castaldo & Ripani, 2016; Paolo Castaldo et al., 2018; Paolo Castaldo, Amendola, et al., 2017; Paolo Castaldo, Palazzo, et al., 2017;

Paolo Castaldo & Tubaldi, 2015) were used: superstructure period along lateral direction T_s equal to 0.6 sec, $\gamma = 0.7$, superstructure yielding lateral displacement u_y equal to 2 cm (superstructure yield base shear coefficient equal to 0.1565), $R_{eff} = 2.25$ m (isolated period: $T_b = 2\pi\sqrt{R_{eff}/g} = 3$ sec), $\mu_{max} = 0.07$, $\mu_{min} = 0.035$, $\mu_s = 0.14$, and r_H=0.05. For the both isolators, DCFP and LIR-DCFP bearings, the lateral capacity is defined as the lateral horizontal displacement of the top plate with respect to the bottom plate (or the ground) needed to observe the impact between the inner slider and the restraining rims of the spherical sliding surfaces. For the LIR-DCFP bearing, a lateral capacity of 25 cm was considered with an internal gap of 5 cm. Whereas, two lateral capacities were considered for the DCFP bearings. The first DCFP device has sliding plates of the same size adopted for the LIR-DCFP bearing (i.e., a lateral capacity of 25 cm). The second considered DCFP isolator has a lateral capacity of 30 cm. In Figure 4-5, an example of the geometry of the three isolators is shown: the dimensions of the plates are slightly bigger to allow the lateral capacity due to the rotation of the slider. The results show that the maximum displacement of the superstructure $u_{s,max}$ is reduced from 12 cm to 7.7 cm by using the LIR-DCFP bearings, decreasing the ductility demand $\mu = u_{s,max}/u_y$ from 6 to 3.85. The demanded ductility of the superstructure equipped with LIR-DCFP bearing is lower than the ductility demanded in the building isolated through a larger capacity DCFP device due to the infinite curvature of the internal gap combined with a higher friction coefficient. As shown in the work carried out by Bao and Becker concerning the inelastic response of base-isolated subjected to extreme seismic loads (Bao & Becker, 2018c), if the internal impact is observed, the forces generated in the isolation system tend to have higher magnitudes than the forces developed in the superstructure. Note that the impact triggers the nonlinear behavior of the superstructure. Since the inelastic range of the superstructure is characterized by low stiffness, it is not possible to compensate the transient load of the impact with the inelastic internal force developed in the superstructure. As a result of the described phenomenon, an important rise in the inertial forces is developed in the building (Komodromos, 2008; Polycarpou & Komodromos, 2010).

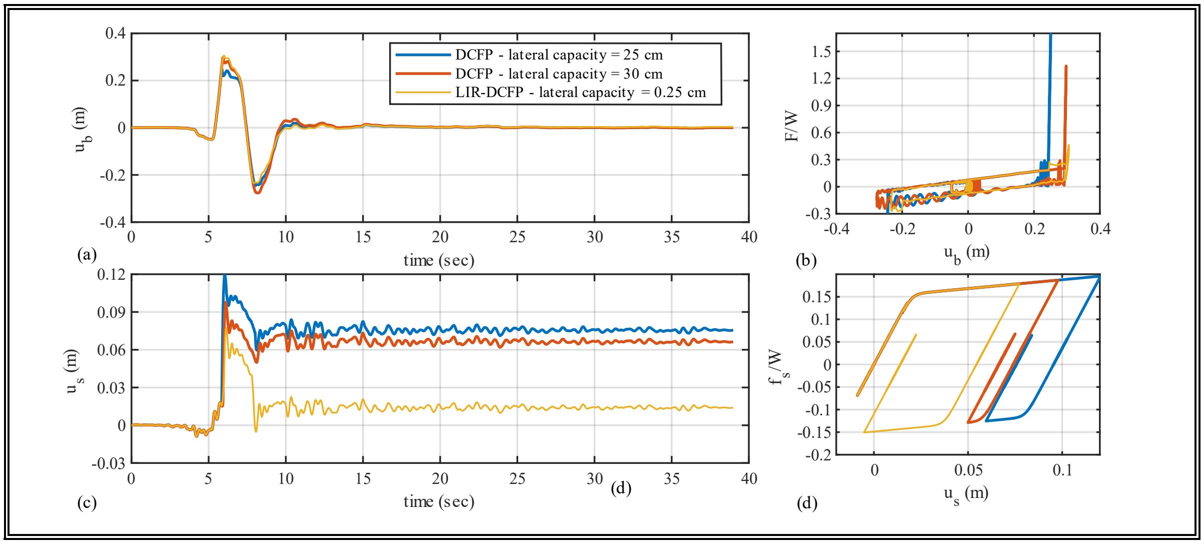

Figure 4-4: Comparative dynamic response of an isolated structure with DCFP bearings or LIR-DCFP bearings: (a) Base displacement; (b) Hysteretic loops of the isolation system; (c) Superstructure displacement; (d) Hysteretic loops of the superstructure.

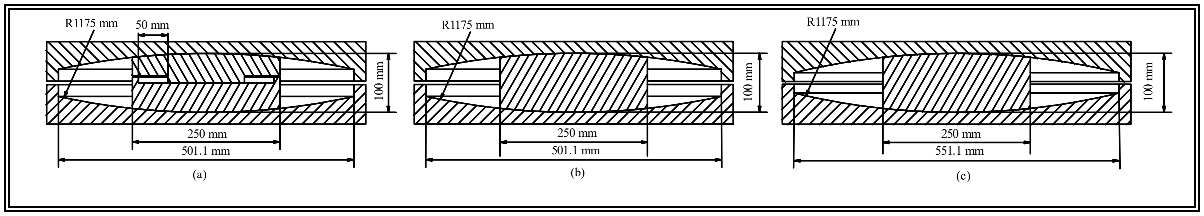

Figure 4-5: Geometry of the compared isolators (a) LIR-DCFP bearing with a lateral capacity of 25 cm and an internal gap of 5 cm; (b) DCFP bearing with a lateral capacity of 25 cm; (c) DCFP bearing with a lateral capacity of 30 cm.

4.4 Uncertainties within the seismic reliability assessment

The friction coefficient and earthquake event characteristics have been selected as the relevant random variables. Other aleatory uncertainties corresponding to the mechanical and geometrical properties of the superstructure and the isolation device are not considered as random variables since they do not produce great effects on the statistical values of the response parameters, especially for high values of the isolation degree $I_d = T_b/T_s$ (Adam et al., 2004; Gupta, 1999; Palazzo, 1991). In these cases, the response is mainly governed by the frictional isolators with their most relevant uncertainty: the friction coefficient.

Experimental data on the frictional isolators, described in Mokha *et al*. (Mokha et al., 1990) and Constantinou *et al.* (M. Constantinou et al., 2007), show the variability of the frictional phenomenon depending on some factors. Referring to the two curved surfaces of the LIR-DCFP bearing, the aleatory uncertainty on the sliding friction coefficient at large velocity (i.e., μ_{max}) has been modelled adopting an appropriate Gaussian probability density function (PDF), truncated on both sides to 3% and 7% with a mean value equal to 5% and a coefficient of variation equal to 0.17, as presented in (P. Castaldo & Alfano, 2020; Paolo Castaldo et al., 2018; Paolo Castaldo, Palazzo, et al., 2017). From this Gaussian PDF, 15 values were sampled using the Latin Hypercube Sampling (LHS) method (McKay et al., 2000; Vořechovský & Novák, 2009). The friction coefficient of the high-friction interface of the LIR-DCFP bearing μ_s has been assumed to be correlated with the maximum value of μ_d (i.e., $\mu_s = 2\mu_{max}$).

An intensity measure (IM) is introduced into the reliability analysis to consider the uncertainties of the seismic input intensity, whereas the uncertainties on the characteristics of the records are taken into account by means of a set of natural ground motions. In this work, the selected IM is the spectral acceleration at the isolated period $S_a(T_b)$. Two isolated periods were considered $T_b = 3$ and $T_b = 5$ sec. The parameter $S_a(T_b)$ is associated with a particular location and soil condition and linked with a specific return period T_r according to the seismic hazard of the specific site. Ten different return periods were selected (43; 144; 289; 475; 949; 1,485; 2,475; 3,899; 7,462; and 10,000 years) to determine ten corresponding values for the IM (i.e., 0.02g, 0.05g, 0.09g, 0.12g, 0.17g, 0.21g, 0.26g, 0.32g, 0.40g and 0.44g for $T_b = 3$ sec; 0.01g, 0.02g, 0.05g, 0.07g, 0.11g, 0.14g, 0.18g, 0.21g, 0.27g and 0.29g for $T_b = 5$ sec; being g the gravity acceleration). The algorithm proposed by Baker and Lee (Baker & Lee, 2018) was employed to perform the ground motion selection. In the following subsection, the details of the procedure are presented.

4.4.1 Ground motion selection matching the Conditional Spectrum

Assuming that the analyzed dynamic systems are located in Riverside, California (latitude/longitude = 33.979/-117.335) with a class C soil ($V_s = 537$ m/sec), it is possible to determine the magnitude M and the distance R of the mean causal earthquake related to a specific return period. These parameters were obtained from de-aggregation of the ground motion hazard using the Unified Hazard Tool (*Unified Hazard Tool*, n.d.). Additionally, it is also possible to determine the value of the IM $= S_a(T_b)$) linked to each return period T_r. The de-aggregation information allows determining a Conditional Mean Spectrum (CMS)

(Baker, 2011) for each considered return period. The used conditional periods are equal to the two considered isolated periods: $T^* = T_b = 3$ sec and $T^* = T_b = 5$ sec. The models of Boore *et al.* (Boore et al., 2014) and of Baker and Jayaram (Baker & Jayaram, 2008) were employed to construct the CMSs (Figure 4-6).

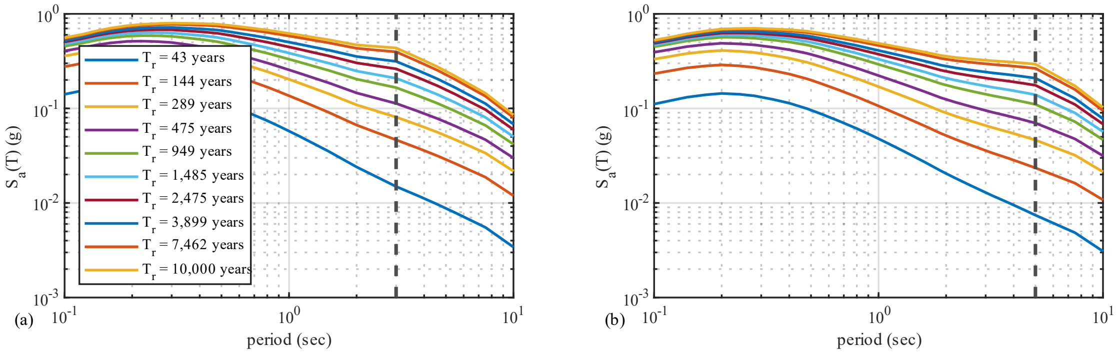

Figure 4-6: Conditional Mean Spectra for different conditioning period: (a) $T^* = 3$ sec; (b) $T^* = 5$ sec.

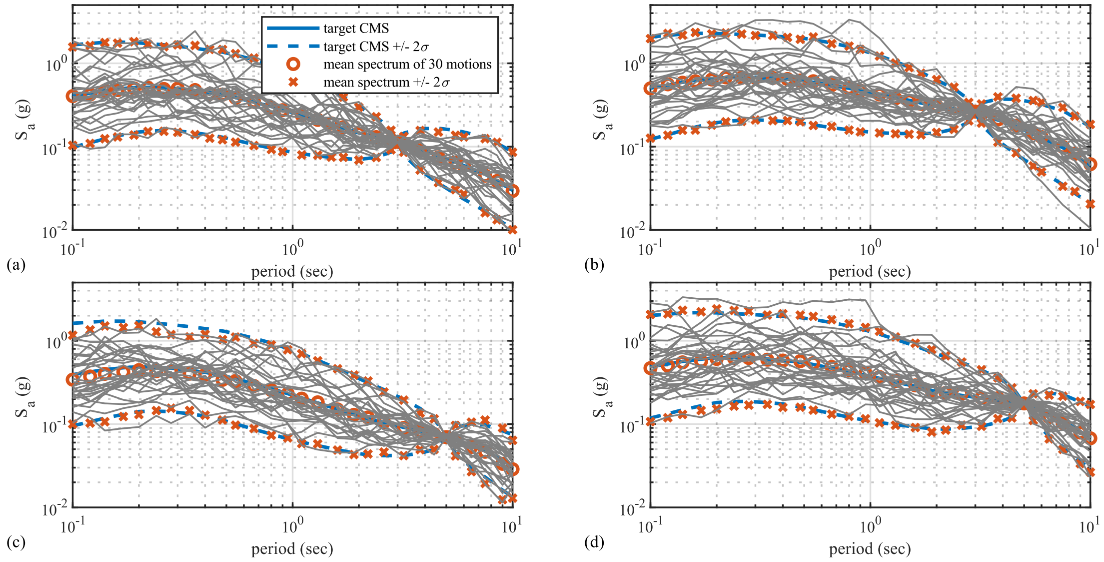

Figure 4-7: Spectra of the scaled selected ground motions for different T_r and conditioning periods T^*: (a) $T_r = 475$ years and $T^* = 3$ sec; (b) $T_r = 2{,}475$ years and $T^* = 3$ sec; (c) $T_r = 475$ years and $T^* = 5$ sec; (d) $T_r = 2{,}475$ years and $T^* = 5$ sec.

The ground motion selection was performed matching the Conditional Spectra (CSs) (T. Lin et al., 2013b, 2013d) and considering their distribution for each hazard level (i.e., return period T_r). The distribution of the target spectrum is contemplated by including the conditional standard deviation. For each couple of return period - isolated period, a set of 30 seismic records was selected. In this way, for each considered isolated period T_b, ten different sets of 30 ground motions scaled at the different IM $= S_a(T_b)$ values, were chosen (see Appendix C). All the selected natural seismic records were modified only by scaling the amplitude to match the IM value (Paolo Castaldo et al., 2018; Paolo Castaldo, Amendola, et al., 2017; Paolo Castaldo, Palazzo, et al., 2017). The spectra of four sets of 30 seismic records linked to $T_r = 475$ and $T_r = 2{,}475$ years for isolated periods of $T_b = 3$ and $T_b = 5$ sec are shown in Figure 4-7.

4.5 Design of the isolation system and superstructure

The design of the isolation system and superstructure were carried out by the criteria of the ASCE/SEI 7-16 standard (ASCE, 2016). The two-dimensional model of the superstructure equipped with DCFP bearings presented in Section 3 was employed to design both the isolation system lateral capacity and the superstructure properties. Since the main objectives of this research are to assess a comparative seismic performance analysis between LIR-DCFP devices and classical DCFP isolators with the same size and to evaluate the effects of rising the internal gap of LIR-DCFP bearings, the design of the base-isolated structures is the same for the both types of bearings.

The maximum (horizontal) base displacement D_M was estimated using the Response History Analysis (RHA) procedure. A total of 30 seismic records related to $T_r = 2{,}475$, for each considered isolated period, scaled to the same ordinate in terms of spectral acceleration of the Maximum Considered Earthquake (MCE) spectrum were used to estimate the maximum base displacement achieving a more effective design as remarked in (P. Castaldo & Alfano, 2020; Paolo Castaldo, Amendola, et al., 2017; Paolo Castaldo, Palazzo, et al., 2017). The MCE level corresponds to an earthquake with a return period of 2,475 years. The spectra of the scaled selected ground motions linked to $T_b = 3$ sec and $T_b = 5$ sec are those presented in Figure 4-7((b) and (d)), respectively. The lower bound of the friction coefficient at large velocity $\mu_{max} = 0.03$, characterizing the PDF (Section 4), was employed to design the lateral capacity of the isolation system. The lateral capacity was defined using the mean value of the maximum base displacement responses. The American code requires an increment of the maximum displacement capacity to account for accidental torsion that shall not be taken less than 1.15 times the D_M. This minimum limit was employed in this study, defining the total lateral capacity as $D_{TM} = 1.15 D_M$. The lateral capacities of both considered isolation systems for $T_b = 3$ sec and $T_b = 5$ sec are reported in Table 4-1. In this way, the two isolators have the same size for both the plates and slider. As for the LIR-DCFP device, the dimension of the internal gap has to be added as developed in the parametric analysis described in the next sections.

The yielding lateral displacement of the superstructure, defined as $u_y = f_y / k_s$ (Figure 4-3), is computed using the unreduced lateral seismic design force on elements above the base level V_{st} (i.e., $f_y = V_{st}$), employing the Equivalent Lateral Force (ELF) procedure with the upper bound value of the friction coefficient at large velocity of sliding: $\mu_{max} = 0.07$.

Combining the RHA and ELF procedures, the isolation lateral capacities are larger and the superstructures present overstrength resistances, being designed to behave elastic if the internal impact is not observed. Several researchers have studied the effects of allowing the inelastic response of simplified models, concluding that the yielding of isolated buildings generates significantly greater ductility demands than in a conventional fixed-base structure (Kikuchi et al., 2008; Vassiliou et al., 2013). In the following parametric analysis, the numerical coefficient related to the type of force-resisting system above the isolation system R_I (reduction factor) (ASCE, 2016) will be applied, allowing inelastic behavior of the superstructure before reaching the lateral capacity of the isolation system with respect to the different seismic inputs (Tsiavos et al., 2021). In cases where the parameter R_I is greater than one, the reduced design lateral seismic force is computed as V_{st}/R_I. With this magnitude of the design force, the superstructure has to be designed and the corresponding yielding displacement applies:

$$u_y = \frac{V_{st}}{k_s R_I} = \frac{u_y^{(R_I=1)}}{R_I} \tag{4-6}$$

in which, $u_y^{(R_I=1)} = V_{st}/k_s$ is the yielding displacement computed without reducing the lateral seismic design force. Table 4-1 reports the values of $u_y^{(R_I=1)}$ for the different structural properties adopted in this study.

Table 4-1: Design parameters of base-isolated systems

Isolation period, T_b (sec)	Superstructure period, T_s (sec)	Lateral capacity (cm)	$u_y^{(R_I=1)}$ related to cases with γ = 0.7 (cm)	$u_y^{(R_I=1)}$ related to cases with γ = 0.9 (cm)
3	0.3	41	0.46	0.53
	0.6	41	1.86	2.13
	0.9	41	4.18	4.79
5	0.3	54	0.31	0.34
	0.6	54	1.27	1.37
	0.9	54	2.84	3.06

4.6 Parametric study within incremental dynamic analysis (IDA)

Performing incremental dynamic analyses (IDAs) is the first step to determine the seismic reliability of non-linear base-isolated equivalent systems equipped with DCFP and LIR-DCFP bearings. Developing IDAs allows to evaluate the structural responses with respect to increasing IM levels, selected in compliance with the seismic hazard curve of the reference site, as described in Section 4. In the present work, several values related to elastic and inelastic properties of the superstructure, combined with the 15 sampled input values of the friction coefficient at large velocity, are used to estimate the probabilistic distribution of the Engineering Demand Parameters (EDPs) of interest. Within the parametric analysis, the isolated period is taken as $T_b = 3$ sec and $T_b = 5$ sec and the superstructure period as $T_s = 0.3,\ 0.6$ and 0.9 sec; the mass ratio is assumed as $\gamma = 0.7$ and $\gamma = 0.9$; the numerical coefficient related to the type of seismic force-resisting system above the isolation system is set as $R_I = 1, 1.25, 1.5$ and 2; the post-yield hardening or softening ratio are taken equal to $r_{H|S} = \pm 0.05$ and $r_{H|S} = \pm 0.1$; furthermore, for the cases of structures equipped with LIR-DCFP bearings, internal gaps ranging from 2 cm to 10 cm with a step of 2 cm have been used. All the combinations of the deterministic parameters lead to a total of 1,152 simplified and equivalent systems. The hardening or softening post-yield behavior is introduced to consider structural cases in which the superstructure is not sensitive or is sensitive to $P-\Delta$ effects. Note that the softening superstructure fails when the strength is completely nullified (Figure 4-3(c)). Furthermore, it is important to highlight that the instability failure of the isolators was never detected in all simulations.

The differential equations of motion (Chopra, 1995) have been repeatedly solved using the ode23t solver available in the MATLAB environment (Hunt et al., 2006). One IDA of one studied case consists of 4,500 simulations, using 30 seismic records properly selected and scaled to 10 different IM (i.e., $S_a(T_b)$) values (Section 4 and Appendix C), combined with the 15 samples of μ_{max}. The IDAs allow estimating the EDPs. Two EDPs are studied: the maximum (horizontal) displacement of the upper plate of the isolation device relative to the ground $u_{b,max}=|u_b(t)|_{max}$ (this parameter takes into account the total displacement of the isolation devices, summing the sliding in low friction contacts and in the high-friction interface, if any); and the ductility demand of the superstructure $\mu=u_{s,max}/u_y$, where $u_{s,max}=|u_s(t)|_{max}$ is the maximum lateral displacement of the superstructure relative to the base. The response parameters are assumed to follow a lognormal distribution (P. Castaldo et al., 2015, 2016; P. Castaldo & Alfano, 2020; P. Castaldo & Ripani, 2016; Paolo Castaldo et al., 2018; Paolo Castaldo, Amendola, et al., 2017; Paolo Castaldo, Palazzo, et al., 2017; Paolo Castaldo & Tubaldi, 2015). This distribution allows estimating the response in terms of different percentile levels. The lognormal distribution is fitted by estimating the sample lognormal mean $mean_{ln}(EDP)$ and the sample lognormal standard deviation $\sigma_{ln}(EDP)$ using the maximum likelihood estimation method and without considering the collapses when the softening behavior is analyzed (P. Castaldo et al., 2015, 2016; P. Castaldo & Alfano, 2020; P. Castaldo & Ripani, 2016; Paolo Castaldo et al., 2018;

Paolo Castaldo, Amendola, et al., 2017; Paolo Castaldo, Palazzo, et al., 2017; Paolo Castaldo & Tubaldi, 2015). In this way, it is possible to generate the IDA curves illustrated in the next sub-section.

4.6.1 Incremental dynamic analyses (IDAs) results

The IDAs results regarding the isolation level response $u_{b,max}$ are shown in Figure 4-8 only for cases with a mass distribution ratio of $\gamma = 07$ and hardening post-yield ratio of $r_H = 0.05$, with an internal gap of 10 cm for the structures equipped with LIR-DCFP bearings, due to space constraints. However, other important results, useful to the reliability assessment, are commented in the text. The maximum lateral displacement of the isolation system is highly influenced by T_b. Both the lognormal mean and dispersion rise by increasing the isolation period (e.g., Figure 4-8((a), and (e))). In all the analyzed cases, the influence of the parameters T_s, γ and $r_{H|S}$ is slight for low values of R_I but affects the statistics of the maximum displacement demand if the superstructure is designed allowing the nonlinear behavior before the occurrence of the internal impact (i.e., $R_I = 1.25$, $R_I = 1.5$ and $R_I = 2$). For structures characterized by a hardening behavior, a rise in T_s as well as in γ, or a decrease in r_H, leads to a reduction of the $u_{b,max}$ EDP (e.g., Figure 4-8((e), and (f))). The opposite occurs for softening cases, a rise in T_s as well as in γ, or a decrease in the absolute values of r_S, leads to an increase of the maximum base displacement response. This result is influenced by the increase of the number of collapses monitored for higher absolute values of r_S. For high values of IM ($\text{i.e.}, S_a(T_b)$) the percentiles of $u_{b,max}$ for structures equipped with LIR-DCFP bearings tends to rise with a higher slope than the cases equipped with DCFP bearings especially for $T_b = 3$ sec (e.g., Figure 4-8((a), and (c))). This is due to the presence of an additional sliding surface combined with the aleatory uncertainty characterizing the plane high-frictional surface.

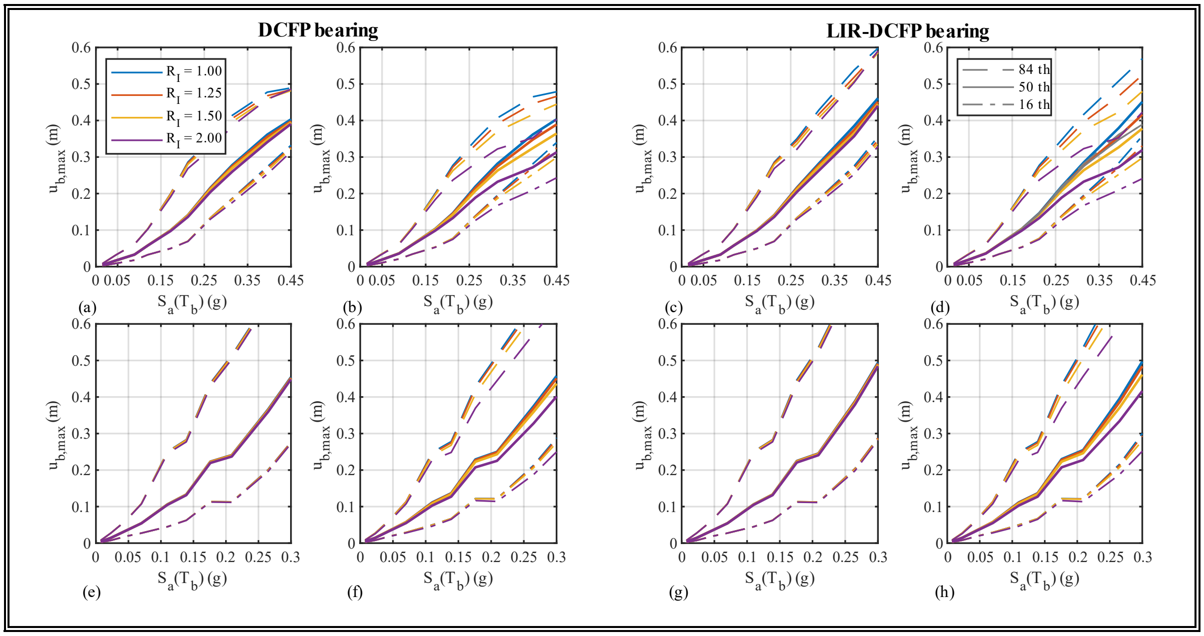

Figure 4-8: Incremental dynamic analyses curves of the isolation level with $\gamma = 0.7$ and $r_H = 0.05$: (a) DCFP, $T_b = 3$ sec, $T_s = 0.3$ sec; (b) DCFP, $T_b = 3$ sec, $T_s = 0.9$ sec; (c) LIR-DCFP, $T_b = 3$ sec, $T_s = 0.3$ sec; (d) LIR-DCFP, $T_b = 3$ sec, $T_s = 0.9$ sec; (e) DCFP, $T_b = 5$ sec, $T_s = 0.3$ sec; (f) DCFP, $T_b = 5$ sec, $T_s = 0.9$ sec; (g) LIR-DCFP, $T_b = 5$ sec, $T_s = 0.3$ sec; (h) LIR-DCFP, $T_b = 5$ sec, $T_s = 0.9$ sec.

The IDAs results regarding the ductility demand μ are plotted in Figure 4-9. In all the studied cases, the deterministic parameter T_s strongly influences the statistics of this EDP. The lognormal mean decreases if the period of the superstructure rises due to the increase of the yielding displacement (e.g., Figure 4-9((a), and (b))). For low superstructure period and high values of the parameter R_I (reduction factor), the design yielding displacement is low and can be overpassed more easily leading to higher ductility demand. In all the cases, sensitive or not sensitive to $P-\Delta$ effects, a rise in the mass distribution ratio γ leads to a reduction of the $mean_{ln}(\mu)$. The parameter R_I highly influences the ductility demand of the superstructure. An increase of this parameter leads to a rise in the EDP because the yielding in the structure is observed for lower values of IM (i.e., $S_a(T_b)$). If the superstructure remains essentially elastic before the impact (i.e., $R_I = 1.0$), the 50th and 84th percentiles decrease if LIR-DCFP bearings are used due to the presence of the internal gap that provides additional energy dissipation and limits the maximum force transmitted to the superstructure if the impact between the inner sliders and the restraining rims of the sliding surfaces is observed (e.g., Figure 4-9((d), and (h))). Considering superstructures that present hardening behavior, an increase in the post-yield hardening ratio r_H leads to a decrease in the ductility demand. For cases that exhibit softening behavior, an increase of the absolute value of r_S leads to an apparent reduction of the statistics of the ductility demand EDP due to the increase of the number of collapses monitored.

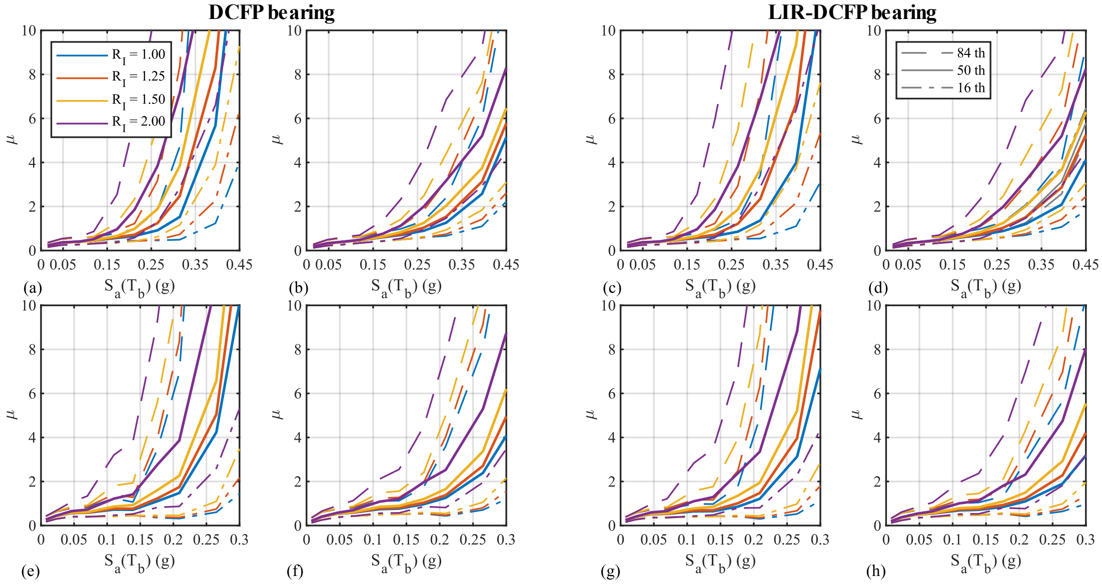

Figure 4-9: Incremental dynamic analyses curves of the superstructure with $\gamma = 0.7$ and $r_H = 0.05$: (a) DCFP, $T_b = 3$ sec, $T_s = 0.3$ sec; (b) DCFP, $T_b = 3$ sec, $T_s = 0.9$ sec; (c) LIR-DCFP, $T_b = 3$ sec, $T_s = 0.3$ sec; (d) LIR-DCFP, $T_b = 3$ sec, $T_s = 0.9$ sec; (e) DCFP, $T_b = 5$ sec, $T_s = 0.3$ sec; (f) DCFP, $T_b = 5$ sec, $T_s = 0.9$ sec; (g) LIR-DCFP, $T_b = 5$ sec, $T_s = 0.3$ sec; (h) LIR-DCFP, $T_b = 5$ sec, $T_s = 0.9$ sec.

4.7 Seismic fragility

The next step is the evaluation of the seismic fragility, defined as the probability P_f exceeding a limit state (LS) at each IM level. The LS thresholds need to be defined for the seismic fragility assessment. On the one hand, the performance levels of the isolation system are defined in terms of the maximum (horizontal) displacement of the upper plate of the isolators $u_{b,max}$ (i.e., $\mathrm{LS}_{u_{b,max}} = 5;\ 10;\ 15;\ 20;\ 25;\ 30;\ 35;\ 40;\ 45;\ 50;\ 55$ cm) (Paolo Castaldo et al., 2018; Paolo Castaldo, Amendola, et al., 2017; Paolo Castaldo, Palazzo, et al., 2017). On the other hand, the performance levels related to the superstructure are defined in terms of the ductility demand μ of the superstructure (i.e., $\mathrm{LS}_{\mu} = 1;\ 2;\ 3;\ 4;\ 5;\ 6;\ 7;\ 8;\ 9;\ 10$) (Paolo Castaldo et al., 2018; Paolo Castaldo, Amendola, et al., 2017; Paolo Castaldo, Palazzo, et al., 2017). Although not realistic, several limit state thresholds have been adopted to achieve an accurate numerical assessment of the seismic fragility and, successively, reliability (Paolo Castaldo et al., 2018; Paolo Castaldo, Amendola, et al., 2017; Paolo Castaldo, Palazzo, et al., 2017). The probabilities exceeding the different LSs at each IM level are determined fitting lognormal complementary cumulative distribution function (CCDFs). In cases with softening post-yield behavior (see Figure 4-3(c)), the fragility evaluation considered the collapse and not-collapse results using the total probability theorem, as carried out in (Bazzurro et al., n.d.; P. Castaldo & Alfano, 2020; Paolo Castaldo et al., 2018). In these softening cases, the collapse is reached if the strength of the superstructure is completely nullified.

As an example and due to space constraints, the fragility curves related to the isolation level representing the probability P_f exceeding $\mathrm{LSs}_{u_{b,max}} = 10, 30$ and 45 cm for an isolated period of $T_b = 3$ sec and a hardening post-yield ratio of $r_H = 0.05$ are presented in Figure 4-10 (for $T_s = 0.3$ sec) and Figure 4-11 (for $T_s = 0.6$ sec). However, other important results, useful to the reliability assessment, are commented in the text.

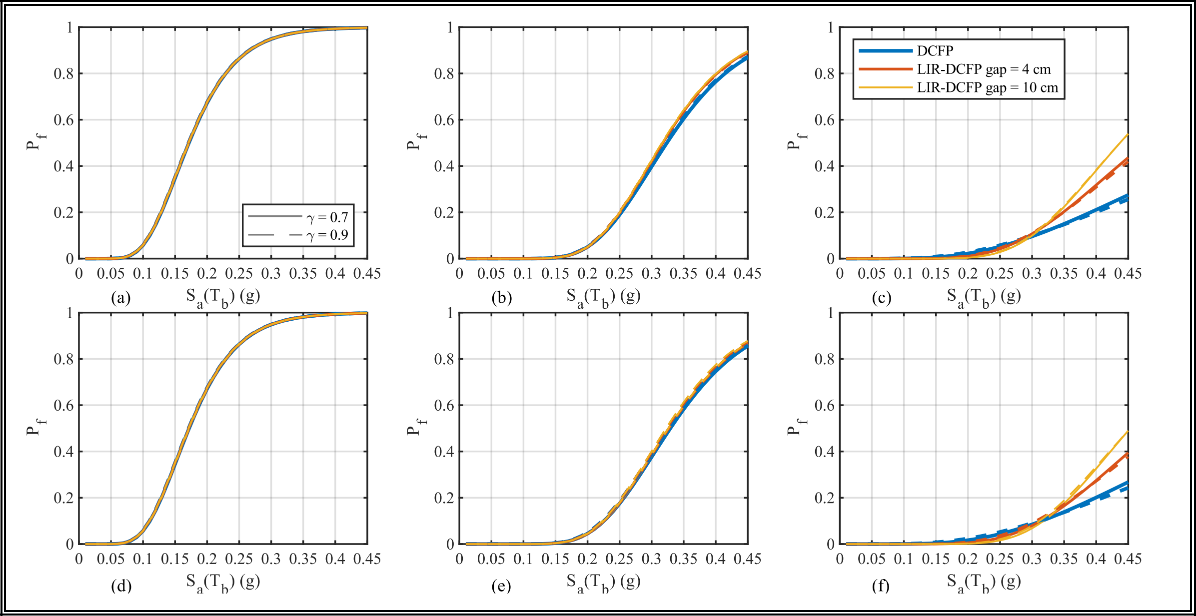

Figure 4-10: Seismic fragility curves of the isolation level related to $T_s = 0.3$ sec and $r_H = 0.05$: (a) $\mathrm{LS}_{u_{b,max}} = 10$ cm and $R_I = 1$; (b) $\mathrm{LS}_{u_{b,max}} = 30$ cm and $R_I = 1$; (c) $\mathrm{LS}_{u_{b,max}} = 45$ cm and $R_I = 1$; (d) $\mathrm{LS}_{u_{b,max}} = 10$ cm and $R_I = 2$; (e) $\mathrm{LS}_{u_{b,max}} = 30$ cm and $R_I = 2$; (f) $\mathrm{LS}_{u_{b,max}} = 45$ cm and $R_I = 2$.

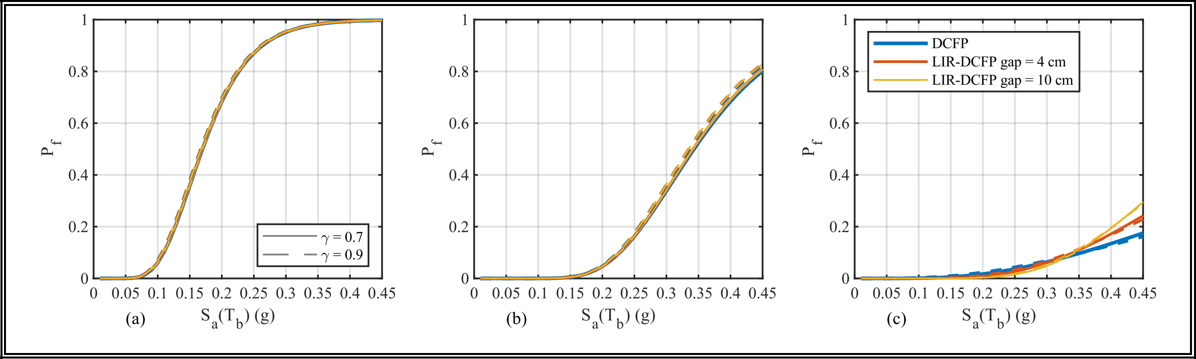

Figure 4-11: Seismic fragility curves of the isolation level related to $T_s = 0.6$ sec, $r_H = 0.05$ and $R_I = 2$: (a) $\mathrm{LS}_{u_{b,max}} = 10$ cm; (b) $\mathrm{LS}_{u_{b,max}} = 30$ cm; (c) $\mathrm{LS}_{u_{b,max}} = 45$.

The seismic fragility of the isolation level decreases for increasing the LS thresholds. In fact, for low IM and LS thresholds the seismic fragility is higher (e.g., Figure 4-10(a), and Figure 4-11(a)). For cases with $R_I = 1$ and $\mathrm{LSs}_{u_{b,max}}$ lower than 40 cm, the fragility curves are slightly affected by the superstructure period T_s and mass ratio γ (e.g., Figure 4-10(b), and

Figure 4-11(b)). The influence of the superstructure period is stronger for $\mathrm{LS}_{u_{b,max}} = 45$ cm (the internal impact is produced) and $R_I = 2$ (e.g., Figure 4-10(c), and Figure 4-11(c)). Under these last conditions, in all the studied cases, an increment in T_s or γ leads to a seismic fragility reduction for the isolation level. The effect of increasing the mass distribution ratio is stronger for the softening behavior. For cases related to superstructures with a hardening lateral behavior, a rise in the parameter r_H leads to a slight increase in the probabilities of exceeding $\mathrm{LS}_{u_{b,max}}$ thresholds. For cases with superstructures sensitive to $P - \Delta$ effects, an increment in the absolute value of r_S leads to a rise in the fragility curves. This increment is due to the higher number of collapses previously monitored. The influence of the internal gap for the LIR-DCFP bearings in the probability exceeding high $\mathrm{LS}_{u_{b,max}}$ thresholds is noticeable. In fact, a rise in the internal gap leads to an increment of the fragility curves due to the additional displacement developed along the high-friction interface (e.g., Figure 4-10((c) and (f)), and Figure 4-11(c)).

The fragility curves related to the superstructure for ductility demand thresholds $\mathrm{LS}_{\mu} = 1, 4$ and 7 are presented in Figure 4-12 (for $T_s = 0.3$ sec) and Figure 4-13 (for $T_s = 0.6$ sec). The period of the superstructure T_s influences the fragility curves. The stiffer the structure, the higher probabilities exceeding the LS_{μ}. In general, higher values of mass ratio γ decrease the fragility curves (e.g., Figure 4-12(a) and Figure 4-13(a)).

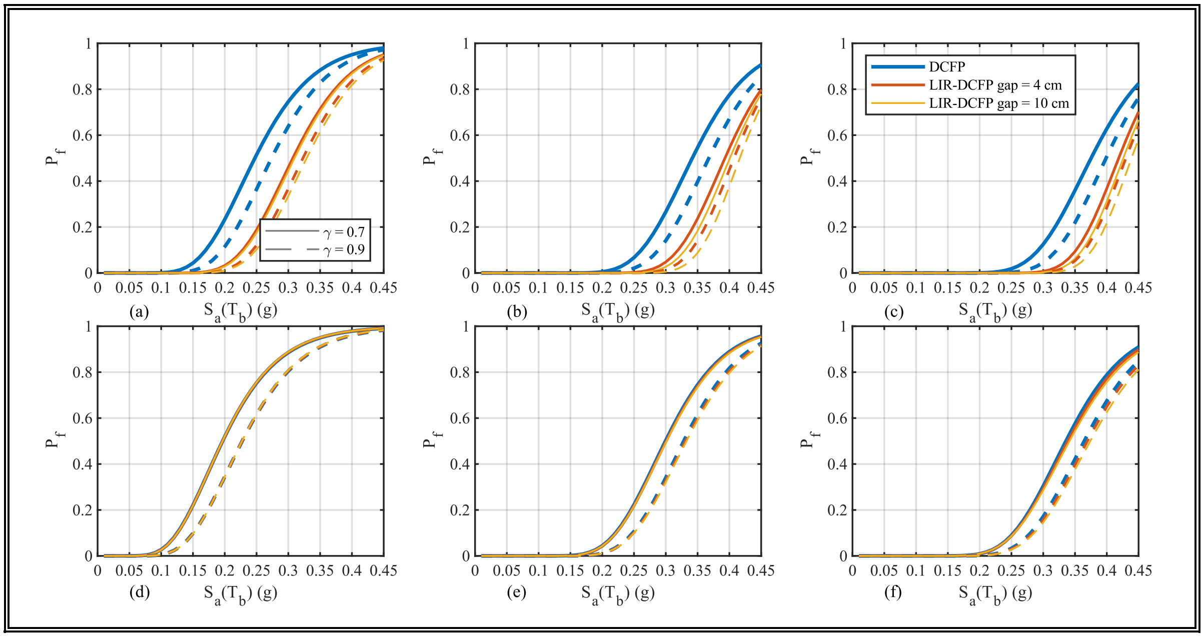

Figure 4-12: Seismic fragility curves of superstructure related to $T_s = 0.3$ sec and $r_H = 0.05$: (a) $\mathrm{LS}_\mu = 1$ and $R_I = 1$; (b) $\mathrm{LS}_\mu = 4$ and $R_I = 1$; (c) $\mathrm{LS}_\mu = 7$ and $R_I = 1$; (d) $\mathrm{LS}_\mu = 1$ and $R_I = 2$; (e) $\mathrm{LS}_\mu = 4$ and $R_I = 2$; (f) $\mathrm{LS}_\mu = 7$ and $R_I = 2$.

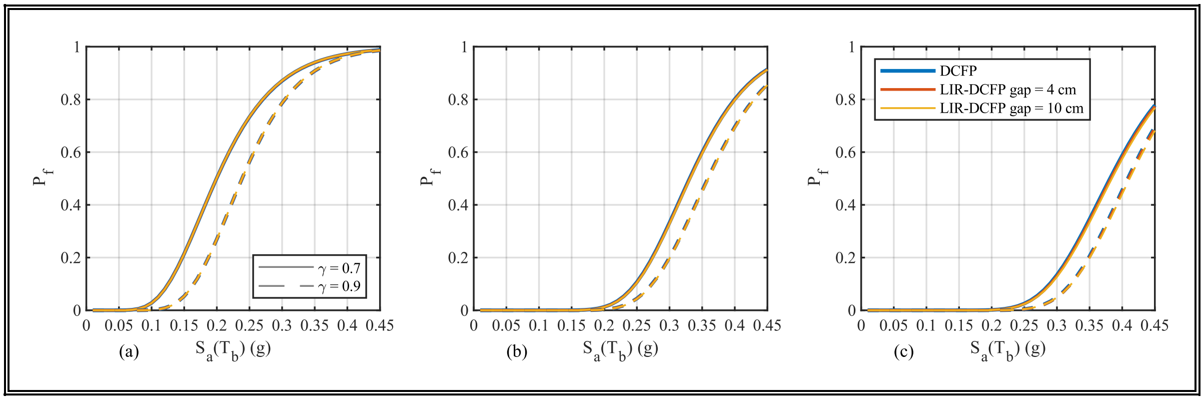

Figure 4-13: Seismic fragility curves of superstructure related to $T_s = 0.6$ sec, $r_H = 0.05$ and $R_I = 2$: (a) $\mathrm{LS}_\mu = 1$; (b) $\mathrm{LS}_\mu = 4$; (c) $\mathrm{LS}_\mu = 7$.

As expected, an increment in R_I leads to a rise of the probabilities exceeding the LS_μ (e.g., Figure 4-12((a) and (d))). If the superstructure behaves essentially elastic before the impact (i.e., low values of R_I), an increase of the internal gap reduces the fragility curves demonstrating the advantages of the LIR-DCFP devices, especially for lower T_s (e.g., Figure 4-12((a), (b), and (c)). This improvement in the seismic performance, in cases that present hardening behavior, increases for higher values of r_H. In cases of superstructures with a softening behavior, the use of the studied seismic isolator is valuable, especially, for structures designed to remain elastic if internal impact is not observed (i.e., $R_I = 1$). These advantages derive from the presence of the internal gap with infinite curvature combined with the higher friction coefficient.

4.8 Seismic reliability of structures equipped with DCFP and LIR-DCFP bearings

The convolution integral between the defined fragility curves and the seismic hazard curves, expressed in terms of the same IM (i.e., $S_a(T_b)$), allows calculating the mean annual rate exceeding the LSs through the following equation:

$$\lambda_{LS}(EDP > y) = \int_0^{\infty} P(EDP > y \mid S_a(T_b) = x) |\lambda(\mathrm{d}S_a(T_b) > x)| \tag{4-7}$$

in which, $\lambda(\mathrm{d}S_a(T_b) > x)$ is the derivative of the hazard curve for $S_a(T_b)$ (i.e., the annual mean rate exceeding the specific value of the IM $= S_a(T_b) = x$) multiplied by an increment of $dS_a(T_b)$; and $P(EDP > y \mid S_a(T_b) = x)$ is the probability of the EDP exceeding y (i.e., a specific LS) given a ground motion with $S_a(T_b) = x$. The term $P(EDP > y \mid S_a(T_b) = x)$ represents the fragility curves computed in Section 7. The evaluation of the seismic reliability of base-isolated systems can be achieved by using a Poisson distribution considering a time frame (e.g., 50 years) on the results of the convolution integral, as follows:

$$P_f(50\text{ years}) = 1 - \exp\left(-\lambda_{LS}(EDP > y) \cdot (50\text{ years})\right) \tag{4-8}$$

The seismic reliability curves of the isolation level are plotted in logarithmic scale in Figure 4-14 for $T_b = 3$ sec and $r_H = 0.10$. The increase of R_I leads to a decrease on the probabilities exceeding $\mathrm{LS}_{u_{b,max}}$ thresholds. This reduction in the base displacement demand is increased for higher values of T_s (e.g., Figure 4-14((a), and (c))). This phenomenon decreases the benefits of using LIR-DCFP bearings for the isolation level itself. The main difference in the dynamic behavior of the suggested new frictional isolator is exhibited if the internal lateral impact is observed. A high value of the parameter R_I implies that the yielding of the superstructure is observed before the occurrence of the internal impact. The nonlinear behavior of the superstructure causes an elongation of its fundamental period losing the effectiveness of the seismic isolation technique, expressed in a reduction of the base displacement demand with an increase on the ductility demand of the superstructure (e.g., Figure 4-14((c), and (f))).

The effects of considering softening post-yield behavior ($r_S = -0.10$) on the maximum base displacement is presented in Figure 4-15. Under this scenario, the differences in the lateral displacement of the isolation system using DCFP bearings or LIR-DCFP bearings are negligible. The increment in the probabilities exceeding $\mathrm{LS}_{u_{b,max}}$ thresholds is generated by an increase in the number of superstructure collapses.

In Figures 4-16 to 4-23, the seismic reliability curves in 50 years of all the studied superstructures are plotted in logarithm scale for the different LS_{μ} thresholds. Blue lines in the figures represent cases of isolated structures equipped with DCFP bearings. Other colors represent systems equipped with the LIR-DCFP bearings for different gap sizes. In general, the seismic reliability of the superstructure declines for higher values of R_I. The post-yield ratio affects the performance of the studied seismically isolated structures. In fact, an increase of the hardening post-yield ratio r_H leads to a rise in the seismic reliability (hardening behavior: Figures 4-16, 4-17, 4-20 and 4-21), whereas an increase in the absolute values of r_S (softening behavior: Figures 4-18, 4-19, 4-22 and 4-23) causes worse seismic performance of the superstructure. The influence of the described parameters of dynamic systems are in concordance with previous studies (P. Castaldo & Alfano, 2020; Paolo Castaldo et al., 2018; Paolo Castaldo, Amendola, et al., 2017; Paolo Castaldo, Palazzo, et al., 2017).

The exceeding probabilities are slightly decreased for higher values of γ (e.g., Figure 4-17((c), and (f))). As mentioned in Section 3, an increment in the inertial forces developed in the superstructure is produced by lateral impacts (Komodromos, 2008; Polycarpou & Komodromos, 2010). This rise in the inertial forces increases the ductility demand specially if an important portion of the total mass is concentrated in the base (i.e., lower values of the mass ratio γ). The opposite happens for higher values of γ.

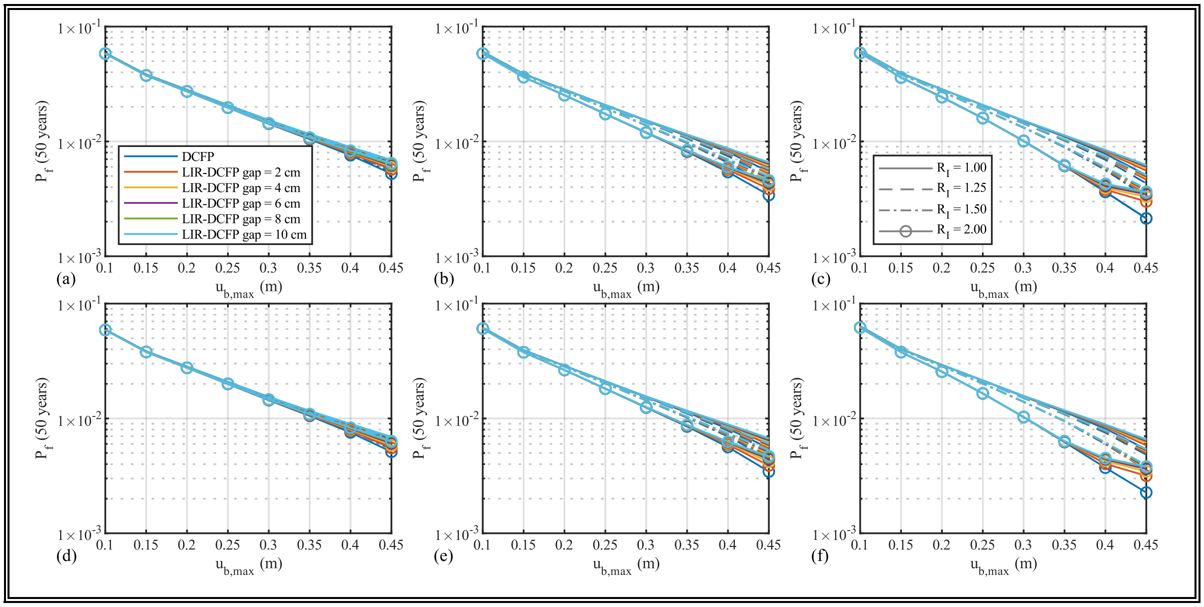

Figure 4-14: Seismic reliability of the isolation level for $T_b = 3$ sec and $r_H = 0.10$: (a) $\gamma = 0.7$ and $T_s = 0.3$ sec; (b) $\gamma = 0.7$ and $T_s = 0.6$ sec; (c) $\gamma = 0.7$ and $T_s = 0.9$ sec; (d) $\gamma = 0.9$ and $T_s = 0.3$ sec; (e) $\gamma = 0.9$ and $T_s = 0.6$ sec; (f) $\gamma = 0.9$ and $T_s = 0.9$ sec.

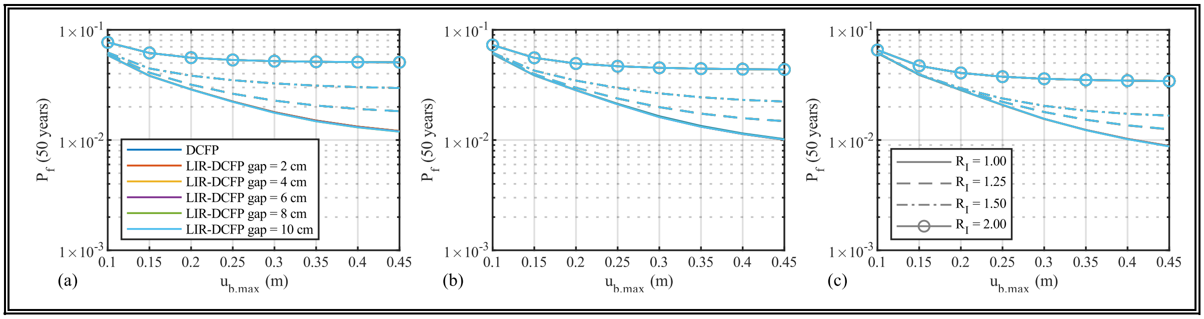

Figure 4-15: Seismic reliability of the isolation level for $T_b = 3$ sec, $\gamma = 0.7$ and $r_S = -0.10$: (a) $T_s = 0.3$ sec; (b) $T_s = 0.6$ sec; (c) $T_s = 0.9$ sec.

Analyzing the benefits of using the LIR-DCFP bearings, an increase in the internal gap of the enhanced inner slider leads to a better seismic performance of the superstructure (e.g., Figure 4-16((a), and (d)), Figure 4-17((a), and (d)), Figure 4-20((a), and (d)), and Figure 4-21((a), and (d))). The presence of an internal gap in the inner slider limits the maximum lateral force that the devices can transmit to the superstructure after the internal impact between the inner slider and the restraining rims of the sliding plates, reducing the ductility demand on the isolated building. Furthermore, the high-friction sliding produced by the internal impact dissipates an additional amount of energy. An increase in the size of the internal gap of the LIR-DCFP bearings leads to a larger capacity of frictional energy dissipation, improving the seismic performance. The enhancing of the seismic performance is highlighted, especially, for low values of R_I (e.g., Figure 4-16((a), and (d)), Figure 4-17((a), and (d)), Figure 4-20((a), and (d)), and Figure 4-21((a), and (d))). It is important to emphasize that in no case the use of LIR-DCFP bearings increases the ductility demand. Consequently, using the suggested isolator ensures quite always a better seismic performance than structures equipped with DCFP isolators having same size for both the plates and slider.

Analyzing cases with hardening post-yield behavior, even for cases with $R_I = 1.25$, $R_I = 1.5$, or $R_I = 2.0$, better seismic performance is achieved using the proposed seismic isolator if the superstructure is stiff and the post-yield hardening ratio is relatively high (e.g., Figure 4-16((a), and (d)), Figure 4-17((a), and (d)), Figure 4-20((a), and (d)), and Figure 4-21((a), and (d))). On the contrary, for flexible superstructures with lower post-yield hardening ratios, the benefits of using the suggested isolator are slightly lower (e.g., Figure 4-16(c) and Figure 4-17(c)).

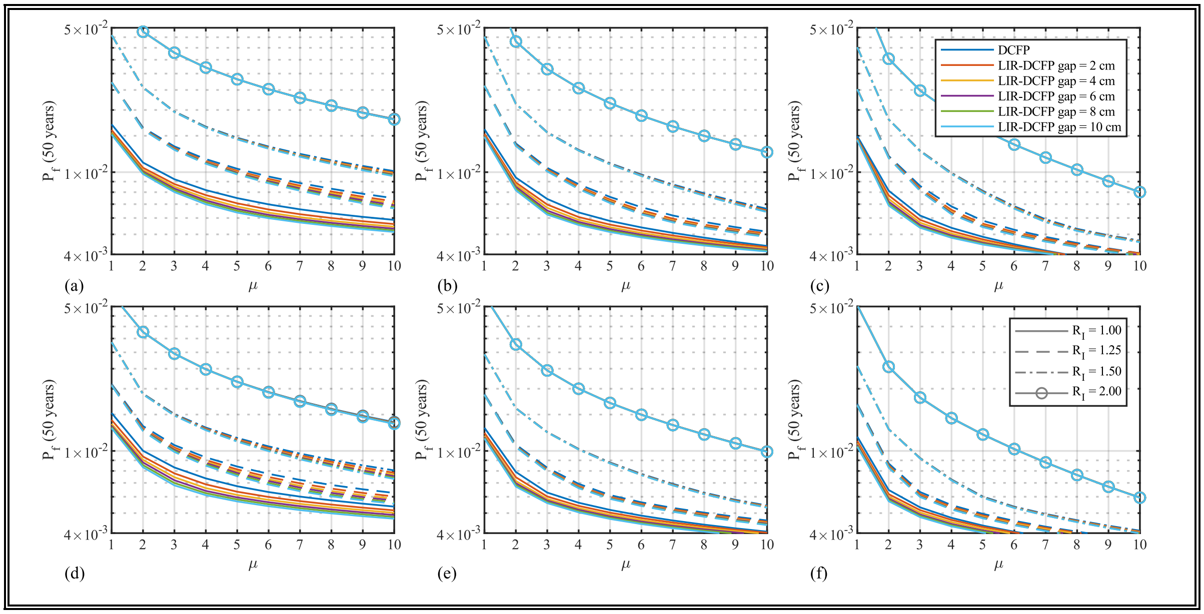

Figure 4-16: Seismic reliability of the superstructure for $T_b = 3$ sec and $r_H = 0.05$: (a) $\gamma = 0.7$ and $T_s = 0.3$ sec; (b) $\gamma = 0.7$ and $T_s = 0.6$ sec; (c) $\gamma = 0.7$ and $T_s = 0.9$ sec; (d) $\gamma = 0.9$ and $T_s = 0.3$ sec; (e) $\gamma = 0.9$ and $T_s = 0.6$ sec; (f) $\gamma = 0.9$ and $T_s = 0.9$ sec.

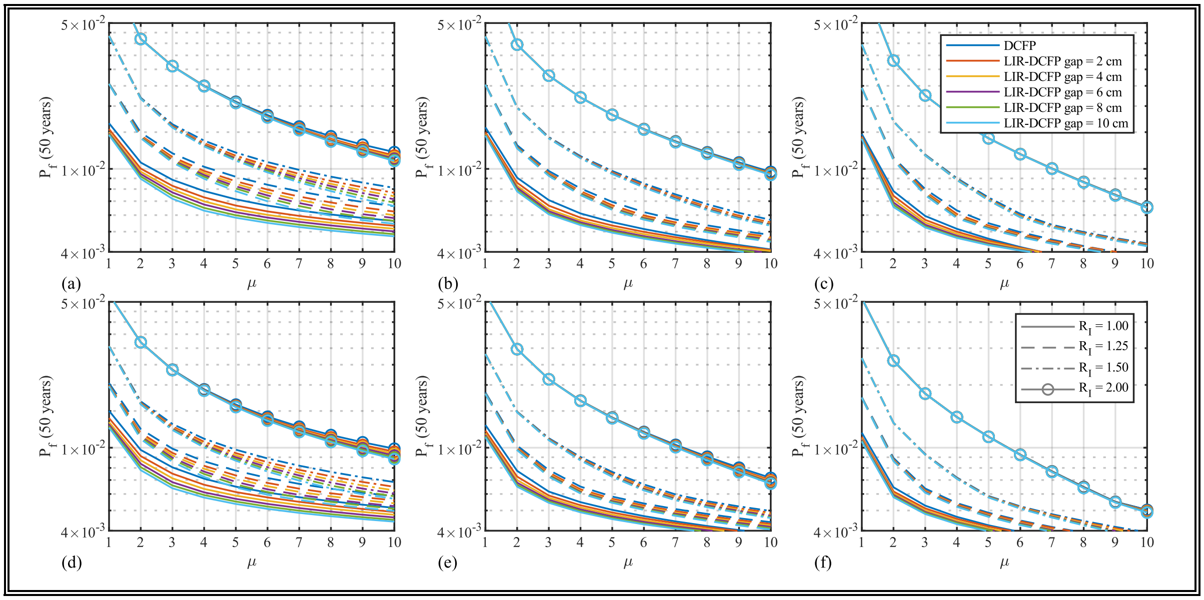

Figure 4-17: Seismic reliability of the superstructure for $T_b = 3$ sec and $r_H = 0.10$: (a) $\gamma = 0.7$ and $T_s = 0.3$ sec; (b) $\gamma = 0.7$ and $T_s = 0.6$ sec; (c) $\gamma = 0.7$ and $T_s = 0.9$ sec; (d) $\gamma = 0.9$ and $T_s = 0.3$ sec; (e) $\gamma = 0.9$ and $T_s = 0.6$ sec; (f) $\gamma = 0.9$ and $T_s = 0.9$ sec.

For cases with softening post-yield behavior, higher values of the absolute value of r_S strongly affect the ductility demand on the superstructure, decreasing the seismic performance. The benefits of using the proposed frictional device to isolate superstructures sensitive to $P-\Delta$ effects are exhibited for $R_I=1$ and in some cases with $R_I=1.25$ (e.g., Figure 4-18(e), Figure 4-22, and Figure 4-23). In all the studied cases with $R_I=1.5$ or $R_I=2$, the softening behavior leads to the occurrence of collapse before the occurrence of the internal lateral impact. This phenomenon is observed for post-yield ratios of $r_S=-0.05$ and -0.10. Consequently, the dynamics behavior of systems with these characteristics is the same using DCFP bearings or LIR-DCFP bearings (e.g., Figures 4-18 and Figure 4-19, and Figures 22 and Figure 4-23).

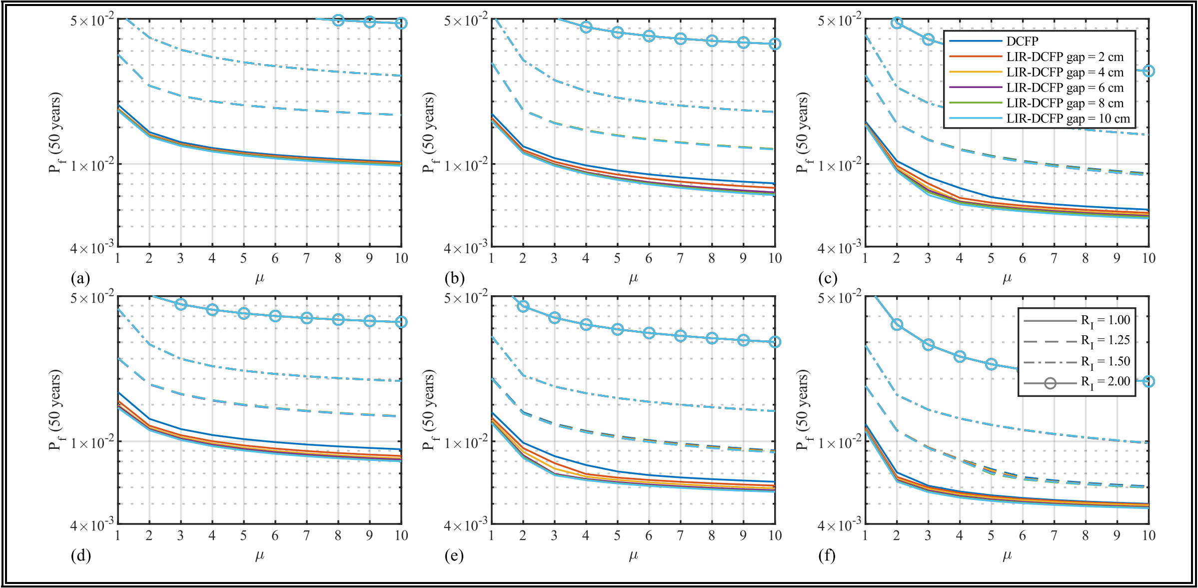

Figure 4-18: Seismic reliability of the superstructure for $T_b=3$ sec and $r_S=-0.05$: (a) $\gamma=0.7$ and $T_s=0.3$ sec; (b) $\gamma=0.7$ and $T_s=0.6\ sec$; (c) $\gamma=0.7$ and $T_s=0.9$ sec; (d) $\gamma=0.9$ and $T_s=0.3$ sec; (e) $\gamma=0.9$ and $T_s=0.6$ sec; (f) $\gamma=0.9$ and $T_s=0.9$ sec.

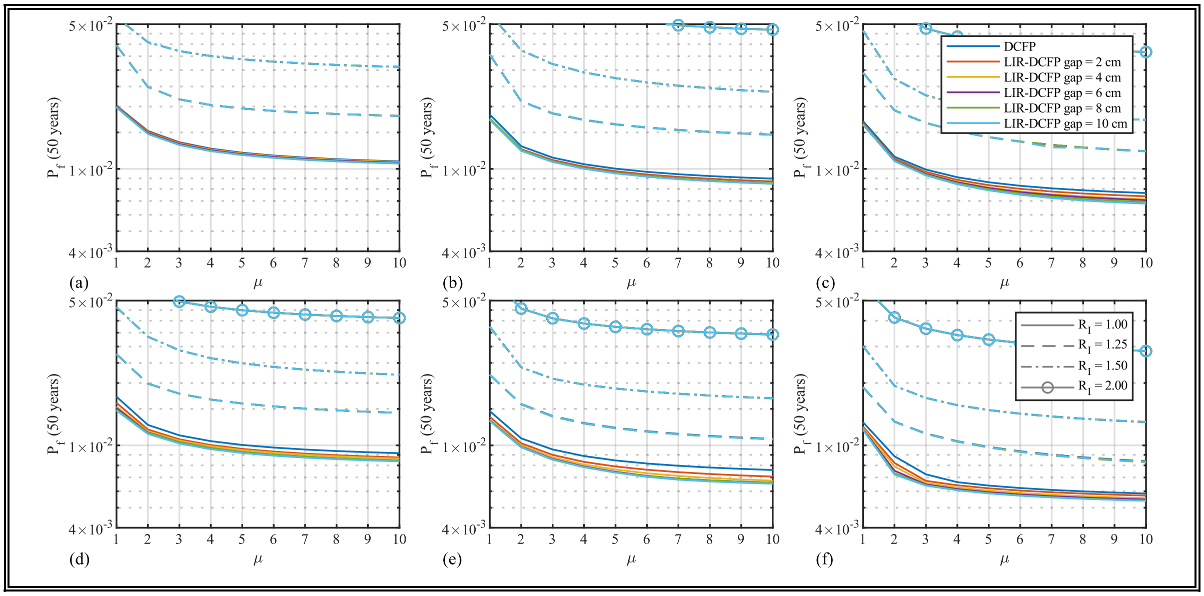

Figure 4-19: Seismic reliability of the superstructure for $T_b = 3$ sec and $r_S = -0.10$: (a) $\gamma = 0.7$ and $T_s = 0.3$ sec; (b) $\gamma = 0.7$ and $T_s = 0.6$ sec; (c) $\gamma = 0.7$ and $T_s = 0.9$ sec; (d) $\gamma = 0.9$ and $T_s = 0.3$ sec; (e) $\gamma = 0.9$ and $T_s = 0.6$ sec; (f) $\gamma = 0.9$ and $T_s = 0.9$ sec.

These reliability curves (Figures 4-16 to 4-23) can be adopted as SRBD curves according to studies dealing with DCFP devices (Paolo Castaldo et al., 2018; Paolo Castaldo, Palazzo, et al., 2017) to define relationships between R_I and μ for the superstructure when LIR-DCFP bearings are employed with important design suggestions for the internal gap as well as to assess the performance. Within this last issue, the reduction of the probabilities in 50 years exceeding thresholds of $\mathrm{LS}_{\mu} = 3$ and 5 for cases related to $R_I = 1.00$ and 1.25 having LIR-DCFP bearings instead of DCFP devices is plotted, respectively, in Figures 4-24 and 4-25. The results demonstrate an improved seismic performance of buildings equipped with LIR-DCFP bearings. In general, an increment of the size of the internal gap of the inner slider leads to an increase of the reduction of the exceedance probability of the ductility demand thresholds. The increase of the reduction percentage is larger for increasing internal gap values (e.g., Figure 4-24((a), and (f))). The role of the parameter R_I is crucial to achieve a better seismic performance by using LIR-DCFP bearings. The benefits of using frictional isolators with enhanced inner sliders are increased for low values of R_I (e.g., Figure 4-24).

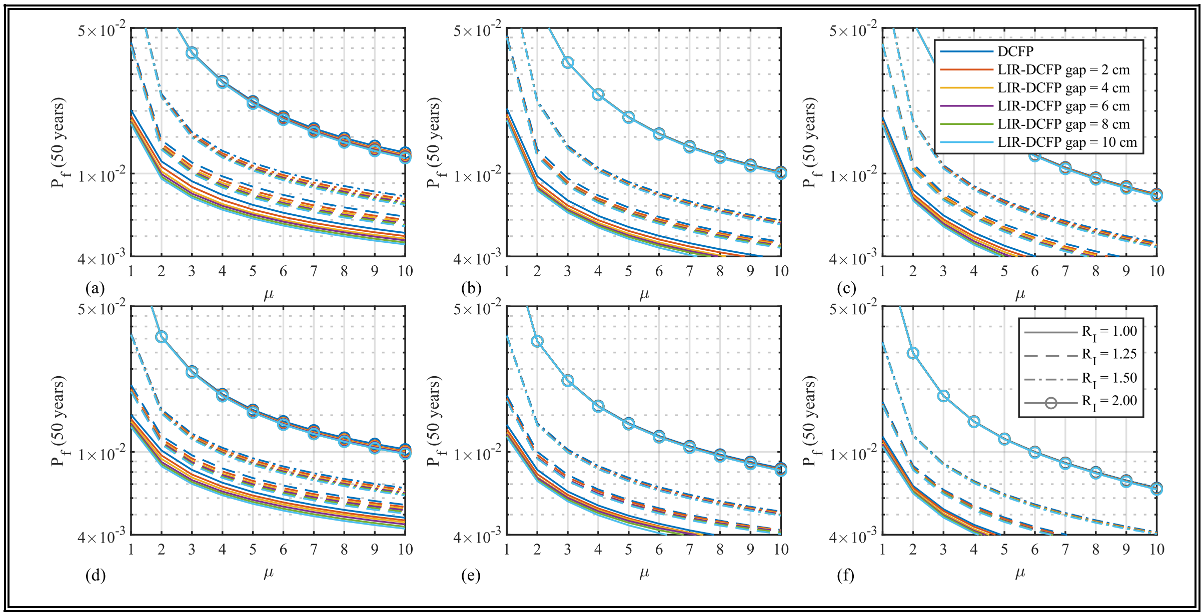

Figure 4-20: Seismic reliability of the superstructure for $T_b = 5$ sec and $r_H = 0.05$: (a) $\gamma = 0.7$ and $T_s = 0.3$ sec; (b) $\gamma = 0.7$ and $T_s = 0.6$ sec; (c) $\gamma = 0.7$ and $T_s = 0.9$ sec; (d) $\gamma = 0.9$ and $T_s = 0.3$ sec; (e) $\gamma = 0.9$ and $T_s = 0.6$ sec; (f) $\gamma = 0.9$ and $T_s = 0.9$ sec.

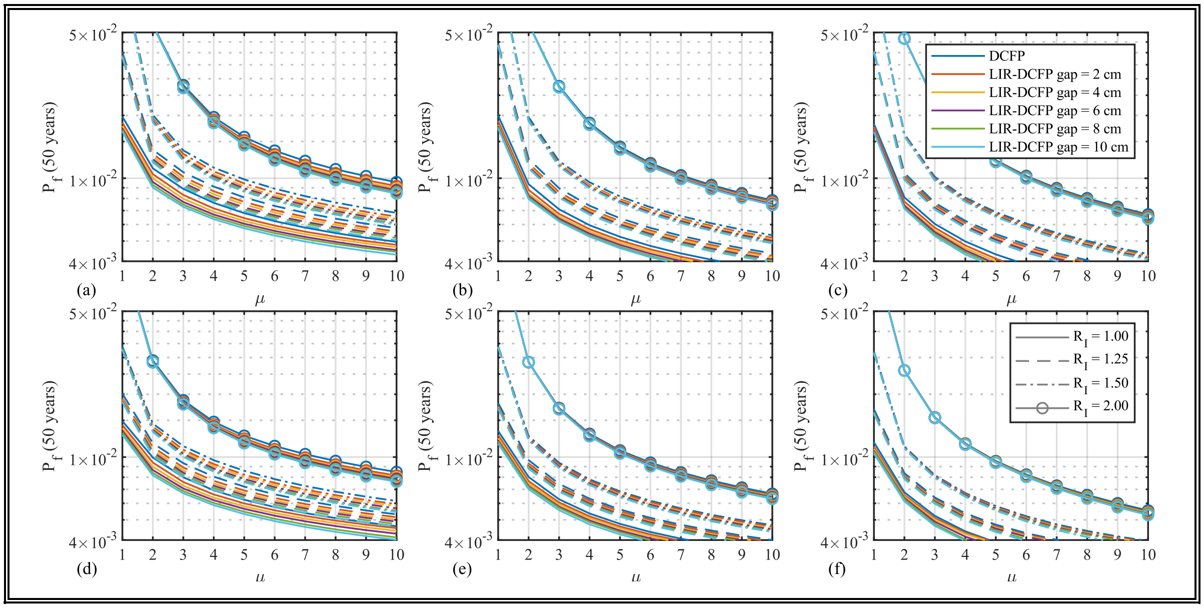

Figure 4-21: Seismic reliability of the superstructure for $T_b = 5$ sec and $r_H = 0.10$: (a) $\gamma = 0.7$ and $T_s = 0.3$ sec; (b) $\gamma = 0.7$ and $T_s = 0.6$ sec; (c) $\gamma = 0.7$ and $T_s = 0.9$ sec; (d) $\gamma = 0.9$ and $T_s = 0.3$ sec; (e) $\gamma = 0.9$ and $T_s = 0.6$ sec; (f) $\gamma = 0.9$ and $T_s = 0.9$ sec.

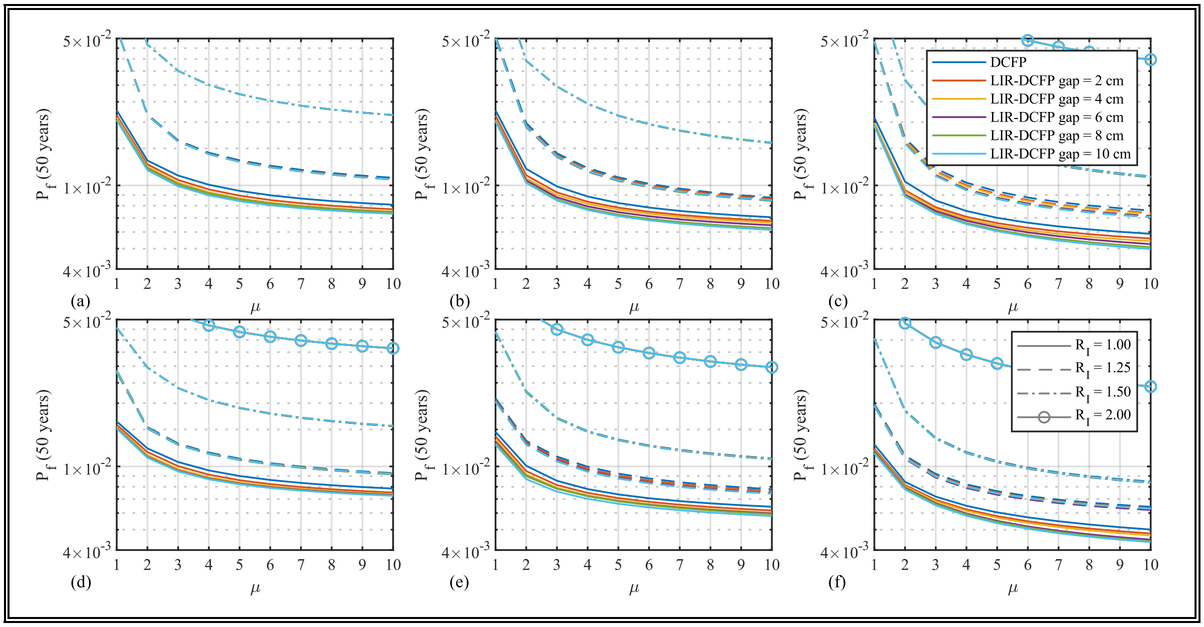

Figure 4-22: Seismic reliability of the superstructure for $T_b = 5$ sec and $r_S = -0.05$: (a) $\gamma = 0.7$ and $T_s = 0.3$ sec; (b) $\gamma = 0.7$ and $T_s = 0.6$ sec; (c) $\gamma = 0.7$ and $T_s = 0.9$ sec; (d) $\gamma = 0.9$ and $T_s = 0.3$ sec; (e) $\gamma = 0.9$ and $T_s = 0.6$ sec; (f) $\gamma = 0.9$ and $T_s = 0.9$ sec.

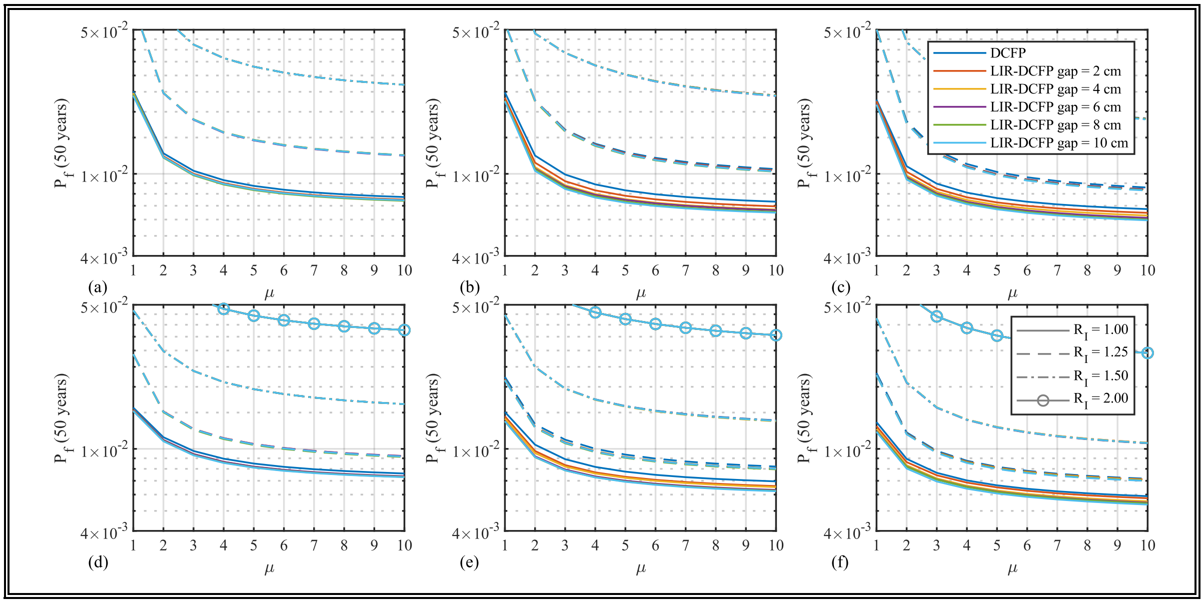

Figure 4-23: Seismic reliability of the superstructure for $T_b = 5$ sec and $r_S = -0.10$: (a) $\gamma = 0.7$ and $T_s = 0.3$ sec; (b) $\gamma = 0.7$ and $T_s = 0.6$ sec; (c) $\gamma = 0.7$ and $T_s = 0.9$ sec; (d) $\gamma = 0.9$ and $T_s = 0.3$ sec; (e) $\gamma = 0.9$ and $T_s = 0.6$ sec; (f) $\gamma = 0.9$ and $T_s = 0.9$ sec.

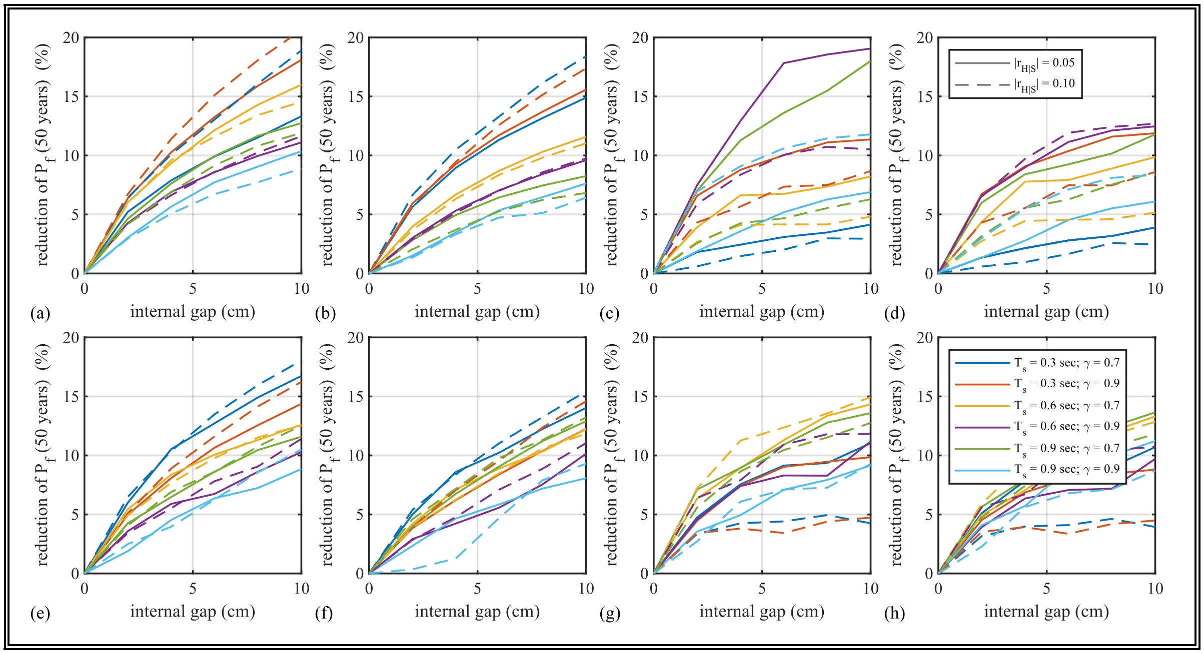

Figure 4-24: Reduction of the ductility demand for increasing values of internal gap of LIR-DCFP bearings for $R_I = 1.0$: (a) Hardening $\mathrm{LS}_\mu = 3$ and $T_b = 3$ sec; (b) Hardening $\mathrm{LS}_\mu = 5$ and $T_b = 3$ sec; (c) Softening $\mathrm{LS}_\mu = 3$ and $T_b = 3$ sec; (d) Softening $\mathrm{LS}_\mu = 5$ and $T_b = 3$ sec; (e) Hardening $\mathrm{LS}_\mu = 3$ and $T_b = 5$ sec; (f) Hardening $\mathrm{LS}_\mu = 5$ and $T_b = 5$ sec; (g) Softening $\mathrm{LS}_\mu = 3$ and $T_b = 5$ sec; (h) Softening $\mathrm{LS}_\mu = 5$ and $T_b = 5$ sec.

Considering cases with hardening behavior and $R_I = 1.00$, the improvement in the seismic performance using LIR-DCFP bearings is highlighted for low values of T_s, low values of γ and high values of r_H (Figure 4-24). By using LIR-DCFP bearings with internal gaps of 10 cm reduction in the probabilities of exceeding $\mathrm{L}Ss_{\mu}$ up to 20% are achievable (Figure 4-24(a)). This result is coherent with the fragility curves and several studies indicating that stiff base-isolated superstructures (e.g., concentrically braced steel frames and non-slender reinforce concrete buildings) are very sensitive to impact forces (Bao et al., 2018; Bao & Becker, 2018a, 2018c). Hence, using LIR-DCFP bearing is very attractive to improve the seismic performance of stiff base-isolated structures. The improvement in the seismic performance is noticeable even for cases with $R_I = 1.25$ and superstructures characterized, especially, by a hardening behavior (Figure 4-25). This better performance is highlighted for stiff structures (i.e., $T_S = 3$ sec) and a relatively high post-yield ratio ($r_H = 0.10$). In Figure 4-25((a), (b), (e), and (f)), these cases are plotted using red and blue dashed lines.

The results obtained considering cases sensitive to $P - \Delta$ effects also present important reductions in the probability of exceedance $\mathrm{L}S_{\mu} = 3$ and $\mathrm{L}S_{\mu} = 5$. Not negligible benefits of using LIR-DCFP bearings are achieved also for the rise of the parameter R_I in cases of structures characterized by softening behavior, particularly, for low absolute values of the post-yield ratio (i.e., $|r_S| = 0.05$).

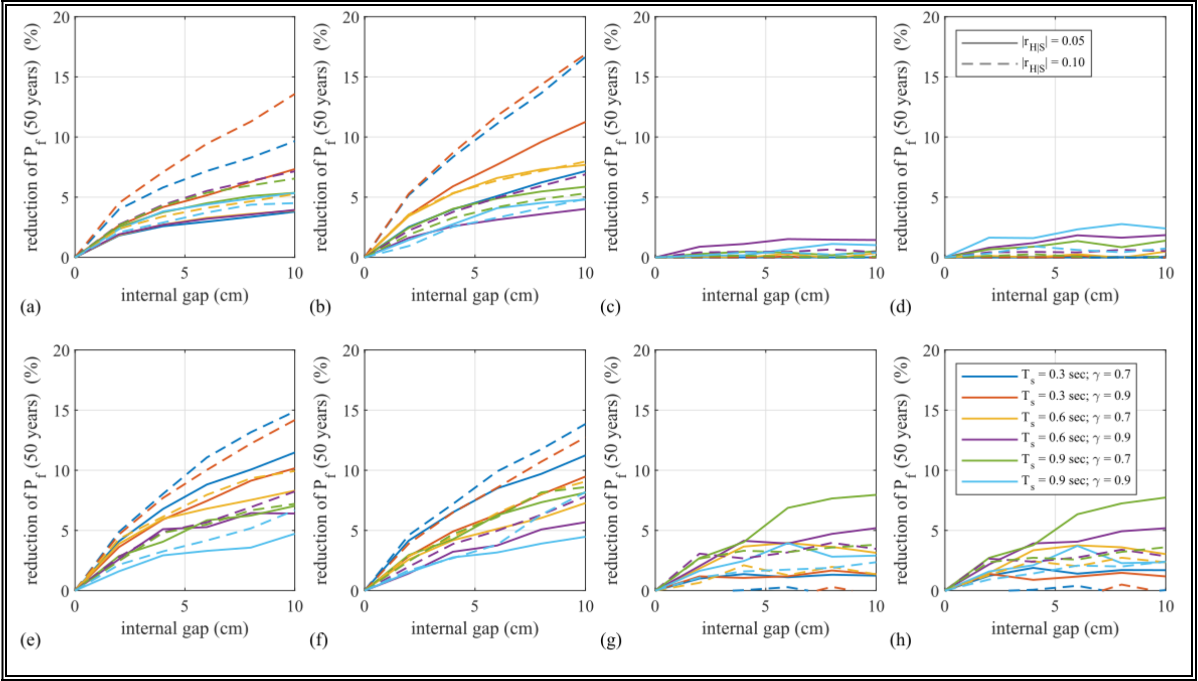

Figure 4-25: Reduction of the ductility demand for increasing values of internal gap of LIR-DCFP bearings for $R_I = 1.0$: (a) Hardening $\mathrm{LS}_\mu = 3$ and $T_b = 3$ sec; (b) Hardening $\mathrm{LS}_\mu = 5$ and $T_b = 3$ sec; (c) Softening $\mathrm{LS}_\mu = 3$ and $T_b = 3$ sec; (d) Softening $\mathrm{LS}_\mu = 5$ and $T_b = 3$ sec; (e) Hardening $\mathrm{LS}_\mu = 3$ and $T_b = 5$ sec; (f) Hardening $\mathrm{LS}_\mu = 5$ and $T_b = 5$ sec; (g) Softening $\mathrm{LS}_\mu = 3$ and $T_b = 5$ sec; (h) Softening $\mathrm{LS}_\mu = 5$ and $T_b = 5$ sec.

4.9 Conclusions

This paper describes the seismic reliability-based performance of nonlinear structures seismically isolated using frictional devices, highlighting the scenarios in which using Lateral Impact Double Concave Friction Pendulum (LIR-DCFP) bearings is recommended over DCFP bearings having the same size for both the plates and slider. This novel seismic isolator has been proposed as a solution to problems generated by the internal impact between the inner slider and the restraining rims of the isolators: the failure of this type of bearings and the dramatic rise in the ductility demand generated by internal lateral impacts. Within a wide parametric analysis, several elastic and inelastic properties of the superstructure and isolation system were considered, assuming the friction coefficients and characteristics of the seismic inputs as the relevant random variables. The superstructure was characterized by a 1dof system, exhibiting nonlinear behavior in the lateral direction. The post-yield stiffness of the superstructure was considered having hardening or softening post-yield lateral stiffness (not sensitive or sensitive to $P - \Delta$ effects). The isolation system was modeled using a rigid body approach that allows, among other physical phenomena, including the internal lateral impact behavior. A comparison between two frictional isolators were considered in the analysis: non-articulated DCFP and LIR-DCFP bearings. The lateral capacity of the isolation system and the inelastic properties of the superstructure were designed according to the criteria of the ASCE/SEI 7-16 standard.

For each considered isolated period, ten sets of 30 natural records scaled to match Conditional Spectra of a site in Riverside (California) were selected. Incremental Dynamic Analyses were performed to determine the statistics of the maximum base displacement of the upper sliding surface and ductility demand of the superstructure. The results of the IDAs were used to construct the seismic fragility curves related to different limit state thresholds. Finally, the seismic reliability curves of 1,152 equivalent seismically isolated systems equipped with DCFP or LIR-DCFP bearings, in a time frame of 50 years, were constructed. These curves were valuable to compare the seismic performance of the DCFP and LIR-DCFP devices with important design suggestions for the superstructure and internal gap.

In the studied cases with hardening post-yield stiffness (equipped with DCFP or LIR-DCFP bearings), an increment in the post-yield ratio leads to better seismic performance in terms of ductility demand thresholds. The opposite happens if softening behavior is exhibited. An increment in the absolute value of the post-yield softening stiffness generates a reduction of the seismic reliability. In cases in which the superstructure is designed to behave essentially elastic if the internal lateral capacity is not reached, better seismic performance is achieved using LIR-DCFP bearings. In these cases, an increment in the internal gap of the LIR-DCFP bearing, increasing the additional energy dissipation capacity and limiting the magnitude of impact forces, reduces the probabilities exceeding ductility demands thresholds. Considering superstructures with hardening post-yield behavior, the benefits of using the proposed seismic isolator are highlighted, especially, for low values of the period of the superstructure and low values of the mass distribution ratios. In the cases in which the yielding of the superstructure is allowed before the occurrence of the internal lateral impact, using LIR-DCFP bearings is recommended if the superstructure is stiff and has a relatively high post-yield hardening stiffness. In cases with softening behavior, the adverse effects of internal impacts are mitigated if the superstructure is designed to remain essentially elastic before the occurrence of the impact. However, not negligible benefits are achieved also for superstructures designed to exhibit the nonlinear softening behavior before the occurrence of the internal impact combined with low absolute values of the post-yield ratios. In cases in which the nonlinear behavior of the superstructure is exhibited before the occurrence of the lateral impact, the benefits of using the novel seismic isolator are reduced.

In general, better seismic performance is quite always achieved using LIR-DCFP bearings reaching reduction up to 20% in the probabilities exceeding ductility demand thresholds in a time frame of 50 years. These advantages derive from the presence of the internal gap with infinite curvature combined with the higher friction coefficient and are not necessarily achievable by increasing the size of classical DCFP devices.

4.10 Acknowledgements

This research has been funded by the National Agency for Research and Development (ANID) through the ANID-PCHA/Doctorado Nacional/2018-21180434 and the FONDECYT project N◦1201841, the authors are grateful for the support.

5. CONCLUSIONS

This research presents a numerical study on using two strategies to mitigate the adverse effects of internal lateral impacts. In structures equipped with frictional isolators, these impacts jeopardize the benefits of using seismic isolation by dramatically increasing the maximum inter-story drift, absolute acceleration, and shear-base responses. One of the most important causes of the failure of frictional bearings is the impact generated between the inner sliders and the restraining rims of sliding surfaces. Considering the problems driven by lateral impacts, the main two objectives of this investigation were:

i. Evaluate using variable curvature frictional isolators as an alternative to mitigate the mentioned negative consequences of internal impacts.

ii. Develop and evaluate a new configuration of multiple sliding surfaces frictional isolator capable of ensuring a better seismic performance under extreme seismic inputs that generate internal impacts.

This manuscript is divided into three parts. The first part (Chapter 2) evaluates the use of frictional bearing that exhibits “smooth-hardening” behavior at large lateral displacement as a solution to problems generated by the high-magnitude forces developed during internal impacts. This feature is achieved by constructing elliptical-shaped sliding surfaces. Instead of having a constant curvature (i.e., spherical shape), the studied passive adaptive frictional isolator has a sliding surface with a decreasing curvature for increasing the lateral displacement. This characteristic generates a soft rise of the pendular stiffness valuable to reduce the maximum base displacement demand. The second part of this research (Chapter

3) proposes a new seismic isolator denominated “Lateral Impact Resilient Double Concave Friction Pendulum” (LIR-DCFP) bearing. The suggested isolator, based on multiple sliding surfaces, has an enhanced slider with an internal gap capable of dissipating an additional amount of energy and limiting the maximum force generated during the internal impact. The third part of this research (Chapter 4) examines and evaluates the benefits of using the proposed new frictional bearing.

The first part of this thesis evaluated the use of variable curvature sliding surfaces to improve the seismic performance of base-isolated structures subjected to high-magnitude earthquakes. One specific geometry was studied generated by revolving an ellipse around a vertical axis. The curvature at the contact point between the slider and the sliding surface decreases as the inner slider moves away from the undeformed configuration of the isolator. This continuous decrease in curvature increases the pendular contribution of the lateral force transmitted by the device leading to a smooth-hardening behavior. The main idea of using this approach is to reduce the maximum base displacement demand, diminishing the probabilities of the occurrence of the internal lateral impacts.

A physical model of variable curvature frictional isolators was proposed and validated to perform non-linear dynamic analyses. Within a parametric analysis, 64 equivalent dynamics systems were studied to assess the effectivity of using frictional isolators with smooth-hardening behavior to mitigate the indicated problems. In cases with strong smooth-hardening behavior (i.e., fast changes in curvature), the average probability of observing the internal lateral impact in 50 years is reduced by 11% using the studied isolator. A reduction in the ductility demand is also observed in cases where the superstructure is designed to behave essentially elastic if the lateral impact does not occur. The reduction in the probabilities of exceeding ductility demand thresholds is highlighted for stiff superstructures and high values of the mass distribution ratio and hardening post-yield ratio.

One crucial problem arises if superstructures designed to exhibit the non-linear before the internal impact are equipped with a smooth-hardening frictional isolator. If large base displacements are demanded but without exceeding the lateral capacity of the isolation system, an undesired increment in the seismic forces transmitted to the superstructure is detected. This increment in the base shear raises the probabilities of exceeding limit state thresholds related to maximum ductility demand. Hence, in some cases, using frictional isolators with smooth-hardening behavior can lead to worse seismic performance.

Motivated by the detected limitation of using variable curvature isolators as an alternative to diminishing the magnitude of lateral impacts, in Chapter 3, a new frictional device is proposed. Unlike frictional devices with elliptical sliding surfaces, the use of LIR-DCFP bearing does not change the dynamic behavior of the base-isolated structure in the absence of lateral impacts. Hence, the same dynamic response is expected under standard seismic inputs if a structure is equipped with the classical Double Concave Friction Pendulum (DCFP) bearings or the proposed LIR-DCFP device. The main feature of the novel isolator is its enhanced inner slider which consists of two rigid bodies: the top slider and the bottom slider. These two pieces generate a plane high-frictional interface that is activated only in the presence of internal lateral impacts. If this condition is reached, a high-friction sliding will be produced, limiting the maximum force developed inside the isolator and dissipating a critical amount of energy. The energy dissipation capacity is defined by the internal gap that the bottom slider and the top slider leave inside the bearing. The larger the internal gap, the larger the energy dissipation capacity. It is possible to reduce the seismic loads that the superstructure must resist, dropping the maximum inter-story drift and absolute acceleration demands by using the novel frictional isolator.

The second part of the investigation (Chapter 3) presents a complete description of the lateral behavior of the LIR-DCFP bearing, describing the phases that characterize the device. A proper numerical model was required to evaluate the dynamics response of structures equipped with this new frictional device subjected to extreme ground motions. A three-dimensional formulation based on rigid body dynamics was developed. This approach allows accounting for essential modeling features such as lateral impact behavior, large displacement, $P-\Delta$ effects, kinematics constraints, uplift (even partial uplifting), among other phenomena. The forces developed inside the isolators are determined using contact-projection points couples. This strategy allows computing the forces transmitted inside the devices, allowing to represent the force distribution between the different pieces of the bearing. Since the numerical model is based on rigid body dynamics, parametric analysis concerning the geometry of the isolator can be conducted. This feature can help study the best geometrical configuration of the isolation devices, ensuring good seismic performance in terms of stability and optimal use of material.

A three-dimensional model of a reinforced concrete base-isolated structure was elaborated to show the advantages of using LIR-DCFP bearings as an alternative to using traditional isolators under extreme ground motions. This model was analyzed using three seismic records. Suppose LIR-DCFP devices are employed to achieve seismic isolation. In that case, mean reductions of 57% in the shear base, 48% in the maximum inter-story drift, and 58% in the maximum acceleration responses are reached.

The final phase of this research (Chapter 4) presents an assessment of the seismic performance of structures equipped with LIR-DCFP bearings. The seismic performance of base-isolated structures isolated through the suggested frictional device was compared with the performance of buildings isolated with classical frictional bearings (i.e., DCFP bearings) to determine the improvement in the dynamic response under extreme seismic loads.

A comprehensive parametric analysis was performed using equivalent numerical models. The isolation system was modeled considering one isolator and employing the numerical formulation based on rigid body dynamics presented in Chapter 3. The superstructure was modeled as a non-linear system using a Bouc-Wen element. Within the parametric analysis, different properties were considered as the relevant parameters: superstructure period, isolated period, mass ratio, numerical coefficient related to the type of seismic force-resisting system above the isolation system, hardening or softening post-yield ratio, and the size of the internal gap of LIR-DCFP bearings. In total, 1,152 equivalent models were assessed. The main objective of this parametric analysis was to determine the structural properties that highlight the benefits of using the novel suggested isolator.

An Incremental Dynamic Analysis (IDA) was performed for each equivalent model, considering the friction coefficient as a random variable by sampling the friction coefficient at large velocity using the Latin Hypercube Sampling method. The uncertainties of the seismic input were accounted for by selecting ten sets of 30 seismic records matching conditional spectra. With the data generated in the IDAs, fragility curves were constructed. These fragility curves were defined for limit states threshold related to the maximum base displacement response and maximum ductility demand. Using the derived fragility curves, the hazard curves, and assuming Poisson's distributions, seismic reliability curves linked to each equivalent system were obtained. These reliability curves were an excellent tool to determine the improvement of the seismic performance if the isolation system is formed by LIR-DCFP bearings.

The reliability curves related to maximum base displacement thresholds gave important information about under what scenario using the developed isolator is recommendable. In general, if the non-linear behavior of the superstructure is exhibited before the occurrence of the lateral impact, a reduction of maximum base displacement demand is observed. Hence, the probabilities of observing the internal impact are reduced, and the benefits of using a device resistant to this condition will not produce a significant difference. This phenomenon is evident for flexible superstructures and buildings sensitive to $P-\Delta$ effects (i.e., softening post-yield behavior).

Some interesting conclusions can be made by analyzing the obtained reliability curves related to maximum ductility demand thresholds. Since LIR-DCFP bearings limit the maximum force transmitted to the superstructure if an internal impact is observed, better seismic performance is obtained by using the novel frictional isolator, especially if the superstructure is designed to behave elastically under the maximum considered earthquake. This statement is true even for a small internal gap size of 2 cm. For superstructures designed using a unitary numerical coefficient related to the type of seismic force-resisting system above the isolation system, an increment of the size of the internal gap of LIR-DCFP bearings leads to better seismic performance. The increment of the internal gap leads to a rise in the energy dissipation capacity that is expressed in lower ductility demands. This improvement in seismic performance is observed even for superstructures designed to exhibit the non-linear range before the internal impact. This enhancement is important for cases with high hardening post-yield ratios.

In general, LIR-DCFP bearings are recommended for stiff superstructures with low values of mass ratio and high values of hardening post-yield stiffness. The novel device can achieve reductions up to 20% in the probabilities of exceeding limit state thresholds in a time frame of 50 years related to maximum ductility demand. It is important to mention that, since the high-friction sliding is triggered only after an internal impact, for seismic inputs with low magnitude, the seismic performance of structures equipped with LIR-DCFP bearings is the same that using DCFP isolators. Furthermore, in no case, under high-magnitude ground motions, a worse seismic performance was obtained using the suggested isolator.

In summary, two approaches were analyzed to mitigate the adverse effects of internal lateral impacts in structures equipped with frictional isolators. The first studied alternative was to employ variable curvature sliding surfaces with smooth-hardening behavior. Although this strategy decreases the probability of observing internal impacts, the increasing stiffness of these devices can negatively affect the seismic performance of dynamic systems. Using LIR-bearings, the second assessed alternative, is a better method. The new frictional isolator ensures an equal or better seismic performance than classical frictional devices. These two approaches can be used simultaneously, taking advantage of the features of each one. The data generated on this investigation suggest that using LIR-DCFP bearings is an effective way to construct safer projects (or retrofitting constructed structures), advancing in the development of one of the most effective ways of protecting buildings and infrastructure: seismic isolation.

This research presents numerical results of evaluating the described alternatives to mitigate the adverse effects of internal lateral impacts. Experimental data must support the conclusions of this study. As future work, experimental tests of both analyzed frictional isolators must be performed. The assessment of the benefits of using the new seismic isolator was done using equivalent models. The next step for future studies should be to analyze more complex dynamic systems. In Chapter 3, a new frictional isolator was introduced, the Impact Resilient Double Concave Friction Pendulum (IR-DCFP) bearing. In addition to resisting lateral impacts, this device has been created to resist vertical impacts. In the future, numerical models for dynamic analyses of the IR-DCFP bearing should be developed. In addition to the numerical models, experimental tests should accompany the generated data.

BIBLIOGRAPHY

Adam, C., Ibarra, L. F., & Krawinkler, H. (2004). Evaluation of P-delta effects in non-deteriorating MDOF structures from equivalent SDOF systems. *13th World Conference on Earthquake Engineering*. http://www.iitk.ac.in/nicee/wcee/article/13_3407.pdf

Almazán, José L., & De la Llera, J. C. (2003). Physical model for dynamic analysis of structures with FPS isolators. *Earthquake Engineering and Structural Dynamics*, *32*(8), 1157–1184. https://doi.org/10.1002/eqe.266

Almazán, José Luis. (2001). *Torsión accidental y natural en estructuras aisladas con el sistema de péndulo friccional*. Pontificia Universidad Católica de Chile.

Anagnostopoulos, S. A. (2004). Equivalent viscous damping for modeling inelastic impacts in earthquake pounding problems. *Earthquake Engineering & Structural Dynamics*, *33*(8), 897–902. https://doi.org/10.1002/eqe.377

ASCE. (2016). Minimum Design Loads and Associated Criteria for Buildings and Other Structures. *ASCE/SEI 7-16*. https://doi.org/10.1016/B978-0-7234-5558-5.00006-3

Asher, J. W., Young, R. P., & Ewing, R. D. (1996). Seismic isolation design of the San Bernardino County Medical Center replacement project. *The Structural Design of Tall Buildings*, *5*(4), 265–279. https://doi.org/10.1002/(SICI)1099-1794(199612)5:4<265::AID-TAL77>3.0.CO;2-X

Auad, G. A., & Almazán, J. L. (2017). Non linear vertical-rocking isolation system: Application to legged wine storage tanks. *Engineering Structures*, *152*. https://doi.org/10.1016/j.engstruct.2017.09.061

Auad, G., & Almazán, J. L. (2021). Lateral Impact Resilient double concave Friction Pendulum (LIR-DCFP) bearing: Formulation, parametric study of the slider and three-dimensional numerical example. *Engineering Structures*, *233*. https://doi.org/10.1016/j.engstruct.2021.111892

Baker, J. W. (2011). Conditional Mean Spectrum: Tool for Ground-Motion Selection. *Journal of Structural Engineering*, *137*(3), 322–331. https://doi.org/10.1061/(asce)st.1943-541x.0000215

Baker, J. W., & Jayaram, N. (2008). Correlation of spectral acceleration values from NGA ground motion models. *Earthquake Spectra*, *24*(1), 299–317. https://doi.org/10.1193/1.2857544

Baker, J. W., & Lee, C. (2018). An Improved Algorithm for Selecting Ground Motions to Match a Conditional Spectrum. *Journal of Earthquake Engineering*, *22*(4), 708–723. https://doi.org/10.1080/13632469.2016.1264334

Bao, Y., & Becker, T. (2019). Three-dimensional double friction pendulum bearing model including uplift and impact behavior: Formulation and numerical example. *Engineering Structures*, *199*(March), 109579. https://doi.org/10.1016/j.engstruct.2019.109579

Bao, Y., & Becker, T. C. (2018a). Effect of Design Methodology on Collapse of Friction Pendulum Isolated Moment-Resisting and Concentrically Braced Frames. *Journal of Structural Engineering*, *144*(11), 04018203. https://doi.org/10.1061/(asce)st.1943-541x.0002183

Bao, Y., & Becker, T. C. (2018b). Effect of Design Methodology on Collapse of Friction

Pendulum Isolated Moment-Resisting and Concentrically Braced Frames. *Journal of Structural Engineering*, *144*(11), 04018203. https://doi.org/10.1061/(ASCE)ST.1943-541X.0002183

Bao, Y., & Becker, T. C. (2018c). Inelastic response of base-isolated structures subjected to impact. *Engineering Structures*, *171*, 86–93. https://doi.org/10.1016/j.engstruct.2018.05.091

Bao, Y., Becker, T. C., & Hamaguchi, H. (2017). Failure of double friction pendulum bearings under pulse-type motions. *Earthquake Engineering and Structural Dynamics*, *46*(5), 715–732. https://doi.org/10.1002/eqe.2827

Bao, Y., Becker, T. C., Sone, T., & Hamaguchi, H. (2018). To limit forces or displacements: Collapse study of steel frames isolated by sliding bearings with and without restraining rims. *Soil Dynamics and Earthquake Engineering*, *112*(December 2017), 203–214. https://doi.org/10.1016/j.soildyn.2018.05.006

Bazzurro, P., Cornell, A., Member, Z., Asce, N., Shome, /, & Carballo, J. E. (n.d.). *Three proposals for characterizing MDOF nonlinear seismic response*.

Becker, T. C., Bao, Y., & Mahin, S. A. (2017). Extreme behavior in a triple friction pendulum isolated frame. *Earthquake Engineering and Structural Dynamics*, *46*(15), 2683–2698. https://doi.org/10.1002/eqe.2924

Becker, T. C., & Mahin, S. A. (2012). Experimental and analytical study of the bi-directional behavior of the triple friction pendulum isolator. *Earthquake Engineering & Structural Dynamics*, *41*(3), 355–373. https://doi.org/10.1002/eqe.1133

Boore, D. M., Stewart, J. P., Seyhan, E., & Atkinson, G. M. (2014). NGA-West2 equations for predicting PGA, PGV, and 5% damped PSA for shallow crustal earthquakes. *Earthquake Spectra*, *30*(3), 1057–1085. https://doi.org/10.1193/070113EQS184M

Braun, C. (2009). The sliding isolation pendulum - an improved recentring bridge bearing. *Steel Construction*, *2*(3), 203–206. https://doi.org/10.1002/stco.200910025

Calvi, P. M., David, •, & Ruggiero, M. (n.d.). *Numerical modelling of variable friction sliding base isolators*. https://doi.org/10.1007/s10518-015-9834-y

Castaldo, P., & Alfano, G. (2020). Seismic reliability-based design of hardening and softening structures isolated by double concave sliding devices. *Soil Dynamics and Earthquake Engineering*, *129*, 105930. https://doi.org/10.1016/j.soildyn.2019.105930

Castaldo, P., Palazzo, B., & Della Vecchia, P. (2015). Seismic reliability of base-isolated structures with friction pendulum bearings. *Engineering Structures*, *95*, 80–93. https://doi.org/10.1016/j.engstruct.2015.03.053

Castaldo, P., Palazzo, B., & Della Vecchia, P. (2016). Life-cycle cost and seismic reliability analysis of 3D systems equipped with FPS for different isolation degrees. *Engineering Structures*, *125*, 349–363. https://doi.org/10.1016/j.engstruct.2016.06.056

Castaldo, P., & Ripani, M. (2016). Optimal design of friction pendulum system properties for isolated structures considering different soil conditions. *Soil Dynamics and Earthquake Engineering*, *90*, 74–87. https://doi.org/10.1016/j.soildyn.2016.08.025

Castaldo, Paolo, Amendola, G., & Palazzo, B. (2017). Seismic fragility and reliability of structures isolated by friction pendulum devices: seismic reliability-based design (SRBD). *Earthquake Engineering and Structural Dynamics*, *46*(3), 425–446. https://doi.org/10.1002/eqe.2798

Castaldo, Paolo, Gino, D., Bertagnoli, G., & Mancini, G. (2020). Resistance model uncertainty in non-linear finite element analyses of cyclically loaded reinforced concrete systems. *Engineering Structures*, *211*(February), 110496. https://doi.org/10.1016/j.engstruct.2020.110496

Castaldo, Paolo, Gino, D., & Mancini, G. (2019). Safety formats for non-linear finite element analysis of reinforced concrete structures: discussion, comparison and proposals. *Engineering Structures*, *193*(April), 136–153. https://doi.org/10.1016/j.engstruct.2019.05.029

Castaldo, Paolo, Palazzo, B., Alfano, G., & Palumbo, M. F. (2018). Seismic reliability-based ductility demand for hardening and softening structures isolated by friction pendulum bearings. *Structural Control and Health Monitoring*, *25*(11), 2256. https://doi.org/10.1002/stc.2256

Castaldo, Paolo, Palazzo, B., & Ferrentino, T. (2017). Seismic reliability-based ductility demand evaluation for inelastic base-isolated structures with friction pendulum devices. *Earthquake Engineering and Structural Dynamics*, *46*(8), 1245–1266. https://doi.org/10.1002/eqe.2854

Castaldo, Paolo, & Tubaldi, E. (2015). Influence of FPS bearing properties on the seismic performance of base-isolated structures. *Earthquake Engineering and Structural Dynamics*, *44*(15), 2817–2836. https://doi.org/10.1002/eqe.2610

Celarec, D., & Dolšek, M. (2013). The impact of modelling uncertainties on the seismic performance assessment of reinforced concrete frame buildings. *Engineering Structures*, *52*, 340–354. https://doi.org/10.1016/j.engstruct.2013.02.036

Chimamphant, S., & Kasai, K. (2016). Comparative response and performance of base-isolated and fixed-base structures. *Earthquake Engineering & Structural Dynamics*, *45*(1), 5–27. https://doi.org/10.1002/eqe.2612

Chopra, A. K. (1995). Dynamics of Structures: Theory and Applications to Earthquake Engineering. In *Dynamics of Structures*. Prentice Hall. https://doi.org/10.1193/1.2720354

Colombo, J. I., & Almazán, J. L. (2017). Seismic reliability of legged wine storage tanks retrofitted by means of a seismic isolation device. *Engineering Structures*, *134*, 303–316. https://doi.org/10.1016/j.engstruct.2016.12.058

Constantinou, M. C., Whittaker, A. S., Kalpakidis, Y., Fenz, D. M., & Warn, G. P. (2007). Performance of Seismic Isolation Hardware under Service and Seismic Loading. *Mceer-07-0012*, 471.

Constantinou, M., Mokha, A., & Reinhorn, A. (1990). Teflon Bearings in Base Isolation II: Modeling. *Journal of Structural Engineering*, *116*(2), 455–474. https://doi.org/10.1061/(ASCE)0733-9445(1990)116:2(455)

Constantinou, M., Mokha, A., & Reinhorn, A. (2007). Teflon Bearings in Base Isolation II: Modeling. *Journal of Structural Engineering*. https://doi.org/10.1061/(asce)0733-9445(1990)116:2(455)

De Baets, P., Ost, W., Samyn, P., Schoukens, G., & Van Parys, F. (2002). The friction and wear of different polymers under high-load conditions. *Journal of Synthetic Lubrication*, *19*(2), 109–118. https://doi.org/10.1002/jsl.3000190203

Fenz, D. M., & Constantinou, M. C. (2006). Behaviour of the double concave Friction Pendulum bearing. *Earthquake Engineering & Structural Dynamics*, *35*(11), 1403–1424. https://doi.org/10.1002/eqe.589

Fenz, D. M., & Constantinou, M. C. (2008a). Spherical sliding isolation bearings with adaptive behavior: Experimental verification. *Earthquake Engineering & Structural Dynamics*, *37*(2), 185–205. https://doi.org/10.1002/eqe.750

Fenz, D. M., & Constantinou, M. C. (2008b). Spherical sliding isolation bearings with adaptive behavior: Theory. *Earthquake Engineering & Structural Dynamics*, *37*(2), 163–183. https://doi.org/10.1002/eqe.751

Fenz, D. M., & Constantinou, M. C. (2008c). Modeling triple friction pendulum bearings for response-history analysis. *Earthquake Spectra*, *24*(4), 1011–1028. https://doi.org/10.1193/1.2982531

Gidaris, I., Taflanidis, A. A., Lopez-Garcia, D., & Mavroeidis, G. P. (2016). Multi-objective risk-informed design of floor isolation systems. *Earthquake Engineering & Structural Dynamics*, *45*(8), 1293–1313. https://doi.org/10.1002/eqe.2708

Gupta, A. (1999). *Seismic demands for performance evaluation of steel moment resisting frame structures*. Stanford University. https://search.proquest.com/openview/ef7a72fac33b77666ffdc583ad1714da/1?pq-origsite=gscholar&cbl=18750&diss=y

Hall, J. F., Heaton, T. H., Halling, M. W., & Wald, D. J. (1995a). Near-Source Ground Motion and its Effects on Flexible Buildings. *Earthquake Spectra*, *11*(4), 569–605. https://doi.org/10.1193/1.1585828

Hall, J. F., Heaton, T. H., Halling, M. W., & Wald, D. J. (1995b). Near-Source Ground Motion and its Effects on Flexible Buildings. *Earthquake Spectra*, *11*(4), 569–605. https://doi.org/10.1193/1.1585828

Han, Q., Liang, X., Wen, J., Zhang, J., Du, X., & Wang, Z. (2020). Multiple-variable frequency pendulum isolator with high-performance materials. *Smart Materials and Structures*, *29*(7), 075002. https://doi.org/10.1088/1361-665X/AB8749

Hunt, B. R., Lipsman, R. L., Rosenberg, J. M., Coombes, K. R., Osborn, J. E., & Stuck, G. J. (2006). A Guide to MATLAB ® . In *A Guide to MATLAB ®* . https://doi.org/10.1017/cbo9780511791284

Jangid, R. S. (2005). Optimum friction pendulum system for near-fault motions. *Engineering Structures*, *27*(3), 349–359. https://doi.org/10.1016/j.engstruct.2004.09.013

Jangid, R. S., & Kelly, J. M. (2001a). Base isolation for near-fault motions. *Earthquake Engineering & Structural Dynamics*, *30*(5), 691–707. https://doi.org/10.1002/eqe.31

Jangid, R. S., & Kelly, J. M. (2001b). Base isolation for near-fault motions. *Earthquake Engineering & Structural Dynamics*, *30*(5), 691–707. https://doi.org/10.1002/eqe.31

Jónsson, M. H., Bessason, B., & Haflidason, E. (2010). Earthquake response of a base-isolated bridge subjected to strong near-fault ground motion. *Soil Dynamics and Earthquake Engineering*, *30*(6), 447–455. https://doi.org/10.1016/j.soildyn.2010.01.001

Kelly, J. M. (1993). Earthquake-Resistant Design with Rubber. In *Earthquake-Resistant Design with Rubber* (1st ed.). Springer London. https://doi.org/10.1007/978-1-4471-3359-9

Kelly, J. M. (1999). The role of damping in seismic isolation. *Earthquake Engineering & Structural Dynamics*, *28*(1), 3–20. https://doi.org/10.1002/(SICI)1096-9845(199901)28:1<3::AID-EQE801>3.0.CO;2-D

Kikuchi, M., Black, C. J., & Aiken, I. D. (2008). On the response of yielding seismically isolated structures. *Earthquake Engineering and Structural Dynamics*, *37*(5), 659–

679. https://doi.org/10.1002/eqe.777

Kitayama, S., & Constantinou, M. C. (2019a). Effect of displacement restraint on the collapse performance of seismically isolated buildings. *Bulletin of Earthquake Engineering 2019 17:5*, *17*(5), 2767–2786. https://doi.org/10.1007/S10518-019-00554-Y

Kitayama, S., & Constantinou, M. C. (2019b). Probabilistic seismic performance assessment of seismically isolated buildings designed by the procedures of ASCE/SEI 7 and other enhanced criteria. *Engineering Structures*, *179*, 566–582. https://doi.org/10.1016/J.ENGSTRUCT.2018.11.014

Komodromos, P. (2008). Simulation of the earthquake-induced pounding of seismically isolated buildings. *Computers and Structures*, *86*(7–8), 618–626. https://doi.org/10.1016/j.compstruc.2007.08.001

Le, T. N., Battini, J. M., & Hjiaj, M. (2011). Efficient formulation for dynamics of corotational 2D beams. *Computational Mechanics*, *48*(2), 153–161. https://doi.org/10.1007/s00466-011-0585-6

Lee, H.-H. (2018). *Finite element simulations with ansys workbench 18*. SDC PUBNS. https://books.google.es/books?hl=es&lr=&id=LdNTDwAAQBAJ&oi=fnd&pg=PP2&dq=Finite+element+simulations+with+ANSYS+Workbench+17&ots=m6IZ7O409c&sig=gWnuYTWU-zZyUXmEYtFJIfh0950#v=onepage&q=Finite element simulations with ANSYS Workbench 17&f=false

Lin, S.-C., Han, J.-Q., & Zhao, H.-T. (2020). Experimental and Theoretical Studies of Bidirectional Variable Curvature Friction Pendulum Bearing. *KSCE Journal of Civil Engineering*, *24*(5), 1568–1580. https://doi.org/10.1007/s12205-020-1525-9

Lin, T., Haselton, C. B., & Baker, J. W. (2013a). Conditional spectrum-based ground motion selection. Part I: Hazard consistency for risk-based assessments. *Earthquake Engineering and Structural Dynamics*, *42*(12), 1847–1865. https://doi.org/10.1002/eqe.2301

Lin, T., Haselton, C. B., & Baker, J. W. (2013b). Conditional spectrum-based ground motion selection. Part I: Hazard consistency for risk-based assessments. *Earthquake Engineering & Structural Dynamics*, *42*(12), 1847–1865. https://doi.org/10.1002/eqe.2301

Lin, T., Haselton, C. B., & Baker, J. W. (2013c). Conditional spectrum-based ground motion selection. Part II: Intensity-based assessments and evaluation of alternative target spectra. *Earthquake Engineering and Structural Dynamics*, *42*(12), 1867–1884. https://doi.org/10.1002/eqe.2303

Lin, T., Haselton, C. B., & Baker, J. W. (2013d). Conditional spectrum-based ground motion selection. Part II: Intensity-based assessments and evaluation of alternative target spectra. *Earthquake Engineering & Structural Dynamics*, *42*(12), 1867–1884. https://doi.org/10.1002/eqe.2303

Lu, L.-Y., Lee, T.-Y., & Yeh, S.-W. (2011). Theory and experimental study for sliding isolators with variable curvature. *Earthquake Engineering & Structural Dynamics*, *40*(14), 1609–1627. https://doi.org/10.1002/eqe.1106

Lu, L. Y., Huang, H. W., Wu, Y., & Wang, S. J. (2021). Theory and experimental verification of a double sliding isolator with variable curvature. *Engineering Structures*, *238*, 112265. https://doi.org/10.1016/J.ENGSTRUCT.2021.112265

Lu, L. Y., Lee, T. Y., Juang, S. Y., & Yeh, S. W. (2013). Polynomial friction pendulum isolators (PFPIs) for building floor isolation: An experimental and theoretical study. *Engineering Structures*, *56*, 970–982. https://doi.org/10.1016/j.engstruct.2013.06.016

M.C.Constantinou, P.Tsopelas, Kim, Y.-S., & S.Okamoto. (1993). *NCEER-Taisei Corporation Research Program on Sliding Seismic Isolation Systems for Bridges: Experimental and Analytical Study of a Friction Pendulum System (FPS)*. 180. c:%5CCS%5Call refs%5Ctechnical%5CMCEER reports%5C93-0020.pdf

Mavronicola, E. A., Polycarpou, P. C., & Komodromos, P. (2017). *Spatial seismic modeling of base-isolated buildings pounding against moat walls : effects of ground motion directionality and mass eccentricity*. *December 2016*, 1161–1179. https://doi.org/10.1002/eqe

Mazza, F. (2018). Seismic demand of base-isolated irregular structures subjected to pulse-type earthquakes. *Soil Dynamics and Earthquake Engineering*, *108*(August 2017), 111–129. https://doi.org/10.1016/j.soildyn.2017.11.030

Mazza, F., Mazza, M., & Vulcanob, A. (2017). Nonlinear response of r.c. framed buildings retrofitted by different base-isolation systems under horizontal and vertical components of near-fault earthquakes. *Earthquake and Structures*, *12*(1), 135–144. https://doi.org/10.12989/eas.2017.12.1.135

Mazza, F., & Vulcano, A. (2012). Effects of near-fault ground motions on the nonlinear dynamic response of base-isolated r.c. framed buildings. *Earthquake Engineering & Structural Dynamics*, *41*(2), 211–232. https://doi.org/10.1002/eqe.1126

Mazzoni, S., McKenna, F., Scott, M. H., & Fenves, G. L. (2006). Open System for Earthquake Engineering Simulation (OpenSEES) User Command-Language Manual. *Pacific Earthquake Engineering Research Center*, 465.

McKay, M. D., Beckman, R. J., & Conover, W. J. (2000). A comparison of three methods for selecting values of input variables in the analysis of output from a computer code. *Technometrics*, *42*(1), 55–61. https://doi.org/10.1080/00401706.2000.10485979

Mokha, A., Constantinou, M., & Reinhorn, A. (1990). Teflon Bearings in Base Isolation I: Testing. *Journal of Structural Engineering*, *116*(2), 438–454. https://doi.org/10.1061/(ASCE)0733-9445(1990)116:2(438)

Morgan, T. A., & Mahin, S. A. (2010). Achieving reliable seismic performance enhancement using multi-stage friction pendulum isolators. *Earthquake Engineering & Structural Dynamics*, *39*(13), 1443–1461. https://doi.org/10.1002/eqe.1043

Murnal, P., & Sinha, R. (2002). Earthquake resistant design of structures using the variable frequency pendulum isolator. *Journal of Structural Engineering*, *128*(7), 870–880. https://doi.org/10.1061/(ASCE)0733-9445(2002)128:7(870)

Naeim, F., & Kelly, J. (1999). *Design of seismic isolated structures: from theory to practice*.

Nagarajaiah, S., Reinhorn, A. M., & Constantinou, M. C. (1991). Nonlinear Dynamic Analysis of 3-D-Base-Isolated Structures. *Journal of Structural Engineering*, *117*(7), 2035–2054. https://doi.org/10.1061/(ASCE)0733-9445(1991)117:7(2035)

Nagarajaiah, S., & Xiaohong, S. (2000). Response of Base-Isolated USC Hospital Building in Northridge Earthquake. *Journal of Structural Engineering*, *126*(10), 1177–1186. https://doi.org/10.1061/(ASCE)0733-9445(2000)126:10(1177)

Palazzo, B. (1991). Seismic behavior of base isolated buildings. *International Meeting on Earthquake Protection of Buildings, Ancona*.

Panchal, V. R., & Jangid, R. S. (2008). Variable friction pendulum system for seismic isolation of liquid storage tanks. *Nuclear Engineering and Design*, *238*(6), 1304–1315. https://doi.org/10.1016/j.nucengdes.2007.10.011

Panchal, V. R., & Jangid, R. S. (2009). Seismic response of structures with variable friction pendulum system. *Journal of Earthquake Engineering*, *13*(2), 193–216. https://doi.org/10.1080/13632460802597786

Park, Y. J., Wen, Y. K., & Ang, A. H.-S. (1986). Random vibration of hysteretic systems under bi-directional ground motions. *Earthquake Engineering & Structural Dynamics*, *14*(4), 543–557. https://doi.org/10.1002/eqe.4290140405

PEER, P. E. E. R. C. (2013). *PEER Ground Motion Database*. Shallow Crustal Earthquakes in Active Tectonic Regimes, NGA-West2.

Polycarpou, P. C., & Komodromos, P. (2010). Earthquake-induced poundings of a seismically isolated building with adjacent structures. *Engineering Structures*, *32*(7), 1937–1951. https://doi.org/10.1016/j.engstruct.2010.03.011

Pranesh, M., & Sinha, R. (2000). VFPI: An isolation device for aseismic design. *Earthquake Engineering and Structural Dynamics*, *29*(5), 603–627. https://doi.org/10.1002/(SICI)1096-9845(200005)29:5<603::AID-EQE927>3.0.CO;2-W

Quaglini, V., Dubini, P., & Poggi, C. (2012). Experimental assessment of sliding materials for seismic isolation systems. *Bulletin of Earthquake Engineering*, *10*(2), 717–740. https://doi.org/10.1007/s10518-011-9308-9

Ricker, N. (1944). Wavelet Functions and Their Polynomials. *Geophysics*, *9*(3), 314–323. https://doi.org/10.1190/1.1445082

Sarlis, A. A., & Constantinou, M. C. (2016). A model of triple friction pendulum bearing for general geometric and frictional parameters. *Earthquake Engineering & Structural Dynamics*, *45*(11), 1837–1853. https://doi.org/10.1002/eqe.2738

Shahbazi, P., & Taghikhany, T. (2017). Sensitivity analysis of variable curvature friction pendulum isolator under near-fault ground motions. *Smart Structures and Systems*, *20*(1), 23–33. https://doi.org/10.12989/sss.2017.20.1.023

Shaikhzadeh, A. A., & Karamoddin, A. (2016). Effectiveness of sliding isolators with variable curvature in near-fault ground motions. *Structural Design of Tall and Special Buildings*, *25*(6), 278–296. https://doi.org/10.1002/tal.1258

Shang, J., Tan, P., Zhang, Y., Han, J., & Qin, J. (2021). *Experimental and analytical investigation of variable friction pendulum isolator*. https://doi.org/10.1016/j.engstruct.2021.112575

Shenton, H. W., & Lin, A. N. (1993). Relative Performance of Fixed-Base and Base-Isolated Concrete Frames. *Journal of Structural Engineering*, *119*(10), 2952–2968. https://doi.org/10.1061/(ASCE)0733-9445(1993)119:10(2952)

Tsai, C. S., Chen, W.-S., Chiang, T.-C., & Chen, B.-J. (2006). Component and shaking table tests for full-scale multiple friction pendulum system. *Earthquake Engineering & Structural Dynamics*, *35*(13), 1653–1675. https://doi.org/10.1002/eqe.598

Tsai, C. S., Chen, W. S., & Lu, P. C. (2006). Shaking table tests of a building isolated with trench friction pendulum system. *American Society of Mechanical Engineers, Pressure Vessels and Piping Division (Publication) PVP*, *2006*, 169–173. https://doi.org/10.1115/PVP2006-ICPVT-11-93253

Tsai, C. S., Chiang, T. C., & Chen, B. J. (2003). Finite element formulations and theoretical study for variable curvature friction pendulum system. *Engineering*

Structures, *25*(14), 1719–1730. https://doi.org/10.1016/S0141-0296(03)00151-2

Tsai, C. S., & Lin, Y. C. (2009). Mechanical characteristics and modeling of multiple trench friction pendulum system with multi-intermediate sliding plates. *World Academy of Science, Engineering and Technology*, *38*, 347–364.

Tsai, C. S., Lin, Y. C., & Su, H. C. (2010). Characterization and modeling of multiple friction pendulum isolation system with numerous sliding interfaces. *Earthquake Engineering & Structural Dynamics*, *39*(13), 1463–1491. https://doi.org/10.1002/eqe.1044

Tsiavos, A., Markic, T., Schlatter, D., & Stojadinovic, B. (2021). Shaking table investigation of inelastic deformation demand for a structure isolated using friction-pendulum sliding bearings. *Structures*, *31*(February), 1041–1052. https://doi.org/10.1016/j.istruc.2021.02.040

Unified Hazard Tool. (n.d.). Retrieved June 17, 2021, from https://earthquake.usgs.gov/hazards/interactive/

Vassiliou, M. F., Tsiavos, A., & Stojadinović, B. (2013). Dynamics of inelastic base-isolated structures subjected to analytical pulse ground motions. *Earthquake Engineering and Structural Dynamics*, *42*(14), 2043–2060. https://doi.org/10.1002/eqe.2311

Vořechovský, M., & Novák, D. (2009). Correlation control in small-sample Monte Carlo type simulations I: A simulated annealing approach. *Probabilistic Engineering Mechanics*, *24*(3), 452–462. https://doi.org/10.1016/j.probengmech.2009.01.004

Wang, L. W., & Lu, L. Y. (2018). Generic 3D formulation for sliding isolators with variable curvature and its experimental verification. *Engineering Structures*, *177*, 12–29. https://doi.org/10.1016/J.ENGSTRUCT.2018.09.038

Weber, F., Obholzer, F., Huber, P., Hartinger, M., Meier, L., Distl, J., & Braun, C. (2018). New Adaptive Curved Surface Slider for Enhanced Structural Isolation, Reduced Displacement Capacity. *16th European Conference on Earthquake Engineering, 18-21 June*.

Wen, Y. K. (1976). Method for Random Vibration of Hysteretic Systems. *ASCE J Eng Mech Div*, *102*(2), 249–263. https://doi.org/10.1061/jmcea3.0002106

Zayas, V. A., Low, S. S., & Mahin, S. A. (1990). A Simple Pendulum Technique for Achieving Seismic Isolation. *Earthquake Spectra*, *6*(2), 317–333. https://doi.org/10.1193/1.1585573

APPENDICES

A. APPENDIX A: PRELIMINARY EXPERIMENTAL TEST OF AN SH-FPS DEVICE

In this Appendix, the results of a preliminary experimental test conducted to validate the smooth hardening behavior of variable curvature frictional isolators with sliding surfaces obtained by revolving a plane ellipse around a vertical axis are presented. The experimental test was performed using an isolator with two identical sliding surfaces. The parameters of the plane ellipse used to create the variable curvature surface are $a = 180$ mm and $b = 43.2$ mm. In Figure A-1, photographs of the experimental setup and the tested prototype are shown.

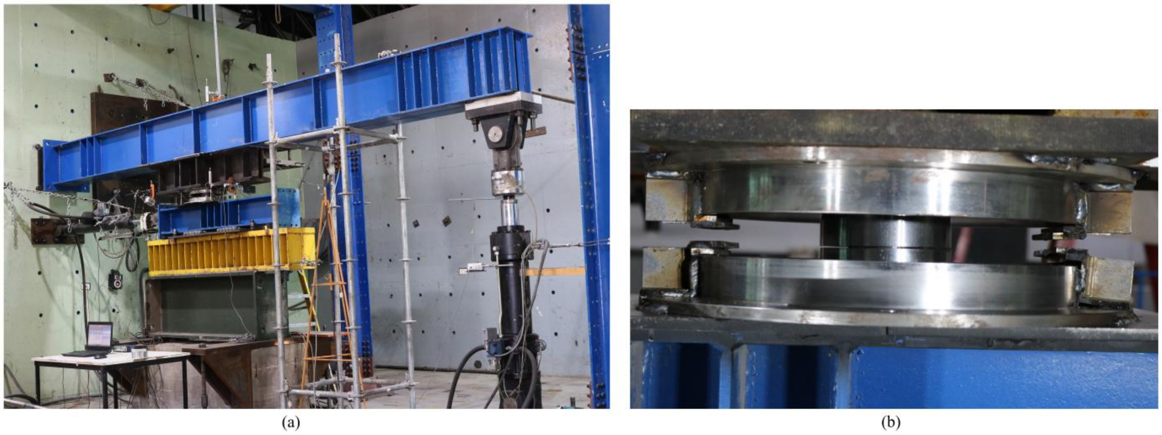
(a)
(b)

Figure A-1: Experimental test: (a) Experimental setup. (b) Tested prototype

The experimental test was divided into two stages. First, a vertical load of 90 kN was applied on the bearing employing a vertical actuator. Then, nine cycles of lateral displacement were imposed using an actuator horizontally orientated. The lateral displacement was imposed at a constant velocity, producing triangular-shaped waves (see Figure A-2(a)). The amplitude of the controlled displacement cycles was increased starting from 45 mm, following with an amplitude of 90 mm, and ending with an amplitude of 180 mm. Three cycles were imposed at each different amplitude. A Finite Element Model (FEM) of the tested variable curvature isolator was developed to reproduce the experimental results. A comparison between the hysteretic loops obtained in the experimental test and the numerical model results is presented in Figure A-2(b). It is possible to note that, at small lateral displacement (45 mm and 90 mm), the lateral behavior is similar to the behavior exhibited by constant curvature frictional isolators. In contrast, if large displacements are imposed (180 mm), the hardening stage is observed. This experimental test validates the presence of the smooth hardening feature that differentiates SH-FPS bearings from isolators with spherical sliding surfaces. Note that the experimental test results do not exhibit a symmetric response in terms of the maximum amplitude of the force transmitted by the isolator. On the one hand, the maximum force amplitude developed at 180 mm is 25 kN. On the other hand, a maximum amplitude of 30.5 kN is reached at -180 mm of lateral displacement. This change in the lateral force is produced by variations of the vertical load applied to the device. Even though the vertical actuator applies a constant load, the vertical load transmitted to the isolator changes as the lateral prototype is deformed. In Figure A-2(c), the mentioned variations in the lateral force are corrected by dividing the lateral force by the vertical reaction on the specimen. In this way, the experimental normalized lateral force shows a good agreement with results obtained in the FEM model.

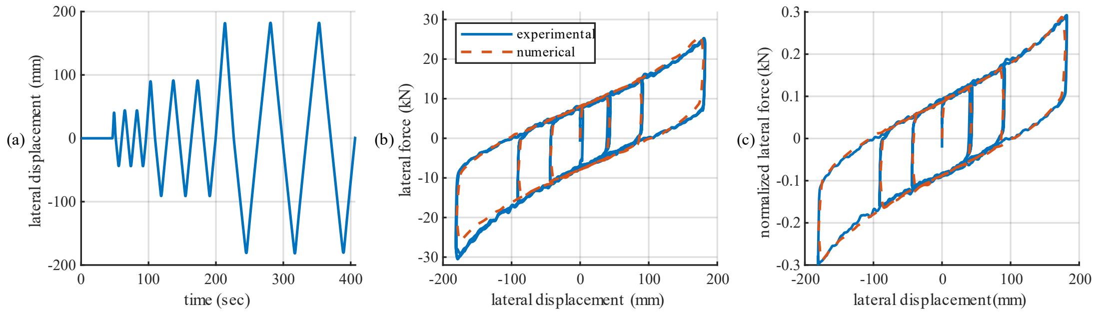

Figure A-2: Experimental test result: (a) Displacement imposed on the bottom plate of the tested isolator. (b) Comparison of the experimental and numerical hysteretic loops. (c) Comparison of the experimental and numerical hysteretic loops considering the normalized lateral force.

As described in Section 2-3, the sliding plate placed between the slider and the sliding surface is made of Ertalyte. In Figure A-3, two photographs of this piece are shown, one before the experimental test and one after the experimental test. Once the experimental test was conducted, the sliding plate was removed from the specimen, and no plastic displacement was observed. Due to this observation, in Section 2-3, this body was modeled considering elastic behavior.

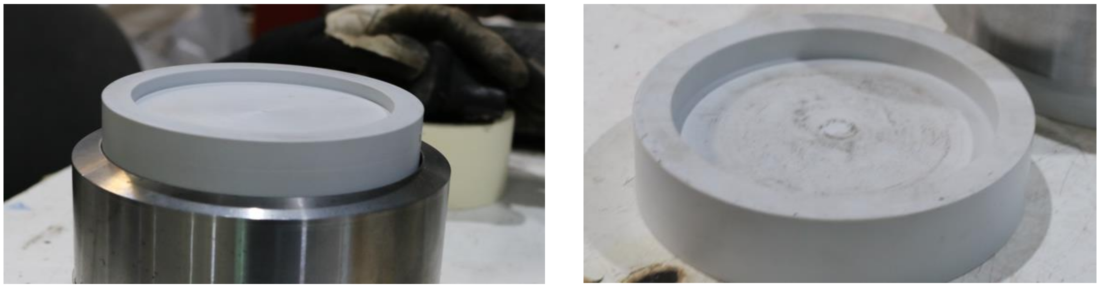
(a) (b)

Figure A-3: Experimental test result: (a) Before conducting the experimental test. (b) After conducting the experimental test.

Several experimental tests were conducted in order to characterize the friction properties of the interaction Structural Steel – Ertalyte. In Figure A-4, the friction coefficient of this interaction is plotted for different values of sliding velocity. This curve was obtained by applying a contact pressure of 60 MPa. Note that the coefficient at high velocity is slightly larger than $f_{max} = 0.07$ and the friction coefficient at slow velocity is slightly lower than $f_{min} = 0.04$.

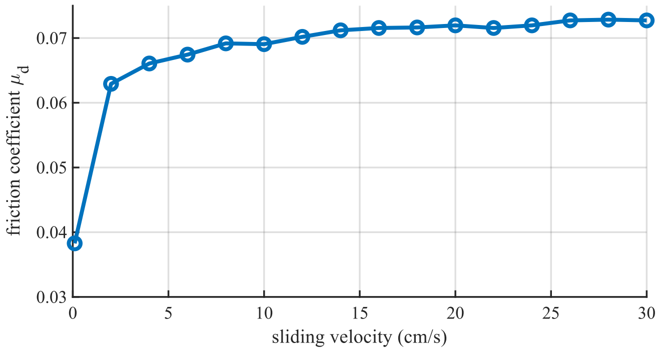

Figure A-4: Friction characterization of the interaction Structural Steel - Ertalyte

B. APPENDIX B: PRELIMINARY EXPERIMENTAL TEST OF AN LIR-DCFP DEVICE

The results of an experimental test conducted to validate the lateral behavior of a Lateral Impact Resilient Double Concave Friction Pendulum (LIR-DCFP) specimen is presented in this appendix. The experimental setup and the prototype of the frictional isolator in the deformed configuration are shown in Figure B-1. The prototype has identical sliding surfaces with a radius of $R = 0.75$ m and restraining rims setting the lateral capacity equal to 17.5 cm (i.e., the first impact between the inner sliders and the restraining rims of sliding surfaces is observed for a bearing displacement of 17.5 cm). The total height of the inner slider is $h_s = 8.5$ cm setting the effective radius to $R_{eff} = 1.415$ m.


(a)

(b)

Figure B-1: (a) Experimental Setup; (b) Specimen in deformed configuration.

The experimental test was conducted by applying a constant vertical load of $W = 150$ kN with a vertically orientated actuator. The lateral bearing displacement was imposed employing a horizontally orientated actuator working in the bottom plate of the isolator. Two cycles of lateral displacement with constant velocity and amplitude of 18.5 cm were imposed. In Figure B-2(a), the evolution of the bearing displacement is plotted. In Figure B-

2(b), the obtained normalized hysteretic loops are shown. Additionally, in Figure B-2(b), the different configurations during the first hysterical loop of the device are illustrated. The identified friction coefficient in low friction interactions (i.e., between spherical surfaces of sliders and plates) was $\mu_d = 0.066$. The high-friction interface is characterized by a friction coefficient of $\mu_s = 0.126$. Note that the first high-friction sliding, between the top and bottom sliders, of 1 cm occurs for a normalized displacement of 0.124 (i.e., lateral displacement of 17.5 cm). This first relative displacement explains why the second high-friction sliding starts for a lateral displacement of 16.5 cm (normalized displacement of 0.117). It follows that both the experimental hysteretic loops are not symmetric (Figure B-2(b)). The preliminary results obtained from the experimental test validate the lateral behavior of LIR-DCFP bearings, showing the correct functioning of the high-friction interface.

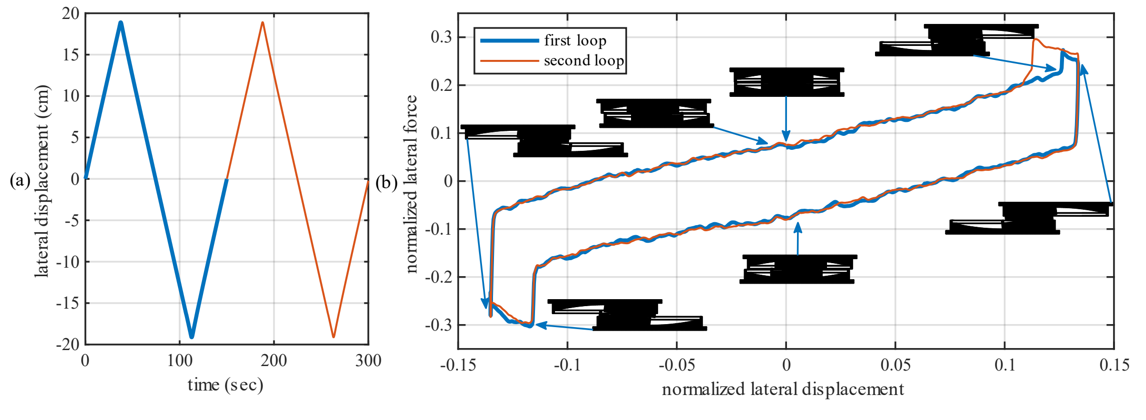

Figure B-2: (a) Displacement imposed on the bottom plate of the tested isolator. (b) Experimental hysteretic loops.

C. APPENDIX C: SELECTED SEISMIC RECORDS MATCHING CONDITIONAL SPECTRA

Table C-1: Characteristics of selected natural ground motions related to $T^* = T_b = 3$ sec and $T_r = 43$ years.

Record Sequence Number	Earthquake Name	YEAR	Station Name	Earthquake Magnitude (Mw)	EpiD (km)	PGA (g)	PGV (cm/sec)	PGD (cm)	Vs30 (m/s)	Scaling factor	Component file name
31	'Parkfield'	'1966'	'Cholame - Shandon Array #8'	6.19	34.0	0.12	4.30	1.63	256.82	0.55	'PARKF\C08050.AT2'
163	'Imperial Valley-06'	'1979'	'Calipatria Fire Station'	6.53	57.1	0.06	4.17	3.16	205.78	0.24	'IMPVALL.H\H-CAL225.AT2'
183	'Imperial Valley-06'	'1979'	'El Centro Array #8'	6.53	28.1	0.47	23.59	14.75	206.08	0.11	'IMPVALL.H\H-E08140.AT2'
451	'Morgan Hill'	'1984'	'Coyote Lake Dam - Southwest Abutment'	6.19	24.6	0.39	15.60	2.25	561.43	0.25	'MORGAN\CYC195.AT2'
781	'Loma Prieta'	'1989'	'Lower Crystal Springs Dam dwnst'	6.93	68.9	0.03	4.78	2.95	586.08	0.99	'LOMAP\XSP000.AT2'
1049	'Northridge-01'	'1994'	'Pacific Palisades - Sunset'	6.69	18.2	0.17	14.84	3.51	191.06	0.41	'NORTHR\SUN190.AT2'
1184	'Chi-Chi, Taiwan'	'1999'	'CHY010'	7.62	51.2	0.12	10.04	5.22	538.69	0.31	'CHICHI\CHY010-N.AT2'
1301	'Chi-Chi, Taiwan'	'1999'	'HWA056'	7.62	78.9	0.06	7.54	8.65	511.30	0.79	'CHICHI\HWA056-E.AT2'
1380	'Chi-Chi, Taiwan'	'1999'	'KAU054'	7.62	64.6	0.03	3.02	2.51	497.22	0.76	'CHICHI\KAU054-E.AT2'
1485	'Chi-Chi, Taiwan'	'1999'	'TCU045'	7.62	77.5	0.36	20.57	21.18	704.64	0.31	'CHICHI\TCU045-E.AT2'
1520	'Chi-Chi, Taiwan'	'1999'	'TCU088'	7.62	57.6	0.23	12.62	12.99	665.20	0.28	'CHICHI\TCU088-N.AT2'
1549	'Chi-Chi, Taiwan'	'1999'	'TCU129'	7.62	14.2	0.34	38.84	24.40	511.18	0.12	'CHICHI\TCU129-E.AT2'
1787	'Hector Mine'	'1999'	'Hector'	7.13	26.5	0.15	11.92	7.58	726.00	0.24	'HECTOR\HEC000.AT2'
1836	'Hector Mine'	'1999'	'Twentynine Palms'	7.13	68.4	0.04	3.87	2.42	635.01	0.66	'HECTOR\29P090.AT2'
3011	'Chi-Chi, Taiwan-05'	'1999'	'HWA024'	6.20	55.5	0.03	2.41	0.71	671.52	2.99	'CHICHI.05\HWA024N.AT2'
3028	'Chi-Chi, Taiwan-05'	'1999'	'HWA043'	6.20	48.2	0.02	1.37	1.16	543.06	3.72	'CHICHI.05\HWA043N.AT2'
3460	'Chi-Chi, Taiwan-06'	'1999'	'TCU053'	6.30	50.0	0.02	2.46	1.38	454.55	1.23	'CHICHI.06\TCU053N.AT2'
3462	'Chi-Chi, Taiwan-06'	'1999'	'TCU057'	6.30	52.8	0.02	2.80	1.65	555.23	1.11	'CHICHI.06\TCU057N.AT2'
3477	'Chi-Chi, Taiwan-06'	'1999'	'TCU082'	6.30	45.9	0.02	4.10	1.87	472.81	0.88	'CHICHI.06\TCU082N.AT2'
3492	'Chi-Chi, Taiwan-06'	'1999'	'TCU105'	6.30	61.5	0.02	2.18	1.49	575.54	1.00	'CHICHI.06\TCU105N.AT2'
4206	'Niigata, Japan'	'2004'	'NIG016'	6.63	37.8	0.04	1.98	1.79	370.03	0.62	'NIIGATA\NIG016NS.AT2'
4207	'Niigata, Japan'	'2004'	'NIG017'	6.63	15.0	0.33	15.53	5.97	274.17	0.21	'NIIGATA\NIG017NS.AT2'
4212	'Niigata, Japan'	'2004'	'NIG022'	6.63	30.1	0.12	3.79	1.54	193.20	0.43	'NIIGATA\NIG022NS.AT2'
4466	'L"Aquila, Italy'	'2009'	'Carsoli 1'	6.30	36.5	0.02	1.72	1.01	415.23	4.06	'L-AQUILA\BY003XTE.AT2'
5239	'Chuetsu-oki'	'2007'	'NGNH29'	6.80	71.9	0.05	3.07	1.91	464.92	1.74	'CHUETSU\NGNH29NS.AT2'
5622	'Iwate'	'2008'	'IWT014'	6.90	55.9	0.06	2.16	1.50	314.60	1.01	'IWATE\IWT014NS.AT2'
5651	'Iwate'	'2008'	'IWTH19'	6.90	48.6	0.07	3.68	2.08	482.08	1.49	'IWATE\IWTH19NS.AT2'
5745	'Iwate'	'2008'	'YMT002'	6.90	58.1	0.03	4.82	3.38	365.59	0.51	'IWATE\YMT002NS.AT2'
5830	'El Mayor-Cucapah'	'2010'	'RANCHO SAN LUIS'	7.20	57.8	0.04	2.39	2.31	523.99	1.16	'SIERRA.MEX\RSL000.AT2'
5972	'El Mayor-Cucapah'	'2010'	'Brawley Airport'	7.20	80.3	0.08	4.01	2.84	208.71	0.39	'SIERRA.MEX\BRA360.AT2'

Table C-2: Characteristics of selected natural ground motions related to $T^* = T_b = 3$ sec and $T_r = 144$ years.

Record Sequence Number	Earthquake Name	YEAR	Station Name	Earthquake Magnitude (Mw)	EpiD (km)	PGA (g)	PGV (cm/sec)	PGD (cm)	Vs30 (m/s)	Scaling factor	Component file name
31	'Parkfield'	'1966'	'Cholame - Shandon Array #8'	6.19	34.0	0.12	4.30	1.63	256.82	1.58	'PARKF\C08050.AT2'
139	'Tabas, Iran'	'1978'	'Dayhook'	7.35	20.6	0.19	11.18	3.41	471.53	0.66	'TABAS\DAY-L1.AT2'
161	'Imperial Valley-06'	'1979'	'Brawley Airport'	6.53	43.2	0.15	8.74	3.60	208.71	0.50	'IMPVALL.H\H-BRA225.AT2'
163	'Imperial Valley-06'	'1979'	'Calipatria Fire Station'	6.53	57.1	0.06	4.17	3.16	205.78	0.76	'IMPVALL.H\H-CAL225.AT2'
172	'Imperial Valley-06'	'1979'	'El Centro Array #1'	6.53	35.2	0.07	3.59	1.53	237.33	0.94	'IMPVALL.H\H-E01140.AT2'
753	'Loma Prieta'	'1989'	'Corralitos'	6.93	7.2	0.46	19.51	12.99	462.24	0.59	'LOMAP\CLS000.AT2'
761	'Loma Prieta'	'1989'	'Fremont - Emerson Court'	6.93	55.2	0.07	8.93	6.89	284.79	1.36	'LOMAP\FMS090.AT2'
791	'Loma Prieta'	'1989'	'SAGO South - Surface'	6.93	53.9	0.06	8.26	6.53	608.67	3.21	'LOMAP\SG3261.AT2'
900	'Landers'	'1992'	'Yermo Fire Station'	7.28	86.0	0.14	12.93	4.91	353.63	0.37	'LANDERS\YER270.AT2'
1301	'Chi-Chi, Taiwan'	'1999'	'HWA056'	7.62	78.9	0.06	7.54	8.65	511.30	2.40	'CHICHI\HWA056-E.AT2'
1481	'Chi-Chi, Taiwan'	'1999'	'TCU038'	7.62	73.1	0.07	32.32	30.60	297.86	0.49	'CHICHI\TCU038-E.AT2'
1490	'Chi-Chi, Taiwan'	'1999'	'TCU050'	7.62	41.5	0.09	42.16	31.36	542.41	0.43	'CHICHI\TCU050-E.AT2'
1618	'Duzce, Turkey'	'1999'	'Lamont 531'	7.14	27.7	0.06	8.84	7.35	638.39	2.50	'DUZCE\531-N.AT2'
1626	'Sitka, Alaska'	'1972'	'Sitka Observatory'	7.68	42.9	0.05	4.78	3.22	649.67	2.28	'SITKA\212V5090.AT2'
2458	'Chi-Chi, Taiwan-03'	'1999'	'CHY025'	6.20	34.4	0.07	25.07	13.81	277.50	0.76	'CHICHI.03\CHY025N.AT2'
2709	'Chi-Chi, Taiwan-04'	'1999'	'CHY035'	6.20	25.7	0.05	5.73	2.62	573.04	2.01	'CHICHI.04\CHY035N.AT2'
2717	'Chi-Chi, Taiwan-04'	'1999'	'CHY052'	6.20	47.6	0.03	2.36	1.74	573.04	2.80	'CHICHI.04\CHY052N.AT2'
2743	'Chi-Chi, Taiwan-04'	'1999'	'CHY087'	6.20	39.0	0.03	4.29	2.57	505.20	1.20	'CHICHI.04\CHY087N.AT2'
3269	'Chi-Chi, Taiwan-06'	'1999'	'CHY029'	6.30	56.8	0.05	8.76	4.26	544.74	0.65	'CHICHI.06\CHY029N.AT2'
3455	'Chi-Chi, Taiwan-06'	'1999'	'TCU048'	6.30	54.6	0.03	2.76	1.80	551.21	3.14	'CHICHI.06\TCU048N.AT2'
3492	'Chi-Chi, Taiwan-06'	'1999'	'TCU105'	6.30	61.5	0.02	2.18	1.49	575.54	3.11	'CHICHI.06\TCU105N.AT2'
3757	'Landers'	'1992'	'North Palm Springs Fire Sta #36'	7.28	32.3	0.10	6.98	2.43	367.84	1.11	'LANDERS\NPF090.AT2'
4851	'Chuetsu-oki'	'2007'	'Joetsu Itakuraku needle'	6.80	61.3	0.03	4.08	2.71	572.37	1.52	'CHUETSU\65017NS.AT2'
4854	'Chuetsu-oki'	'2007'	'Nadachiku Joetsu City'	6.80	62.9	0.05	5.27	3.64	570.62	1.32	'CHUETSU\65020NS.AT2'
5662	'Iwate'	'2008'	'MYG003'	6.90	49.6	0.14	4.30	5.38	482.07	3.66	'IWATE\MYG003NS.AT2'
5668	'Iwate'	'2008'	'MYG009'	6.90	64.6	0.06	3.51	1.70	540.42	1.05	'IWATE\MYG009NS.AT2'
5760	'Iwate'	'2008'	'YMT017'	6.90	55.5	0.05	7.29	3.95	410.57	0.75	'IWATE\YMT017NS.AT2'
5830	'El Mayor-Cucapah'	'2010'	'RANCHO SAN LUIS'	7.20	57.8	0.04	2.39	2.31	523.99	3.61	'SIERRA.MEX\RSL000.AT2'
5831	'El Mayor-Cucapah'	'2010'	'EJIDO SALTILLO'	7.20	18.7	0.18	19.32	13.98	242.05	0.29	'SIERRA.MEX\SAL000.AT2'
5969	'El Mayor-Cucapah'	'2010'	'Bonds Corner'	7.20	44.2	0.11	6.93	5.51	223.03	0.88	'SIERRA.MEX\BCR360.AT2'

Table C-3: Characteristics of selected natural ground motions related to $T^* = T_b = 3$ sec and $T_r = 289$ years.

Record Sequence Number	Earthquake Name	YEAR	Station Name	Earthquake Magnitude (Mw)	EpiD (km)	PGA (g)	PGV (cm/sec)	PGD (cm)	Vs30 (m/s)	Scaling factor	Component file name
172	'Imperial Valley-06'	'1979'	'El Centro Array #1'	6.53	35.2	0.07	3.59	1.53	237.33	1.65	'IMPVALL.H\H-E01140.AT2'
266	'Victoria, Mexico'	'1980'	'Chihuahua'	6.33	36.7	0.10	5.65	1.92	242.05	1.49	'VICT\CHI102.AT2'
751	'Loma Prieta'	'1989'	'Calaveras Reservoir'	6.93	46.3	0.06	7.37	6.15	571.99	2.62	'LOMAP\CLR090.AT2'
1148	'Kocaeli, Turkey'	'1999'	'Arcelik'	7.51	53.7	0.08	7.99	7.32	523.00	1.28	'KOCAELI\ARE000.AT2'
1227	'Chi-Chi, Taiwan'	'1999'	'CHY074'	7.62	37.8	0.10	15.09	8.19	553.43	0.52	'CHICHI\CHY074-E.AT2'
1283	'Chi-Chi, Taiwan'	'1999'	'HWA034'	7.62	63.7	0.07	8.02	6.16	379.18	3.19	'CHICHI\HWA034-E.AT2'
1301	'Chi-Chi, Taiwan'	'1999'	'HWA056'	7.62	78.9	0.06	7.54	8.65	511.30	4.27	'CHICHI\HWA056-E.AT2'
1489	'Chi-Chi, Taiwan'	'1999'	'TCU049'	7.62	38.9	0.18	27.49	23.44	487.27	0.64	'CHICHI\TCU049-E.AT2'
1493	'Chi-Chi, Taiwan'	'1999'	'TCU053'	7.62	41.2	0.12	32.53	27.96	454.55	0.73	'CHICHI\TCU053-E.AT2'
1515	'Chi-Chi, Taiwan'	'1999'	'TCU082'	7.62	36.2	0.13	34.95	28.92	472.81	0.47	'CHICHI\TCU082-E.AT2'
1521	'Chi-Chi, Taiwan'	'1999'	'TCU089'	7.62	7.0	0.19	21.03	21.04	671.52	0.89	'CHICHI\TCU089-E.AT2'
1526	'Chi-Chi, Taiwan'	'1999'	'TCU098'	7.62	99.7	0.05	17.20	17.44	346.56	0.52	'CHICHI\TCU098-E.AT2'
1538	'Chi-Chi, Taiwan'	'1999'	'TCU112'	7.62	46.3	0.07	19.14	20.08	190.54	0.55	'CHICHI\TCU112-E.AT2'
2111	'Denali, Alaska'	'2002'	'R109 (temp)'	7.90	62.0	0.05	6.41	2.46	341.56	2.85	'DENALI\R109-90.AT2'
2111	'Denali, Alaska'	'2002'	'R109 (temp)'	7.90	62.0	0.05	6.41	2.46	341.56	3.32	'DENALI\R109-90.AT2'
2604	'Chi-Chi, Taiwan-03'	'1999'	'TCU048'	6.20	48.7	0.02	3.02	2.31	551.21	3.28	'CHICHI.03\TCU048N.AT2'
2643	'Chi-Chi, Taiwan-03'	'1999'	'TCU105'	6.20	56.2	0.01	2.65	2.68	575.54	3.45	'CHICHI.03\TCU105N.AT2'
3463	'Chi-Chi, Taiwan-06'	'1999'	'TCU059'	6.30	63.4	0.02	2.94	1.52	272.67	4.37	'CHICHI.06\TCU059N.AT2'
3477	'Chi-Chi, Taiwan-06'	'1999'	'TCU082'	6.30	45.9	0.02	4.10	1.87	472.81	4.78	'CHICHI.06\TCU082N.AT2'
4009	'San Simeon, CA'	'2003'	'POINT BUCHON - LOS OSOS'	6.52	50.4	0.06	8.25	7.11	486.19	2.07	'SANSIMEO\36427090.AT2'
5768	'Iwate'	'2008'	'YMTH09'	6.90	67.9	0.02	2.39	2.52	291.48	4.40	'IWATE\YMTH09NS.AT2'
5804	'Iwate'	'2008'	'Yamauchi Tsuchibuchi Yokote'	6.90	35.2	0.17	4.96	1.96	561.59	3.43	'IWATE\55446NS.AT2'
5831	'El Mayor-Cucapah'	'2010'	'EJIDO SALTILLO'	7.20	18.7	0.18	19.32	13.98	242.05	0.50	'SIERRA.MEX\SAL000.AT2'
5990	'El Mayor-Cucapah'	'2010'	'El Centro Array #7'	7.20	62.9	0.12	7.26	5.69	210.51	0.98	'SIERRA.MEX\E07360.AT2'
6886	'Darfield, New Zealand'	'2010'	'Canterbury Aero Club'	7.00	41.4	0.31	20.19	16.10	280.26	1.03	'DARFIELD\CACSN40E.AT2'
6896	'Darfield, New Zealand'	'2010'	'DORC'	7.00	31.7	0.08	5.65	3.19	280.26	1.33	'DARFIELD\DORCN20W.AT2'
6928	'Darfield, New Zealand'	'2010'	'LPCC'	7.00	54.3	0.16	9.92	6.06	649.67	1.02	'DARFIELD\LPCCN80E.AT2'
8075	'Christchurch, New Zealand'	'2011'	'DSLC'	6.20	42.1	0.03	4.03	2.01	295.74	3.19	'CCHURCH\DSLCN27W.AT2'
8160	'El Mayor-Cucapah'	'2010'	'El Centro Array #4'	7.20	64.6	0.13	7.63	5.24	208.91	0.87	'SIERRA.ADD\E04360.AT2'
8161	'El Mayor-Cucapah'	'2010'	'El Centro Array #12'	7.20	58.0	0.27	17.04	9.25	196.88	0.62	'SIERRA.ADD\E12360.AT2'

Table C-4: Characteristics of selected natural ground motions related to $\boldsymbol{T^* = T_b = 3}$ sec and $\boldsymbol{T_r = 475}$ years.

Record Sequence Number	Earthquake Name	YEAR	Station Name	Earthquake Magnitude (Mw)	EpiD (km)	PGA (g)	PGV (cm/sec)	PGD (cm)	Vs30 (m/s)	Scaling factor	Component file name
172	'Imperial Valley-06'	'1979'	'El Centro Array #1'	6.53	35.2	0.07	3.59	1.53	237.33	4.31	'IMPVALL.H\H-E01140.AT2'
286	'Irpinia, Italy-01'	'1980'	'Bisaccia'	6.90	23.3	0.05	16.17	13.61	496.46	1.91	'ITALY\A-BIS000.AT2'
302	'Irpinia, Italy-02'	'1980'	'Rionero In Vulture'	6.20	29.8	0.06	6.33	1.19	574.88	2.75	'ITALY\B-VLT000.AT2'
731	'Loma Prieta'	'1989'	'APEEL 10 - Skyline'	6.93	62.3	0.04	8.40	3.96	391.91	1.75	'LOMAP\A10000.AT2'
1074	'Northridge-01'	'1994'	'Sandberg - Bald Mtn'	6.69	61.8	0.04	6.37	3.20	421.00	3.68	'NORTHR\SAN090.AT2'
1144	'Gulf of Aqaba'	'1995'	'Eilat'	7.20	93.4	0.11	4.30	1.13	354.88	2.34	'AQABA\EIL-EW.AT2'
1148	'Kocaeli, Turkey'	'1999'	'Arcelik'	7.51	53.7	0.08	7.99	7.32	523.00	2.50	'KOCAELI\ARE000.AT2'
1161	'Kocaeli, Turkey'	'1999'	'Gebze'	7.51	47.0	0.19	14.12	5.77	792.00	0.92	'KOCAELI\GBZ000.AT2'
1228	'Chi-Chi, Taiwan'	'1999'	'CHY076'	7.62	65.4	0.03	8.82	7.18	169.84	1.80	'CHICHI\CHY076-E.AT2'
1477	'Chi-Chi, Taiwan'	'1999'	'TCU031'	7.62	80.1	0.07	26.61	29.89	489.22	0.76	'CHICHI\TCU031-E.AT2'
1482	'Chi-Chi, Taiwan'	'1999'	'TCU039'	7.62	71.5	0.12	50.44	38.36	540.66	0.58	'CHICHI\TCU039-E.AT2'
1489	'Chi-Chi, Taiwan'	'1999'	'TCU049'	7.62	38.9	0.18	27.49	23.44	487.27	0.89	'CHICHI\TCU049-E.AT2'
1489	'Chi-Chi, Taiwan'	'1999'	'TCU049'	7.62	38.9	0.18	27.49	23.44	487.27	0.80	'CHICHI\TCU049-E.AT2'
1491	'Chi-Chi, Taiwan'	'1999'	'TCU051'	7.62	38.5	0.11	29.90	26.37	350.06	0.84	'CHICHI\TCU051-E.AT2'
1499	'Chi-Chi, Taiwan'	'1999'	'TCU060'	7.62	45.4	0.09	28.04	27.10	375.42	1.03	'CHICHI\TCU060-E.AT2'
1510	'Chi-Chi, Taiwan'	'1999'	'TCU075'	7.62	20.7	0.23	50.92	25.02	573.02	0.76	'CHICHI\TCU075-E.AT2'
1546	'Chi-Chi, Taiwan'	'1999'	'TCU122'	7.62	21.8	0.24	41.10	30.80	475.46	0.94	'CHICHI\TCU122-E.AT2'
1548	'Chi-Chi, Taiwan'	'1999'	'TCU128'	7.62	63.3	0.09	44.89	29.12	599.64	0.80	'CHICHI\TCU128-E.AT2'
1554	'Chi-Chi, Taiwan'	'1999'	'TCU145'	7.62	51.2	0.05	19.51	17.65	240.43	1.41	'CHICHI\TCU145-N.AT2'
1619	'Duzce, Turkey'	'1999'	'Mudurnu'	7.14	41.5	0.06	8.63	7.08	535.24	3.19	'DUZCE\MDR000.AT2'
2607	'Chi-Chi, Taiwan-03'	'1999'	'TCU051'	6.20	43.9	0.02	3.16	2.75	350.06	4.89	'CHICHI.03\TCU051N.AT2'
2619	'Chi-Chi, Taiwan-03'	'1999'	'TCU067'	6.20	34.0	0.07	6.41	4.36	433.63	4.02	'CHICHI.03\TCU067N.AT2'
2654	'Chi-Chi, Taiwan-03'	'1999'	'TCU120'	6.20	30.7	0.05	9.37	8.56	459.34	3.18	'CHICHI.03\TCU120N.AT2'
3512	'Chi-Chi, Taiwan-06'	'1999'	'TCU141'	6.30	55.7	0.15	10.19	5.61	223.04	1.08	'CHICHI.06\TCU141N.AT2'
3751	'Cape Mendocino'	'1992'	'South Bay Union School'	7.01	45.5	0.05	5.81	2.22	459.04	2.86	'CAPEMEND\SBH270.AT2'
5745	'Iwate'	'2008'	'YMT002'	6.90	58.1	0.03	4.82	3.38	365.59	2.05	'IWATE\YMT002NS.AT2'
5760	'Iwate'	'2008'	'YMT017'	6.90	55.5	0.05	7.29	3.95	410.57	1.82	'IWATE\YMT017NS.AT2'
5829	'El Mayor-Cucapah'	'2010'	'RIITO'	7.20	32.4	0.67	15.19	11.26	242.05	1.44	'SIERRA.MEX\RII000.AT2'
6886	'Darfield, New Zealand'	'2010'	'Canterbury Aero Club'	7.00	41.4	0.31	20.19	16.10	280.26	0.85	'DARFIELD\CACSN40E.AT2'
6948	'Darfield, New Zealand'	'2010'	'OXZ'	7.00	32.2	0.10	7.43	4.67	481.62	3.91	'DARFIELD\OXZE.AT2'

Table C-5: Characteristics of selected natural ground motions related to $\boldsymbol{T^{*}=T_{b}=3}$ sec and $\boldsymbol{T_{r}=949}$ years.

Record Sequence Number	Earthquake Name	YEAR	Station Name	Earthquake Magnitude (Mw)	EpiD (km)	PGA (g)	PGV (cm/sec)	PGD (cm)	Vs30 (m/s)	Scaling factor	Component file name
15	'Kern County'	'1952'	'Taft Lincoln School'	7.36	43.5	0.11	6.81	5.77	385.43	3.47	'KERN\TAF111.AT2'
172	'Imperial Valley-06'	'1979'	'El Centro Array #1'	6.53	35.2	0.07	3.59	1.53	237.33	3.37	'IMPVALL.H\H-E01230.AT2'
173	'Imperial Valley-06'	'1979'	'El Centro Array #10'	6.53	28.8	0.11	9.09	6.59	202.85	1.11	'IMPVALL.H\H-E10320.AT2'
175	'Imperial Valley-06'	'1979'	'El Centro Array #12'	6.53	32.0	0.07	6.88	4.98	196.88	2.37	'IMPVALL.H\H-E12230.AT2'
187	'Imperial Valley-06'	'1979'	'Parachute Test Site'	6.53	48.6	0.16	7.25	5.04	348.69	2.53	'IMPVALL.H\H-PTS315.AT2'
778	'Loma Prieta'	'1989'	'Hollister Differential Array'	6.93	45.1	0.15	8.47	4.16	215.54	1.21	'LOMAP\HDA255.AT2'
1148	'Kocaeli, Turkey'	'1999'	'Arcelik'	7.51	53.7	0.08	7.99	7.32	523.00	2.62	'KOCAELI\ARE090.AT2'
1148	'Kocaeli, Turkey'	'1999'	'Arcelik'	7.51	53.7	0.08	7.99	7.32	523.00	3.67	'KOCAELI\ARE090.AT2'
1476	'Chi-Chi, Taiwan'	'1999'	'TCU029'	7.62	79.2	0.06	20.78	25.64	406.53	0.76	'CHICHI\TCU029-N.AT2'
1482	'Chi-Chi, Taiwan'	'1999'	'TCU039'	7.62	71.5	0.12	50.44	38.36	540.66	0.89	'CHICHI\TCU039-N.AT2'
1488	'Chi-Chi, Taiwan'	'1999'	'TCU048'	7.62	43.3	0.10	24.65	21.48	551.21	1.28	'CHICHI\TCU048-N.AT2'
1491	'Chi-Chi, Taiwan'	'1999'	'TCU051'	7.62	38.5	0.11	29.90	26.37	350.06	1.23	'CHICHI\TCU051-N.AT2'
1492	'Chi-Chi, Taiwan'	'1999'	'TCU052'	7.62	39.6	0.20	144.05	154.05	579.10	0.34	'CHICHI\TCU052-N.AT2'
1493	'Chi-Chi, Taiwan'	'1999'	'TCU053'	7.62	41.2	0.12	32.53	27.96	454.55	1.49	'CHICHI\TCU053-N.AT2'
1494	'Chi-Chi, Taiwan'	'1999'	'TCU054'	7.62	37.6	0.14	30.14	24.90	460.69	1.12	'CHICHI\TCU054-N.AT2'
1497	'Chi-Chi, Taiwan'	'1999'	'TCU057'	7.62	41.8	0.08	33.88	27.81	555.23	1.26	'CHICHI\TCU057-N.AT2'
1509	'Chi-Chi, Taiwan'	'1999'	'TCU074'	7.62	19.1	0.28	19.59	7.00	549.43	2.71	'CHICHI\TCU074-N.AT2'
1511	'Chi-Chi, Taiwan'	'1999'	'TCU076'	7.62	16.0	0.28	32.19	20.75	614.98	1.16	'CHICHI\TCU076-N.AT2'
1550	'Chi-Chi, Taiwan'	'1999'	'TCU136'	7.62	48.8	0.11	33.33	31.45	462.10	1.06	'CHICHI\TCU136-W.AT2'
1554	'Chi-Chi, Taiwan'	'1999'	'TCU145'	7.62	51.2	0.05	19.51	17.65	240.43	2.07	'CHICHI\TCU145-W.AT2'
1598	'Chi-Chi, Taiwan'	'1999'	'WTC'	7.62	54.9	0.05	8.85	8.05	207.69	3.05	'CHICHI\WTC-N.AT2'
2710	'Chi-Chi, Taiwan-04'	'1999'	'CHY036'	6.20	34.8	0.05	4.35	2.58	233.14	2.43	'CHICHI.04\CHY036E.AT2'
2744	'Chi-Chi, Taiwan-04'	'1999'	'CHY088'	6.20	48.9	0.02	3.57	1.64	318.52	1.29	'CHICHI.04\CHY088E.AT2'
2894	'Chi-Chi, Taiwan-04'	'1999'	'TCU123'	6.20	54.4	0.01	3.78	2.04	270.22	2.85	'CHICHI.04\TCU123E.AT2'
3503	'Chi-Chi, Taiwan-06'	'1999'	'TCU122'	6.30	41.2	0.13	10.29	4.43	475.46	2.94	'CHICHI.06\TCU122E.AT2'
5256	'Chuetsu-oki'	'2007'	'NIG010'	6.80	54.3	0.02	2.99	2.85	173.09	3.27	'CHUETSU\NIG010EW.AT2'
5827	'El Mayor-Cucapah'	'2010'	'MICHOACAN DE OCAMPO'	7.20	18.8	0.80	16.98	8.56	242.05	0.94	'SIERRA.MEX\MDO090.AT2'
5831	'El Mayor-Cucapah'	'2010'	'EJIDO SALTILLO'	7.20	18.7	0.18	19.32	13.98	242.05	1.02	'SIERRA.MEX\SAL090.AT2'
6005	'El Mayor-Cucapah'	'2010'	'Holtville Post Office'	7.20	57.9	0.10	8.10	5.45	202.89	1.79	'SIERRA.MEX\HVP090.AT2'
6886	'Darfield, New Zealand'	'2010'	'Canterbury Aero Club'	7.00	41.4	0.31	20.19	16.10	280.26	1.25	'DARFIELD\CACSN50W.AT2'

Table C-6: Characteristics of selected natural ground motions related to $\boldsymbol{T^* = T_b = 3}$ sec and $\boldsymbol{T_r = 1,485}$ years.

Record Sequence Number	Earthquake Name	YEAR	Station Name	Earthquake Magnitude (Mw)	EpiD (km)	PGA (g)	PGV (cm/sec)	PGD (cm)	Vs30 (m/s)	Scaling factor	Component file name
15	'Kern County'	'1952'	'Taft Lincoln School'	7.36	43.5	0.11	6.81	5.77	385.43	4.35	'KERN\TAF021.AT2'
68	'San Fernando'	'1971'	'LA - Hollywood Stor FF'	6.61	39.5	0.16	5.16	4.00	316.46	4.77	'SFERN\PEL090.AT2'
163	'Imperial Valley-06'	'1979'	'Calipatria Fire Station'	6.53	57.1	0.06	4.17	3.16	205.78	3.40	'IMPVALL.H\H-CAL225.AT2'
266	'Victoria, Mexico'	'1980'	'Chihuahua'	6.33	36.7	0.10	5.65	1.92	242.05	2.30	'VICT\CHI102.AT2'
767	'Loma Prieta'	'1989'	'Gilroy Array #3'	6.93	31.4	0.34	15.65	7.04	349.85	1.64	'LOMAP\G03000.AT2'
806	'Loma Prieta'	'1989'	'Sunnyvale - Colton Ave.'	6.93	42.1	0.11	8.91	4.38	267.71	0.68	'LOMAP\SVL270.AT2'
838	'Landers'	'1992'	'Barstow'	7.28	94.8	0.07	7.28	2.88	370.08	2.69	'LANDERS\BRS000.AT2'
879	'Landers'	'1992'	'Lucerne'	7.28	44.0	0.82	41.09	29.83	1369.00	0.65	'LANDERS\LCN260.AT2'
900	'Landers'	'1992'	'Yermo Fire Station'	7.28	86.0	0.14	12.93	4.91	353.63	1.67	'LANDERS\YER270.AT2'
1161	'Kocaeli, Turkey'	'1999'	'Gebze'	7.51	47.0	0.19	14.12	5.77	792.00	1.71	'KOCAELI\GBZ000.AT2'
1166	'Kocaeli, Turkey'	'1999'	'Iznik'	7.51	39.8	0.08	8.76	4.49	476.62	2.51	'KOCAELI\IZN180.AT2'
1212	'Chi-Chi, Taiwan'	'1999'	'CHY054'	7.62	79.7	0.03	7.93	7.74	172.10	3.41	'CHICHI\CHY054-E.AT2'
1227	'Chi-Chi, Taiwan'	'1999'	'CHY074'	7.62	37.8	0.10	15.09	8.19	553.43	1.33	'CHICHI\CHY074-E.AT2'
1487	'Chi-Chi, Taiwan'	'1999'	'TCU047'	7.62	86.4	0.27	22.39	21.45	520.37	1.54	'CHICHI\TCU047-E.AT2'
1488	'Chi-Chi, Taiwan'	'1999'	'TCU048'	7.62	43.3	0.10	24.65	21.48	551.21	1.42	'CHICHI\TCU048-E.AT2'
1488	'Chi-Chi, Taiwan'	'1999'	'TCU048'	7.62	43.3	0.10	24.65	21.48	551.21	1.61	'CHICHI\TCU048-E.AT2'
1489	'Chi-Chi, Taiwan'	'1999'	'TCU049'	7.62	38.9	0.18	27.49	23.44	487.27	1.48	'CHICHI\TCU049-E.AT2'
1490	'Chi-Chi, Taiwan'	'1999'	'TCU050'	7.62	41.5	0.09	42.16	31.36	542.41	1.91	'CHICHI\TCU050-E.AT2'
1532	'Chi-Chi, Taiwan'	'1999'	'TCU105'	7.62	50.8	0.06	23.14	18.92	575.54	1.35	'CHICHI\TCU105-E.AT2'
1538	'Chi-Chi, Taiwan'	'1999'	'TCU112'	7.62	46.3	0.07	19.14	20.08	190.54	1.41	'CHICHI\TCU112-E.AT2'
1538	'Chi-Chi, Taiwan'	'1999'	'TCU112'	7.62	46.3	0.07	19.14	20.08	190.54	0.91	'CHICHI\TCU112-E.AT2'
1542	'Chi-Chi, Taiwan'	'1999'	'TCU117'	7.62	48.3	0.09	22.41	17.60	198.58	1.01	'CHICHI\TCU117-E.AT2'
1548	'Chi-Chi, Taiwan'	'1999'	'TCU128'	7.62	63.3	0.09	44.89	29.12	599.64	1.48	'CHICHI\TCU128-E.AT2'
1554	'Chi-Chi, Taiwan'	'1999'	'TCU145'	7.62	51.2	0.05	19.51	17.65	240.43	2.60	'CHICHI\TCU145-N.AT2'
2652	'Chi-Chi, Taiwan-03'	'1999'	'TCU118'	6.20	48.4	0.04	7.11	5.38	236.19	2.98	'CHICHI.03\TCU118N.AT2'
2710	'Chi-Chi, Taiwan-04'	'1999'	'CHY036'	6.20	34.8	0.05	4.35	2.58	233.14	3.05	'CHICHI.04\CHY036N.AT2'
3749	'Cape Mendocino'	'1992'	'Fortuna Fire Station'	7.01	30.0	0.08	7.28	2.75	355.18	2.43	'CAPEMEND\FFT270.AT2'
4844	'Chuetsu-oki'	'2007'	'Tokamachi Matsunoyama'	6.80	50.5	0.04	5.59	2.74	640.14	4.57	'CHUETSU\65007NS.AT2'
5256	'Chuetsu-oki'	'2007'	'NIG010'	6.80	54.3	0.02	2.99	2.85	173.09	4.11	'CHUETSU\NIG010NS.AT2'
5256	'Chuetsu-oki'	'2007'	'NIG010'	6.80	54.3	0.02	2.99	2.85	173.09	4.30	'CHUETSU\NIG010NS.AT2'

Table C-7: Characteristics of selected natural ground motions related to $\boldsymbol{T^*} = \boldsymbol{T_b} = \mathbf{3}$ sec and $\boldsymbol{T_r} = \mathbf{2,475}$ years.

Record Sequence Number	Earthquake Name	YEAR	Station Name	Earthquake Magnitude (Mw)	EpiD (km)	PGA (g)	PGV (cm/sec)	PGD (cm)	Vs30 (m/s)	Scaling factor	Component file name
5991	'El Mayor-Cucapah'	'2010'	'El Centro Array #10'	7.20	60.5	0.21	10.20	7.75	202.85	2.89	'SIERRA.MEX\E10230.AT2'
1477	'Chi-Chi, Taiwan'	'1999'	'TCU031'	7.62	80.1	0.07	26.61	29.89	489.22	1.11	'CHICHI\TCU031-N.AT2'
6923	'Darfield, New Zealand'	'2010'	'Kaiapoi North School '	7.00	56.2	0.09	10.10	8.40	255.00	1.62	'DARFIELD\KPOCS75E.AT2'
1196	'Chi-Chi, Taiwan'	'1999'	'CHY027'	7.62	59.4	0.05	7.98	6.20	210.01	2.46	'CHICHI\CHY027-N.AT2'
1494	'Chi-Chi, Taiwan'	'1999'	'TCU054'	7.62	37.6	0.14	30.14	24.90	460.69	1.77	'CHICHI\TCU054-N.AT2'
1533	'Chi-Chi, Taiwan'	'1999'	'TCU106'	7.62	37.7	0.12	23.55	21.52	451.37	1.14	'CHICHI\TCU106-N.AT2'
6969	'Darfield, New Zealand'	'2010'	'Styx Mill Transfer Station '	7.00	48.4	0.23	12.36	9.37	247.50	1.49	'DARFIELD\SMTCS02W.AT2'
1483	'Chi-Chi, Taiwan'	'1999'	'TCU040'	7.62	69.0	0.08	18.07	18.09	362.03	1.56	'CHICHI\TCU040-N.AT2'
36	'Borrego Mtn'	'1968'	'El Centro Array #9'	6.63	70.8	0.03	3.42	3.01	213.44	3.30	'BORREGO\A-ELC270.AT2'
5664	'Iwate'	'2008'	'MYG005'	6.90	32.1	0.66	19.56	8.45	361.24	1.17	'IWATE\MYG005EW.AT2'
1505	'Chi-Chi, Taiwan'	'1999'	'TCU068'	7.62	47.9	0.53	213.12	222.68	487.34	0.49	'CHICHI\TCU068-N.AT2'
5760	'Iwate'	'2008'	'YMT017'	6.90	55.5	0.05	7.29	3.95	410.57	4.24	'IWATE\YMT017EW.AT2'
180	'Imperial Valley-06'	'1979'	'El Centro Array #5'	6.53	27.8	0.59	39.54	22.32	205.63	1.13	'IMPVALL.H\H-E05230.AT2'
1515	'Chi-Chi, Taiwan'	'1999'	'TCU082'	7.62	36.2	0.13	34.95	28.92	472.81	1.51	'CHICHI\TCU082-N.AT2'
5831	'El Mayor-Cucapah'	'2010'	'EJIDO SALTILLO'	7.20	18.7	0.18	19.32	13.98	242.05	1.61	'SIERRA.MEX\SAL090.AT2'
1527	'Chi-Chi, Taiwan'	'1999'	'TCU100'	7.62	42.8	0.09	39.53	32.65	535.13	2.31	'CHICHI\TCU100-N.AT2'
192	'Imperial Valley-06'	'1979'	'Westmorland Fire Sta'	6.53	52.8	0.09	7.01	2.68	193.67	3.05	'IMPVALL.H\H-WSM180.AT2'
1537	'Chi-Chi, Taiwan'	'1999'	'TCU111'	7.62	44.8	0.08	23.86	21.44	237.53	1.42	'CHICHI\TCU111-N.AT2'
187	'Imperial Valley-06'	'1979'	'Parachute Test Site'	6.53	48.6	0.16	7.25	5.04	348.69	4.00	'IMPVALL.H\H-PTS315.AT2'
1239	'Chi-Chi, Taiwan'	'1999'	'CHY093'	7.62	71.9	0.04	5.91	4.94	190.49	4.10	'CHICHI\CHY093-W.AT2'
1497	'Chi-Chi, Taiwan'	'1999'	'TCU057'	7.62	41.8	0.08	33.88	27.81	555.23	1.99	'CHICHI\TCU057-N.AT2'
1501	'Chi-Chi, Taiwan'	'1999'	'TCU063'	7.62	35.5	0.14	56.98	40.47	476.14	1.00	'CHICHI\TCU063-N.AT2'
5810	'Iwate'	'2008'	'Machimukai Town'	6.90	43.2	0.10	11.31	5.46	655.45	2.11	'IWATE\56362EW.AT2'
8161	'El Mayor-Cucapah'	'2010'	'El Centro Array #12'	7.20	58.0	0.27	17.04	9.25	196.88	2.02	'SIERRA.ADD\E12090.AT2'
1611	'Duzce, Turkey'	'1999'	'Lamont 1058'	7.14	13.4	0.07	15.22	12.17	529.18	3.38	'DUZCE\1058-E.AT2'
2700	'Chi-Chi, Taiwan-04'	'1999'	'CHY025'	6.20	37.1	0.06	6.93	4.40	277.50	3.54	'CHICHI.04\CHY025E.AT2'
1491	'Chi-Chi, Taiwan'	'1999'	'TCU051'	7.62	38.5	0.11	29.90	26.37	350.06	1.95	'CHICHI\TCU051-N.AT2'
4849	'Chuetsu-oki'	'2007'	'Kubikiku Hyakken Joetsu City'	6.80	46.7	0.06	9.16	3.28	342.74	2.87	'CHUETSU\65012EW.AT2'
6953	'Darfield, New Zealand'	'2010'	'Pages Road Pumping Station'	7.00	53.5	0.32	19.59	12.46	206.00	1.01	'DARFIELD\PRPCS.AT2'
3473	'Chi-Chi, Taiwan-06'	'1999'	'TCU078'	6.30	17.9	0.31	21.77	14.40	443.04	3.49	'CHICHI.06\TCU078E.AT2'

Table C-8: Characteristics of selected natural ground motions related to $\boldsymbol{T^* = T_b = 3}$ sec and $\boldsymbol{T_r = 3,899}$ years.

Record Sequence Number	Earthquake Name	YEAR	Station Name	Earthquake Magnitude (Mw)	EpiD (km)	PGA (g)	PGV (cm/sec)	PGD (cm)	Vs30 (m/s)	Scaling factor	Component file name
180	'Imperial Valley-06'	'1979'	'El Centro Array #5'	6.53	27.8	0.59	39.54	22.32	205.63	1.36	'IMPVALL.H\H-E05230.AT2'
183	'Imperial Valley-06'	'1979'	'El Centro Array #8'	6.53	28.1	0.47	23.59	14.75	206.08	2.22	'IMPVALL.H\H-E08230.AT2'
185	'Imperial Valley-06'	'1979'	'Holtville Post Office'	6.53	19.8	0.26	9.85	5.62	202.89	1.59	'IMPVALL.H\H-HVP315.AT2'
192	'Imperial Valley-06'	'1979'	'Westmorland Fire Sta'	6.53	52.8	0.09	7.01	2.68	193.67	3.65	'IMPVALL.H\H-WSM180.AT2'
1196	'Chi-Chi, Taiwan'	'1999'	'CHY027'	7.62	59.4	0.05	7.98	6.20	210.01	2.95	'CHICHI\CHY027-N.AT2'
1233	'Chi-Chi, Taiwan'	'1999'	'CHY082'	7.62	55.0	0.08	9.02	7.20	193.69	3.25	'CHICHI\CHY082-N.AT2'
1233	'Chi-Chi, Taiwan'	'1999'	'CHY082'	7.62	55.0	0.08	9.02	7.20	193.69	4.61	'CHICHI\CHY082-N.AT2'
1477	'Chi-Chi, Taiwan'	'1999'	'TCU031'	7.62	80.1	0.07	26.61	29.89	489.22	2.10	'CHICHI\TCU031-N.AT2'
1477	'Chi-Chi, Taiwan'	'1999'	'TCU031'	7.62	80.1	0.07	26.61	29.89	489.22	1.33	'CHICHI\TCU031-N.AT2'
1482	'Chi-Chi, Taiwan'	'1999'	'TCU039'	7.62	71.5	0.12	50.44	38.36	540.66	1.63	'CHICHI\TCU039-N.AT2'
1483	'Chi-Chi, Taiwan'	'1999'	'TCU040'	7.62	69.0	0.08	18.07	18.09	362.03	1.87	'CHICHI\TCU040-N.AT2'
1488	'Chi-Chi, Taiwan'	'1999'	'TCU048'	7.62	43.3	0.10	24.65	21.48	551.21	2.14	'CHICHI\TCU048-N.AT2'
1489	'Chi-Chi, Taiwan'	'1999'	'TCU049'	7.62	38.9	0.18	27.49	23.44	487.27	2.23	'CHICHI\TCU049-N.AT2'
1490	'Chi-Chi, Taiwan'	'1999'	'TCU050'	7.62	41.5	0.09	42.16	31.36	542.41	2.87	'CHICHI\TCU050-N.AT2'
1491	'Chi-Chi, Taiwan'	'1999'	'TCU051'	7.62	38.5	0.11	29.90	26.37	350.06	2.34	'CHICHI\TCU051-N.AT2'
1501	'Chi-Chi, Taiwan'	'1999'	'TCU063'	7.62	35.5	0.14	56.98	40.47	476.14	1.20	'CHICHI\TCU063-N.AT2'
1519	'Chi-Chi, Taiwan'	'1999'	'TCU087'	7.62	55.6	0.09	58.39	60.48	538.69	2.77	'CHICHI\TCU087-N.AT2'
1526	'Chi-Chi, Taiwan'	'1999'	'TCU098'	7.62	99.7	0.05	17.20	17.44	346.56	2.04	'CHICHI\TCU098-N.AT2'
1527	'Chi-Chi, Taiwan'	'1999'	'TCU100'	7.62	42.8	0.09	39.53	32.65	535.13	2.76	'CHICHI\TCU100-N.AT2'
1532	'Chi-Chi, Taiwan'	'1999'	'TCU105'	7.62	50.8	0.06	23.14	18.92	575.54	3.44	'CHICHI\TCU105-N.AT2'
1538	'Chi-Chi, Taiwan'	'1999'	'TCU112'	7.62	46.3	0.07	19.14	20.08	190.54	1.37	'CHICHI\TCU112-N.AT2'
1541	'Chi-Chi, Taiwan'	'1999'	'TCU116'	7.62	24.4	0.12	34.16	28.67	493.09	2.39	'CHICHI\TCU116-N.AT2'
1543	'Chi-Chi, Taiwan'	'1999'	'TCU118'	7.62	43.8	0.10	19.33	20.26	236.19	2.17	'CHICHI\TCU118-N.AT2'
1543	'Chi-Chi, Taiwan'	'1999'	'TCU118'	7.62	43.8	0.10	19.33	20.26	236.19	2.48	'CHICHI\TCU118-N.AT2'
1552	'Chi-Chi, Taiwan'	'1999'	'TCU140'	7.62	48.4	0.07	19.30	18.41	223.60	3.00	'CHICHI\TCU140-W.AT2'
1602	'Duzce, Turkey'	'1999'	'Bolu'	7.14	41.3	0.20	23.47	13.96	293.57	2.92	'DUZCE\BOL090.AT2'
1611	'Duzce, Turkey'	'1999'	'Lamont 1058'	7.14	13.4	0.07	15.22	12.17	529.18	4.06	'DUZCE\1058-E.AT2'
3512	'Chi-Chi, Taiwan-06'	'1999'	'TCU141'	6.30	55.7	0.15	10.19	5.61	223.04	3.01	'CHICHI.06\TCU141W.AT2'
3748	'Cape Mendocino'	'1992'	'Ferndale Fire Station'	7.01	27.9	0.07	6.64	3.62	387.95	1.44	'CAPEMEND\FFS360.AT2'
3843	'Chi-Chi (aftershock 2), Taiwan'	'1999'	'CHY002'	6.20	45.7	0.04	15.98	12.08	235.13	1.77	'CHICHI.03\CHY002W.AT2'

Table C-9: Characteristics of selected natural ground motions related to $\boldsymbol{T}^* = \boldsymbol{T_b} = \boldsymbol{3}$ sec and $\boldsymbol{T_r} = \boldsymbol{7,462}$ years.

Record Sequence Number	Earthquake Name	YEAR	Station Name	Earthquake Magnitude (Mw)	EpiD (km)	PGA (g)	PGV (cm/sec)	PGD (cm)	Vs30 (m/s)	Scaling factor	Component file name
185	'Imperial Valley-06'	'1979'	'Holtville Post Office'	6.53	19.8	0.26	9.85	5.62	202.89	2.00	'IMPVALL.H\H-HVP315.AT2'
728	'Superstition Hills-02'	'1987'	'Westmorland Fire Sta'	6.54	19.5	0.23	8.71	4.27	193.67	2.59	'SUPER.B\B-WSM180.AT2'
729	'Superstition Hills-02'	'1987'	'Imperial Valley Wildlife Liquefaction Array'	6.54	29.4	0.40	6.15	4.17	179.00	2.70	'SUPER.B\B-IVW360.AT2'
787	'Loma Prieta'	'1989'	'Palo Alto - SLAC Lab'	6.93	51.2	0.09	10.32	2.73	425.30	3.34	'LOMAP\SLC360.AT2'
827	'Cape Mendocino'	'1992'	'Fortuna - Fortuna Blvd'	7.01	29.6	0.05	5.96	4.43	457.06	4.06	'CAPEMEND\FOR090.AT2'
900	'Landers'	'1992'	'Yermo Fire Station'	7.28	86.0	0.14	12.93	4.91	353.63	3.18	'LANDERS\YER360.AT2'
1196	'Chi-Chi, Taiwan'	'1999'	'CHY027'	7.62	59.4	0.05	7.98	6.20	210.01	3.71	'CHICHI\CHY027-N.AT2'
1200	'Chi-Chi, Taiwan'	'1999'	'CHY033'	7.62	70.6	0.03	8.32	7.99	197.63	4.67	'CHICHI\CHY033-N.AT2'
1200	'Chi-Chi, Taiwan'	'1999'	'CHY033'	7.62	70.6	0.03	8.32	7.99	197.63	4.30	'CHICHI\CHY033-N.AT2'
1238	'Chi-Chi, Taiwan'	'1999'	'CHY092'	7.62	35.4	0.11	28.45	25.62	253.72	2.78	'CHICHI\CHY092-W.AT2'
1477	'Chi-Chi, Taiwan'	'1999'	'TCU031'	7.62	80.1	0.07	26.61	29.89	489.22	2.65	'CHICHI\TCU031-N.AT2'
1477	'Chi-Chi, Taiwan'	'1999'	'TCU031'	7.62	80.1	0.07	26.61	29.89	489.22	1.68	'CHICHI\TCU031-N.AT2'
1488	'Chi-Chi, Taiwan'	'1999'	'TCU048'	7.62	43.3	0.10	24.65	21.48	551.21	2.70	'CHICHI\TCU048-N.AT2'
1489	'Chi-Chi, Taiwan'	'1999'	'TCU049'	7.62	38.9	0.18	27.49	23.44	487.27	2.81	'CHICHI\TCU049-N.AT2'
1497	'Chi-Chi, Taiwan'	'1999'	'TCU057'	7.62	41.8	0.08	33.88	27.81	555.23	3.01	'CHICHI\TCU057-N.AT2'
1505	'Chi-Chi, Taiwan'	'1999'	'TCU068'	7.62	47.9	0.53	213.12	222.68	487.34	0.75	'CHICHI\TCU068-N.AT2'
1521	'Chi-Chi, Taiwan'	'1999'	'TCU089'	7.62	7.0	0.19	21.03	21.04	671.52	3.30	'CHICHI\TCU089-N.AT2'
1526	'Chi-Chi, Taiwan'	'1999'	'TCU098'	7.62	99.7	0.05	17.20	17.44	346.56	2.57	'CHICHI\TCU098-N.AT2'
1533	'Chi-Chi, Taiwan'	'1999'	'TCU106'	7.62	37.7	0.12	23.55	21.52	451.37	1.73	'CHICHI\TCU106-N.AT2'
1538	'Chi-Chi, Taiwan'	'1999'	'TCU112'	7.62	46.3	0.07	19.14	20.08	190.54	2.68	'CHICHI\TCU112-N.AT2'
1538	'Chi-Chi, Taiwan'	'1999'	'TCU112'	7.62	46.3	0.07	19.14	20.08	190.54	1.73	'CHICHI\TCU112-N.AT2'
1540	'Chi-Chi, Taiwan'	'1999'	'TCU115'	7.62	37.7	0.08	21.80	21.67	215.34	1.78	'CHICHI\TCU115-N.AT2'
1543	'Chi-Chi, Taiwan'	'1999'	'TCU118'	7.62	43.8	0.10	19.33	20.26	236.19	2.74	'CHICHI\TCU118-N.AT2'
1544	'Chi-Chi, Taiwan'	'1999'	'TCU119'	7.62	52.3	0.06	15.30	11.83	221.70	4.55	'CHICHI\TCU119-N.AT2'
1547	'Chi-Chi, Taiwan'	'1999'	'TCU123'	7.62	33.8	0.09	26.37	26.31	270.22	2.21	'CHICHI\TCU123-N.AT2'
2114	'Denali, Alaska'	'2002'	'TAPS Pump Station #10'	7.90	84.4	0.24	51.10	19.75	329.40	1.02	'DENALI\PS10-317.AT2'
2459	'Chi-Chi, Taiwan-03'	'1999'	'CHY026'	6.20	44.7	0.03	14.26	9.86	226.01	3.19	'CHICHI.03\CHY026E.AT2'
3747	'Cape Mendocino'	'1992'	'College of the Redwoods'	7.01	41.5	0.07	7.26	3.85	492.74	4.56	'CAPEMEND\CRW360.AT2'
3843	'Chi-Chi (aftershock 2), Taiwan'	'1999'	'CHY002'	6.20	45.7	0.04	15.98	12.08	235.13	3.62	'CHICHI.03\CHY002W.AT2'
5801	'Iwate'	'2008'	'Hirakamachi Asamai Yokote'	6.90	42.2	0.07	8.07	3.89	325.79	1.00	'IWATE\55442EW.AT2'

Table C-10: Characteristics of selected natural ground motions related to $\boldsymbol{T^* = T_b = 3}$ sec and $\boldsymbol{T_r = 10,000}$ years.

Record Sequence Number	Earthquake Name	YEAR	Station Name	Earthquake Magnitude (Mw)	EpiD (km)	PGA (g)	PGV (cm/sec)	PGD (cm)	Vs30 (m/s)	Scaling factor	Component file name
170	'Imperial Valley-06'	'1979'	'EC County Center FF'	6.53	29.1	0.24	18.92	9.60	192.05	1.84	'IMPVALL.H\H-ECC092.AT2'
181	'Imperial Valley-06'	'1979'	'El Centro Array #6'	6.53	27.5	1.90	63.58	23.63	203.22	0.86	'IMPVALL.H\H-E06230.AT2'
736	'Loma Prieta'	'1989'	'APEEL 9 - Crystal Springs Res'	6.93	61.5	0.05	7.44	2.64	449.64	4.53	'LOMAP\A09227.AT2'
777	'Loma Prieta'	'1989'	'Hollister City Hall'	6.93	47.9	0.22	15.25	7.53	198.77	2.79	'LOMAP\HCH180.AT2'
879	'Landers'	'1992'	'Lucerne'	7.28	44.0	0.82	41.09	29.83	1369.00	1.35	'LANDERS\LCN345.AT2'
1195	'Chi-Chi, Taiwan'	'1999'	'CHY026'	7.62	42.0	0.07	24.11	15.69	226.01	3.99	'CHICHI\CHY026-N.AT2'
1196	'Chi-Chi, Taiwan'	'1999'	'CHY027'	7.62	59.4	0.05	7.98	6.20	210.01	4.09	'CHICHI\CHY027-N.AT2'
1199	'Chi-Chi, Taiwan'	'1999'	'CHY032'	7.62	61.7	0.06	6.93	5.48	192.71	2.82	'CHICHI\CHY032-N.AT2'
1200	'Chi-Chi, Taiwan'	'1999'	'CHY033'	7.62	70.6	0.03	8.32	7.99	197.63	4.73	'CHICHI\CHY033-N.AT2'
1240	'Chi-Chi, Taiwan'	'1999'	'CHY094'	7.62	51.2	0.04	14.07	9.95	221.92	4.23	'CHICHI\CHY094-W.AT2'
1477	'Chi-Chi, Taiwan'	'1999'	'TCU031'	7.62	80.1	0.07	26.61	29.89	489.22	1.85	'CHICHI\TCU031-N.AT2'
1482	'Chi-Chi, Taiwan'	'1999'	'TCU039'	7.62	71.5	0.12	50.44	38.36	540.66	2.33	'CHICHI\TCU039-N.AT2'
1488	'Chi-Chi, Taiwan'	'1999'	'TCU048'	7.62	43.3	0.10	24.65	21.48	551.21	2.97	'CHICHI\TCU048-N.AT2'
1492	'Chi-Chi, Taiwan'	'1999'	'TCU052'	7.62	39.6	0.20	144.05	154.05	579.10	0.90	'CHICHI\TCU052-N.AT2'
1496	'Chi-Chi, Taiwan'	'1999'	'TCU056'	7.62	39.7	0.12	41.78	31.50	403.20	3.78	'CHICHI\TCU056-N.AT2'
1497	'Chi-Chi, Taiwan'	'1999'	'TCU057'	7.62	41.8	0.08	33.88	27.81	555.23	3.31	'CHICHI\TCU057-N.AT2'
1500	'Chi-Chi, Taiwan'	'1999'	'TCU061'	7.62	42.1	0.09	26.97	23.25	379.64	3.04	'CHICHI\TCU061-N.AT2'
1501	'Chi-Chi, Taiwan'	'1999'	'TCU063'	7.62	35.5	0.14	56.98	40.47	476.14	1.66	'CHICHI\TCU063-N.AT2'
1511	'Chi-Chi, Taiwan'	'1999'	'TCU076'	7.62	16.0	0.28	32.19	20.75	614.98	3.05	'CHICHI\TCU076-N.AT2'
1526	'Chi-Chi, Taiwan'	'1999'	'TCU098'	7.62	99.7	0.05	17.20	17.44	346.56	4.11	'CHICHI\TCU098-N.AT2'
1536	'Chi-Chi, Taiwan'	'1999'	'TCU110'	7.62	29.5	0.12	32.66	22.63	212.72	1.98	'CHICHI\TCU110-N.AT2'
1537	'Chi-Chi, Taiwan'	'1999'	'TCU111'	7.62	44.8	0.08	23.86	21.44	237.53	1.85	'CHICHI\TCU111-N.AT2'
1538	'Chi-Chi, Taiwan'	'1999'	'TCU112'	7.62	46.3	0.07	19.14	20.08	190.54	1.90	'CHICHI\TCU112-N.AT2'
1538	'Chi-Chi, Taiwan'	'1999'	'TCU112'	7.62	46.3	0.07	19.14	20.08	190.54	2.95	'CHICHI\TCU112-N.AT2'
1552	'Chi-Chi, Taiwan'	'1999'	'TCU140'	7.62	48.4	0.07	19.30	18.41	223.60	4.16	'CHICHI\TCU140-W.AT2'
2459	'Chi-Chi, Taiwan-03'	'1999'	'CHY026'	6.20	44.7	0.03	14.26	9.86	226.01	3.50	'CHICHI.03\CHY026E.AT2'
5801	'Iwate'	'2008'	'Hirakamachi Asamai Yokote'	6.90	42.2	0.07	8.07	3.89	325.79	1.10	'IWATE\55442EW.AT2'
5831	'El Mayor-Cucapah'	'2010'	'EJIDO SALTILLO'	7.20	18.7	0.18	19.32	13.98	242.05	2.67	'SIERRA.MEX\SAL090.AT2'
6888	'Darfield, New Zealand'	'2010'	'Christchurch Cathedral College'	7.00	48.9	0.20	20.48	13.16	198.00	1.18	'DARFIELD\CCCCN64E.AT2'
6953	'Darfield, New Zealand'	'2010'	'Pages Road Pumping Station'	7.00	53.5	0.32	19.59	12.46	206.00	3.41	'DARFIELD\PRPCS.AT2'

Table C-11: Characteristics of selected natural ground motions related to $\boldsymbol{T^* = T_b = 5}$ sec and $\boldsymbol{T_r = 43}$ years.

Record Sequence Number	Earthquake Name	YEAR	Station Name	Earthquake Magnitude (Mw)	EpiD (km)	PGA (g)	PGV (cm/sec)	PGD (cm)	Vs30 (m/s)	Scaling factor	Component file name
180	'Imperial Valley-06'	'1979'	'El Centro Array #5'	6.53	27.8	0.59	39.54	22.32	205.63	0.09	'IMPVALL.H\H-E05230.AT2'
187	'Imperial Valley-06'	'1979'	'Parachute Test Site'	6.53	48.6	0.16	7.25	5.04	348.69	0.17	'IMPVALL.H\H-PTS315.AT2'
188	'Imperial Valley-06'	'1979'	'Plaster City'	6.53	54.3	0.03	1.68	0.60	316.64	2.07	'IMPVALL.H\H-PLS135.AT2'
732	'Loma Prieta'	'1989'	'APEEL 2 - Redwood City'	6.93	63.5	0.08	9.71	3.47	133.11	0.23	'LOMAP\A02133.AT2'
767	'Loma Prieta'	'1989'	'Gilroy Array #3'	6.93	31.4	0.34	15.65	7.04	349.85	0.25	'LOMAP\G03090.AT2'
801	'Loma Prieta'	'1989'	'San Jose - Santa Teresa Hills'	6.93	20.1	0.23	18.68	9.27	671.77	0.56	'LOMAP\SJTE315.AT2'
897	'Landers'	'1992'	'Twentynine Palms'	7.28	44.1	0.04	3.30	1.79	635.01	0.97	'LANDERS\29P090.AT2'
1087	'Northridge-01'	'1994'	'Tarzana - Cedar Hill A'	6.69	5.4	1.05	72.20	18.97	257.21	0.09	'NORTHR\TAR360.AT2'
1102	'Kobe, Japan'	'1995'	'Chihaya'	6.90	61.9	0.08	2.43	1.58	609.00	1.13	'KOBE\CHY090.AT2'
1144	'Gulf of Aqaba'	'1995'	'Eilat'	7.20	93.4	0.11	4.30	1.13	354.88	0.47	'AQABA\EIL-NS.AT2'
1273	'Chi-Chi, Taiwan'	'1999'	'HWA024'	7.62	73.7	0.03	5.11	6.00	671.52	0.74	'CHICHI\HWA024-N.AT2'
1489	'Chi-Chi, Taiwan'	'1999'	'TCU049'	7.62	38.9	0.18	27.49	23.44	487.27	0.11	'CHICHI\TCU049-N.AT2'
1493	'Chi-Chi, Taiwan'	'1999'	'TCU053'	7.62	41.2	0.12	32.53	27.96	454.55	0.14	'CHICHI\TCU053-N.AT2'
1613	'Duzce, Turkey'	'1999'	'Lamont 1060'	7.14	44.4	0.02	6.34	6.24	782.00	0.57	'DUZCE\1060-E.AT2'
1615	'Duzce, Turkey'	'1999'	'Lamont 1062'	7.14	29.3	0.09	7.43	5.78	338.00	0.54	'DUZCE\1062-E.AT2'
1618	'Duzce, Turkey'	'1999'	'Lamont 531'	7.14	27.7	0.06	8.84	7.35	638.39	0.58	'DUZCE\531-E.AT2'
1626	'Sitka, Alaska'	'1972'	'Sitka Observatory'	7.68	42.9	0.05	4.78	3.22	649.67	0.37	'SITKA\212V5180.AT2'
2605	'Chi-Chi, Taiwan-03'	'1999'	'TCU049'	6.20	44.2	0.01	3.29	2.53	487.27	0.89	'CHICHI.03\TCU049E.AT2'
2626	'Chi-Chi, Taiwan-03'	'1999'	'TCU075'	6.20	26.0	0.10	10.13	8.85	573.02	0.29	'CHICHI.03\TCU075E.AT2'
2635	'Chi-Chi, Taiwan-03'	'1999'	'TCU089'	6.20	10.5	0.04	3.53	1.54	671.52	0.56	'CHICHI.03\TCU089E.AT2'
2753	'Chi-Chi, Taiwan-04'	'1999'	'CHY102'	6.20	44.7	0.02	3.08	1.81	804.36	1.99	'CHICHI.04\CHY102E.AT2'
3453	'Chi-Chi, Taiwan-06'	'1999'	'TCU044'	6.30	64.6	0.02	2.85	1.11	512.88	3.21	'CHICHI.06\TCU044E.AT2'
3477	'Chi-Chi, Taiwan-06'	'1999'	'TCU082'	6.30	45.9	0.02	4.10	1.87	472.81	1.12	'CHICHI.06\TCU082E.AT2'
3493	'Chi-Chi, Taiwan-06'	'1999'	'TCU107'	6.30	52.8	0.06	3.91	2.55	409.00	0.62	'CHICHI.06\TCU107E.AT2'
3854	'Chi-Chi (aftershock 3), Taiwan'	'1999'	'CHY010'	6.20	31.9	0.08	3.55	1.46	538.69	0.81	'CHICHI.04\CHY010W.AT2'
3943	'Tottori, Japan'	'2000'	'SMN015'	6.61	18.7	0.16	7.52	3.74	616.55	0.30	'TOTTORI\SMN015EW.AT2'
3962	'Tottori, Japan'	'2000'	'TTR005'	6.61	46.5	0.06	2.50	0.80	169.16	1.24	'TOTTORI\TTR005EW.AT2'
4846	'Chuetsu-oki'	'2007'	'Joetsu Yanagishima paddocks'	6.80	55.3	0.18	12.23	4.25	605.71	0.44	'CHUETSU\65009EW.AT2'
5829	'El Mayor-Cucapah'	'2010'	'RIITO'	7.20	32.4	0.67	15.19	11.26	242.05	0.07	'SIERRA.MEX\RII090.AT2'
6948	'Darfield, New Zealand'	'2010'	'OXZ'	7.00	32.2	0.10	7.43	4.67	481.62	0.43	'DARFIELD\OXZN.AT2'

Table C-12: Characteristics of selected natural ground motions related to $\boldsymbol{T^*} = \boldsymbol{T_b} = \mathbf{5}$ sec and $\boldsymbol{T_r} = \mathbf{144}$ years.

Record Sequence Number	Earthquake Name	YEAR	Station Name	Earthquake Magnitude (Mw)	EpiD (km)	PGA (g)	PGV (cm/sec)	PGD (cm)	Vs30 (m/s)	Scaling factor	Component file name
15	'Kern County'	'1952'	'Taft Lincoln School'	7.36	43.5	0.11	6.81	5.77	385.43	0.91	'KERN\TAF111.AT2'
187	'Imperial Valley-06'	'1979'	'Parachute Test Site'	6.53	48.6	0.16	7.25	5.04	348.69	0.54	'IMPVALL.H\H-PTS315.AT2'
364	'Coalinga-01'	'1983'	'Parkfield - Vineyard Cany 4W'	6.36	42.4	0.03	2.79	0.61	386.19	3.70	'COALINGA.H\H-VC4090.AT2'
897	'Landers'	'1992'	'Twentynine Palms'	7.28	44.1	0.04	3.30	1.79	635.01	1.85	'LANDERS\29P090.AT2'
1193	'Chi-Chi, Taiwan'	'1999'	'CHY024'	7.62	24.1	0.14	47.29	29.19	427.73	0.27	'CHICHI\CHY024-N.AT2'
1270	'Chi-Chi, Taiwan'	'1999'	'HWA020'	7.62	62.5	0.05	8.43	9.58	626.43	1.77	'CHICHI\HWA020-N.AT2'
1279	'Chi-Chi, Taiwan'	'1999'	'HWA030'	7.62	64.4	0.05	8.46	9.75	592.18	1.94	'CHICHI\HWA030-N.AT2'
1301	'Chi-Chi, Taiwan'	'1999'	'HWA056'	7.62	78.9	0.06	7.54	8.65	511.30	1.81	'CHICHI\HWA056-N.AT2'
1402	'Chi-Chi, Taiwan'	'1999'	'NST'	7.62	88.8	0.09	23.32	8.65	491.08	0.64	'CHICHI\NST-N.AT2'
1493	'Chi-Chi, Taiwan'	'1999'	'TCU053'	7.62	41.2	0.12	32.53	27.96	454.55	0.44	'CHICHI\TCU053-N.AT2'
1504	'Chi-Chi, Taiwan'	'1999'	'TCU067'	7.62	28.7	0.24	49.83	34.93	433.63	0.23	'CHICHI\TCU067-N.AT2'
1515	'Chi-Chi, Taiwan'	'1999'	'TCU082'	7.62	36.2	0.13	34.95	28.92	472.81	0.28	'CHICHI\TCU082-N.AT2'
1549	'Chi-Chi, Taiwan'	'1999'	'TCU129'	7.62	14.2	0.34	38.84	24.40	511.18	0.24	'CHICHI\TCU129-N.AT2'
1598	'Chi-Chi, Taiwan'	'1999'	'WTC'	7.62	54.9	0.05	8.85	8.05	207.69	0.97	'CHICHI\WTC-N.AT2'
1620	'Duzce, Turkey'	'1999'	'Sakarya'	7.14	64.2	0.01	3.06	3.84	411.91	2.54	'DUZCE\SKR180.AT2'
1626	'Sitka, Alaska'	'1972'	'Sitka Observatory'	7.68	42.9	0.05	4.78	3.22	649.67	1.83	'SITKA\212V5180.AT2'
2642	'Chi-Chi, Taiwan-03'	'1999'	'TCU104'	6.20	54.6	0.01	2.52	2.40	410.45	3.41	'CHICHI.03\TCU104E.AT2'
2661	'Chi-Chi, Taiwan-03'	'1999'	'TCU138'	6.20	28.8	0.08	19.61	11.20	652.85	1.31	'CHICHI.03\TCU138W.AT2'
2703	'Chi-Chi, Taiwan-04'	'1999'	'CHY028'	6.20	22.2	0.07	5.79	3.79	542.61	0.69	'CHICHI.04\CHY028E.AT2'
2935	'Chi-Chi, Taiwan-04'	'1999'	'TTN051'	6.20	50.0	0.04	3.24	1.76	665.20	2.81	'CHICHI.04\TTN051E.AT2'
3925	'Tottori, Japan'	'2000'	'OKYH07'	6.61	25.6	0.12	10.82	4.29	940.20	2.47	'TOTTORI\OKYH07EW.AT2'
3979	'San Simeon, CA'	'2003'	'Cambria - Hwy 1 Caltrans Bridge'	6.52	12.1	0.09	6.24	2.34	362.42	1.07	'SANSIMEO\37737360.AT2'
4054	'Bam, Iran'	'2003'	'Mohammad Abad-e-Madkoon'	6.60	46.6	0.07	2.41	0.69	574.88	1.04	'BAM\MOH-T.AT2'
5830	'El Mayor-Cucapah'	'2010'	'RANCHO SAN LUIS'	7.20	57.8	0.04	2.39	2.31	523.99	3.96	'SIERRA.MEX\RSL090.AT2'
5837	'El Mayor-Cucapah'	'2010'	'El Centro - Imperial & Ross'	7.20	60.4	0.27	11.40	8.03	229.25	0.28	'SIERRA.MEX\01711-90.AT2'
5838	'El Mayor-Cucapah'	'2010'	'El Centro - Meloland Geotechnic'	7.20	55.3	0.13	9.11	6.50	186.21	0.18	'SIERRA.MEX\01794270.AT2'
6928	'Darfield, New Zealand'	'2010'	'LPCC'	7.00	54.3	0.16	9.92	6.06	649.67	0.53	'DARFIELD\LPCCS10E.AT2'
6959	'Darfield, New Zealand'	'2010'	'Christchurch Resthaven '	7.00	48.3	0.21	20.23	13.12	141.00	0.18	'DARFIELD\REHSS88E.AT2'
6965	'Darfield, New Zealand'	'2010'	'SBRC'	7.00	27.2	0.10	6.12	3.82	263.20	0.38	'DARFIELD\SBRCS59W.AT2'
8597	'El Mayor-Cucapah'	'2010'	'Sam W. Stewart'	7.20	87.4	0.05	6.68	7.07	503.00	0.98	'ELMAYOR\CISWSHNE.AT2'

Table C-13: Characteristics of selected natural ground motions related to $\boldsymbol{T^{*}} = \boldsymbol{T_b} = \mathbf{5}$ sec and $\boldsymbol{T_r} = \mathbf{289}$ years.

Record Sequence Number	Earthquake Name	YEAR	Station Name	Earthquake Magnitude (Mw)	EpiD (km)	PGA (g)	PGV (cm/sec)	PGD (cm)	Vs30 (m/s)	Scaling factor	Component file name
163	'Imperial Valley-06'	'1979'	'Calipatria Fire Station'	6.53	57.1	0.06	4.17	3.16	205.78	1.08	'IMPVALL.H\H-CAL225.AT2'
286	'Irpinia, Italy-01'	'1980'	'Bisaccia'	6.90	23.3	0.05	16.17	13.61	496.46	1.64	'ITALY\A-BIS000.AT2'
761	'Loma Prieta'	'1989'	'Fremont - Emerson Court'	6.93	55.2	0.07	8.93	6.89	284.79	2.06	'LOMAP\FMS090.AT2'
1144	'Gulf of Aqaba'	'1995'	'Eilat'	7.20	93.4	0.11	4.30	1.13	354.88	2.23	'AQABA\EIL-EW.AT2'
1161	'Kocaeli, Turkey'	'1999'	'Gebze'	7.51	47.0	0.19	14.12	5.77	792.00	0.53	'KOCAELI\GBZ000.AT2'
1489	'Chi-Chi, Taiwan'	'1999'	'TCU049'	7.62	38.9	0.18	27.49	23.44	487.27	0.70	'CHICHI\TCU049-E.AT2'
1493	'Chi-Chi, Taiwan'	'1999'	'TCU053'	7.62	41.2	0.12	32.53	27.96	454.55	0.88	'CHICHI\TCU053-E.AT2'
1504	'Chi-Chi, Taiwan'	'1999'	'TCU067'	7.62	28.7	0.24	49.83	34.93	433.63	0.45	'CHICHI\TCU067-E.AT2'
1505	'Chi-Chi, Taiwan'	'1999'	'TCU068'	7.62	47.9	0.53	213.12	222.68	487.34	0.13	'CHICHI\TCU068-E.AT2'
1517	'Chi-Chi, Taiwan'	'1999'	'TCU084'	7.62	8.9	0.32	25.63	13.24	665.20	0.63	'CHICHI\TCU084-E.AT2'
1524	'Chi-Chi, Taiwan'	'1999'	'TCU095'	7.62	95.7	0.26	23.02	21.70	446.63	0.54	'CHICHI\TCU095-E.AT2'
1546	'Chi-Chi, Taiwan'	'1999'	'TCU122'	7.62	21.8	0.24	41.10	30.80	475.46	0.41	'CHICHI\TCU122-E.AT2'
1611	'Duzce, Turkey'	'1999'	'Lamont 1058'	7.14	13.4	0.07	15.22	12.17	529.18	2.04	'DUZCE\1058-N.AT2'
1613	'Duzce, Turkey'	'1999'	'Lamont 1060'	7.14	44.4	0.02	6.34	6.24	782.00	3.56	'DUZCE\1060-N.AT2'
1613	'Duzce, Turkey'	'1999'	'Lamont 1060'	7.14	44.4	0.02	6.34	6.24	782.00	2.44	'DUZCE\1060-N.AT2'
1620	'Duzce, Turkey'	'1999'	'Sakarya'	7.14	64.2	0.01	3.06	3.84	411.91	4.21	'DUZCE\SKR090.AT2'
1626	'Sitka, Alaska'	'1972'	'Sitka Observatory'	7.68	42.9	0.05	4.78	3.22	649.67	2.33	'SITKA\212V5090.AT2'
1626	'Sitka, Alaska'	'1972'	'Sitka Observatory'	7.68	42.9	0.05	4.78	3.22	649.67	3.62	'SITKA\212V5090.AT2'
3752	'Landers'	'1992'	'Forest Falls Post Office'	7.28	46.2	0.08	3.53	1.16	436.14	2.82	'LANDERS\FFP210.AT2'
3757	'Landers'	'1992'	'North Palm Springs Fire Sta #36'	7.28	32.3	0.10	6.98	2.43	367.84	2.97	'LANDERS\NPF090.AT2'
3760	'Landers'	'1992'	'Big Bear Lake - Civic Center'	7.28	46.1	0.08	4.15	1.68	430.36	1.38	'LANDERS\BLC360.AT2'
3884	'Tottori, Japan'	'2000'	'HRS021'	6.61	41.8	0.21	4.08	2.79	409.29	3.23	'TOTTORI\HRS021NS.AT2'
5796	'Iwate'	'2008'	'Yokote Central City'	6.90	41.3	0.06	5.96	4.91	531.68	2.55	'IWATE\55203NS.AT2'
5823	'El Mayor-Cucapah'	'2010'	'Chihuahua'	7.20	20.6	0.28	15.91	12.99	242.05	0.51	'SIERRA.MEX\CHI000.AT2'
5969	'El Mayor-Cucapah'	'2010'	'Bonds Corner'	7.20	44.2	0.11	6.93	5.51	223.03	1.10	'SIERRA.MEX\BCR360.AT2'
5985	'El Mayor-Cucapah'	'2010'	'El Centro Differential Array'	7.20	60.7	0.31	10.34	6.26	202.26	0.69	'SIERRA.MEX\EDA360.AT2'
6879	'Darfield, New Zealand'	'2010'	'ADCS'	7.00	40.3	0.06	4.21	2.59	249.28	1.47	'DARFIELD\ADCSN42W.AT2'
6886	'Darfield, New Zealand'	'2010'	'Canterbury Aero Club'	7.00	41.4	0.31	20.19	16.10	280.26	0.39	'DARFIELD\CACSN40E.AT2'
6948	'Darfield, New Zealand'	'2010'	'OXZ'	7.00	32.2	0.10	7.43	4.67	481.62	2.65	'DARFIELD\OXZE.AT2'
6969	'Darfield, New Zealand'	'2010'	'Styx Mill Transfer Station '	7.00	48.4	0.23	12.36	9.37	247.50	0.63	'DARFIELD\SMTCN88W.AT2'

Table C-14: Characteristics of selected natural ground motions related to $\boldsymbol{T^*} = \boldsymbol{T_b} = \mathbf{5}$ sec and $\boldsymbol{T_r} = \mathbf{475}$ years.

Record Sequence Number	Earthquake Name	YEAR	Station Name	Earthquake Magnitude (Mw)	EpiD (km)	PGA (g)	PGV (cm/sec)	PGD (cm)	Vs30 (m/s)	Scaling factor	Component file name
36	'Borrego Mtn'	'1968'	'El Centro Array #9'	6.63	70.8	0.03	3.42	3.01	213.44	2.17	'BORREGO\A-ELC180.AT2'
163	'Imperial Valley-06'	'1979'	'Calipatria Fire Station'	6.53	57.1	0.06	4.17	3.16	205.78	1.63	'IMPVALL.H\H-CAL225.AT2'
163	'Imperial Valley-06'	'1979'	'Calipatria Fire Station'	6.53	57.1	0.06	4.17	3.16	205.78	1.64	'IMPVALL.H\H-CAL225.AT2'
172	'Imperial Valley-06'	'1979'	'El Centro Array #1'	6.53	35.2	0.07	3.59	1.53	237.33	2.98	'IMPVALL.H\H-E01140.AT2'
187	'Imperial Valley-06'	'1979'	'Parachute Test Site'	6.53	48.6	0.16	7.25	5.04	348.69	1.61	'IMPVALL.H\H-PTS225.AT2'
292	'Irpinia, Italy-01'	'1980'	'Sturno (STN)'	6.90	30.4	0.23	24.02	10.49	382.00	0.65	'ITALY\A-STU000.AT2'
1161	'Kocaeli, Turkey'	'1999'	'Gebze'	7.51	47.0	0.19	14.12	5.77	792.00	0.80	'KOCAELI\GBZ000.AT2'
1208	'Chi-Chi, Taiwan'	'1999'	'CHY046'	7.62	55.2	0.08	7.59	6.83	442.15	2.39	'CHICHI\CHY046-E.AT2'
1287	'Chi-Chi, Taiwan'	'1999'	'HWA038'	7.62	68.8	0.04	6.42	6.57	642.73	4.30	'CHICHI\HWA038-E.AT2'
1486	'Chi-Chi, Taiwan'	'1999'	'TCU046'	7.62	68.9	0.10	32.44	39.08	465.55	0.87	'CHICHI\TCU046-E.AT2'
1487	'Chi-Chi, Taiwan'	'1999'	'TCU047'	7.62	86.4	0.27	22.39	21.45	520.37	1.10	'CHICHI\TCU047-E.AT2'
1488	'Chi-Chi, Taiwan'	'1999'	'TCU048'	7.62	43.3	0.10	24.65	21.48	551.21	0.37	'CHICHI\TCU048-E.AT2'
1489	'Chi-Chi, Taiwan'	'1999'	'TCU049'	7.62	38.9	0.18	27.49	23.44	487.27	1.06	'CHICHI\TCU049-E.AT2'
1491	'Chi-Chi, Taiwan'	'1999'	'TCU051'	7.62	38.5	0.11	29.90	26.37	350.06	0.65	'CHICHI\TCU051-E.AT2'
1494	'Chi-Chi, Taiwan'	'1999'	'TCU054'	7.62	37.6	0.14	30.14	24.90	460.69	0.69	'CHICHI\TCU054-E.AT2'
1539	'Chi-Chi, Taiwan'	'1999'	'TCU113'	7.62	44.4	0.08	15.33	15.33	230.30	1.06	'CHICHI\TCU113-E.AT2'
1545	'Chi-Chi, Taiwan'	'1999'	'TCU120'	7.62	25.6	0.17	35.30	22.96	459.34	0.63	'CHICHI\TCU120-E.AT2'
1549	'Chi-Chi, Taiwan'	'1999'	'TCU129'	7.62	14.2	0.34	38.84	24.40	511.18	0.72	'CHICHI\TCU129-E.AT2'
1585	'Chi-Chi, Taiwan'	'1999'	'TTN040'	7.62	86.8	0.02	4.66	5.17	728.01	4.50	'CHICHI\TTN040-N.AT2'
1626	'Sitka, Alaska'	'1972'	'Sitka Observatory'	7.68	42.9	0.05	4.78	3.22	649.67	3.52	'SITKA\212V5090.AT2'
2604	'Chi-Chi, Taiwan-03'	'1999'	'TCU048'	6.20	48.7	0.02	3.02	2.31	551.21	2.72	'CHICHI.03\TCU048N.AT2'
2626	'Chi-Chi, Taiwan-03'	'1999'	'TCU075'	6.20	26.0	0.10	10.13	8.85	573.02	2.72	'CHICHI.03\TCU075N.AT2'
2632	'Chi-Chi, Taiwan-03'	'1999'	'TCU084'	6.20	9.6	0.05	4.91	2.68	665.20	3.25	'CHICHI.03\TCU084N.AT2'
2654	'Chi-Chi, Taiwan-03'	'1999'	'TCU120'	6.20	30.7	0.05	9.37	8.56	459.34	4.16	'CHICHI.03\TCU120N.AT2'
4230	'Niigata, Japan'	'2004'	'NIGH13'	6.63	48.2	0.03	3.39	2.86	461.10	4.63	'NIIGATA\NIGH13NS.AT2'
5831	'El Mayor-Cucapah'	'2010'	'EJIDO SALTILLO'	7.20	18.7	0.18	19.32	13.98	242.05	0.83	'SIERRA.MEX\SAL000.AT2'
5831	'El Mayor-Cucapah'	'2010'	'EJIDO SALTILLO'	7.20	18.7	0.18	19.32	13.98	242.05	0.84	'SIERRA.MEX\SAL000.AT2'
5832	'El Mayor-Cucapah'	'2010'	'TAMAULIPAS'	7.20	27.9	0.21	14.10	10.00	242.05	1.21	'SIERRA.MEX\TAM000.AT2'
6886	'Darfield, New Zealand'	'2010'	'Canterbury Aero Club'	7.00	41.4	0.31	20.19	16.10	280.26	0.59	'DARFIELD\CACSN40E.AT2'
6969	'Darfield, New Zealand'	'2010'	'Styx Mill Transfer Station '	7.00	48.4	0.23	12.36	9.37	247.50	0.95	'DARFIELD\SMTCN88W.AT2'

Table C-15: Characteristics of selected natural ground motions related to $\boldsymbol{T^{*}=T_{b}=5}$ sec and $\boldsymbol{T_{r}=949}$ years.

Record Sequence Number	Earthquake Name	YEAR	Station Name	Earthquake Magnitude (Mw)	EpiD (km)	PGA (g)	PGV (cm/sec)	PGD (cm)	Vs30 (m/s)	Scaling factor	Component file name
36	'Borrego Mtn'	'1968'	'El Centro Array #9'	6.63	70.8	0.03	3.42	3.01	213.44	3.42	'BORREGO\A-ELC180.AT2'
163	'Imperial Valley-06'	'1979'	'Calipatria Fire Station'	6.53	57.1	0.06	4.17	3.16	205.78	2.57	'IMPVALL.H\H-CAL225.AT2'
178	'Imperial Valley-06'	'1979'	'El Centro Array #3'	6.53	28.7	0.13	9.15	5.05	162.94	1.25	'IMPVALL.H\H-E03140.AT2'
187	'Imperial Valley-06'	'1979'	'Parachute Test Site'	6.53	48.6	0.16	7.25	5.04	348.69	2.53	'IMPVALL.H\H-PTS225.AT2'
827	'Cape Mendocino'	'1992'	'Fortuna - Fortuna Blvd'	7.01	29.6	0.05	5.96	4.43	457.06	2.82	'CAPEMEND\FOR000.AT2'
1057	'Northridge-01'	'1994'	'Playa Del Rey - Saran'	6.69	29.6	0.05	9.10	3.86	345.72	4.21	'NORTHR\SAR000.AT2'
1161	'Kocaeli, Turkey'	'1999'	'Gebze'	7.51	47.0	0.19	14.12	5.77	792.00	0.99	'KOCAELI\GBZ000.AT2'
1206	'Chi-Chi, Taiwan'	'1999'	'CHY042'	7.62	59.8	0.06	8.63	4.77	665.20	3.65	'CHICHI\CHY042-E.AT2'
1239	'Chi-Chi, Taiwan'	'1999'	'CHY093'	7.62	71.9	0.04	5.91	4.94	190.49	0.83	'CHICHI\CHY093-N.AT2'
1402	'Chi-Chi, Taiwan'	'1999'	'NST'	7.62	88.8	0.09	23.32	8.65	491.08	3.57	'CHICHI\NST-E.AT2'
1479	'Chi-Chi, Taiwan'	'1999'	'TCU034'	7.62	87.9	0.07	12.55	13.70	393.77	0.95	'CHICHI\TCU034-E.AT2'
1489	'Chi-Chi, Taiwan'	'1999'	'TCU049'	7.62	38.9	0.18	27.49	23.44	487.27	0.87	'CHICHI\TCU049-E.AT2'
1491	'Chi-Chi, Taiwan'	'1999'	'TCU051'	7.62	38.5	0.11	29.90	26.37	350.06	1.02	'CHICHI\TCU051-E.AT2'
1499	'Chi-Chi, Taiwan'	'1999'	'TCU060'	7.62	45.4	0.09	28.04	27.10	375.42	1.66	'CHICHI\TCU060-E.AT2'
1508	'Chi-Chi, Taiwan'	'1999'	'TCU072'	7.62	21.4	0.28	28.72	32.92	468.14	1.68	'CHICHI\TCU072-E.AT2'
1527	'Chi-Chi, Taiwan'	'1999'	'TCU100'	7.62	42.8	0.09	39.53	32.65	535.13	1.19	'CHICHI\TCU100-E.AT2'
1534	'Chi-Chi, Taiwan'	'1999'	'TCU107'	7.62	37.7	0.10	26.26	22.70	409.00	0.84	'CHICHI\TCU107-E.AT2'
1540	'Chi-Chi, Taiwan'	'1999'	'TCU115'	7.62	37.7	0.08	21.80	21.67	215.34	0.79	'CHICHI\TCU115-E.AT2'
1546	'Chi-Chi, Taiwan'	'1999'	'TCU122'	7.62	21.8	0.24	41.10	30.80	475.46	0.97	'CHICHI\TCU122-E.AT2'
1551	'Chi-Chi, Taiwan'	'1999'	'TCU138'	7.62	24.2	0.11	25.95	19.83	652.85	1.62	'CHICHI\TCU138-N.AT2'
2604	'Chi-Chi, Taiwan-03'	'1999'	'TCU048'	6.20	48.7	0.02	3.02	2.31	551.21	4.29	'CHICHI.03\TCU048N.AT2'
2616	'Chi-Chi, Taiwan-03'	'1999'	'TCU063'	6.20	40.9	0.03	5.29	4.80	476.14	3.11	'CHICHI.03\TCU063N.AT2'
5823	'El Mayor-Cucapah'	'2010'	'Chihuahua'	7.20	20.6	0.28	15.91	12.99	242.05	1.22	'SIERRA.MEX\CHI000.AT2'
5831	'El Mayor-Cucapah'	'2010'	'EJIDO SALTILLO'	7.20	18.7	0.18	19.32	13.98	242.05	1.31	'SIERRA.MEX\SAL000.AT2'
5831	'El Mayor-Cucapah'	'2010'	'EJIDO SALTILLO'	7.20	18.7	0.18	19.32	13.98	242.05	1.33	'SIERRA.MEX\SAL000.AT2'
5972	'El Mayor-Cucapah'	'2010'	'Brawley Airport'	7.20	80.3	0.08	4.01	2.84	208.71	1.97	'SIERRA.MEX\BRA360.AT2'
6886	'Darfield, New Zealand'	'2010'	'Canterbury Aero Club'	7.00	41.4	0.31	20.19	16.10	280.26	1.17	'DARFIELD\CACSN40E.AT2'
6897	'Darfield, New Zealand'	'2010'	'DSLC'	7.00	13.4	0.32	14.58	9.50	295.74	1.39	'DARFIELD\DSLCN27W.AT2'
6942	'Darfield, New Zealand'	'2010'	'NNBS North New Brighton School '	7.00	55.5	0.15	18.94	11.69	211.00	1.02	'DARFIELD\NNBSS13E.AT2'
6969	'Darfield, New Zealand'	'2010'	'Styx Mill Transfer Station '	7.00	48.4	0.23	12.36	9.37	247.50	1.50	'DARFIELD\SMTCN88W.AT2'

Table C-16: Characteristics of selected natural ground motions related to $T^* = T_b = 5$ sec and $T_r = 1{,}485$ years.

Record Sequence Number	Earthquake Name	YEAR	Station Name	Earthquake Magnitude (Mw)	EpiD (km)	PGA (g)	PGV (cm/sec)	PGD (cm)	Vs30 (m/s)	Scaling factor	Component file name
163	'Imperial Valley-06'	'1979'	'Calipatria Fire Station'	6.53	57.1	0.06	4.17	3.16	205.78	3.26	'IMPVALL.H\H-CAL315.AT2'
172	'Imperial Valley-06'	'1979'	'El Centro Array #1'	6.53	35.2	0.07	3.59	1.53	237.33	3.77	'IMPVALL.H\H-E01230.AT2'
174	'Imperial Valley-06'	'1979'	'El Centro Array #11'	6.53	29.5	0.14	11.59	7.21	196.25	2.29	'IMPVALL.H\H-E11230.AT2'
1148	'Kocaeli, Turkey'	'1999'	'Arcelik'	7.51	53.7	0.08	7.99	7.32	523.00	1.40	'KOCAELI\ARE090.AT2'
1206	'Chi-Chi, Taiwan'	'1999'	'CHY042'	7.62	59.8	0.06	8.63	4.77	665.20	4.62	'CHICHI\CHY042-N.AT2'
1228	'Chi-Chi, Taiwan'	'1999'	'CHY076'	7.62	65.4	0.03	8.82	7.18	169.84	2.79	'CHICHI\CHY076-N.AT2'
1240	'Chi-Chi, Taiwan'	'1999'	'CHY094'	7.62	51.2	0.04	14.07	9.95	221.92	1.12	'CHICHI\CHY094-W.AT2'
1476	'Chi-Chi, Taiwan'	'1999'	'TCU029'	7.62	79.2	0.06	20.78	25.64	406.53	0.60	'CHICHI\TCU029-N.AT2'
1488	'Chi-Chi, Taiwan'	'1999'	'TCU048'	7.62	43.3	0.10	24.65	21.48	551.21	0.74	'CHICHI\TCU048-N.AT2'
1491	'Chi-Chi, Taiwan'	'1999'	'TCU051'	7.62	38.5	0.11	29.90	26.37	350.06	1.29	'CHICHI\TCU051-N.AT2'
1496	'Chi-Chi, Taiwan'	'1999'	'TCU056'	7.62	39.7	0.12	41.78	31.50	403.20	1.00	'CHICHI\TCU056-N.AT2'
1499	'Chi-Chi, Taiwan'	'1999'	'TCU060'	7.62	45.4	0.09	28.04	27.10	375.42	2.11	'CHICHI\TCU060-N.AT2'
1504	'Chi-Chi, Taiwan'	'1999'	'TCU067'	7.62	28.7	0.24	49.83	34.93	433.63	1.22	'CHICHI\TCU067-N.AT2'
1505	'Chi-Chi, Taiwan'	'1999'	'TCU068'	7.62	47.9	0.53	213.12	222.68	487.34	0.40	'CHICHI\TCU068-N.AT2'
1508	'Chi-Chi, Taiwan'	'1999'	'TCU072'	7.62	21.4	0.28	28.72	32.92	468.14	2.24	'CHICHI\TCU072-N.AT2'
1536	'Chi-Chi, Taiwan'	'1999'	'TCU110'	7.62	29.5	0.12	32.66	22.63	212.72	1.53	'CHICHI\TCU110-N.AT2'
1538	'Chi-Chi, Taiwan'	'1999'	'TCU112'	7.62	46.3	0.07	19.14	20.08	190.54	1.57	'CHICHI\TCU112-N.AT2'
1544	'Chi-Chi, Taiwan'	'1999'	'TCU119'	7.62	52.3	0.06	15.30	11.83	221.70	2.38	'CHICHI\TCU119-N.AT2'
1552	'Chi-Chi, Taiwan'	'1999'	'TCU140'	7.62	48.4	0.07	19.30	18.41	223.60	2.03	'CHICHI\TCU140-W.AT2'
1554	'Chi-Chi, Taiwan'	'1999'	'TCU145'	7.62	51.2	0.05	19.51	17.65	240.43	2.10	'CHICHI\TCU145-W.AT2'
1619	'Duzce, Turkey'	'1999'	'Mudurnu'	7.14	41.5	0.06	8.63	7.08	535.24	2.91	'DUZCE\MDR090.AT2'
5831	'El Mayor-Cucapah'	'2010'	'EJIDO SALTILLO'	7.20	18.7	0.18	19.32	13.98	242.05	1.68	'SIERRA.MEX\SAL090.AT2'
5831	'El Mayor-Cucapah'	'2010'	'EJIDO SALTILLO'	7.20	18.7	0.18	19.32	13.98	242.05	1.66	'SIERRA.MEX\SAL090.AT2'
5838	'El Mayor-Cucapah'	'2010'	'El Centro - Meloland Geotechnic'	7.20	55.3	0.13	9.11	6.50	186.21	1.06	'SIERRA.MEX\01794270.AT2'
5989	'El Mayor-Cucapah'	'2010'	'El Centro Array #3'	7.20	66.9	0.13	7.17	5.26	162.94	2.04	'SIERRA.MEX\E03270.AT2'
6013	'El Mayor-Cucapah'	'2010'	'El Centro - Meadows Union School'	7.20	58.9	0.10	8.34	5.39	276.25	1.72	'SIERRA.MEX\2027A090.AT2'
6886	'Darfield, New Zealand'	'2010'	'Canterbury Aero Club'	7.00	41.4	0.31	20.19	16.10	280.26	1.17	'DARFIELD\CACSN50W.AT2'
6953	'Darfield, New Zealand'	'2010'	'Pages Road Pumping Station'	7.00	53.5	0.32	19.59	12.46	206.00	1.22	'DARFIELD\PRPCS.AT2'
6969	'Darfield, New Zealand'	'2010'	'Styx Mill Transfer Station '	7.00	48.4	0.23	12.36	9.37	247.50	1.43	'DARFIELD\SMTCS02W.AT2'
6975	'Darfield, New Zealand'	'2010'	'TPLC'	7.00	34.8	0.87	20.57	12.42	249.28	1.01	'DARFIELD\TPLCS63W.AT2'

Table C-17: Characteristics of selected natural ground motions related to $T^* = T_b = 5$ sec and $T_r = 2{,}475$ years.

Record Sequence Number	Earthquake Name	YEAR	Station Name	Earthquake Magnitude (Mw)	EpiD (km)	PGA (g)	PGV (cm/sec)	PGD (cm)	Vs30 (m/s)	Scaling factor	Component file name
172	'Imperial Valley-06'	'1979'	'El Centro Array #1'	6.53	35.2	0.07	3.59	1.53	237.33	4.75	'IMPVALL.H\H-E01230.AT2'
176	'Imperial Valley-06'	'1979'	'El Centro Array #13'	6.53	36.0	0.05	3.54	2.20	249.92	3.86	'IMPVALL.H\H-E13230.AT2'
777	'Loma Prieta'	'1989'	'Hollister City Hall'	6.93	47.9	0.22	15.25	7.53	198.77	2.11	'LOMAP\HCH180.AT2'
838	'Landers'	'1992'	'Barstow'	7.28	94.8	0.07	7.28	2.88	370.08	4.31	'LANDERS\BRS090.AT2'
1148	'Kocaeli, Turkey'	'1999'	'Arcelik'	7.51	53.7	0.08	7.99	7.32	523.00	1.77	'KOCAELI\ARE090.AT2'
1161	'Kocaeli, Turkey'	'1999'	'Gebze'	7.51	47.0	0.19	14.12	5.77	792.00	1.58	'KOCAELI\GBZ270.AT2'
1194	'Chi-Chi, Taiwan'	'1999'	'CHY025'	7.62	32.2	0.17	38.03	32.64	277.50	1.03	'CHICHI\CHY025-N.AT2'
1228	'Chi-Chi, Taiwan'	'1999'	'CHY076'	7.62	65.4	0.03	8.82	7.18	169.84	3.52	'CHICHI\CHY076-N.AT2'
1476	'Chi-Chi, Taiwan'	'1999'	'TCU029'	7.62	79.2	0.06	20.78	25.64	406.53	0.76	'CHICHI\TCU029-N.AT2'
1488	'Chi-Chi, Taiwan'	'1999'	'TCU048'	7.62	43.3	0.10	24.65	21.48	551.21	0.93	'CHICHI\TCU048-N.AT2'
1494	'Chi-Chi, Taiwan'	'1999'	'TCU054'	7.62	37.6	0.14	30.14	24.90	460.69	1.72	'CHICHI\TCU054-N.AT2'
1499	'Chi-Chi, Taiwan'	'1999'	'TCU060'	7.62	45.4	0.09	28.04	27.10	375.42	2.65	'CHICHI\TCU060-N.AT2'
1499	'Chi-Chi, Taiwan'	'1999'	'TCU060'	7.62	45.4	0.09	28.04	27.10	375.42	1.53	'CHICHI\TCU060-N.AT2'
1505	'Chi-Chi, Taiwan'	'1999'	'TCU068'	7.62	47.9	0.53	213.12	222.68	487.34	0.50	'CHICHI\TCU068-N.AT2'
1508	'Chi-Chi, Taiwan'	'1999'	'TCU072'	7.62	21.4	0.28	28.72	32.92	468.14	2.83	'CHICHI\TCU072-N.AT2'
1526	'Chi-Chi, Taiwan'	'1999'	'TCU098'	7.62	99.7	0.05	17.20	17.44	346.56	1.52	'CHICHI\TCU098-N.AT2'
1527	'Chi-Chi, Taiwan'	'1999'	'TCU100'	7.62	42.8	0.09	39.53	32.65	535.13	1.90	'CHICHI\TCU100-N.AT2'
1531	'Chi-Chi, Taiwan'	'1999'	'TCU104'	7.62	49.3	0.09	23.50	19.80	410.45	0.99	'CHICHI\TCU104-N.AT2'
1536	'Chi-Chi, Taiwan'	'1999'	'TCU110'	7.62	29.5	0.12	32.66	22.63	212.72	1.93	'CHICHI\TCU110-N.AT2'
1538	'Chi-Chi, Taiwan'	'1999'	'TCU112'	7.62	46.3	0.07	19.14	20.08	190.54	1.98	'CHICHI\TCU112-N.AT2'
1538	'Chi-Chi, Taiwan'	'1999'	'TCU112'	7.62	46.3	0.07	19.14	20.08	190.54	1.57	'CHICHI\TCU112-N.AT2'
1544	'Chi-Chi, Taiwan'	'1999'	'TCU119'	7.62	52.3	0.06	15.30	11.83	221.70	2.99	'CHICHI\TCU119-N.AT2'
1548	'Chi-Chi, Taiwan'	'1999'	'TCU128'	7.62	63.3	0.09	44.89	29.12	599.64	1.09	'CHICHI\TCU128-N.AT2'
1554	'Chi-Chi, Taiwan'	'1999'	'TCU145'	7.62	51.2	0.05	19.51	17.65	240.43	1.61	'CHICHI\TCU145-W.AT2'
2616	'Chi-Chi, Taiwan-03'	'1999'	'TCU063'	6.20	40.9	0.03	5.29	4.80	476.14	4.95	'CHICHI.03\TCU063E.AT2'
5776	'Iwate'	'2008'	'Kami, Miyagi Miyazaki City'	6.90	47.2	0.07	5.98	3.71	477.55	4.75	'IWATE\54010EW.AT2'
5823	'El Mayor-Cucapah'	'2010'	'Chihuahua'	7.20	20.6	0.28	15.91	12.99	242.05	1.95	'SIERRA.MEX\CHI090.AT2'
5838	'El Mayor-Cucapah'	'2010'	'El Centro - Meloland Geotechnic'	7.20	55.3	0.13	9.11	6.50	186.21	1.33	'SIERRA.MEX\01794270.AT2'
6886	'Darfield, New Zealand'	'2010'	'Canterbury Aero Club'	7.00	41.4	0.31	20.19	16.10	280.26	1.48	'DARFIELD\CACSN50W.AT2'
6897	'Darfield, New Zealand'	'2010'	'DSLC'	7.00	13.4	0.32	14.58	9.50	295.74	2.21	'DARFIELD\DSLCN63E.AT2'

Table C-18: Characteristics of selected natural ground motions related to $T^* = T_b = 5$ sec and $T_r = 3{,}899$ years.

Record Sequence Number	Earthquake Name	YEAR	Station Name	Earthquake Magnitude (Mw)	EpiD (km)	PGA (g)	PGV (cm/sec)	PGD (cm)	Vs30 (m/s)	Scaling factor	Component file name
187	'Imperial Valley-06'	'1979'	'Parachute Test Site'	6.53	48.6	0.16	7.25	5.04	348.69	4.79	'IMPVALL.H\H-PTS315.AT2'
266	'Victoria, Mexico'	'1980'	'Chihuahua'	6.33	36.7	0.10	5.65	1.92	242.05	3.95	'VICT\CHI192.AT2'
879	'Landers'	'1992'	'Lucerne'	7.28	44.0	0.82	41.09	29.83	1369.00	0.89	'LANDERS\LCN345.AT2'
1148	'Kocaeli, Turkey'	'1999'	'Arcelik'	7.51	53.7	0.08	7.99	7.32	523.00	2.10	'KOCAELI\ARE090.AT2'
1161	'Kocaeli, Turkey'	'1999'	'Gebze'	7.51	47.0	0.19	14.12	5.77	792.00	1.88	'KOCAELI\GBZ270.AT2'
1181	'Chi-Chi, Taiwan'	'1999'	'CHY004'	7.62	71.6	0.04	6.13	5.53	271.30	2.48	'CHICHI\CHY004-W.AT2'
1196	'Chi-Chi, Taiwan'	'1999'	'CHY027'	7.62	59.4	0.05	7.98	6.20	210.01	2.70	'CHICHI\CHY027-N.AT2'
1228	'Chi-Chi, Taiwan'	'1999'	'CHY076'	7.62	65.4	0.03	8.82	7.18	169.84	4.18	'CHICHI\CHY076-N.AT2'
1239	'Chi-Chi, Taiwan'	'1999'	'CHY093'	7.62	71.9	0.04	5.91	4.94	190.49	1.57	'CHICHI\CHY093-W.AT2'
1240	'Chi-Chi, Taiwan'	'1999'	'CHY094'	7.62	51.2	0.04	14.07	9.95	221.92	1.68	'CHICHI\CHY094-W.AT2'
1488	'Chi-Chi, Taiwan'	'1999'	'TCU048'	7.62	43.3	0.10	24.65	21.48	551.21	1.11	'CHICHI\TCU048-N.AT2'
1488	'Chi-Chi, Taiwan'	'1999'	'TCU048'	7.62	43.3	0.10	24.65	21.48	551.21	1.96	'CHICHI\TCU048-N.AT2'
1490	'Chi-Chi, Taiwan'	'1999'	'TCU050'	7.62	41.5	0.09	42.16	31.36	542.41	2.51	'CHICHI\TCU050-N.AT2'
1494	'Chi-Chi, Taiwan'	'1999'	'TCU054'	7.62	37.6	0.14	30.14	24.90	460.69	2.30	'CHICHI\TCU054-N.AT2'
1510	'Chi-Chi, Taiwan'	'1999'	'TCU075'	7.62	20.7	0.23	50.92	25.02	573.02	2.10	'CHICHI\TCU075-N.AT2'
1526	'Chi-Chi, Taiwan'	'1999'	'TCU098'	7.62	99.7	0.05	17.20	17.44	346.56	1.80	'CHICHI\TCU098-N.AT2'
1527	'Chi-Chi, Taiwan'	'1999'	'TCU100'	7.62	42.8	0.09	39.53	32.65	535.13	1.20	'CHICHI\TCU100-N.AT2'
1528	'Chi-Chi, Taiwan'	'1999'	'TCU101'	7.62	45.1	0.17	46.70	48.37	389.41	1.61	'CHICHI\TCU101-N.AT2'
1529	'Chi-Chi, Taiwan'	'1999'	'TCU102'	7.62	45.6	0.18	68.43	51.64	714.27	1.20	'CHICHI\TCU102-N.AT2'
1532	'Chi-Chi, Taiwan'	'1999'	'TCU105'	7.62	50.8	0.06	23.14	18.92	575.54	2.02	'CHICHI\TCU105-N.AT2'
1538	'Chi-Chi, Taiwan'	'1999'	'TCU112'	7.62	46.3	0.07	19.14	20.08	190.54	2.36	'CHICHI\TCU112-N.AT2'
1546	'Chi-Chi, Taiwan'	'1999'	'TCU122'	7.62	21.8	0.24	41.10	30.80	475.46	1.84	'CHICHI\TCU122-N.AT2'
2503	'Chi-Chi, Taiwan-03'	'1999'	'CHY094'	6.20	53.9	0.02	8.07	4.59	221.92	2.49	'CHICHI.03\CHY094W.AT2'
2701	'Chi-Chi, Taiwan-04'	'1999'	'CHY026'	6.20	47.2	0.03	4.22	2.34	226.01	3.83	'CHICHI.04\CHY026E.AT2'
3548	'Loma Prieta'	'1989'	'Los Gatos - Lexington Dam'	6.93	20.4	0.14	27.01	16.59	1070.34	2.94	'LOMAP\LEX090.AT2'
5823	'El Mayor-Cucapah'	'2010'	'Chihuahua'	7.20	20.6	0.28	15.91	12.99	242.05	2.32	'SIERRA.MEX\CHI090.AT2'
5823	'El Mayor-Cucapah'	'2010'	'Chihuahua'	7.20	20.6	0.28	15.91	12.99	242.05	1.71	'SIERRA.MEX\CHI090.AT2'
5831	'El Mayor-Cucapah'	'2010'	'EJIDO SALTILLO'	7.20	18.7	0.18	19.32	13.98	242.05	2.48	'SIERRA.MEX\SAL090.AT2'
6013	'El Mayor-Cucapah'	'2010'	'El Centro - Meadows Union School'	7.20	58.9	0.10	8.34	5.39	276.25	2.58	'SIERRA.MEX\2027A090.AT2'
6886	'Darfield, New Zealand'	'2010'	'Canterbury Aero Club'	7.00	41.4	0.31	20.19	16.10	280.26	1.75	'DARFIELD\CACSN50W.AT2'

Table C-19: Characteristics of selected natural ground motions related to $T^* = T_b = 5$ sec and $T_r = 7{,}462$ years.

Record Sequence Number	Earthquake Name	YEAR	Station Name	Earthquake Magnitude (Mw)	EpiD (km)	PGA (g)	PGV (cm/sec)	PGD (cm)	Vs30 (m/s)	Scaling factor	Component file name
1148	'Kocaeli, Turkey'	'1999'	'Arcelik'	7.51	53.7	0.08	7.99	7.32	523.00	2.66	'KOCAELI\ARE090.AT2'
1161	'Kocaeli, Turkey'	'1999'	'Gebze'	7.51	47.0	0.19	14.12	5.77	792.00	3.02	'KOCAELI\GBZ270.AT2'
1195	'Chi-Chi, Taiwan'	'1999'	'CHY026'	7.62	42.0	0.07	24.11	15.69	226.01	1.99	'CHICHI\CHY026-N.AT2'
1196	'Chi-Chi, Taiwan'	'1999'	'CHY027'	7.62	59.4	0.05	7.98	6.20	210.01	3.42	'CHICHI\CHY027-N.AT2'
1233	'Chi-Chi, Taiwan'	'1999'	'CHY082'	7.62	55.0	0.08	9.02	7.20	193.69	2.78	'CHICHI\CHY082-N.AT2'
1239	'Chi-Chi, Taiwan'	'1999'	'CHY093'	7.62	71.9	0.04	5.91	4.94	190.49	1.99	'CHICHI\CHY093-W.AT2'
1240	'Chi-Chi, Taiwan'	'1999'	'CHY094'	7.62	51.2	0.04	14.07	9.95	221.92	2.13	'CHICHI\CHY094-W.AT2'
1476	'Chi-Chi, Taiwan'	'1999'	'TCU029'	7.62	79.2	0.06	20.78	25.64	406.53	1.14	'CHICHI\TCU029-N.AT2'
1477	'Chi-Chi, Taiwan'	'1999'	'TCU031'	7.62	80.1	0.07	26.61	29.89	489.22	1.69	'CHICHI\TCU031-N.AT2'
1477	'Chi-Chi, Taiwan'	'1999'	'TCU031'	7.62	80.1	0.07	26.61	29.89	489.22	1.87	'CHICHI\TCU031-N.AT2'
1479	'Chi-Chi, Taiwan'	'1999'	'TCU034'	7.62	87.9	0.07	12.55	13.70	393.77	2.90	'CHICHI\TCU034-N.AT2'
1484	'Chi-Chi, Taiwan'	'1999'	'TCU042'	7.62	78.4	0.08	19.40	20.41	578.98	1.68	'CHICHI\TCU042-N.AT2'
1488	'Chi-Chi, Taiwan'	'1999'	'TCU048'	7.62	43.3	0.10	24.65	21.48	551.21	1.41	'CHICHI\TCU048-N.AT2'
1488	'Chi-Chi, Taiwan'	'1999'	'TCU048'	7.62	43.3	0.10	24.65	21.48	551.21	2.49	'CHICHI\TCU048-N.AT2'
1495	'Chi-Chi, Taiwan'	'1999'	'TCU055'	7.62	35.9	0.16	59.08	32.09	359.13	1.94	'CHICHI\TCU055-N.AT2'
1521	'Chi-Chi, Taiwan'	'1999'	'TCU089'	7.62	7.0	0.19	21.03	21.04	671.52	3.67	'CHICHI\TCU089-N.AT2'
1526	'Chi-Chi, Taiwan'	'1999'	'TCU098'	7.62	99.7	0.05	17.20	17.44	346.56	2.29	'CHICHI\TCU098-N.AT2'
1527	'Chi-Chi, Taiwan'	'1999'	'TCU100'	7.62	42.8	0.09	39.53	32.65	535.13	2.86	'CHICHI\TCU100-N.AT2'
1527	'Chi-Chi, Taiwan'	'1999'	'TCU100'	7.62	42.8	0.09	39.53	32.65	535.13	1.53	'CHICHI\TCU100-N.AT2'
1528	'Chi-Chi, Taiwan'	'1999'	'TCU101'	7.62	45.1	0.17	46.70	48.37	389.41	2.05	'CHICHI\TCU101-N.AT2'
1531	'Chi-Chi, Taiwan'	'1999'	'TCU104'	7.62	49.3	0.09	23.50	19.80	410.45	1.50	'CHICHI\TCU104-N.AT2'
1536	'Chi-Chi, Taiwan'	'1999'	'TCU110'	7.62	29.5	0.12	32.66	22.63	212.72	2.91	'CHICHI\TCU110-N.AT2'
1538	'Chi-Chi, Taiwan'	'1999'	'TCU112'	7.62	46.3	0.07	19.14	20.08	190.54	2.99	'CHICHI\TCU112-N.AT2'
5823	'El Mayor-Cucapah'	'2010'	'Chihuahua'	7.20	20.6	0.28	15.91	12.99	242.05	2.94	'SIERRA.MEX\CHI090.AT2'
5837	'El Mayor-Cucapah'	'2010'	'El Centro - Imperial & Ross'	7.20	60.4	0.27	11.40	8.03	229.25	3.17	'SIERRA.MEX\01711-90.AT2'
6013	'El Mayor-Cucapah'	'2010'	'El Centro - Meadows Union School'	7.20	58.9	0.10	8.34	5.39	276.25	3.27	'SIERRA.MEX\2027A090.AT2'
6887	'Darfield, New Zealand'	'2010'	'Christchurch Botanical Gardens'	7.00	47.0	0.12	16.07	13.63	187.00	2.13	'DARFIELD\CBGSS01W.AT2'
6960	'Darfield, New Zealand'	'2010'	'Riccarton High School '	7.00	42.5	0.31	17.39	7.59	293.00	1.99	'DARFIELD\RHSCS04W.AT2'
6969	'Darfield, New Zealand'	'2010'	'Styx Mill Transfer Station '	7.00	48.4	0.23	12.36	9.37	247.50	2.72	'DARFIELD\SMTCS02W.AT2'
6975	'Darfield, New Zealand'	'2010'	'TPLC'	7.00	34.8	0.87	20.57	12.42	249.28	1.92	'DARFIELD\TPLCS63W.AT2'

Table C-20: Characteristics of selected natural ground motions related to $T^* = T_b = 5$ sec and $T_r = 10{,}000$ years.

Record Sequence Number	Earthquake Name	YEAR	Station Name	Earthquake Magnitude (Mw)	EpiD (km)	PGA (g)	PGV (cm/sec)	PGD (cm)	Vs30 (m/s)	Scaling factor	Component file name
192	'Imperial Valley-06'	'1979'	'Westmorland Fire Sta'	6.53	52.8	0.09	7.01	2.68	193.67	3.42	'IMPVALL.H\H-WSM180.AT2'
879	'Landers'	'1992'	'Lucerne'	7.28	44.0	0.82	41.09	29.83	1369.00	1.25	'LANDERS\LCN345.AT2'
1148	'Kocaeli, Turkey'	'1999'	'Arcelik'	7.51	53.7	0.08	7.99	7.32	523.00	2.95	'KOCAELI\ARE090.AT2'
1161	'Kocaeli, Turkey'	'1999'	'Gebze'	7.51	47.0	0.19	14.12	5.77	792.00	2.64	'KOCAELI\GBZ270.AT2'
1196	'Chi-Chi, Taiwan'	'1999'	'CHY027'	7.62	59.4	0.05	7.98	6.20	210.01	3.79	'CHICHI\CHY027-N.AT2'
1233	'Chi-Chi, Taiwan'	'1999'	'CHY082'	7.62	55.0	0.08	9.02	7.20	193.69	3.08	'CHICHI\CHY082-N.AT2'
1239	'Chi-Chi, Taiwan'	'1999'	'CHY093'	7.62	71.9	0.04	5.91	4.94	190.49	2.21	'CHICHI\CHY093-W.AT2'
1240	'Chi-Chi, Taiwan'	'1999'	'CHY094'	7.62	51.2	0.04	14.07	9.95	221.92	2.36	'CHICHI\CHY094-W.AT2'
1477	'Chi-Chi, Taiwan'	'1999'	'TCU031'	7.62	80.1	0.07	26.61	29.89	489.22	1.87	'CHICHI\TCU031-N.AT2'
1477	'Chi-Chi, Taiwan'	'1999'	'TCU031'	7.62	80.1	0.07	26.61	29.89	489.22	2.07	'CHICHI\TCU031-N.AT2'
1479	'Chi-Chi, Taiwan'	'1999'	'TCU034'	7.62	87.9	0.07	12.55	13.70	393.77	2.53	'CHICHI\TCU034-N.AT2'
1488	'Chi-Chi, Taiwan'	'1999'	'TCU048'	7.62	43.3	0.10	24.65	21.48	551.21	2.76	'CHICHI\TCU048-N.AT2'
1490	'Chi-Chi, Taiwan'	'1999'	'TCU050'	7.62	41.5	0.09	42.16	31.36	542.41	3.54	'CHICHI\TCU050-N.AT2'
1491	'Chi-Chi, Taiwan'	'1999'	'TCU051'	7.62	38.5	0.11	29.90	26.37	350.06	2.72	'CHICHI\TCU051-N.AT2'
1492	'Chi-Chi, Taiwan'	'1999'	'TCU052'	7.62	39.6	0.20	144.05	154.05	579.10	0.84	'CHICHI\TCU052-N.AT2'
1496	'Chi-Chi, Taiwan'	'1999'	'TCU056'	7.62	39.7	0.12	41.78	31.50	403.20	2.10	'CHICHI\TCU056-N.AT2'
1499	'Chi-Chi, Taiwan'	'1999'	'TCU060'	7.62	45.4	0.09	28.04	27.10	375.42	2.57	'CHICHI\TCU060-N.AT2'
1503	'Chi-Chi, Taiwan'	'1999'	'TCU065'	7.62	26.7	0.26	69.41	57.36	305.85	0.71	'CHICHI\TCU065-N.AT2'
1505	'Chi-Chi, Taiwan'	'1999'	'TCU068'	7.62	47.9	0.53	213.12	222.68	487.34	0.84	'CHICHI\TCU068-N.AT2'
1526	'Chi-Chi, Taiwan'	'1999'	'TCU098'	7.62	99.7	0.05	17.20	17.44	346.56	2.54	'CHICHI\TCU098-N.AT2'
1531	'Chi-Chi, Taiwan'	'1999'	'TCU104'	7.62	49.3	0.09	23.50	19.80	410.45	1.66	'CHICHI\TCU104-N.AT2'
1538	'Chi-Chi, Taiwan'	'1999'	'TCU112'	7.62	46.3	0.07	19.14	20.08	190.54	3.31	'CHICHI\TCU112-N.AT2'
1546	'Chi-Chi, Taiwan'	'1999'	'TCU122'	7.62	21.8	0.24	41.10	30.80	475.46	2.59	'CHICHI\TCU122-N.AT2'
1548	'Chi-Chi, Taiwan'	'1999'	'TCU128'	7.62	63.3	0.09	44.89	29.12	599.64	1.82	'CHICHI\TCU128-N.AT2'
2710	'Chi-Chi, Taiwan-04'	'1999'	'CHY036'	6.20	34.8	0.05	4.35	2.58	233.14	3.89	'CHICHI.04\CHY036E.AT2'
3843	'Chi-Chi (aftershock 2), Taiwan'	'1999'	'CHY002'	6.20	45.7	0.04	15.98	12.08	235.13	4.69	'CHICHI.03\CHY002W.AT2'
6886	'Darfield, New Zealand'	'2010'	'Canterbury Aero Club'	7.00	41.4	0.31	20.19	16.10	280.26	2.47	'DARFIELD\CACSN50W.AT2'
6952	'Darfield, New Zealand'	'2010'	'Papanui High School '	7.00	46.9	0.28	10.21	8.91	263.20	3.02	'DARFIELD\PPHSS57E.AT2'
6975	'Darfield, New Zealand'	'2010'	'TPLC'	7.00	34.8	0.87	20.57	12.42	249.28	2.13	'DARFIELD\TPLCS63W.AT2'
8064	'Christchurch, New Zealand'	'2011'	'Christchurch Cathedral College'	6.20	5.8	0.80	22.59	9.21	198.00	4.80	'CCHURCH\CCCCN64E.AT2'